Linear Actuators for Locomotion of Microrobots

by

Haiwei Lu

M.Eng., B.Eng. (Elec.)

Submitted in fulfilment of the requirements for the degree of Doctor of Philosophy

University of Technology, Sydney

June 2007

CERTIFICATE OF AUTHORSHIP / ORIGINALITY

I certify that the work in this thesis has not previously been submitted for a degree nor has it been submitted as part of requirements for a degree except as fully acknowledged within the text.

I also certify that the thesis has been written by me. Any help that I have received in my research work and the preparation of the thesis itself has been acknowledged. In addition, I certify that all information sources and literature used are indicated in the thesis.

Name of Candidate: **Haiwei Lu**

Signature of Candidate:

Production Note:
Signature removed prior to publication. 03/10/2007

To my mother, my wife, and my daughter

ABSTRACT

The successful development of the miniaturisation techniques for electronic components and devices has paved the way for the miniaturisation in other technological fields. In the past two decades, the research achievements in micromechatronics have spurred fast development of micro machines and micro robotic systems. Miniature or micro actuators are the critical components to make these machines more dexterous, compact and cost effective.

The main purpose of this dissertation is to develop micro actuators suitable for the locomotion of an in-pipe or endoscopic microrobot. The content of the thesis covers the selection of the actuation principle, robotic system design, actuator design and prototype construction, performance analysis, and design, analysis, and implementation of the appropriate drive control system.

Among different types of actuation principles, piezoelectric and electromagnetic actuators are the two major candidates for the micro robotic systems. In order to find a suitable actuation principle for the desired robotic application, a comparative study was conducted on the scaling effects, attainable energy density, and dynamic performances of both types of actuators. Through the study, it was concluded that the electromagnetic actuator is more suitable for the endoscopic microrobot.

Linear actuators are the common design used for the locomotion of microrobots due to many advantages compared to their rotational counterparts. Through a thorough review and comparison of the electromagnetic linear actuator topologies, a moving-coil tubular linear actuator was chosen as the first design due to its simplest structure. Via the magnetic circuit analysis and numerical magnetic field solutions, the actuator was designed for optimum force capability, and the electromagnetic force and the machine parameters of the actuator were predicted. According to the results obtained from the magnetic field analysis, the dynamic model of the actuation system with a driving

control scheme was established and used in the actuation performance analysis of the robotic system.

Based on the experience achieved through the first design, a new moving-magnet tubular linear actuator was designed. The methodology developed in the design and analysis of the moving-coil linear actuator was adopted for the moving-magnet actuator design. However, the optimal design is more complicated due to the multi-pole and multi-phase structure of the moving-magnet actuator. The electromagnetic force of the actuator was analysed under the condition of different excitation methods. An enhanced parameter computation method is proposed for predicting the actuator parameters. Based on the results of magnetic field analysis, a comprehensive dynamic model of the actuator was developed. Through the coupled field-circuit analysis, this model can predict accurately the dynamic performance of the actuator. The characteristics analysis shows that the performance of the moving-magnet actuator is much better than that of the moving-coil actuator.

Two prototypes of the moving-magnet tubular linear actuator with different dimensions were constructed to verify the performance and the scaling theory. Various precision machining techniques were employed during the fabrication. The performances and parameters of the two different prototypes were measured and the results agree substantially with the theory.

The brushless DC drive method was chosen for the driving control of the proposed linear actuator because of the compact circuit topology and simple implementation, which are two essential factors for micro applications. A sensorless control scheme based on the back EMF was developed as physical position sensors are not permitted in such a micro system. The control scheme was then applied to the locomotion control of the proposed microrobot. The system simulation shows that the control performances of both the actuator and microrobot are satisfactory.

A dSPACE prototyping system based driving control hardware was designed and implemented to experimentally verify the control design. The experimental results agree substantially with the theoretical work.

ACKNOWLEDGMENTS

I am gratefully indebted to my supervisor, Prof. Jianguo Zhu, for his inspiring guidance and encouragement throughout the development of this thesis. His valuable comments and suggestions definitely improved the quality of entire research work.

I wish to express my gratitude to my co-supervisor, A/Prof. Quang Ha for his helpful advice and support.

I also wish to express sincere thanks to Dr. Youguang Guo, Dr. Zhiwei Lin, Mr. Ram Chamdru, Miss Ying Yan, Dr. Peter A. Watterson, Dr. Greg Hunter, and other colleagues in the Centre for Electric Machines and Power Electronics (CEMPE), UTS, for their fruitful discussions, advices and assistances.

Many thanks are due to the staff in the faculty's workshop, i.e. Mr. Ron Smith and Mr. Richard Moore, for their elaborate mechanical work in the manufacturing of the prototypes. Without their professional job, the project would not be successful.

I feel very grateful to Mr. Jiang Chen of the CEMPE Laboratory for his assistance in preparing equipments and experimental setup for the parameter and performance tests. Thanks also go to Mr. Russell Nicholson for his support and advice.

Acknowledgements go to Mr. David Baer, Manager of the Laser Micromachining Solutions (LMS) in Macquarie University, Sydney, for providing the laser cutting services in manufacturing the prototype components.

Special gratitude goes to Mr. Adam Goldsmith and Dr. Shuli Jiao in CHK GridSense Pty. Ltd. for their understanding and support during my thesis work.

Thanks also go to the Department of Education, Training and Youth Affairs, Australia, for providing an International Postgraduate Research Scholarship (IPRS), which allowed me to carry out four years of PhD study.

Last but not the least, my heartfelt gratitude goes to my beloved wife, Wei Li, for her patience, sacrifices, and great support during this work, to my mother and sister in China for their consistent love and encouragement, and to my lovely daughter, Yonghan (Renée) Lu, who brings a lot of happiness into my life, and therefore I would like to dedicate this work to them.

TABLE OF CONTENTS

LIST OF SYMBOLS[1]

$\vec{A}$	Magnetic vector potential (Wb/m)
A	Area (m^2)
A_c	Cross sectional area of a conductor (m^2)
A_{cl}	Area enclosed by a coil (m^2)
A_g	Cross sectional area of an air gap (m^2)
A_p	Contact area (m^2)
A_s	Surface area of a conductor (m^2)
$\vec{B}$	Magnetic flux density vector
B_g	Flux density in an air gap (T)
B_{gr}	Radial component of flux density in an air gap (T)
B_m	Magnetising flux density in a phase winding (T)
B_r	Radial component of flux density (T)
C_d	Clamped capacitance (SI)
D_i	First-rank tensor electrical displacement (C/m^2)
d_{ikl}, d_{in}, d_{mk}	Third-rank and second-rank tensor piezoelectric constant (m/V)
E	Electrical field strength (V/m)
E_k	First-rank tensor electric field strength (V/m)
E_m, e_m	Back electromotive force caused by permanent magnets (V)
$\hat{E}_m$	Complex notation of E_m
e_s	Back electromotive force caused by machine saliencies (V)
F	Force (N)
$\hat{F}$	Complex notation of force
F_{em}	Electromagnetic force (N)
F_{emm}	Electromagnetic force generated by permanent magnets (N)
F_{emp}	Electromagnetic force under one pole (N)
F_{ems}	Electromagnetic force generated by machine saliencies (N)

[1] Symbols which are not listed here are defined where they appear.

F_f	Frictional force (N)
F_{load}	Load force (N)
F_{mm}	Magnetomotive fore (A·t)
F_N	Normal force (N)
F_{sp}	Elastic force of a spring (N)
g	Length of an air gap (m)
$\vec{H}$	Magnetic field strength vector
H_c	Coercive force of a permanent magnet (A/m)
h_c	Height of a coil (m)
h_d	Thickness of friction layer in an ultrasonic motor (m)
h_m	Height of a permanent magnet (m)
h_p	Penetration of stator into friction layer in an ultrasonic motor (m)
h_s	Thickness of a piezoelectric segment (m)
I, i	Current (A)
$\hat{I}$	Complex notation of current $\hat{I} = Ie^{j\omega t}$
I_0	*rms* value of phase current (A)
I_1	Conductor current (A)
I_m	Field excitation current (A)
I_{rated}	Rated winding current (A)
$\vec{J}$	Current density vector
J	Current density (A/m^2)
J_s	Effective current density (A/m^2)
K_e	Back electromotive force coefficient (V·s/m)
K_f	Force coefficient (N/A)
K_{sp}	Elastic constant (N/m)
k_d	Deformation coefficient of friction layer in an ultrasonic motor
k_{ff}	Fill factor
k_m	Magnetic occupation ratio
k_p	Coefficient of restitution
k_T	Thermal conductivity (W/m·K)
k_v	Wave number of a plane wave
L	Inductance (H)

L_a	Self inductance of a coil (H)
L_1	Self inductance of a conductor (H)
L_{1m}	Mutual inductance between a conductor and an excitation coil (H)
L_m	Self inductance of an excitation coil (H)
L_{jk}^{app}	Apparent inductance between windings j and k (H)
L_{jk}^{diff}	Differential inductance between windings j and k (H)
$\vec{l}$	Length vector
l_c	Length of a conductor, or mean circumference of a coil (m)
$\vec{M}$	Magnetisation vector (A/m)
m_a	Mass of a moving coil or translator (kg)
m_s	Mass of a stator (kg)
N_t	Number of turns of a coil (turns)
p	Pressure (N/m^2)
Q	Heat flow (W)
R	Resistance (Ω)
R_a	Winding Resistance (Ω)
R_{coil}	Coil resistance (Ω)
R_{ph}	Phase resistance (Ω)
r_c	Radius of a conductor or mean radius of a coil (m)
r_r	Effective radius of rotor ring in an ultrasonic motor (m)
S_{ij}, S_m	Second-rank and first-rank tensor mechanical strain
s_{ijkl}, s_{mn}	Fourth-rank and second-rank tensor elastic compliance coefficient (m^2/N)
s_{ijkl}^E , s_{mn}^E	Elastic compliance coefficient at constant electric field (m^2/N)
T	Temperature (K)
T_{kl}, T_n	Second-rank and first-rank tensor mechanical stress (N/m^2)
U, u	Voltage (V)
$\hat{U}$	Complex notation of voltage $\hat{U} = Ue^{j\omega t}$
U_0	*rms* value of phase voltage (V)
u_{a0}, u_{b0}, u_{c0}	Phase terminal voltages (V)
u_n	Neutral voltage (V)
V	Volume (m^3)

v_a, v_m	Velocity of a moving coil and a translator, respectively (m/s)
v_r	Rotor velocity (m/s)
v_s	Stator velocity (m/s)
W_E	Electrical field energy (J)
$[W_E]$	Electrical field energy density (J/m^3)
W_M, W'_M	Magnetic field energy and co-energy (J)
$[W_M]$, $[W'_M]$	Magnetic field energy density and co-energy density (J/m^3)
x, y, z	Cartesian coordinates
$\hat{x}$	Complex notation of x
$\dot{x}$	dx/dt
$\hat{\dot{x}}$	Complex notation of $\dot{x}$
Y	Young's Modulus
Z, Z_0	Elastic impedances of a piezoelectric actuator
ε	Electrical permittivity (F/m)
ε_r	Relative electrical permittivity
ε_0	Electrical permittivity of free air (F/m)
ε_{ik}^T, ε_{ik}^S	Electrical permittivity at constant stress and strain, respectively (F/m)
θ	Angle between a stationary and a moving windings
λ_j	Flux linkage of the j-th winding (Wb)
λ_m	Magnetising flux linkage (Wb)
λ_{jk}	k-th component of λ_j (Wb)
μ	Magnetic permeability (T·m/A)
μ_0	Magnetic permeability of free space (T·m/A)
μ_f	Coefficient of friction
μ_m	Permeability of a permanent magnet (T·m/A)
μ_r	Relative magnetic permeability
v_{ph}	Phase velocity of a plane wave
ξ	Characteristic size of an object
ρ	Resistivity (Ω·m)
ρ_e	Resistance per meter (Ω/m)
ρ_m	Mass density of a piezoelectric material (kg/m^3)
Γ	Torque (N·m)

τ	Pole pitch (m)
τ_c	Thickness of a pole-piece (m)
τ_m	Thickness of a permanent magnet (m)
Φ	Electromechanical coupling factor
ϕ	Magnetic flux (Wb)
ϕ_g	Magnetic flux in an air gap (Wb)
ϕ_p	Magnetic flux per pole (Wb)
ω	Angular frequency or speed (rad/s)
$\mathscr{F}$	Magnetic scalar potential (SI)
$\Re$	Reluctance (SI)
$\Re_g$	Reluctance of an air gap (SI)
$\Re_m$	Reluctance of a permanent magnet (SI)

LIST OF ACRONYMS

2D	Two-Dimensional
3D	Three-Dimensional
AC	Alternating Current
CAD	Computer Aided Design
DC	Direct Current
DOF	Degree of Freedom
DSP	Digital Signal Processors
ECDM	Electro-Chemical Discharge Machining
EDM	Electrical Discharge Machining
EMF	Electromotive Force
FE	Finite Element
FEM	Finite Element Method
FMA	Flexible Micro Actuator
GMM	Giant Magnetostrictive Material
GUI	Graphical User Interface
IDM	Impact Drive Mechanism
LIGA	*German:* Lithographisch Galvanoformingung und Abformung
LIM	Linear Induction Machines
LRM	Linear Reluctance Machine
LSM	Linear Synchronous Machine
MIS	Minimally Invasive Surgery
MMF	Magnetomotive Force
NdFeB	Neodymium Iron Boron
PM	Permanent Magnet
PWM	Pulse Width Modulation
PZT	Lead Zirconate Titanate
RTI	Real-Time Interface
SMA	Shape Memory Alloy
SME	Shape Memory Effect

SmCo	Samarium-Cobalt
SPWM	Sinusoidal PWM
TLA	Tubular Linear Actuator
ULSI	Ultra Large Scale Integration
ZCP	Zero-Crossing Point

LIST OF FIGURES

LIST OF TABLES

Chapter 1

INTRODUCTION

1.1 Background

As happened in the past centuries, the main objective of science and technology in the revolution is to explore new areas by finding new frontiers for knowledge. One of the main products of this revolution is the trend towards miniaturisation and this brings out the beginning of a new engineering era: the micro-engineering. Nowadays, miniaturisation technology is not only a new frontier for science and research, but also a tremendous opportunity for application and thus for industrial innovation and competitiveness [Lang 1999].

The trend towards miniaturisation has been driven by the inchoation and development of microelectronics. From vacuum tube to ultra large scale integration (ULSI), the advances of microelectronics paved the way for miniaturisation in other areas of technologies and researches in microscopic field is focusing greatly in the last two decades of the 20^{th} century. Among these advancements, one of the important and pervasive technological impacts could be that it changed drastically the way in which virtually all existing products are designed and fabricated, and brought on an evolution on the mechatronics, which represents the ultimate frontier of the technology. The advent of micromechatronics gives an answer to the question "How do we make such a tiny mechanism?" which was brought out by Professor Richard P. Feynman in his famous talk "There's plenty of room at the bottom" in 1959.

Micro robotics is one of the representative domains in micromechatronics, which incorporates multiple micro technologies such as micromechanics, micromachining, microelectronics and modern control theory. In the past two decades, the research achievements in micromechatronics have spurred fast development of micro machines and micro robotic systems. Many research institutes are involved in the study and development of novel microrobots with different principles, functions, and structures according to their applications.

Due to the nature of being tiny, the businesses in a narrow place are considered to be the optimum job for microrobots. A typical application is the industrial inspection and maintenance. Mobile microrobots equipped with flaw detection device, image sensor, maintenance tools and data transmission/reception device can be used inside the pipes of the energy or chemical plants for detecting and repairing the flaw area by the instruction from the control centre [Takeda 2001]. As a practice, a mobile microrobot proposed by Aoshima *et al.* [Aoshima 1989] which utilises the piezoelectric bimorph vibration to move inside the tubes is perhaps the earliest design found in the literature. After that, a number of in-pipe microrobots was proposed and developed by many researchers in the following decades.

Medical field is another promising application for microrobots. It has long been one of the serious dreams of medical surgeons to operate without any damaging effects on the patient. Endoscopy is an important procedure for the diagnosis of various pathologies. An idea to improve the present endoscopic technology is a self-navigating, independent and intelligent endoscopic microrobot. In considering the measuring within a human body, various data collection and local medicine injection will become possible by a kind of medical microrobot known as smart pill or capsule. In addition, microrobots can also be used for the microsurgery of a blood vessel and a medical treatment. For this purpose, they can be regarded as a biomedical application oriented in-pipe microrobot. A conceived medical microrobot named MEDIWORM was firstly proposed in [Ikuta 1988a]. The concept of the proposed microrobot is that it can be teleoperated by the

doctor and can actively move within the alimentary tract. Although this concept has been proposed for nearly twenty years, the studies on the intelligent medical microrobots are still in the primary stage. Nonetheless, some encouraging progresses have been achieved to make the idea come true. Capsule endoscopy M2A [Given 2004] and NORIKA3 [RF 2004] are the two successful developments towards the dream. In addition, many studies have been conducted to discover the effective methods for locomotion inside the human body and some achievements were applied in the trials to improve the conventional endoscope.

A robotic system is a mechanism composed of a set of links connected with joints that transfer motion and force from an input source to an output end-effector. Various actuators are hence the critical components in any robotic systems. Microsystems, especially microrobots, require new advanced miniature or micro actuators with small dimensions, simple mechanical construction and high reliability. Conventional actuators such as hydraulic, pneumatic, and electromagnetic actuators were naturally attempted in micro machines due to their successful applications in macro robotic systems. On the other hand, many new types of actuators are being researched and applied for micro robotic systems. These actuators rely on the use of different type of transducing materials and energy conversion principles. Examples of these actuators are piezoelectric, shape memory alloys (SMA), electrostatic, electrostrictive, and magnetostrictive actuators.

Among these different types of actuators, the piezoelectric and electromagnetic actuators are the two major candidates for micro robotic systems. Microrobots using the piezoelectric actuators have been developed and experimentally demonstrated by many researchers. In general, the piezoelectric actuators can provide high output force, extremely fine resolution, very fast response, and low power consumption. However, the very small fractional stroke (displacement per unit length) of the actuators severely limits the speed and displacement of the system. Moreover, the piezoelectric actuators usually require medium to high working voltages to achieve desirable displacement.

The electromagnetic actuators, especially electric machines, have been developed for more than a hundred years and they are the most commonly used actuation devices in the macro domain. The electromagnetic actuators feature high power density, medium force capability, large stroke, and fast response. Compared to other actuation principles, electromagnetic actuators have some attractive features for applications in micro systems. Since electromagnetic actuators have low input impedances and are current driven devices, this and the fact that low voltages are involved make packaging feasible and affordable for micro applications [Guckel 1998]. Moreover, electromagnetic actuators are integrated circuit friendly so that they can be co-fabricated and integrated with the up-to-date microelectronic devices. The major disadvantages of the electromagnetic actuators are the relatively small force density, thermal dissipation and the complex magnetic structure. Thanks to the development of the micro system technology, high performance magnetic materials have been successfully developed for micro applications and the manufacturing of micro machines with complicated structures is no longer a problem. The addition of permanent magnet technology to the present soft magnetic materials also produces an environment for many new devices for micro systems.

Although there are different actuation alternatives suitable for microrobots, it is difficult to find solutions that have small size, high resolution, large force, and large displacement at the same time. As a result, the best engineering solution is to select the most appropriate actuator for each specific application. The choice of mechanism is a balance between many different factors, such as actuation benefit, material properties, reproducibility, and process compatibility.

1.2 Thesis Overview

The main purpose of this dissertation is to develop micro actuators suitable for the

locomotion of an in-pipe or endoscopic microrobot. The content of the dissertation covers the following topics: (1) a comparative study of the piezoelectric and electromagnetic actuation principles and the selection of suitable actuation principle for the proposed microrobot; (2) a study on finding suitable topologies for the electromagnetic actuator; (3) design of the actuator based on the analytical and numerical electromagnetic field analysis and experimental verification; (4) dynamic modelling of the designed micro actuator and its application to the coupled field-circuit analysis for actuation performance analysis; (5) design of the proper control scheme for the actuator, its application to the locomotion control for the proposed microrobot, and experimental verification of the locomotion system.

In chapter 2, an extensive literature survey is conducted for an in-depth understanding of the state-of-the-art of the related technologies. The evolution of the robotic systems, especially the development of micro robotic systems is firstly reviewed. Different types of microrobots are thoroughly expounded based on the technology development.

Microrobots are mostly application-oriented and there is no "optimal" motion principle that is suitable to every case. Different applications require different system designs and actuation methods. Hence, various actuation principles and technologies applied in micro robotic systems are examined, including fluidic, electromagnetic, piezoelectric, electrostatic, electro-thermal, and other novel principles. This investigation leads to a thorough understanding of the development of the technologies and the advantages and drawbacks of these principles.

Since several actuation principles could be used in micro systems, the selection of appropriate actuation principles becomes an important issue that must be thought well before the design of the micro machines. In chapter 3, a comparative study on the piezoelectric and electromagnetic actuators is carried out. The scaling effect and attainable energy density are the important indicators to evaluate the performances of different actuation principles when they are downsized. Through the analysis, the

scaling effects and the attainable energy density of the piezoelectric and electromagnetic actuators are discussed and compared. The dynamic performances of the piezoelectric and electromagnetic actuators are then analysed and compared through a case study of the actuator. Based on the results obtained from the study, a proper actuation principle and method for the target application is concluded.

The scope of chapter 4 is to present the design methodology used in the development of linear electromagnetic actuator for the microrobot. Based on the understanding of the basic methods for designing the electromagnetic actuators and the special considerations of linear actuators, a moving-coil linear actuator is designed as the first attempt. Through 2D and 3D numerical magnetic field analysis, the electromagnetic force and machine parameters of the actuator are predicted. The locomotion mechanism for the microrobot is designed and the corresponding dynamic model of the system is established for the analysis of the actuation performances of the robotic system. The applied design and analysis methods set up the basic tools for the actuator design in the thesis.

In chapter 5, an improved design is presented by using the tubular moving-magnet topology. Important design considerations of the moving-magnet tubular linear actuator are examined in advance to determine a proper structure of the actuator. Detailed design and analysis, including the selection of dimensions, analysis of electromagnetic characteristics is performed based on the analytical and numerical magnetic field analysis.

A numerical method for calculating the dynamic inductances of the electromagnetic machines is discussed and applied to the prediction of the dynamic inductances of the designed actuator. Furthermore, a comprehensive dynamic model of the designed actuator is derived based on the results obtained from the magnetic field analysis, which is essential for the analysis and evaluation of the system performance.

Chapter 6 illustrates the construction of two laboratory prototypes of different sizes of the proposed linear actuator. The large size prototype is used for the verification of the conducted design and analysis as its dimensions with desired machining precision can be easily achieved. The small size prototype with the designed dimensions, on the other hand, is used to examine the fabrication techniques when the size of the actuator is getting smaller. The forces and parameters of the prototypes are re-examined according to the construction of the prototypes and the results are verified by experiments on the prototypes.

Chapter 7 is devoted to the design and analysis of the electronic control system for the designed actuator. In order to analyse the actuator performances with electronic converter, an improved machine dynamic model is developed and implemented in the SIMULINK environment by considering the electronic controlled operation of the machine. According to the specific application of the actuator, an appropriate sensorless control scheme is designed and analysed. By applying the proposed control scheme, the hardware of the electronic control system is implemented and experimentally tested based on the dSPACE prototyping system.

The locomotion control of the robot is discussed in chapter 8. Based on the studies conducted in chapter 4, an improved locomotion mechanism is proposed. To analyse the performance of the locomotion driven by the designed actuator, a comprehensive dynamic model of the robotic system is established and implemented by incorporating the kinetic characteristic of the system. An intermittent control strategy combined with the drive control of the linear actuator is developed and studied. The effectiveness of the system is verified by experiments on the actuation system.

Chapter 9 summarises the entire thesis work. Useful conclusions are drawn and possible future works are proposed based on the experiences obtained during the thesis work.

Chapter 2

LITERATURE SURVEY

2.1 Introduction

The scope of this thesis is to focus on the development of an actuator suitable for the locomotion of in-pipe/endoscopic microrobots. Various relevant technologies, such as the micro systems, robotics, actuators, and the corresponding driving control technologies, are involved. In order to have a full understanding of the state of the art of these technologies, an extensive literature survey is conducted and presented in this chapter.

The evolution of robotic systems, especially the development of the microrobots is firstly reviewed. Microrobots designed for various applications are thoroughly reviewed based on the development of the technology. Among those micro robotic applications, the biomedical field is one of the promising applications of the micro robotics and many microrobots have been designed for clinical operations. Hence, the microrobots specially used for the medical inspections and surgeries are discussed in detail in the survey.

Most of the designs of the micro robotic systems are application-oriented and there is no "optimal" motion principle that can be used for every case [Magnussen 1995]. Different applications suggest different system designs and actuation methods. Hence, various actuation principles and technologies applied in the micro robotic systems are examined, including the fluidic, electromagnetic, piezoelectric, electro-thermal, electrostatic, and

other novel principles. The investigation of these technologies leads to an in-depth understanding of the evolution of technologies and their advantages and drawbacks.

2.2 Microrobots

2.2.1 Introduction to robotics

The word "robot" was coined by the Czech playwright Karel Capek in his play *Rossum's Universal Robots* in 1920's [Rover 2006], which means forced labour or worker. Science fiction writer Isaac Asimov firstly used the word "robotics" in 1941 to describe the technology of robots and predicted the rise of a powerful robot industry. According to the definition released by the Robot Institute of America in 1979, a robot is a "reprogrammable, multifunctional manipulator designed to move material, parts, tools, or specialized devices through various programmed motions for the performance of a variety of tasks". Generally, a robot is considered to be an intelligent mechanical system with a combination of technologies in hardware/software, intelligent control, and autonomous and distributed system.

In fact, robots are originated by the ancient Greeks, Alexandrian and Roman engineers [Dimarogonas 1993]. The first machines were simple jointed mechanisms that were actuated by human operators. The incorporation of an energy source, other than the human, to actuate and move certain components of the machine was a very important step towards automation of motion. Perhaps one of the earliest "roboticists" was the great Greek engineer and inventor Ctesibios (ca. 283-247 B.C.) who applying knowledge of pneumatics and hydraulics invented the precision clock. Heron of Alexandria (ca. 1st century A.D.) building on Ctesibios' work, wrote the fundamental textbook *On Automatic Theatres, On Pneumatics and On Mechanics,* that is considered as the first well documented robotic system description outside of mythology [Rosheim

1994]. After that time, machines, mechanisms and robotic technology have evolved during the roman and medieval times, and the renaissance.

The industrial revolution in the second half of the 18th century and the following technology developments resulted in a considerable progress of the robotic machines. Newtonian mechanics was the principal driving force for the technologies during the time and enabled the development of heavy, large-scale industrials by replacing the physical work of humans with steam engines, vehicles, ships, general machinery and other equipment.

The discovery of the Voltaic Pile (battery) in the early 19th century led to significant discoveries on electromagnetic technology. H. C. Oersted in Denmark discovered the phenomenon of *electromagnetism* in 1820 and it initiated an extensive study about the mechanical movement caused by electric current. In 1821 British scientist Michael Faraday built an apparatus called "electromagnetic rotation" that the continuous circular motion was realized by a circular magnetic force around the wire. This was the *first primitive electromagnetic motor* and this developed into the earliest ancestor of the modern motors built by American scientist Joseph Henry in 1831. The invention of electric motors/actuators brought on profound changes on traditional industries and electric machines became the major driving power in industrials instead of the conventional pneumatic and hydraulic mechanism. Nowadays, more efficient, complicated and flexible autonomous robotic systems are designed and constructed based on the electromagnetic machines and have been used widely in many fields of the entire industries including manufactures, health, services, and even entertainments.

2.2.2 Micromechatronics

In the first-half of the 20th century, Modern Physics and Quantum Mechanics were established, which formed the basis of the modern science, and promoted the high-tech revolution in late 20th century [Dario 2000]. As happened in the past centuries, the main

objective of science and technology in the revolution is to explore new areas by finding new frontiers for knowledge and for its following exploitation. One of the main products of this revolution is the trend towards miniaturisation that occurred during this process and the beginning of a new engineering era: the Micro-engineering. Today, miniaturisation technology is not only a new frontier for scientific research, but also a tremendous opportunity for application and thus for industrial innovation and competitiveness [Lang 1999].

The trend towards miniaturisation was driven by the advent of the microelectronics. From vacuum tube to semiconductor transistor, small integrated circuits to ultra large scale integration (ULSI), the microelectronic technology has enabled the development of integrated circuits capable of processing information at a rate that was inconceivable just a few tens years ago, and most importantly - with a high reliability at progressively lower costs and smaller dimensions. An obvious paradigm is the development of personal computers, which can now be transported by one hand or even can be put in one's palm.

Due to the advances of the technology, the miniaturisation of electronics paved the way for miniaturisation in other areas of technologies. Microscopic field has been a great research focus since 1980s. The rules of nature are realised more comprehensively and deeply by scientists and many achievements have been made. Among those advancements, one of most important and extremely pervasive technological impacts could be that it has changed drastically the way in which virtually all existing products were designed and fabricated, and brought on an evolution on the mechatronics.

Mechatronics is the harmonic integration of mechanisms, sensors, actuators and embedded electronics for signal processing and control. Fig.2-1 illustrates a typical scheme of mechatronics. Because of the development of the miniaturisation technology, more powerful and effective tools and facilities were invented and the function of these devices became more intelligent and complex while the volumes were greatly

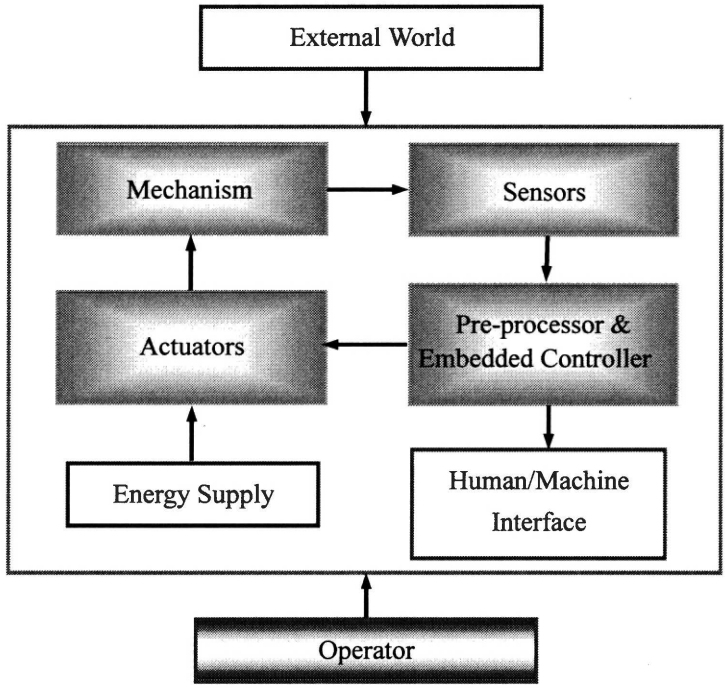

Fig. 2-1 Scheme of mechatronics

downsized.

Examples of those advances in mechatronics can be found in devices such as analysis laboratories built on a chip, smart instrumentation for minimally invasive surgery (MIS) etc., which represent the ultimate frontier of mechatronics: the micromechatronics. Already in the year of 1959, R. P. Feynman foresaw the utility and possible exploitations of machines' miniaturisation. According to his famous talk given at the California Institute of Technology [Feynman 1992], the concepts of microfactory (completely automatic factory, containing lathes and other machine tools at the very small level) and microsurgery (based on tiny microdevices to be inserted in patient blood vessels) were the very interesting possibilities for small machines.

2.2.3 Micro machines and micro robots

The rapid progress of micromechatronics has spurred active research and development of micro machines and micro robotic systems since 80's in last century. At the University of California, Berkeley, MIT, and AT&T Bell Lab., etc., many researches

have been conducted on micro machines and a micro motor about 100 microns in its rotor diameter [Mehregany 1991] gave a shock to the world in year 1990.

To what extent a device could be called "micro"? In Fig.2-2, the range of size of mechanical systems available to human beings is shown in a logarithmic scale [Trimmer 1989] and the scale shows the size of objects in Angstroms (10^{-10} metres). Atoms, about 1 Angstrom in size, are probably the smallest mechanical particles that could be used in future. Human beings are roughly 10^{10} Angstroms (metre sized), and the universe is about 10^{37} Angstroms in diameter. The vertical dotted lines in the figure delineate the normal range of mechanical systems.

Definition of a micro machine differs from individuals. From the word of "micro", it is thought to be under millimetre size. Nevertheless, this is not necessarily restricted. Considering minuteness changing of a machine, it is strictly relative. The problem lies on whether the physical size is small enough to compare with a present machine. Table 2-1 [Fukuda 1993b] gives a comparison of conventional and micro machines.

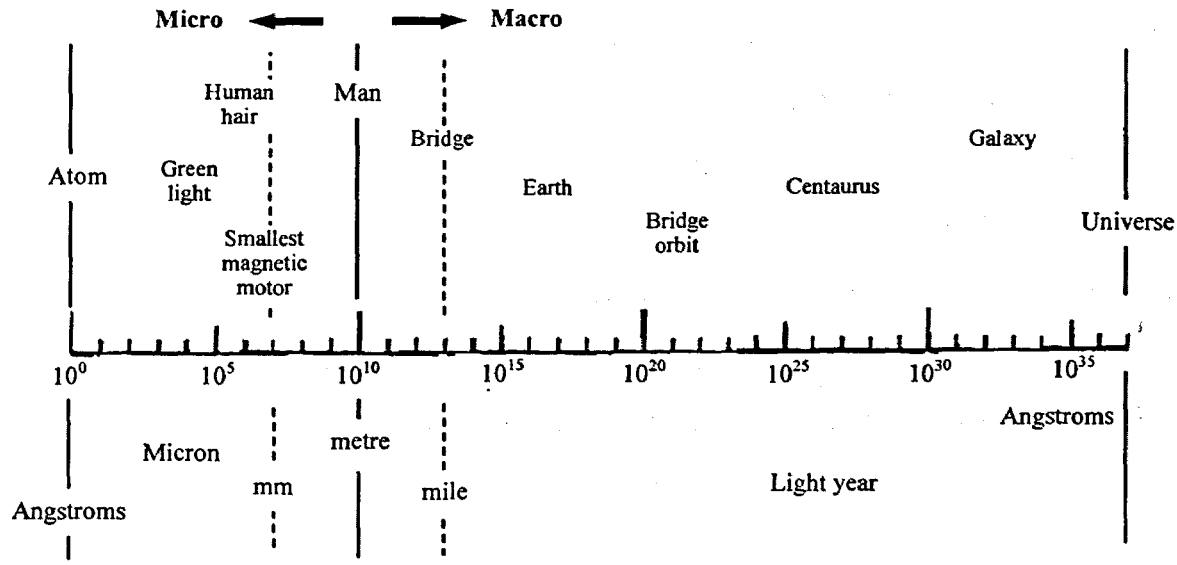

Fig.2-2 The range of size of mechanical systems displayed in logarithmic scale

Table 2-1. Comparison of conventional and micro machines

	Conventional machines	Micro machines		
Classification	cm / m	mm	μm	nm
Size	~ 10 mm	~ 1 mm	~ 10^{-3} mm	~ 10^{-6} mm
Typical size	Robot	Pencil lead	Human hair	Atomic level
Basic technique	NC machine, Special machine tools	Precision machine tools	Microelectronic technique, Laser beam technique	VLSI, ULSI technique
Applications	Robotic and mechatronic products	Micro robotics	Gene Manipulation, Bio-medical treatment	Atom and molecular handling

There is no doubt that small size is the very distinctive feature of micro machines. But they have even more attractive features. The main three features of micro systems are the following three "M"s of the technology [Fujita 1997]:

Miniaturisation

Multiplicity

Microelectronics

Miniaturisation is undoubtedly essential and the most discriminative feature compared to macro systems. Nevertheless, only miniaturisation of macroscopic mechanism is not possible because of the scaling effect. Secondly, cooperative work of many microelements is necessary to carry out an entire task, just like the behaviour of a group of ants. Therefore, multiplicity is the key to successful micro systems. Microelectronics, moreover, is another important part to realize the cooperation between these microelements and to perform a given task. Accordingly, the micro machine requires, in addition to small physical size, the unification of "sensing unit", "actuation unit", "logical and control unit" and integration into one machine (Fig.2-3). If it becomes possible to possess intelligence, autonomous and distributed property, the micro machine will be able to be said a smart micro machine or a micro robot.

Generally, the micro robots can be classified into several types according to their size or functions. With regard to size, micro robots can be categorized to three classes [Dario 1992]: minirobot, microrobot and nanorobot, as shown in Fig.2-4. A minirobot usually

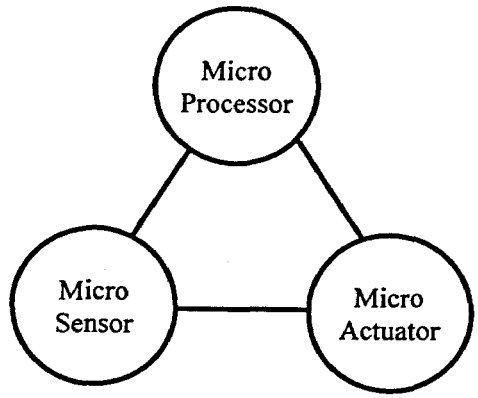

Fig.2-3 Unified micro machine

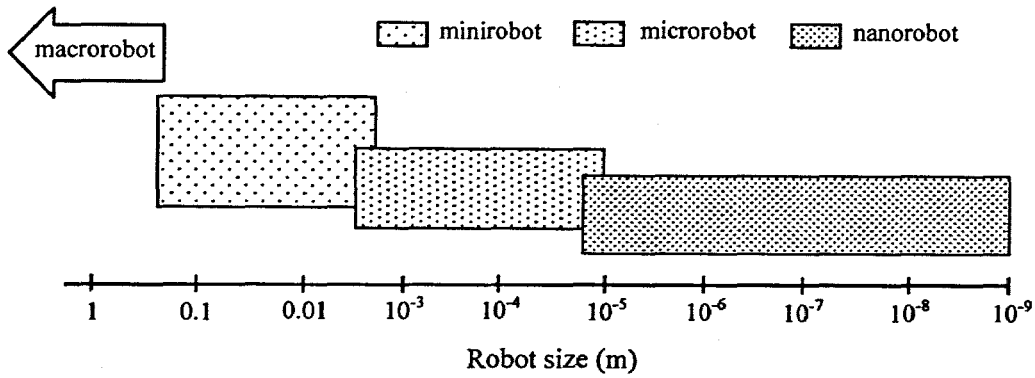

Fig.2-4 Classes of micro robot with respect to linear dimensions

has a size of few cubic centimetres and its workspace and forces is comparable to those of fine human manipulation. They can be fabricated by assembling conventional miniature components and micro machines. An example of minirobot is shown in Fig.2-5. At present, most of micro robots are belong to this class and some complete self-contained working systems have been realised.

A microrobot has its characteristic dimension in the range from tens of micrometers to millimeters. It consists of micro actuators, sensors and signal/control circuit. Millimetre machining technology, ECDM (electro-chemical discharge machining), laser beam technique, and surface/bulk micromachining or LIGA (*German:* lithographisch galvanoformingung und abformung) technology is the key means for the fabrication of microrobot. A flying microrobot developed in the University of California, Berkeley is illustrated in Fig.2-6.

Fig.2-5 An example of minirobot

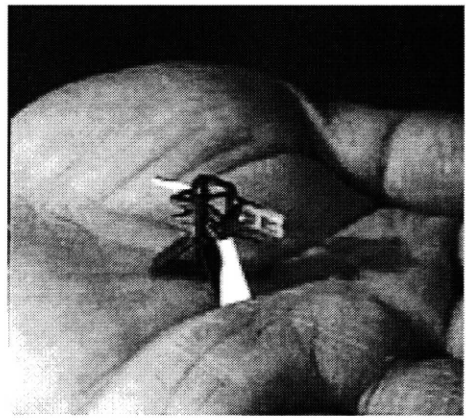

Fig.2-6 A flying microrobot by the University of California, Berkeley

The third class is nanorobot. The size of this type of robots ranges from a few hundred nanometres to a couple of micrometers, which is comparable to the scale of biological cells. The nanorobot cannot use the conventional mechanical methods for their driving and manipulation but the electro-chemical means could be applied (mimicking biological organisms). Meanwhile the solid-state technology is also not suitable for its fabrication but polymer chemistry technology could provide a solution. Fig.2-7 is a conceived design of nanorobot based on molecular electronics.

Micro robots can also be classified into six types according to their mobility, autonomy and control method, as illustrated in Fig.2-8. Fig.2-8(a) shows a type of micro robots that all the elements are physically connected just like the ordinary industrial robot. For

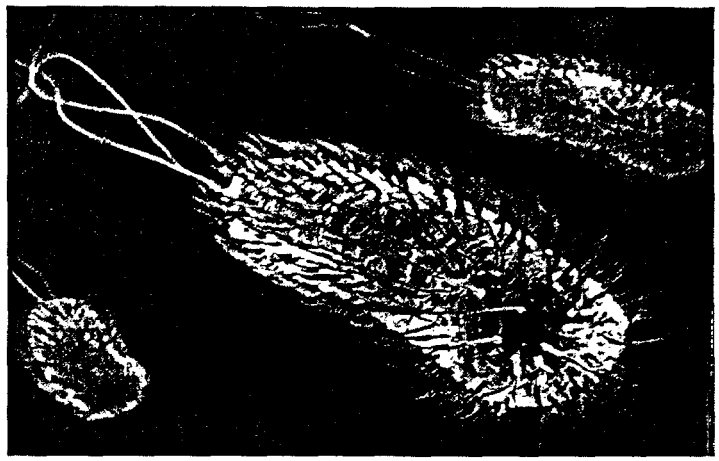

Fig.2-7 Conceived nanorobot with Ion mobility based on molecular electronics

this type, the actuators for operations and the micro gripper need to be miniaturized. Fig.2-8(b) and (c) show micro robots that are similar to (a) in their actuators and micro grippers, but the actuators for positioning and operation are apart from their control and power unit so that they could be more flexible than type (a). The control signals and the power are supplied by electric, hydraulic or pneumatic means through cables. Since type (c) has the feature of mobility, it has greater application potential but has some technological challenges.

In spite of some mobile ability of cable-controlled micro robots, the stiffness of cable still obstructs the action of the micro robots. As a result, wireless operated micro robots

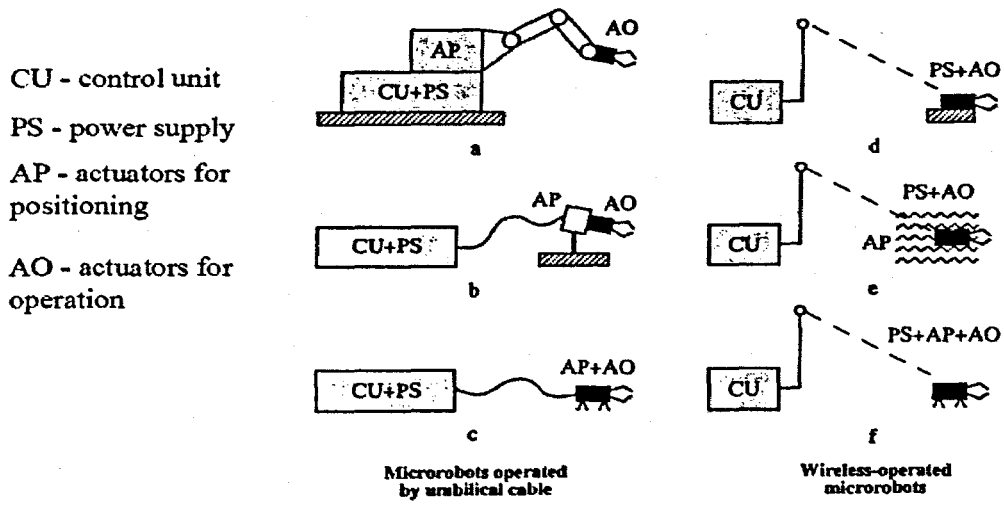

Fig.2-8 Functional classification of micro robots

are brought forward. In Fig.2-8, three types of wireless operated robots are shown as type (d), (e) and (f), respectively. Type (d) is similar to type (b) but its control is wireless transmitted. Type (e) and (d) also has strong mobility but the type (e) is more difficult to control because it is in liquid stream. The power supply is another technical challenge to those wireless types of micro robots. Although battery is a choice as their power supplier, there have many restrictions due to the battery's size and capacity. An effective solution is the wireless energy transmission but it still has a number of problems need to be solved.

2.2.4 Applications of micro robots

During the past two decades, micro robots have been received increasing demand due to the progress in the technologies on the low micrometre and nanometre, and they are thought to be more developed and more widely used in the new century. Micro robots have the various promising application fields such as: (1) medical, (2) bio-engineering, (3) industrial application and (4) service field. Fig.2-9 [Fukuda 1993] describes these application fields of micro robots.

Due to their nature of being tiny, the inspection and operation in a narrow place are thought to be the optimum jobs for micro robots. In the medical field, they can be used for the microsurgery of a blood vessel and a medical treatment. In considering the measuring within a human body, various data collection and local medicine injection will become possible by using medical micro robot. Moreover, by employing active mobile catheter, some incurable angiopathy and other medical treatment of the circular vessel system defect would become partially possible. Another typical application is the industrial inspection. Fig.2-10 shows an example of inspection of water pipe [Takeda 2001]. A mobile micro robot with flaw detection device, a camera, welding arm and a data transmission/reception device is applied in the tested system. The robot can repair the flaw area by the instruction of control centre (i.e. a computer) after detecting the flaw point of the pipe and send the information to the control centre.

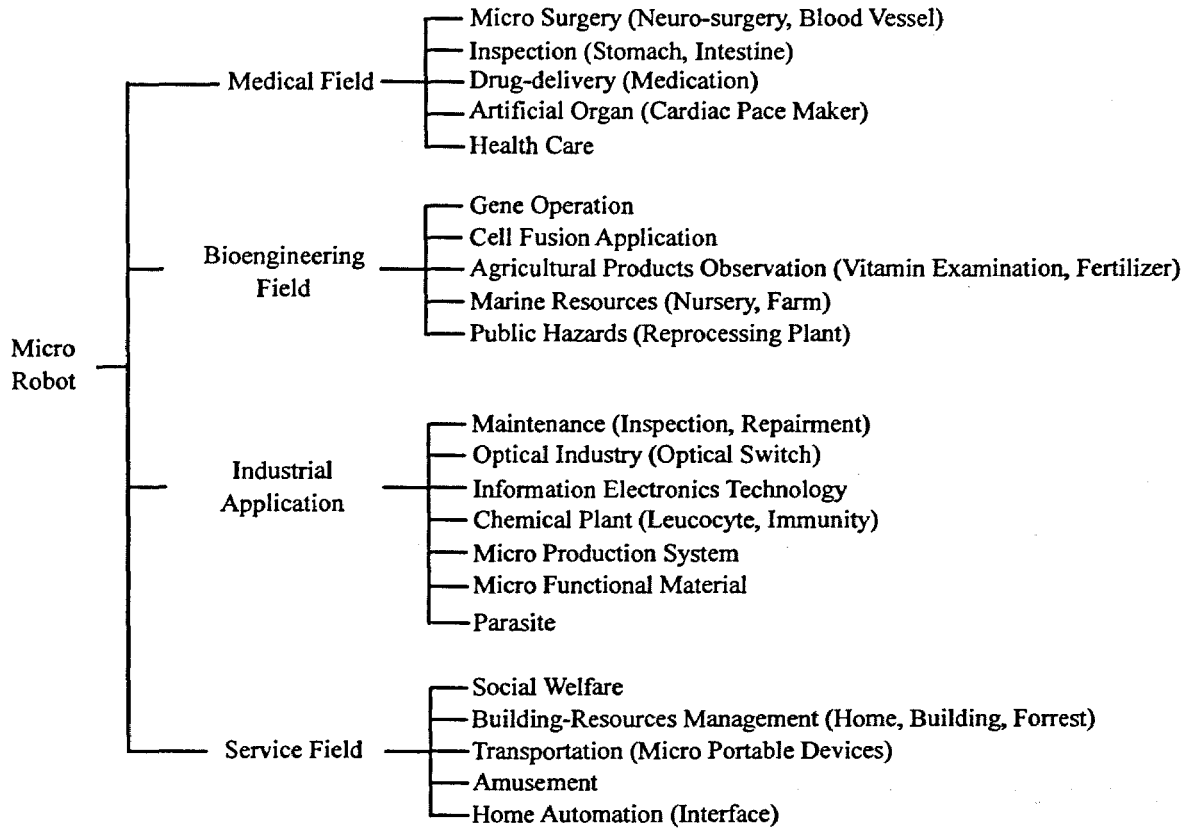

Fig.2-9 Applications of micro robots

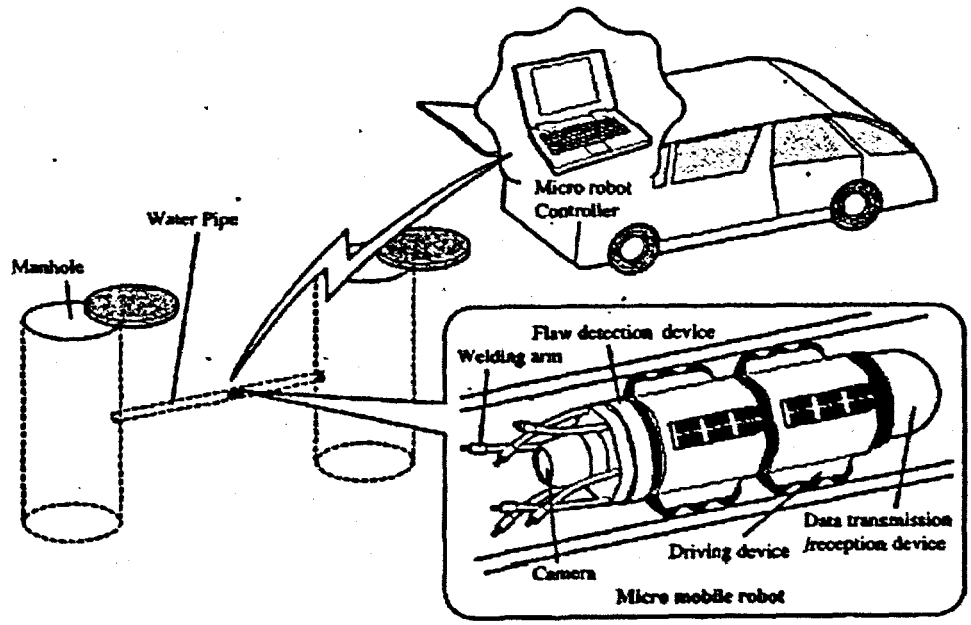

Fig.2-10 Inspection of water pipe

2.2.5 The state-of-the-art

In this thesis, we will focus on the microrobots, which, as we have defined them, have the characteristic dimensions in the millimetre regime. However, in order to have a thorough review of the overall technology, some larger robots that may belong to the minirobot category will also be included in the review. For the sake of convenience, all the micro robots appeared hereafter will be generally called "microrobot".

Distinctive with other "passive" micro machines like microvalves or micromanipulators, microrobots are kinds of "active" micro systems. The capability of motion and manipulation are the important aspects for a micro robotic system to fulfil its on-board control and given tasks.

In order to design effective microrobots with sizes in just a few cubic millimetres or less, a number of problems should be solved. Considering the main components of a microrobot: the mechanical structure, sensors, actuators, processing electronic circuitry and control unit, it can be found that those based on, or deriving from microelectronics do not pose major problems [D'Attanasio 1997]. For instance, the miniaturisation, integration, reliability and the cost of the microelectronics devices for signal processing and servo control are quite satisfactory for the microrobots. Meanwhile, micro sensors have been well researched and developed since 1960's and they can now be readily realised by the silicon technology. On the other hand, the miniaturisation of mechanical structures and of actuators and the implementation of high level control strategies (machine intelligence) in such a small machine are more difficult. Therefore, new technology break-through is required to realise actual microrobots whose performances are comparable with those of macro robots, especially in term of autonomous behaviour.

Nevertheless, the miniaturisation of robots does not mean simply downsizing the existing macro robots. It is often necessary to use new principle for actuation and fabrication. Nowadays, various robotic structures and locomotive mechanisms

according to different application requirements have been researched and reported. An extensive review of those representative designs throughout the time is conducted in the following sections. In order to make it clearer, the proposed microrobots are categorized by their motion behaviour. Additionally, the medical microrobots will be discussed in particular as they are one of the main objectives of the thesis.

2.2.5.1 Walking/jumping microrobots

A robot that can walk and jump is a natural idea inspired by the behaviour of common creatures including human beings. Many microrobots utilise the leg-based mechanism to acquire autonomous capability. A legged micro moving robot with a size of 36.5×27×27 mm^3 was reported in [Aoyama 1993]. The objective of the developed microrobot is to move on the surfaces that are made up of magnetic materials such as iron, and to precisely measure and machine themselves. The schematic configuration of the microrobot is shown in Fig.2-11. The front and rear legs are the small C-shape iron bars with coils acting as electromagnets. The legs are connected with a soft leaf spring and two piezoelectric actuators. The motion mechanism of the robot is similar to an inchworm by synchronizing the excitation of the electromagnets and the piezoelectric actuators. In 2003, an improved design by using four stack-type piezoelectric elements and two U-shaped electromagnets with the size of a few inch cubic was proposed [Fuchiwaki 2003], as shown in Fig.2-12. The new structure allows the robot to move in any directions including rotation on a plane.

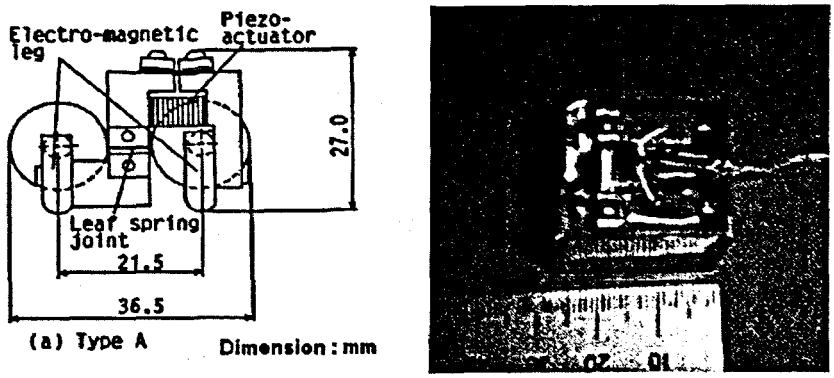

Fig.2-11 Micro moving robot developed by H. Aoyama *et al.*

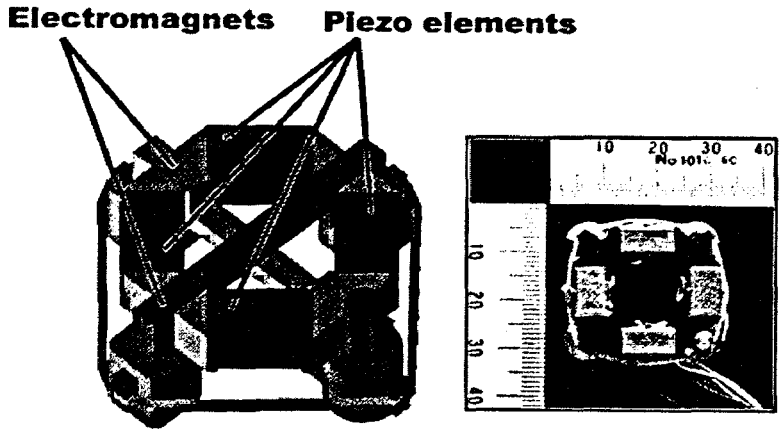

Fig.2-12 Structure of the four stack-type desktop microrobot

Another mobile microrobot with similar structure as Fig.2-11 was presented in [Suzuki 1994]. The difference is that the latter utilises a permanent magnet linear actuation mechanism for its locomotion (Fig.2-13).

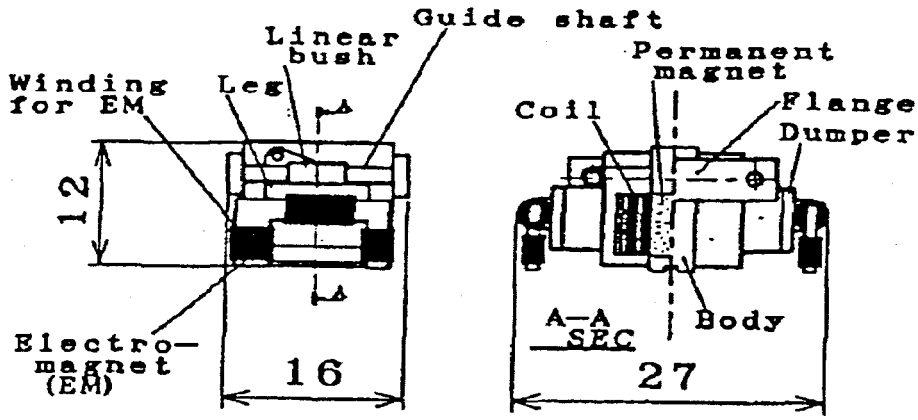

Fig.2-13 Microrobot with permanent magnet linear actuation mechanism

Codourey *et al.* in Switzerland presented a crawling microrobot called Abalone in 1995. The structure is shown in Fig.2-14(a). It composes of two legs: the inner and outer legs, and four electromagnetic elements for fixing the legs [Codourey 1995]. The dimension is about 60×60 mm^2. The operation sequence is that, firstly to fix the outer leg by the electromagnetic element and move the inner leg by expansion/contraction of the piezoelectric stack. After moving the inner leg, it is fixed by electromagnet and the outer leg is released, and then moved by the piezoelectric stack. The maximum step of Abalone is 5μm and the motion resolution is up to 10nm. In the newer design of Abalone II (Fig.2-14(b)), the electromagnetic element was put away and the impact

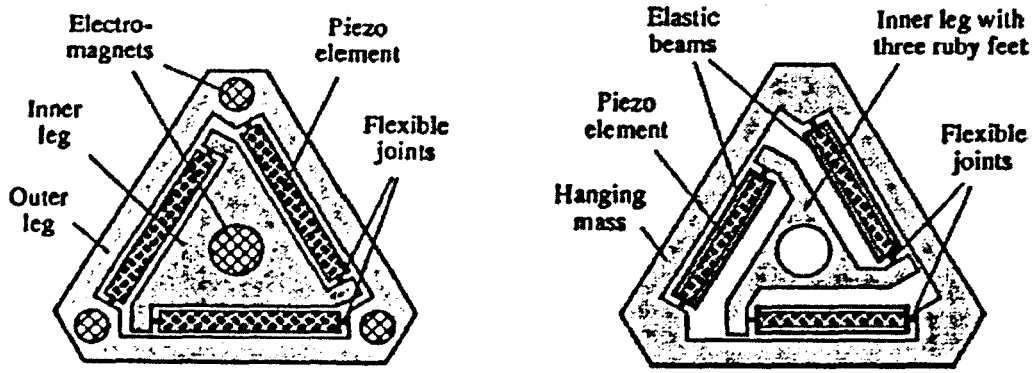

(a) Abalone (b) Abalone II

Fig.2-14 Crawling microrobot - Abalone

drive principle was applied. The outer leg is no longer a leg but a mass for generating the inertia force. The size of Abalone II is then down to 38×35 mm^2 and the maximum step is only 2μm. However, the position accuracy remains 10nm.

Similar micro mobile robots were proposed in [Torii 1999]. Their first prototype is a Y-shaped mechanism consisting of three electromagnets and three stacked-type piezoelectric devices made by lead zirconate titanate (PZT) (Fig.2-15). The size of the electromagnets are 10×10×10mm^3 and the PZT elements are 5×5×18 mm^3. The principle of the actuation is similar to that of an inchworm, as shown in Fig.2-16, where the black square denotes that the electromagnets is excited and the shaded bar denotes the PZT is extended by the applied voltage. When the actuator moves linearly (Fig.2-16(a)), the control sequence is as follows: (1) coils b and c are excited and stick

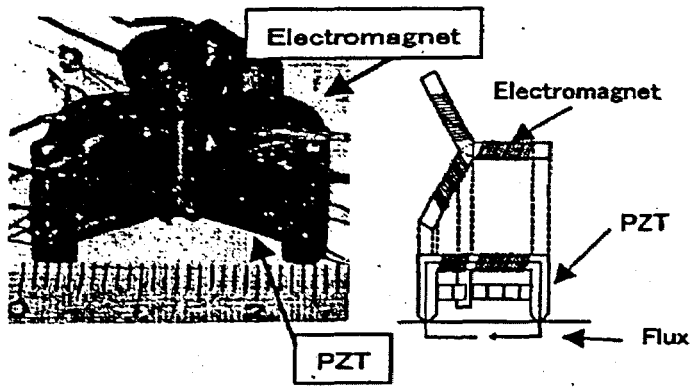

Fig2-15 Y-shaped Microrobot proposed by A. Torii *et al.*

to the substrate, and PZT B and C are extended by applying a voltage; (2) coils a and c are excited and stick to the substrate, and the PZT B is contracted by removing the applied voltage; (3) coils a and b are excited and stick to the substrate and PZT C is contracted by removing the applied voltage. Accordingly, the actuator moves in the X direction by repeating the sequence (1) to (3).

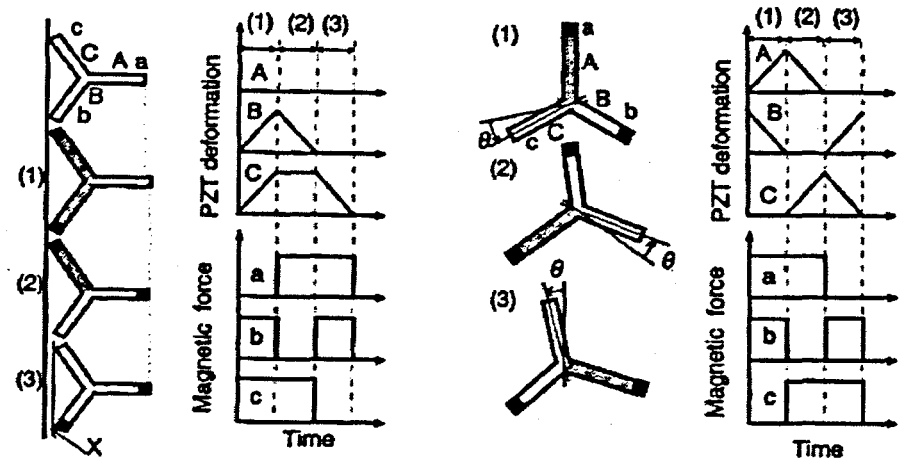

(a) Linear (b) Rotational

Fig.2-16 Moving principle of the Y-shaped microrobot

When a rotational movement is needed, the control is performed in such a way (Fig.2-16(b)): (1) coils a and b are excited and stick to the substrate, PZT A is extended by applying a voltage while PZT B is contracted by removing the voltage; (2) coils a and c are excited and stick to the substrate, and PZT C is extended while PZT A is contracted; (3) coils b and c are excited and stick to the substrate, and PZT B is extended while PZT C is contracted. Accordingly, the actuator rotates to the left direction by repeating the sequence (1) to (3).

Among these developed microrobots with legs, NanoWalk is a famous microrobot family developed in the Bioinstrumentation Laboratory, MIT [Martel 2001]. The first prototype was reported in 1999. It is an autonomous micro system of dimension 32×32 mm^2 with three legs as actuators for the motion and instrumentation. Each leg is a four-quadrant piezoelectric tube for which several parameters such as the rate and angle of deflection are controlled by complex onboard electronics. Fast displacement and extremely high resolution of nanometre range in displacement is obtained by several

thousand steps per second (hence named "NanoWalk"). Presently, several tethered prototypes have been developed and tested. Fig.2-17 shows the photograph of prototypes of the NanoWalk microrobot.

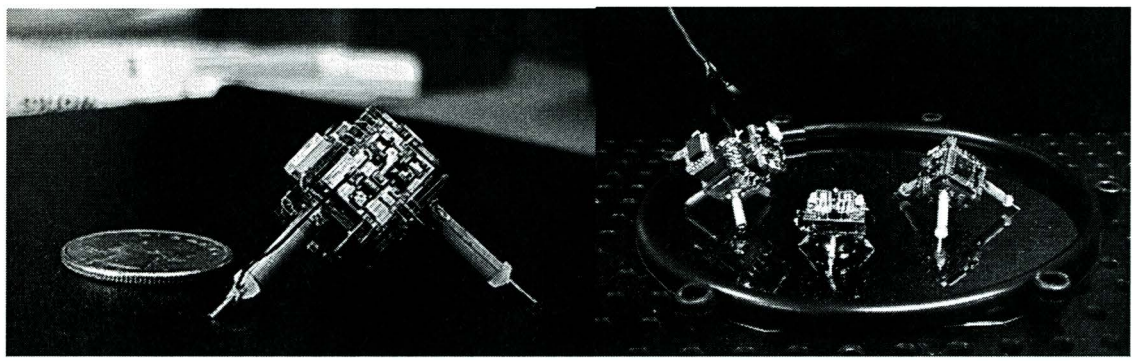

Fig.2-17 The NanoWalk microrobots developed in MIT

Almost the same time, another similar microrobot called MINIMAN used for microassembly was developed in Germany [Fahlbusch 1999]. Fig.2-18 shows the photograph of the robot. It contains three legs and a platform for mounting the manipulator. The construction of each leg is similar to that of the NanoWalk microrobot so that it can bend into any angle. By precisely control the gait of the three legs, the robot can move freely and a maximum speed of 30mm/s can be achieved.

In [Fukuda 1993a], several microrobots with a novel moving principle that was based on the bristle structure were proposed. Fig.2-19 shows the construction of the robot, which consists of permanent magnets, solenoid and bristles on a nylon sheet. A body with leg(s) and stopper construct the whole mechanism. Two versions were developed:

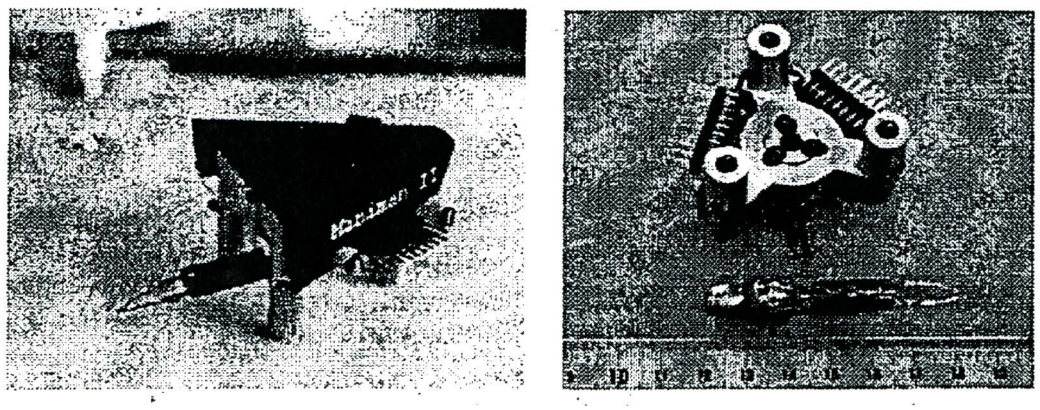

Fig.2-18 Microrobot MINIMAN by S. Fahlbusch

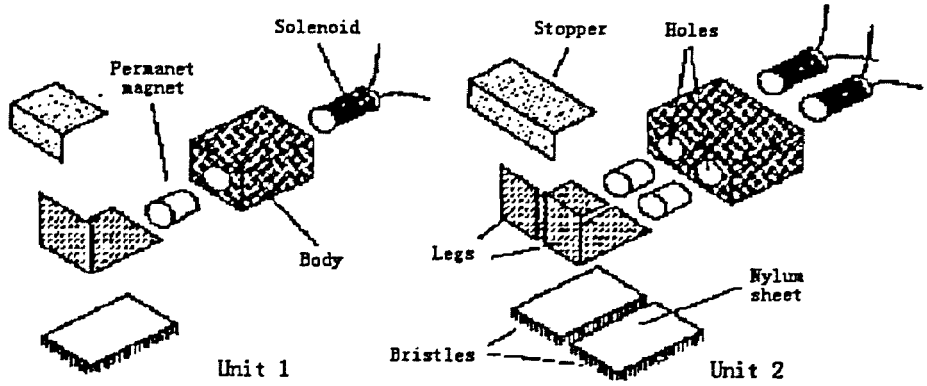

Fig.2-19 Bristle-based micro mobile robots

unit 1 can only move forward and unit 2 can turn left and right.

The driving principle of the microrobot is stick-slip method shown in Fig.2-20. In the initial state, the permanent magnet sticks to the solenoid. When the voltage of solenoid is turned on, the magnet is repulsed by solenoid and slip forward until it is stopped by the stopper. The voltage of solenoid is then turned off and the body with the solenoid sticks to the magnet and a forward displacement is generated. An important point for moving is that the bristles are tilted at an angle of 45°, which makes the movements

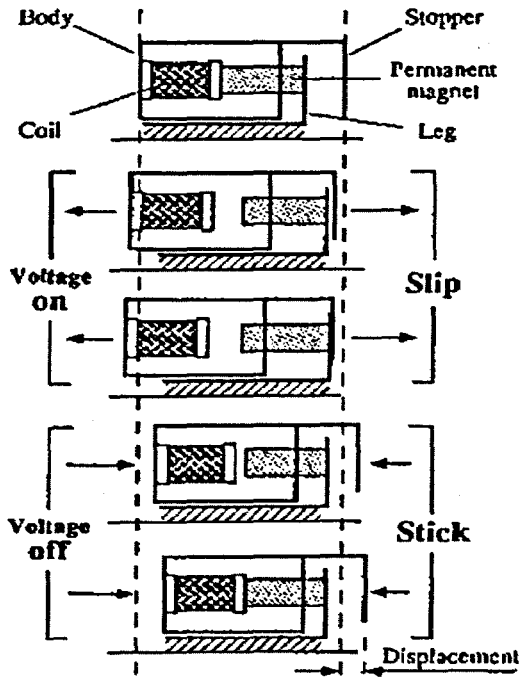

Fig.2-20 Operation principle of the bristle-based micro mobile robot

better forward than backward. In the design of unit 2, two legs are used and this makes the body have the capability of turn left and right when the legs are working alternatively.

Similar to the above design, scientists in the same research group presented another bristle-based microrobot called Micro Line Trace Robot in [Ishihara 1994]. Fig.2-21(a) shows the outline of the robot, which consists of an electromagnetic actuator, a spring, an inclining cloth, and a body with control logic circuit. Fig.2-21(b) illustrates the detailed construction of the electromagnetic actuator. The dimension of the robot is $16\times10\times13$ mm^3 and the weight is about 2.3g.

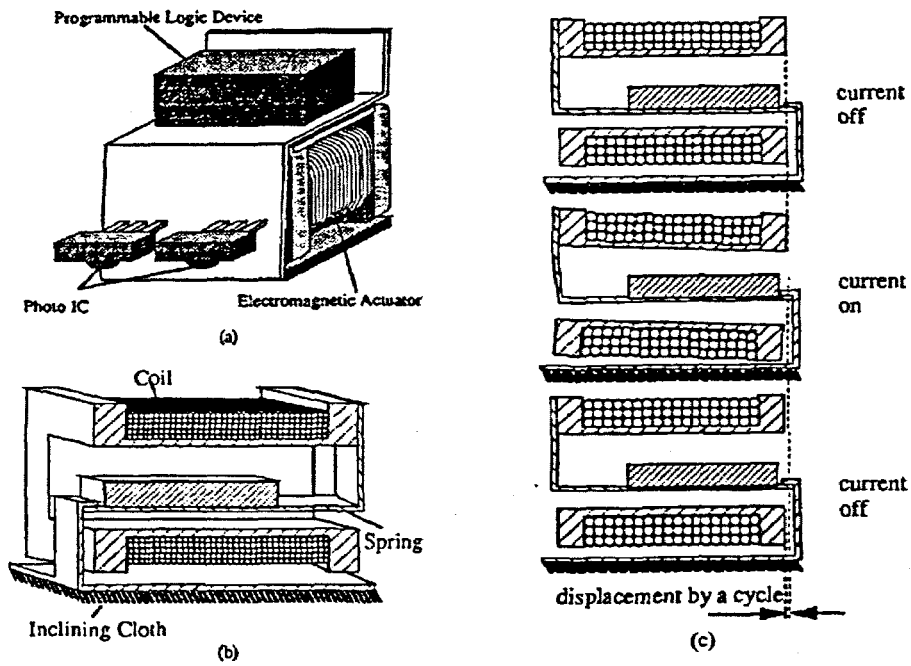

Fig.2-21 Micro Line Trace Robot by H. Ishihara *et al.*
(a) Outline of the microrobot, (b) The structure of the actuator, (c) Moving principle of the robot

The moving mechanism is explained in Fig.2-21(c). When an AC current is input to the electromagnetic actuator, the alternating magnetic field within the solenoid will vibrate the spring, and then the inclining cloth converts the vibration to the displacement in one direction. The experiment on the microrobot showed that the maximum speed could reach 0.15m/s at about 150Hz.

Another autonomous microrobot based on the same principle but with simpler

mechanical structure was also developed (Fig.2-22). The difference is that the latter uses piezoelectric cantilever instead of electromagnetic coils. Hence, the size of the robot is reduced (down to 1 cm^3), and the power consumption can also be reduced such that the robot can be powered by batteries. However, the maximum speed of this type of microrobot is only about 2mm/s because of a very limited strain of the piezoelectric element.

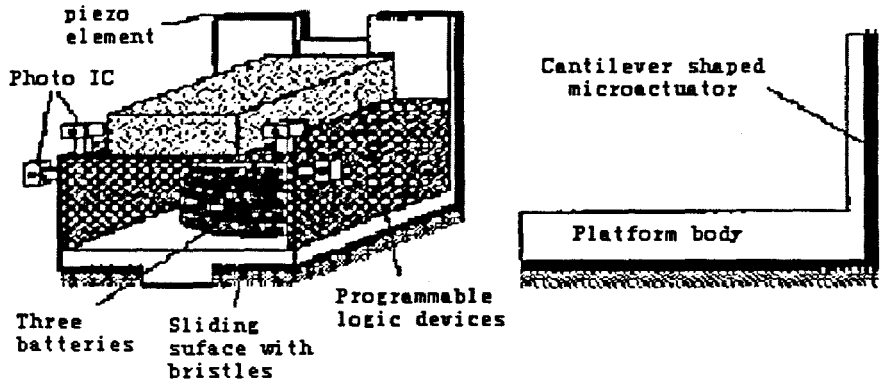

Fig. 2-22 An autonomous microrobot based on bristle structure and piezoelectric device

Addition to the above three types of bristle-based micro moving robots, one interesting design using the bristle structure was proposed in [Ioi 1999]. Quite different from the previous designs, the actuation principle of this microrobot utilises mechanical centrifugal forces. The prototype of the microrobot is shown in Fig.2-23. The size of the robot is about $4.5\times10.7\times28$ mm^3 and the weight is 8g.

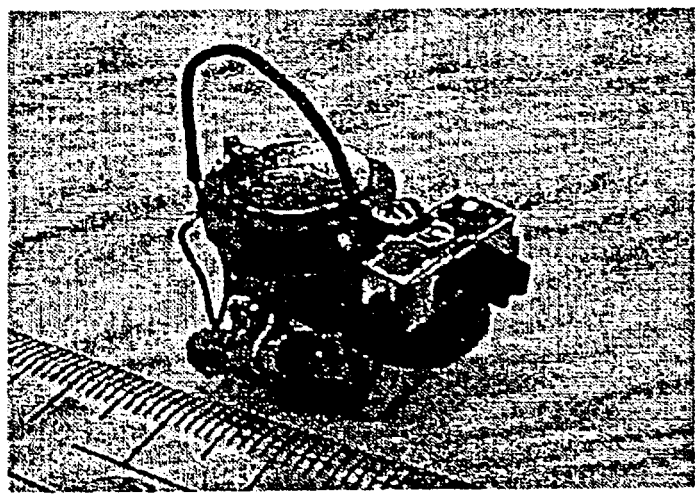

Fig.2-23 Prototype of the bristle-type microrobot using centrifugal forces

The schematic structure of the design is illustrated in Fig.2-24. Like other bristle-type mechanisms, the proposed microrobot has many tilted elastic fibres mounted under the body to support and move the body on the floor. In addition, there are two coreless motors and a switch on the body. The output axis of each motor has an eccentric weight for generating a centrifugal force by rapid angular velocity of the motor. Two motors are used so that the whole system is statically balanced and can be turned by changing the speed of the motors. The proposed robot is clarified with a velocity performance by experiment, whose maximum speed can reach 0.2m/s.

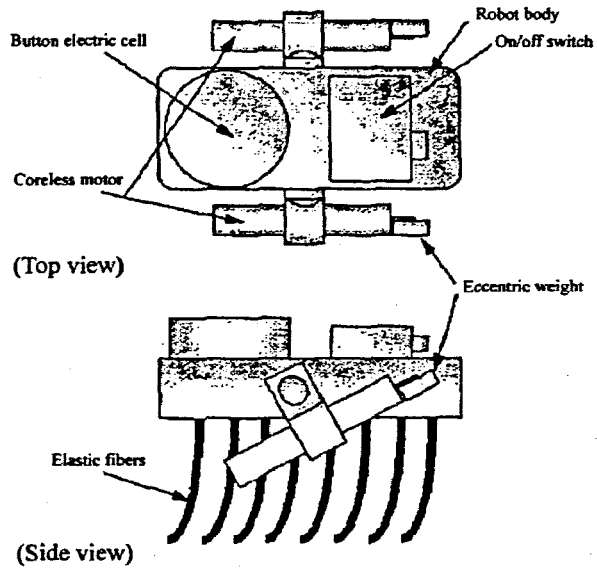

Fig.2-24 Conceptual view of the microrobot using centrifugal forces

Locomotion using wheels is a common design in the macro robotic systems. Hence, the application of wheel mechanism in microrobots was also studied. Researchers in Toshiba Corporation developed a microrobot using wheels named "TOSUMO-KUN" [Hasegawa 1995]. Fig.2-25 shows the prototype of the microrobot and construction of the machine. The microrobot weights 2g, and consists of two ultra small electromagnetic motor, four wheels (each of 4mm in diameter), and a connecting board. Two driving wheels with the motor are mounted on the opposite sides of the robot so that the selection of the running motor can change the moving direction of the robot. The proposed microrobot recorded a capability of running on a gradient of 20° and a maximum speed of 300mm/s. A battery-powered 1-inch^3 prototype was also tested by

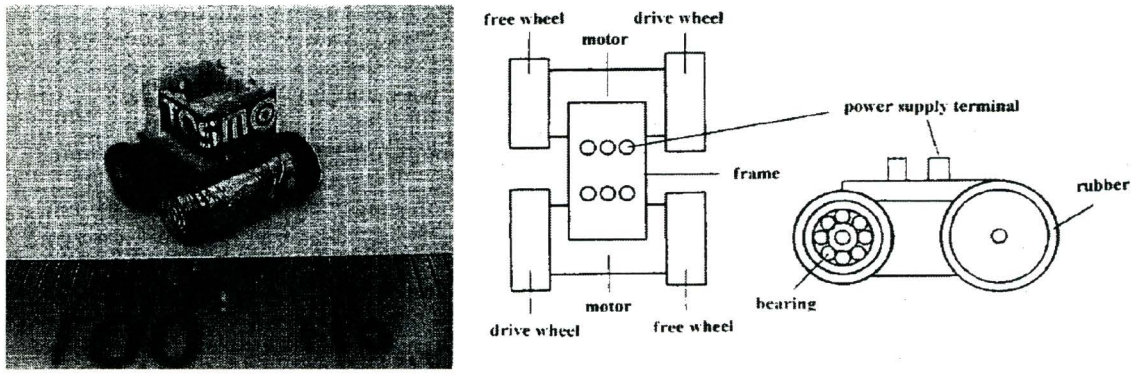

(a) Photograph (b) Schematic

Fig.2-25 TOSUMO-KUN microrobot proposed by Y. Hasegawa

the developers.

Also in 1995, a mobile microrobot actuated by an electromagnetic wobble micro motor was developed. Fig.2-26 shows the prototype and schematic structure of the proposed microrobot named "Pillicino" [Stefanini 1996]. The key components of the microrobot are two newly proposed wobble micro motors. Each micro motor is composed of an internal star-shaped stator and an external ring that forms the rotor of the motor. The rotor also serves as the driving wheel of the microrobot. The stator comprises three miniature coils, star-connected and wrapped around a ferromagnetic core. The overall dimension of the robot is $10\times10\times10$ mm^3.

The working principle of the wobble micro motor can be considered as "wobble-like" stepping variable reluctance motor. At each step only two of the three stator coils are

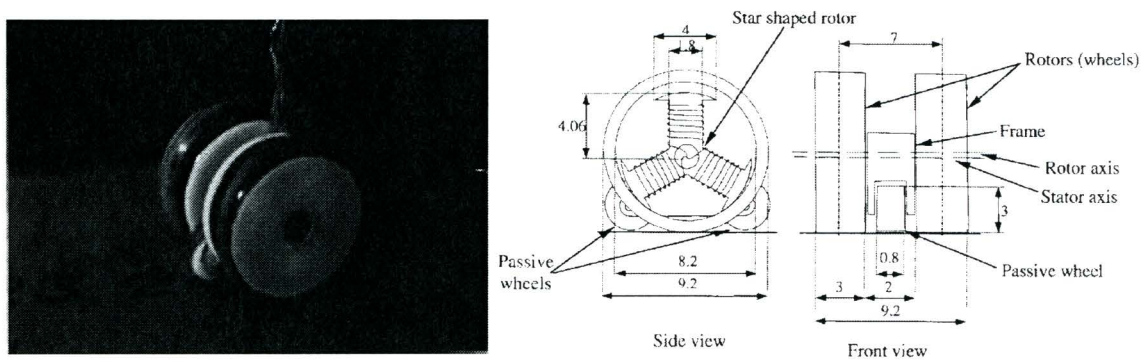

Fig.2-26 Prototype and structure of the Pillicino microrobot

energised and generate a magnetic field, and therefore attractive force is produced between the two poles and the rotor ring. A pseudo-precessional motion is then obtained according to the transition mechanism shown in Fig.2-27.

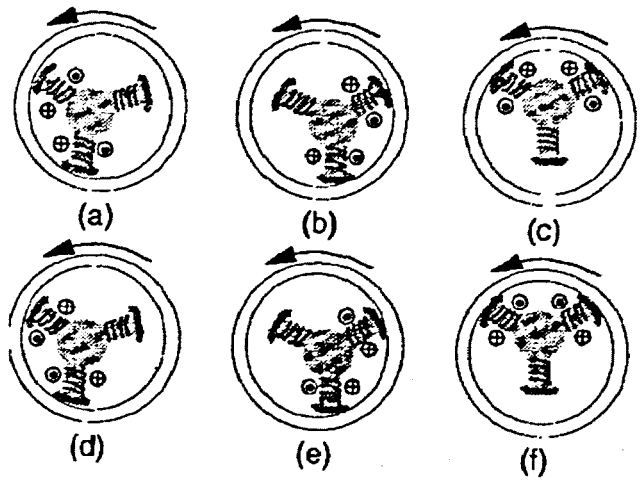

Fig.2-27 Working principle of the wobble micro motor

Although rotating wheels would be the most conventional method for the locomotion of microrobot, the mobility is not sufficient when the robot moves in uneven, slippery or flexible circumstances compared to the legged microrobots since they are capable to negotiate unstructured terrain.

In many cases, Bionics is a beneficial source for the mobile microrobot design. Roboticists have used behaviour of insects as a source of design for many years. Insects are extremely agile and successful in manoeuvring over a wide variety of objectives. Insects with legs are good sample for inspiring new concept of mechanisms of the microrobot. A key feature of insect leg construction is its multi-segment nature. Segment joints can have a single or multiple degrees of freedom (DOF). The result is movement capability that enables successful walking, climbing and jumping in wide varieties of terrains. In [Birch 2000], a cricket-like microrobot fitting within a 2-inch cube was illustrated. Fig.2-28 shows the conceptual design of the microrobot. It has six legs that are similar in function to those of a cricket but with less complexity. The two large powerful rear legs have two DOFs to fulfil the walking and jumping tasks. The front two pairs of legs are much smaller but are more agile with three DOFs. The

arrangement of the legs enables the microrobot to have two desired modes of locomotion. One will be walking used for slower locomotion and manoeuvring, which will allow the robot to navigate to specific locations and orientation. The other mode is the jumping ability for moving over large obstacles and travelling faster with less energy.

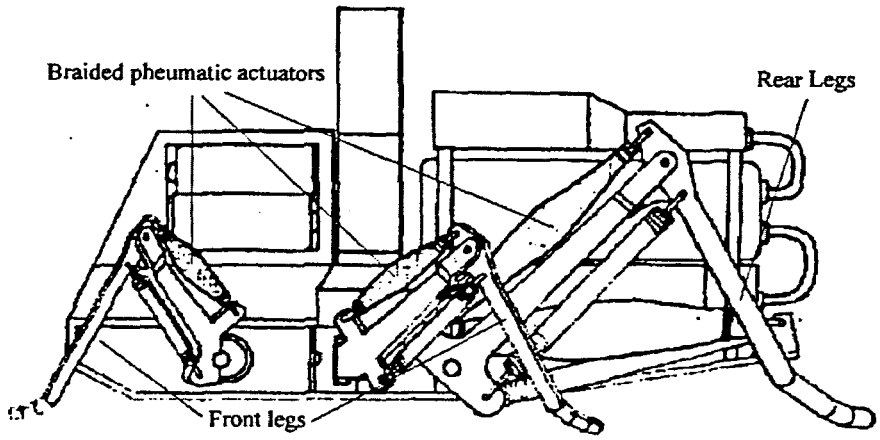

Fig.2-28 Conceptual design of the cricket microrobot

Braided pneumatic actuators, also known as Mckibben artificial muscles, are used for driving the joints of the legs combined with springs as passive tension elements to opposite them. The valves needed for control the braided actuators are fully micro-machined microvalves which consists of a spring, a patterned shape memory alloy (SMA) actuator, and an orifice die. A compressor driven by a Smoovy™ micro motor supplying compressed air for the leg actuation and the power source for the microrobot is lithium batteries.

2.2.5.2 In-pipe microrobots

Microrobots are expected to use for the inspection and maintenance in small tubes in the industries, and to examine and cure blood vessels or organs in the medical treatment. In-pipe mobile microrobots that can operate in narrow space are hence required.

An early design of mobile microrobot for in-pipe inspection using giant magnetostrictive material (GMM) was described in [Fukuda 1991]. GMM is a new

magnetostrictive material with higher strain under small magnetic field and it demonstrates a better performance compared to the piezoelectric material. The structure of the proposed microrobot is shown in Fig.2-29. It contains 4×4 legs made from thin copper sheet and attached to the GMM actuator shown in the figure. When applying an alternating magnetic field, the GMM actuator vibrates perpendicular to the pipe and this will result in a movement due to the inclining legs. Hence, it can operate without any wired power supply.

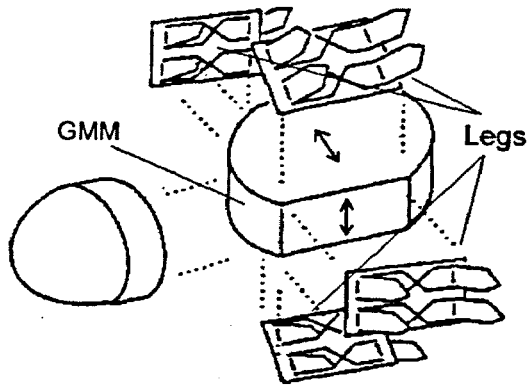

Fig. 2-29 Schematic structure of an in-pipe microrobot using GMM

In [Hayashi 1998], I. Hayashi *et al.* reported a wheel-based in-pipe microrobot using "screw principle" that was developed in 1993. Fig.2-30(a) illustrates the concept of the driving method. The driving unit consists of two wheels mounted on the both sides of the main body, which can rotate freely on their axis. They are also slightly inclined with several angles to the centre axis (Y axis) of the main body and pushed against to the inner wall of small pipe. A rotating torque is applied to the main body when driving, and the wheels rotate and move in the circumferential direction on the inner wall of small pipe. At the same time, due to the small inclined angle of the wheels, the main body will move forward in a spiral motion like a screw rotates and moves along a screw groove. The developed prototype consists of two driving unit and three connecting springs, as shown in Fig.2-30(b). The diameter and length of the robot are 22mm and 250mm, respectively. The rotating torque was supplied by a flexible wire at one end of the robot. The experimentally obtained maximum moving speed is 52mm/s with a maximum traction force of 12N. In [Yamaguchi 1999], an enhanced design was implemented by

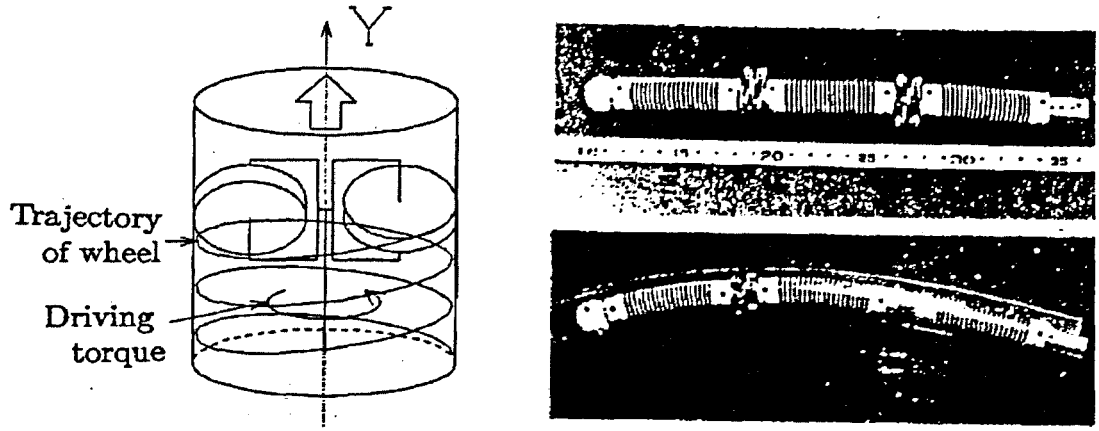

(a) (b)

Fig.2-30 Screw principle microrobot by I. Hayashi *et al.*

improving the wheel structure to a double-wheel mechanism to enable the microrobot travelling in pipes with different diameters.

Another wheel-driven micro inspection robot for 1-inch pipe shown in Fig.2-31 was reported in [Suzumori 1999]. The robot is 23mm in diameter and 110mm long, and 16g in weight. The driving principle is based on a micro electromagnetic motor reduction drive and a planetary wheel mechanism shown in Fig.2-32.

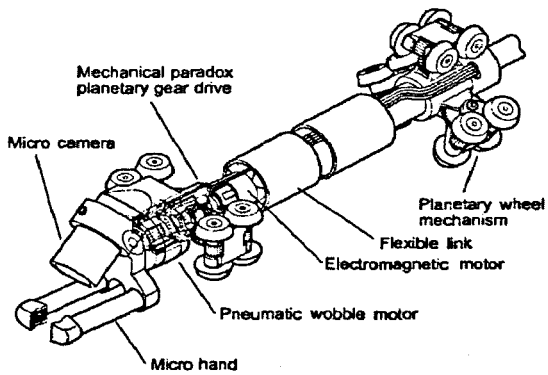

Fig.2-31 Configuration of a wheel-driving micro inspection robot

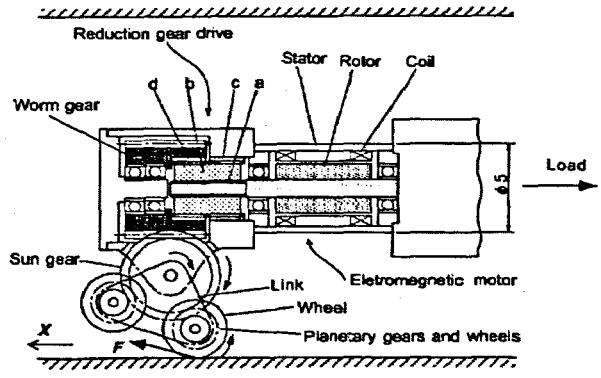

Fig.2-32 Driving principle of the micro inspection robot

The output of electromagnetic motor is connected directly to the input shaft of the reduction gear indicated by "a", and the output from the planetary reduction gear "d" is connected to the worm gear. The electromagnetic motor drives the sun gears through the reduction gear drive and worm gear (only one of the sun gears is shown in Fig.2-32). Each sun gear has two planetary gears, which are carried on a triangle-shaped link that

allows them to revolve around the sun gear. The wheels are fixed to the same shaft as the planetary gears. The planetary gears, wheels, and triangular links turn around the sun gear to push the rear wheels against the pipe wall when driving the robot. The greater load on the robot in the pipe's axial direction causes an increased reaction force from the pipe wall, and the generated force turns the triangular links and pushes the rear wheels firmly onto the pipe wall. Therefore, the force pushing the wheel onto the pipe wall is mechanically controlled without any need for sensors or electric control.

When thinking of moving in small or narrow space like pipes, some natural creatures can give researchers much inspiration. A useful example is earthworm. An earthworm composes of many body units, each of which can become thick and short, or reversely become thin and long. The body produces a wave of swelling along the longitudinal axis of body one after another when moving. Fig.2-33 shows the vermiculation of an earthworm. Based on this locomotion pattern, an actuation unit and moving mechanism, as shown in Fig.2-34, was developed in 1994 [Hayashi 1998].

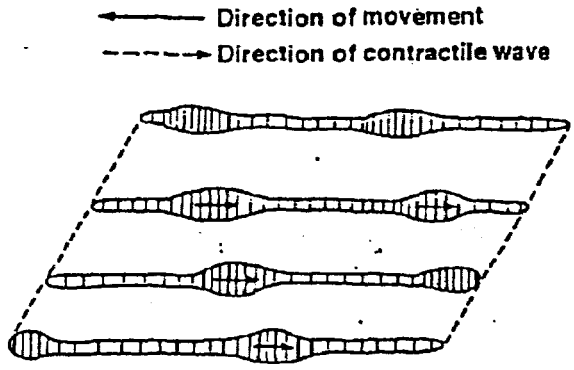

Fig.2-33 The vermiculation of an earthworm

The actuation unit consists of a rubber actuator, which is called flexible micro actuator (FMA) and is activated by air. The FMA is put between two round thin aluminium plate and four link joints fixed equally on the peripherals of the plates. When the FMA is activated and stretched, the link is also stretched and then the leg fixed on the middle of the link extends outsides. Reversely, the leg shrinks inside if the FMA is inactivated and contracted. The moving mechanism has three such actuation units. By propagating the outside stretching motion of leg one after another, the mechanism walks forward like an

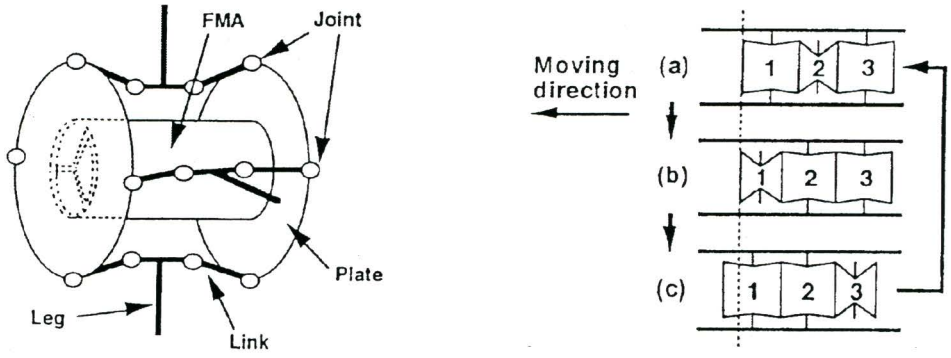

Fig.2-34 An in-pipe microrobot based on FMA structure

earthworm (Figs.2-34(a) to (c)). The developed microrobot using this mechanism can moves at a speed of 2.2mm/s.

In [Idogaki 1995], a functional in-pipe inspection microrobot was reported. The dimension of the robot is Φ5.5mm×L20mm and the weight is 1g. It was perhaps the smallest microrobot at that time with in-pipe inspection capability. Fig.2-35 shows a photograph of the robot. The main parts of the robot contain a shell body, two eddy current sensors, piezoelectric actuation mechanism, and radiator. The locomotive principle of the robot utilises the dynamic relationship between inertial force and maximum static frictional force within a horizontal pipe, as illustrated in Fig.2-36.

Followed by the above design, H. Nishikawa *et al.* in the same research group presented an in-pipe wireless microrobot in [Nishikawa 1999]. The system is designed to move in

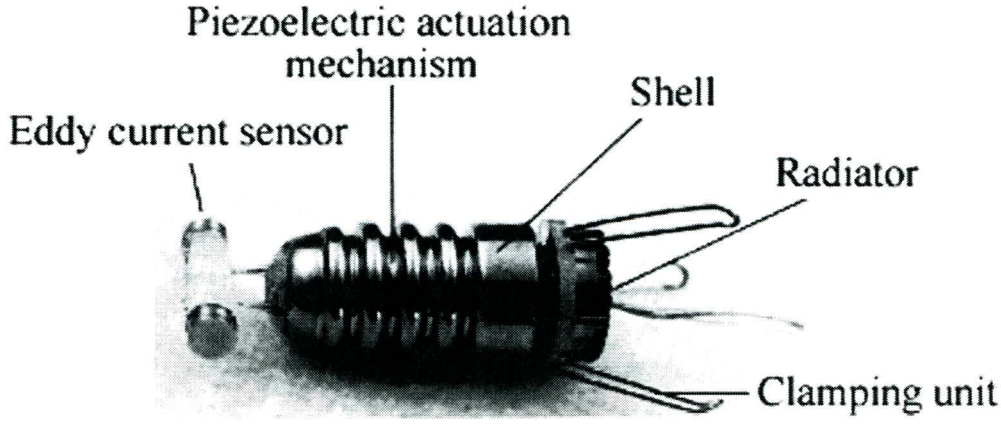

Fig.2-35 In-pipe inspection microrobot by T. Idogaki *et al.*

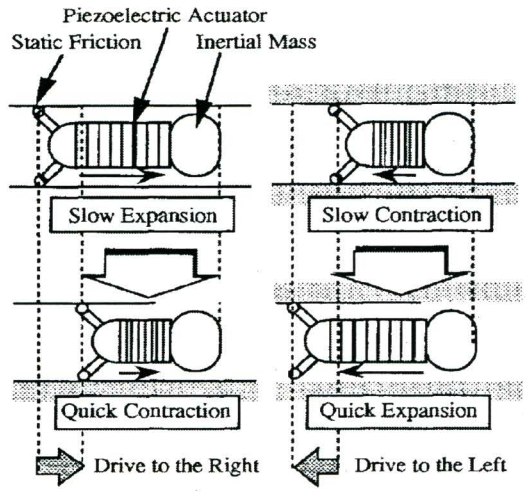

Fig.2-36 Locomotive principle of the in-pipe inspection microrobot

a pipe with a diameter of 10mm, taking pictures of the pipe walls, and transmitting these pictures via a wireless communication system. The robot is also wireless powered by microwave.

The configuration of the robot is shown in Fig.2-37. The robot consists of a RF module, locomotion mechanism, CCD camera device, and control circuit. The RF module receives two frequencies of microwaves and converts them to the power supply and information, respectively. The locomotion mechanism is made up of a multi-layer piezoelectric bimorph actuator driven by the saw-toothed wave voltage for an impact driving like the previous design.

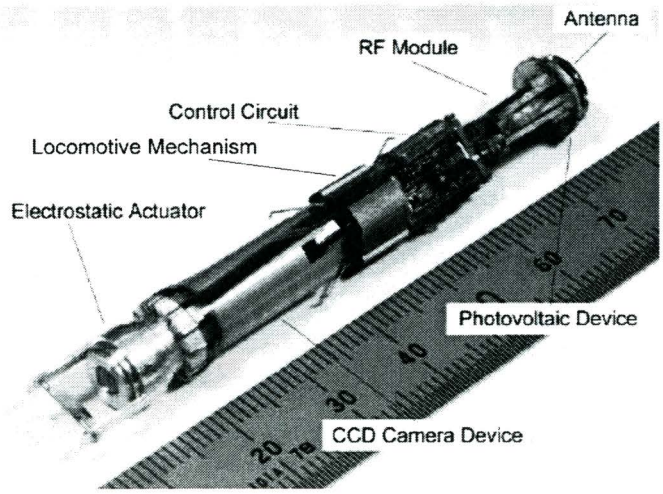

Fig.2-37 In-pipe wireless microrobot by H.Nishikawa *et al.*

An in-pipe inchworm microrobot using linear electromagnetic mechanism is described in [Sun 1998]. Fig.2-38 illustrates the proposed configuration and the overall size is Φ11mm×L24mm. The main components include a moving iron plunger, a cylinder electromagnet, a coil spring between the plunger and electromagnet, and two sets of bronze inclining legs outside the body. By controlling the on/off of the excitation of electromagnet, an inchworm-like motion can be achieved.

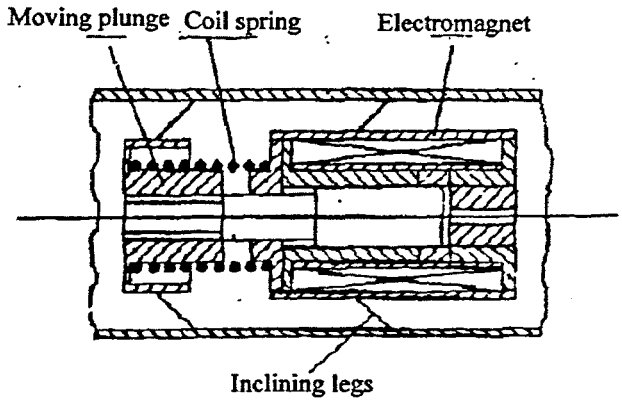

Fig.2-38 An inchworm type in-pipe microrobot
using linear electromagnetic mechanism

The scientists in the French National Centre of the Science Research have conducted many studies on in-pipe microrobots. C. Anthierens *et al.* developed a microrobot for inspection tasks in vapour generation (VG) pipes in nuclear power plant [Anthierens 1999]. The robot is similar to Sun's design but the difference is that the Frenchmen used pneumatic actuation method instead of electromagnet. The main components include a metal bellows actuator and two blocking modules as shown in Fig.2-39. The metal bellows actuator (Fig.2-39(b)) provides stretch force for the locomotion by compressed air flow. A Hall position sensor is embedded in the actuator for measuring the step size. The rear block module with three pneumatic actuated legs (Fig.2-39(c)) work together with metal bellows actuator. Through the same air chamber, the legs can brace on the pipe wall simultaneously. The frontal blocking module, however, has to use other driving source (a micro motor with reductor) due to lack of space (Fig.2-39(d)).

They also proposed other two types of SMA based in-pipe microrobots in [Anthierens 2000]. One of the designs called IntraTube is shown in Fig.2-40. The central unit of the

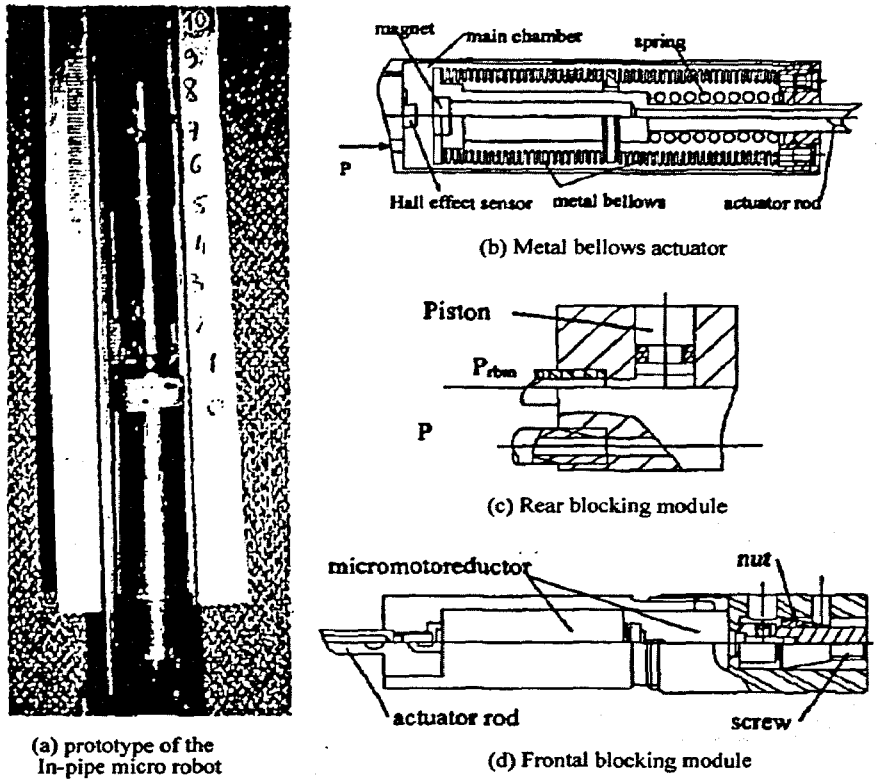

Fig.2-39 Pneumatic in-pipe microrobot by C. Anthierens

robot is made up of a SMA elongate actuator. Six legs placed with a space of 120° on the central unit provide the support of the robot body. Each leg is also actuated by a SMA element simultaneously to realise the clamping mechanism.

Another design with more flexibility is shown in Fig.2-41. It consists of a number of juxtaposed identical modules, called "locomotion modules". The number of the modules can vary according to the different applications. The locomotion module is made by

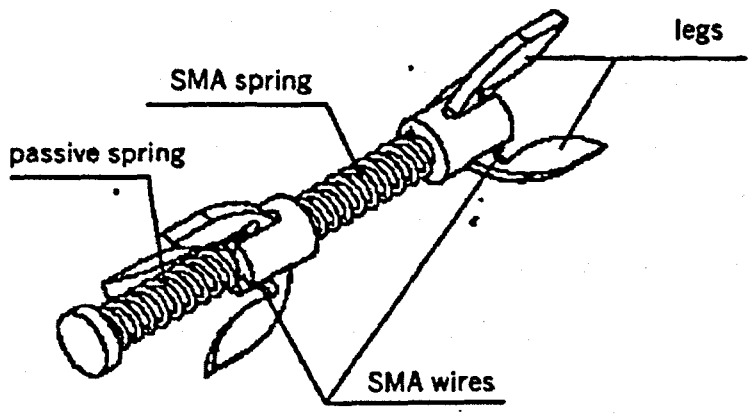

Fig.2-40 Structure of the IntraTube microrobot

mounting a flexible frame on a small rigid skeleton, as shown in Fig 2-41(a). The locomotion modules are jointed together with passive elastic links. An important feature of the locomotion module is that the two stable states of the module can provide both the advance movement and clamping mechanism (Fig.2-41(b)). By using the module, the locomotion can be realized by just using one type of actuator, which would be very attractive when mass production is required.

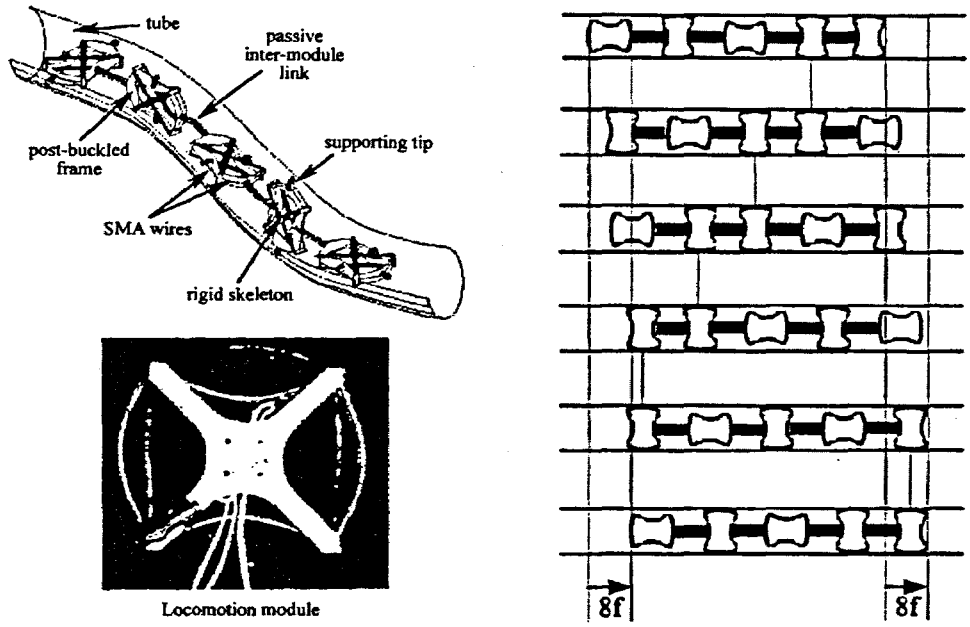

Fig.2-41 A flexible in-pipe microrobot using locomotion module

Power supply is usually a serious challenge when microrobot is travelling within a narrow space. A robotic design without any solid connection to the outside equipment would be an attractive implementation for in-pipe applications. In [Kim 2006], a wireless-controlled inchworm type in-pipe microrobot using SMA actuator was proposed. Fig.2-42 shows a photograph of the prototype and Fig.2-43 the locomotive principle. The microrobot composes of a SMA spring actuator and a silicon bellow. The locomotion of the robot is achieved by repeating the process of contraction and retraction. For temporarily clamping, two simple passive clampers are mounted on the frontal and rear body of the robot, as shown in Fig.2-43.

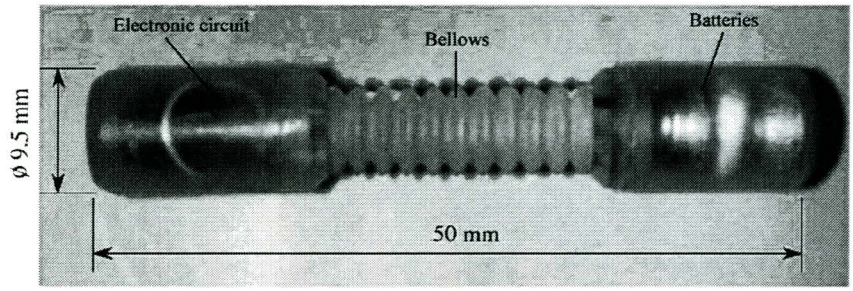

Fig.2-42 An inchworm type in-pipe microrobot based on SMA actuator

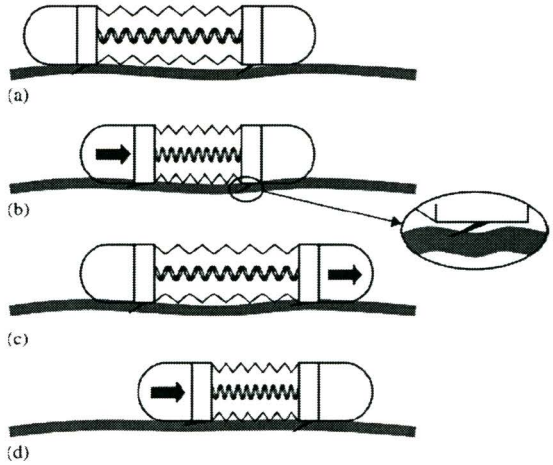

Fig.2-43 The clamping mechanism and locomotive principle

2.2.5.3 Swimming microrobots

As previously discussed, many mechanisms have been developed for the operation in small tubes or pipes. However, some of the applications may be filled with liquid. Swimming mechanisms are therefore necessary for the locomotion of microrobots in these applications.

Figs.2-44 and 2-45 show two types of swimming mechanisms illustrated in [Hayashi 1998]. The aim of the development is to make an effective driving mechanism that can operate in liquid with Reynolds number leas than 1, namely $Re \leq 1$, and without any wires to supply energy for driving. The fin-type swimming actuator is made by sticking a tail of polyimide to a cylindrical samarium-cobalt (SmCo) magnet. The magnet is

axially magnetised and put in an alternative magnetic field in the direction as shown in the figure, and it will swing in the direction of the magnetic field. Accordingly, the tail fin oscillates due to the motion of the magnet and the body swims. The spiral type mechanism is made by connecting a SmCo magnet with a spiral-made copper wire. When the magnet perpendicular to the moving direction is placed in a rotating magnetic field vertical to the axis of spiral wire, it will rotate as a synchronous motor. Thus, a spiral wave is produced in the tail and makes the body swim.

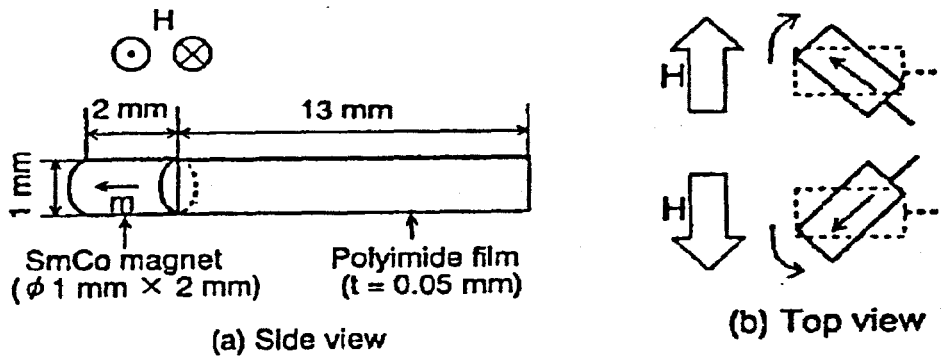

Fig.2-44 A fin-type swimming microrobot

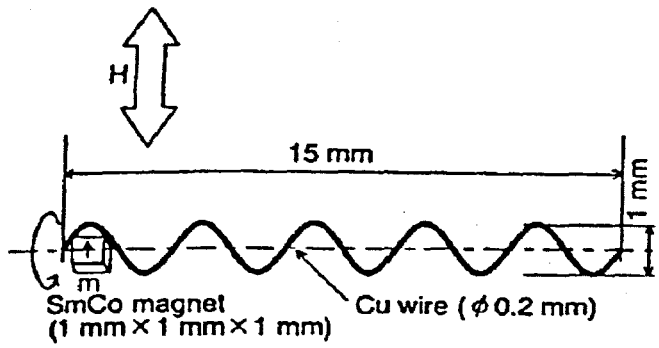

Fig.2-45 A spiral-type swimming microrobot

A swimming microrobot with a steering mechanism of 2-DOF was proposed in [Hayashi 1998]. As illustrated in Fig.2-46(b), a two-stage magnification structure is designed to enlarge the displacement of the left and right piezoelectric actuators. A pair of fins is fixed on the ends of the leg to generate forward and backward propulsive forces according to the operating frequency in water. The overall size of the robot is 32mm in length and 19mm in width. The robot can steer effectively by combination of these propulsive forces to avoid an obstacle in liquid.

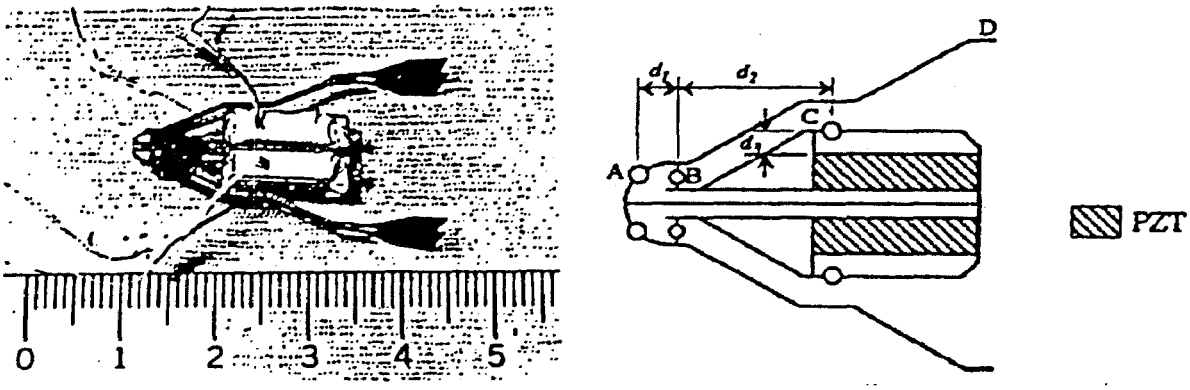

(a) (b)

Fig.2-46 (a) A swimming microrobot with a steering mechanism
(b) Actuation principle of the steering mechanism

In [Ishiyama 2000], a spiral type microrobot for swimming in liquid was presented. Fig.2-47(a) shows its schematic structure. The machine composes of a cylindrical Neodymium Iron Boron (NdFeB) magnet (Φ1.2mm×L7.5mm), a ceramic tube (Φ1.2mm×L3.75mm), and a spiral blade made of Tungsten wire. Another prototype with a tip head was also developed for running in gel (Fig.2-47(b)). When a rotating magnetic field is applied around the microrobot, it will spin and move within the liquid or gel. However, experiments showed that it could only swim in the medium of lower Reynolds number.

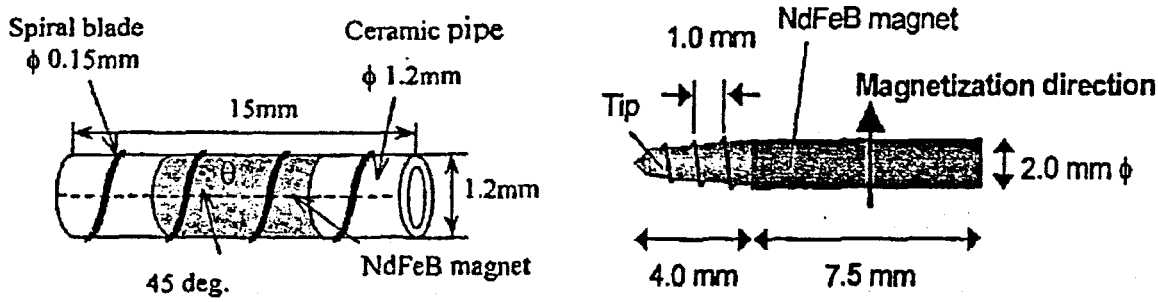

(a) (b)

Fig. 2-47 (a) Schematic structure of a spiral type swimming microrobot
(b) Prototype of the spiral-type swimming microrobot for running in gel

Shuxiang Guo *et al.* described another screw-type swimming microrobot with guide-wheels [Guo 2003]. The schematic structure is shown in Fig.2-48. It consists of a body with driving screw and two guide-wheels. There are eight permanent magnet bars within the body so that the body of the microrobot can spin if there is an external rotating magnetic field.

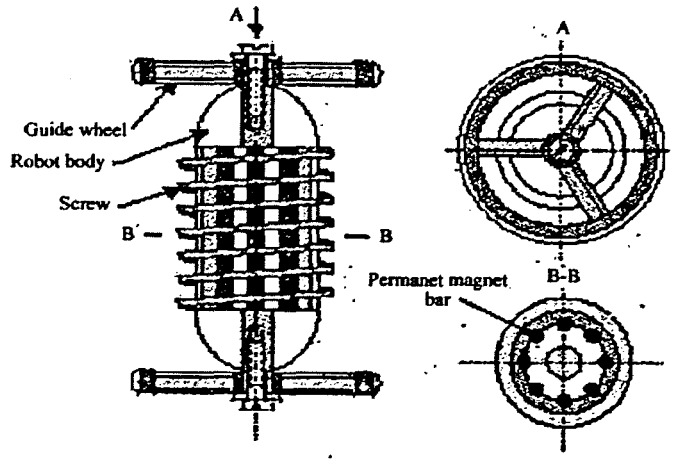

Fig. 2-48 A screw type swimming microrobot with guide-wheel

2.2.5.4 Medical microrobots

It has long been one of the serious dreams of medical surgeons to operate without any damaging effects on the patients. Moreover, there is no doubt that the demands for medical inspection without any pain or discomfort will increase due to the growing number of elder patients. With this in mind, during the past decades, robotic systems have been appearing in the operating room and robotic technology is now regularly used to aid endoscopes in MIS.

Endoscopy is an important procedure for the diagnosis of various pathologies, in particular cancers of the gastrointestinal tract, such as the colon and the rectum. A conventional endoscopic system for inspection is quite rigid and requires the doctor to exert force and rotate the distal part, thus causing discomfort to the patient. An idea to improve the present endoscopy is a self-navigating, independent and intelligent endoscopic microrobot. According to the operational environments and the functionalities, the endoscopic microrobot can be regarded as a biomedical application oriented in-pipe microrobot.

The first concept of medical microrobot named MEDIWORM was proposed in [Ikuta

1988a]. Fig.2-49 shows the basic sketch of the MEDIWORM. The proposed microrobot is thought to be teleoperated by the doctor and can actively move within the alimentary tract by a series of inchworm-like expansions and contractions. Several miniaturised tools such as image sensors, needles, and gripers are installed within the robot for medical inspection and treatment. Nowadays, with the rapid advances in micro-engineering technology, the concept of MEDIWORM is far improved. The idea of intelligent microcapsule as shown in Fig.2-50 [Kassim 2006], which is recognised as the future technology of the medical microrobot, has been brought out in 2000 by the Intelligent Microsystem Centre in Korea.

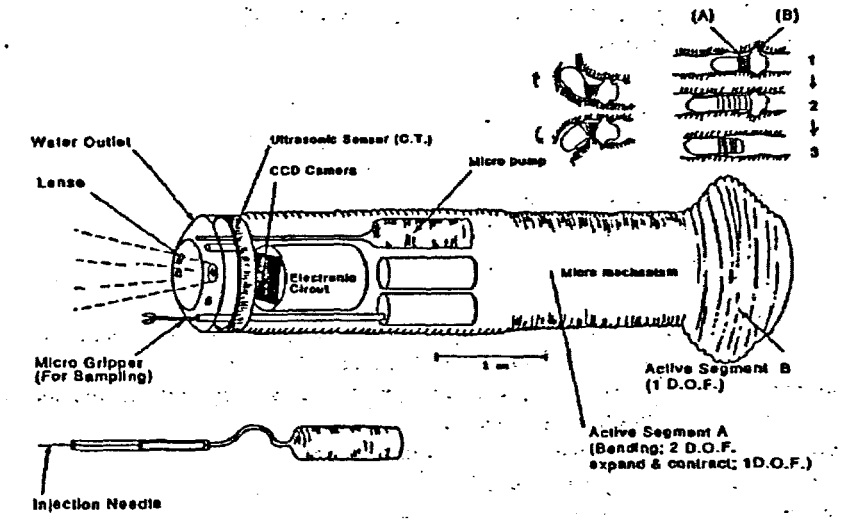

Fig.2-49 Basic concept of medical microrobot MEDIWORM

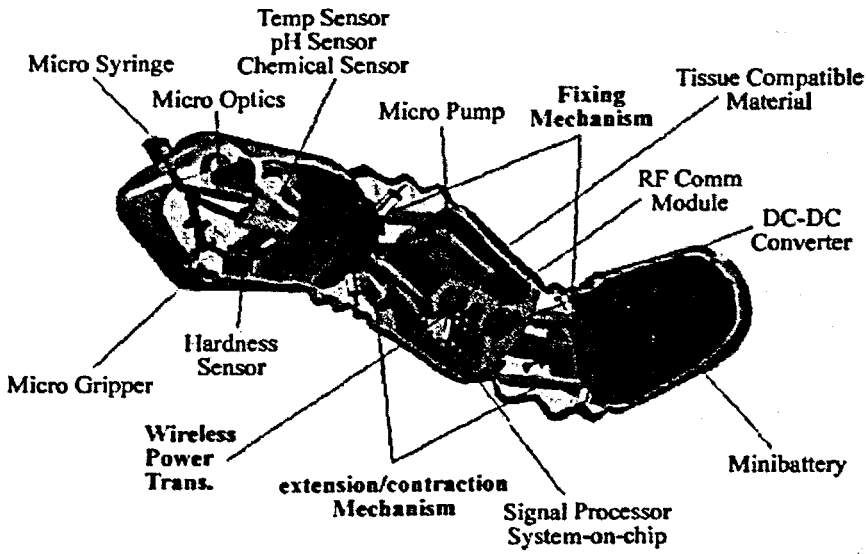

Fig.2-50. Proposed intelligent microcapsule MiRO

Although the concept has been proposed for nearly twenty years, the studies on the intelligent medical microrobot are still in the primary stage. The main challenges lie on the flexible structures and locomotion technologies of the robotic system. Nonetheless, since 1960's, many research and development have been conducted to improve the conventional endoscope to an active device for the reduction of the trauma and discomfort to the patient and enhancement of the manoeuvrability. These achievements provide essential clues for the future technologies on the medical microrobots.

As early as in 1961, an automatic locomotion technique for a catheter using the inchworm locomotion principle was patented [Drapier 1961]. M. Drapier also introduced two methods for acquiring adhesion between the clamper and the colon wall: the suction and expansion. In [Frazer 1979], the inventor illustrated a similar technique with expansion method of clamping, and proposed a pneumatic mechanism consisting two radially expandable blades and an axially expandable bellows.

Since 1994, J. Burdick *et al.* developed robotic endoscopes based on the expansion locomotion technique [Slatkin 1995]. Fig.2-51 shows (a) a photograph of one of the prototypes developed in their laboratory, and (b) the basic structure of endoscope. It is

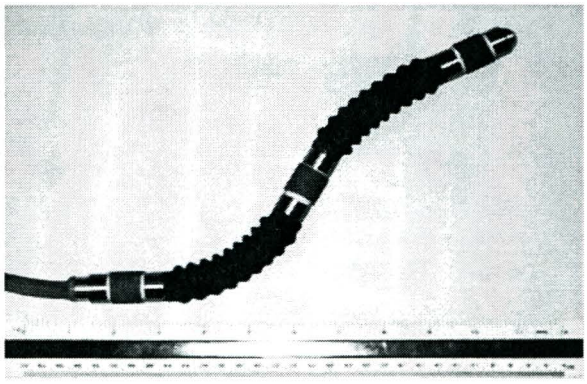

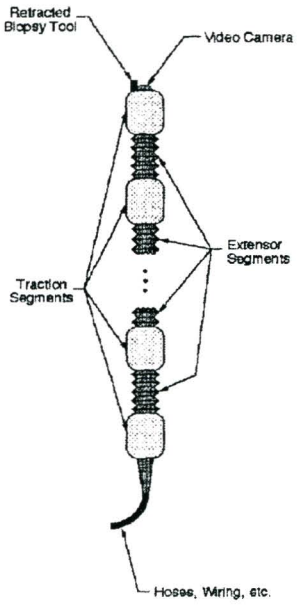

(a) (b)

Fig.2-51 Robotic endoscope by J. Burdick *et al.*

an endoscopic robot with a trailing cable which consists of electric wiring for control signals, tubing to connect the pneumatic actuators to high and low pressure sources, and an optical fibre bundle for illumination and imaging of the area in front of the robot.

In order to propel it self, the robot employs mechanisms along its length, which are described a "gripper" and "extensors". The gripers provide the traction against the lumen wall by expanding radially outward while the extensors provide extensibility between the grippers. Locomotion of the robot is realised by specific sequences of gripping and stretching actions like an earthworm. The fifth generation of the prototype of the robotic endoscope has been developed and tested in a live pig in 2000.

An inchworm type medical microrobot was described in [Hayashi 1998]. As shown in Fig.2-52, the design is composed of three or four plastic bellows-cells and is driven by compressed air through electromagnetic valves into each bellows-cell in the order of 1-2-3-4.

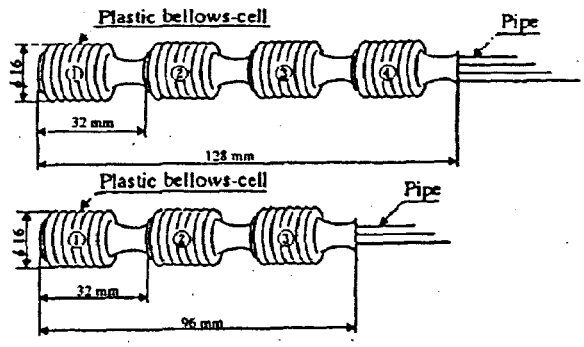

Fig.2-52 An artificial inchworm for medical treatment

In [Asari 2000], a design that comprises of an extensor module sandwiched between two clamper modules was proposed, as shown in Fig.2-53. In the design, each clamper module is a closed toroidal balloon with six passive vacuum cups embedded on its surface to give it a better grip to the colon wall. The connecting module is made up of three extensors where each extensor is a pneumatic bellows with an extension spring. As per the design of the connecting module, if the extension is same for all the three extensors, the head/tail extends parallel to its axis; otherwise it bends. While moving in

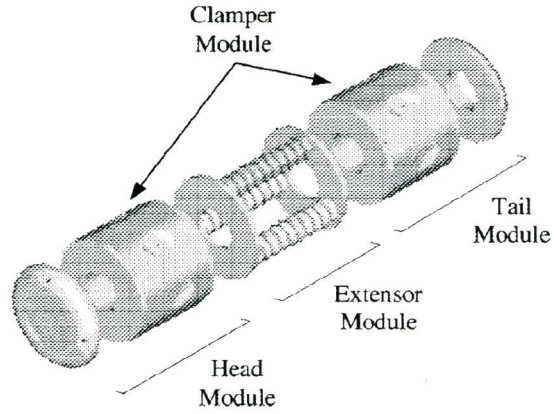

Fig.2-53 Endoscopic microrobot by K. V. Asari *et al.*

the forward direction, the tail clamper firstly expands and holds the colon wall followed by extension of connecting module thus pushing the head. Subsequently the head clamper clamps the head while the tail clamper is released which causes retraction of the tail towards the head.

On the contrary, M. C. Carrozza *et al.* utilised the suction to ascertain the adhesion on to the colon walls and developed a few prototypes of robotic endoscope for testing [Carrozza 1996]. One of the designs consists of three modules: two clamping module and one extension module, as shown in Fig.2-54. In the design, suction is provided by a number of small holes disposed along the surface of the clamping module located at each end of the robot. When a vacuum is introduced to the clamping actuator, the

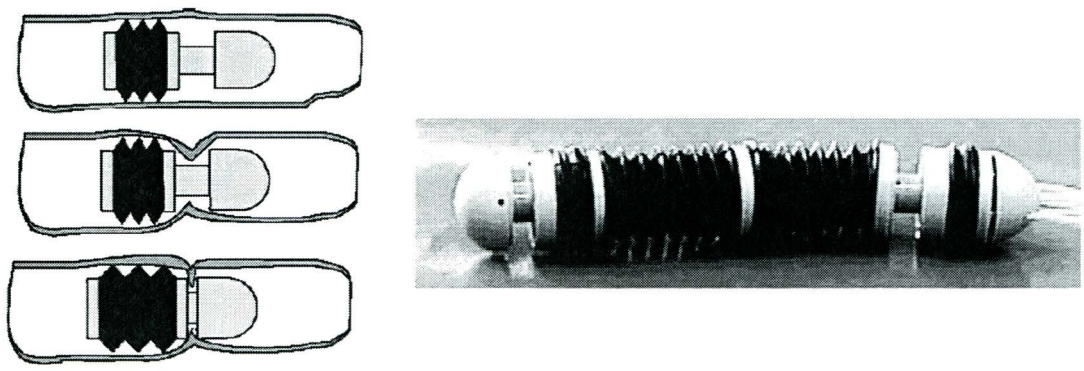

Fig.2-54 Robotic endoscope developed by M. C. Carrozza *et al.*
(a) Clamping mechanism, (b) prototype

negative pressure at the small holes will cause the actuator to "suck" onto the colon wall and hence adhere the colon. The central actuator between the two clamping actuators is used for extension. By a sequence of activating the extension and clamping mechanism, the microrobot can move within the colon like an inchworm.

An endoscopic microrobot that is actuated by pneumatic impulsive mechanism was reported in [Lim 2001]. The conceptual drawing of the proposed self-propelling endoscope is illustrated in Fig.2-55. It compromises an actuator for locomotion, bow-shaped flexible supporter, linear actuator for steering, shock absorber, and several sensing components for diagnosis. The locomotion actuator resembles a pneumatic cylinder, as shown in Fig.2-56(a). When compressed air is injected to the locomotion actuator, the piston moves forward while the body goes in the opposite direction (pneumatic effect). As the air is exhausted, the reverse motion will occur due to the force of the compressed spring (spring effect). By repeating the activation cycle, continuous motion can be achieved. In addition, bi-directional movement can be realised by letting one effect larger than the other.

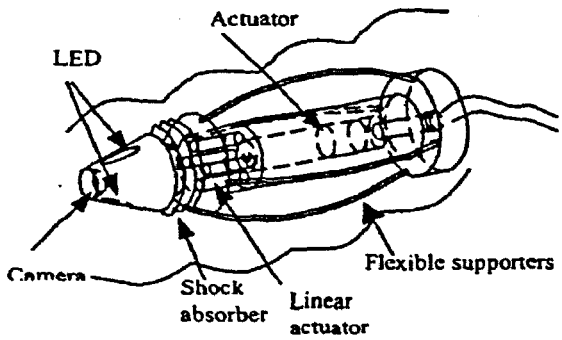

Fig. 2-55 Schematic of a self-propelling endoscope

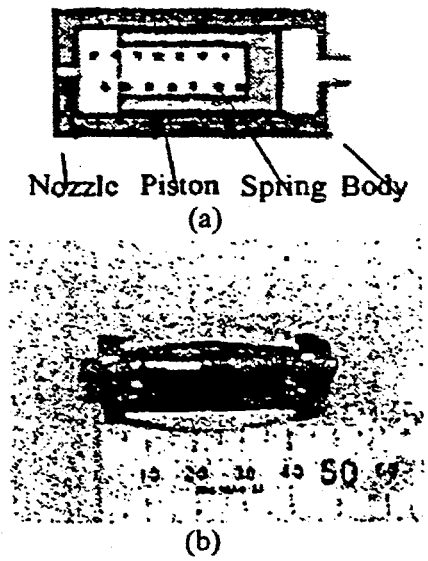

Fig.2-56 (a) Pneumatic locomotion actuator
(b) Prototype with flexible supporter

Another robotic endoscope using similar impact driving principle was proposed in [Hyun 2001]. It is actuated by a movable permanent magnet colliding against two electrically magnetized stationary magnets on each side of a cylinder. Fig.2-57 shows

the proposed mechanism. For a forward motion, the head solenoid is activated, thus causing the permanent magnet to move toward it. A force will be generated due to the impact between the permanent magnet and the electromagnet, which moves the actuator forward. After impact, the current direction of the head solenoid reverses, and a repulsive force is hence induced to the permanent magnet, causing it to move backward. The actuator can move forward continuously by repeating the sequence. Two prototypes of different sizes were built to verify the locomotion idea, and both prototypes move in accordance to the design. However, the force produced to power the robotic colonoscopy is still weak. In addition, the heat generated by the electromagnet is also a safety concern.

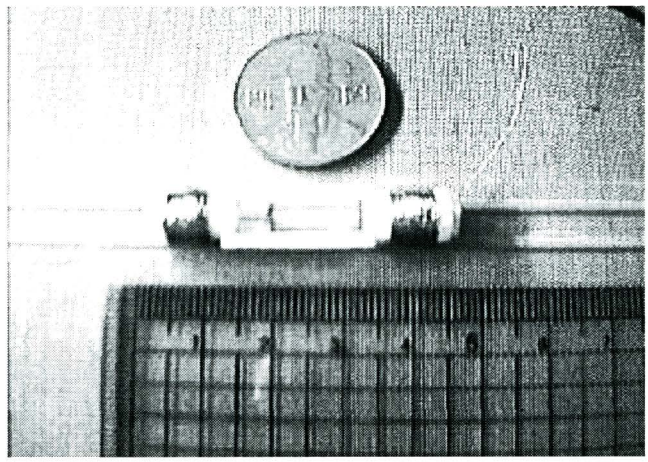

Fig.2-57 A robotic endoscope actuated by impact drive mechanism

Millipedes have many legs that move in waves, and the same principle can be applied to the robotic design. In [Utsugi 1979], the author described a creeping mechanism with three inflatable cuffs that form one section of locomotion unit, which is shown in Fig.2-58. The middle, propellant cuff is the leg that can be pushed backward and forward by the cuffs on either side of it. The operation sequence is that the propellant cuffs are inflated so that they press against the walls of the colon with enough force to prevent slipping. Next, the drive cuffs are inflated, thereby pushing the propellant cuffs backward so that the sheath, and hence the endoscope moves forward. The return cuffs are now inflated so that they first lift the wall of the gut off the propellant cuffs and then push those cuffs back onto the deflated drive cuffs.

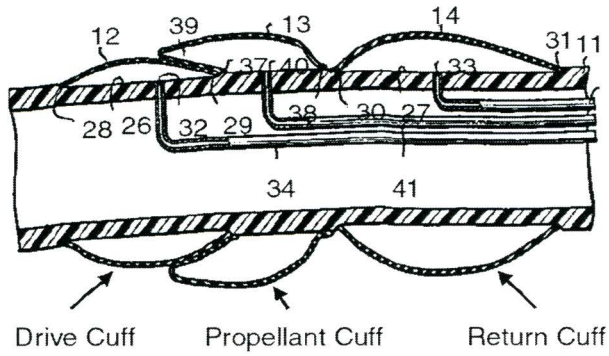

Fig.2-58 Millipedes locomotion mechanism by M. Utsugi

An active endoscope called EndoCrawler based on the pneumatically actuated legs was proposed in [Ng 2000]. The prototype is shown in Fig.2-59(a). It is made up of rigid segments jointed together by passive flexible rubber joints with three DOFs. There are four rubber bellow actuators on each segment with 90° apart each other, as shown in Fig.2-59(b). When compressed air is applied to the base of the actuator, it will inflate and extend longitudinally until it touches the colon wall at an angle of 45°. By alternatively activating the actuators on each segment, the friction between the tip of the actuator and the colon wall will cause the movement of the robot.

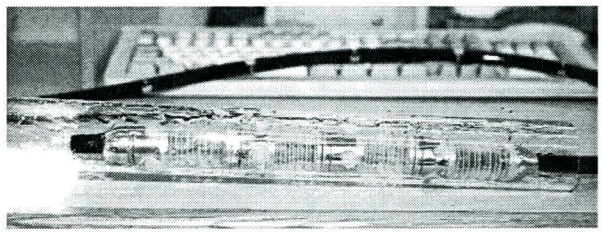

(a) Photograph of the EndoCrawler

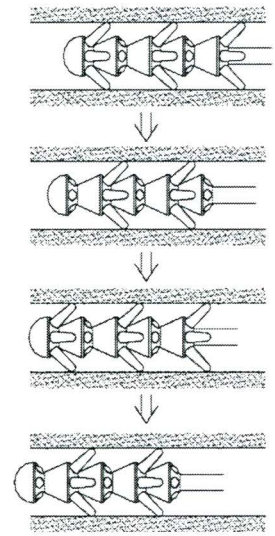

(b) A simple gait sequence

Fig.2-59 EndoCrawler proposed by W. S. Ng

In 2005, M. Quirini *et al.* illustrated their research on a design of autonomous medical microrobot with legged locomotion for minimally invasive endoscope [Quirini 2005]. A hexapod device with a sprawled insect-like posture has been conceived for the

development of the endoscopic capsule, as shown in Fig.2-60. In the prototype testing, the device legs are externally actuated by push-pull cables moved by traditional DC servomotor. They claimed that the advantage of using the electromagnetic motor is the potential of wireless solution in the final capsule. A locomotion gait called *umbrella* shown in Fig.2-60(b) is applied for the propelling of the microrobot. The whole system has been preliminary tested in a porcine intestine and in a latex gastrointestinal simulator for evaluating the performances. Further studies are undergoing on the system modularity and leg disposition and distance.

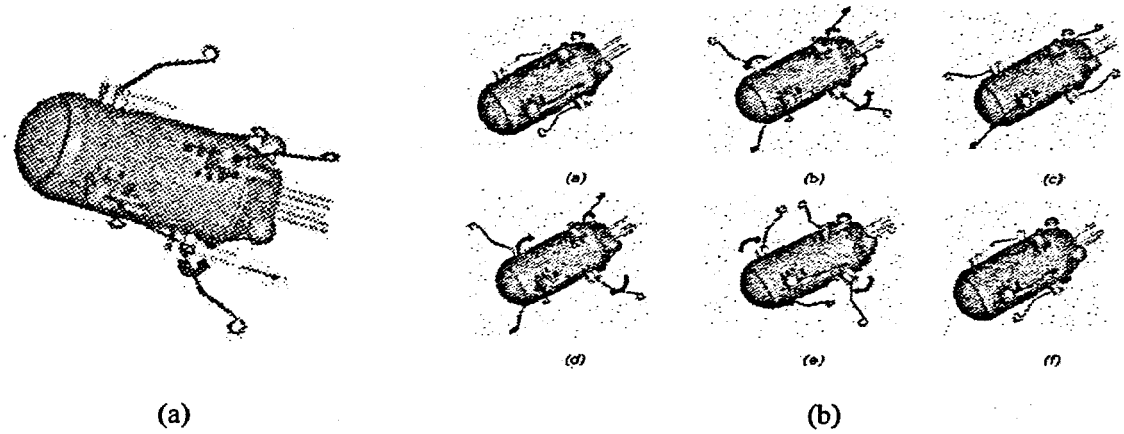

Fig.2-60 An autonomous medical microrobot with legged locomotion
(a) overall scheme with push-pull cables; (b) *umbrella* locomotion gait

From the beginning of the 21st century, some encouraging advances have been achieved in the development of intelligent microcapsules. However, no active locomotion was built but natural peristalsis is utilised for their movement within the human body.

A dual capsule wireless endoscope was proposed in [Gong 2000], which houses a miniature CCD camera, a processor, and a halogen light in one capsule and a microwave transmitter and batteries in the other (Fig.2-61). The prototype was surgically inserted into the stomach of anaesthetized pigs. Although it has to be removed surgically after the experiment, the study demonstrates the feasibility of transmitting high-quality images through the abdominal wall with a small microwave and radio frequency transmitter. It was also the first to report successful wireless transmission of a moving colour television image of the stomach in a living subject.

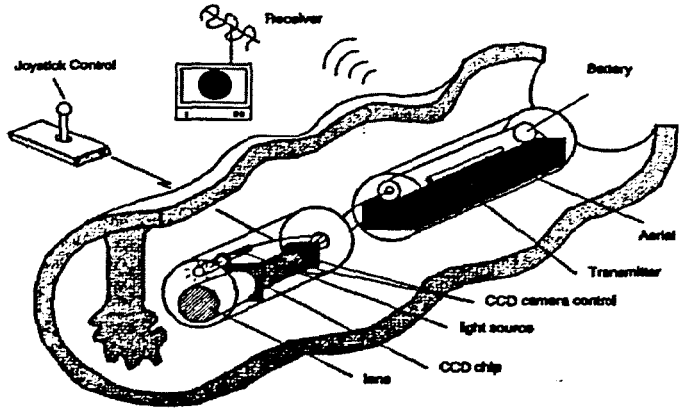

Fig.2-61 Concept of wireless endoscope by F. Gong *et al.*

In 2002, the first commercialised disposable capsule endoscope "M2A" [Given 2004] was introduced by an Israel company, Given Imaging Ltd. As shown in Fig.2-62(a), the capsule is a naturally ingested device for use in the gastrointestinal tract. Without any actuation element, M2A is moved via natural peristalsis throughout the gastrointestinal tract, transmitting colour video images as it passes.

Another endoscopic capsule product NORIKA3 (Fig.2-62(b)), which was developed by RF system Lab in Japan, has the similar function as the M2A but has a wireless power transmission supply and a rotation mechanism [RF 2004]. By applying a rotational magnetic field outside the human body, the capsule can rotate itself within a short period of time to adjust its position for better image capturing. However, its locomotion still relies on natural peristalsis.

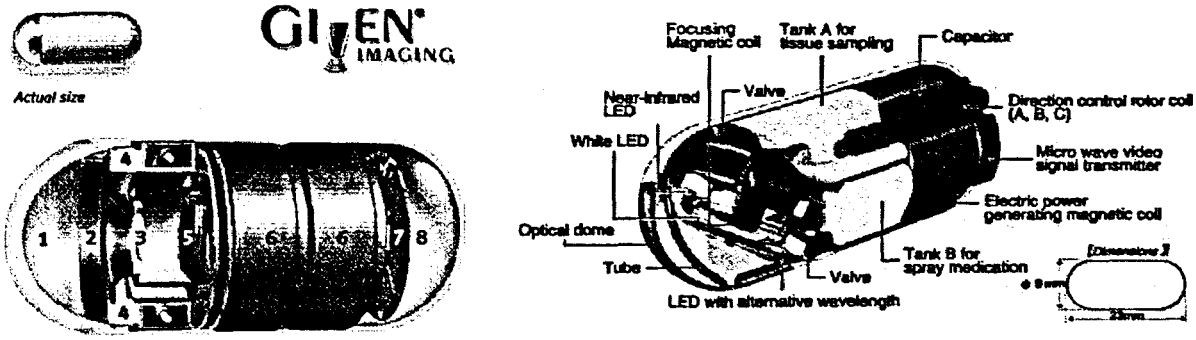

(a) (b)

Fig.2-62 (a) M2A developed by Given Imaging Ltd.
(b) NORIKA3 developed by RF Lab

2.3 Actuators for Microrobots

From the mechanical point of view, a robotic system is a mechanism composed of a set of links connected with joints that transfer motion and force from an input source to an output end-effector. As the critical components in robotic systems, different types of actuators have been developed as the motion and force sources. Microsystems, especially microrobots, require advanced actuators with very small dimensions, simple mechanical construction and high reliability. An actuator for microrobots can be a device of a few millimetres down to a few micrometres in size, and has a functional principle in the micro world.

Three types of actuation have been the cores of motion and force power for most of the robotic systems in macro domain. They are hydraulic, pneumatic, and electromagnetic actuators and are regarded as the "conventional" actuators [Mavroidis 1999]. Because of their successful applications in the macro robots, these principles were naturally attempted in the micro systems. However, some of the conventional designs that are intuitively obvious in macro scale do not work in micro systems [Wood 1998]. Many aspects need to be re-considered in the micro actuators, such as the structure, scaling effects, materials involved, fabrication and reliability. Accordingly, innovations should be conceived for these conventional methods to meet the requirements in the micro applications.

Apart from the conventional principles, many new types of actuators are being researched and used for micro robotic systems. These actuators rely on the use of different types of transducing materials and energy conversion principles. Examples of these actuators are piezoelectric, shape memory alloys, electrostatic, electrostrictive, and magnetostrictive actuators. The purpose of this section is to investigate the properties of these actuators, their advantages and drawbacks, and the applications in micro robotic systems.

2.3.1 Hydraulic/Pneumatic actuators

A hydraulic actuator works by changes of pressure and can be used in both linear and rotary actuation. The general linear mechanism consists of a piston encased in a chamber with a piston rod protruding from the chamber. The piston rod serves as the power transmission link between the piston inside the chamber and the external world. There are two major configurations of this actuator: single or double action. For the single action configuration, it can exert controllable forces in only one direction and uses a spring to return the piston to the neutral or un-energized position. A double action actuator, on the contrary, can be actively controlled in both directions within the chamber. Fig.2-63 shows a cut away view of a double action actuator [Stewart 1987]. In case of rotary actuation, the power unit is a set of vanes attached to a drive shaft and encased in a chamber. Within the chamber the actuator is rotated by differential pressure across the vanes and the action is transmitted through the drive shaft to the external world.

The pneumatic actuators are the direct descendents of hydraulic systems. The difference between the two is that pneumatic systems use a compressible gas (e.g. air) as the medium for energy transmission. This makes the pneumatic system more passively compliant than the hydraulic system. With pneumatic actuators, the pressure within the chambers is lower than that of hydraulic systems resulting in lower force capabilities. Fig.2-64 shows a cut away view of a basic pneumatic actuator. It is quite similar to the hydraulic counterpart however there are no return hydraulic lines for fluid. In a typical

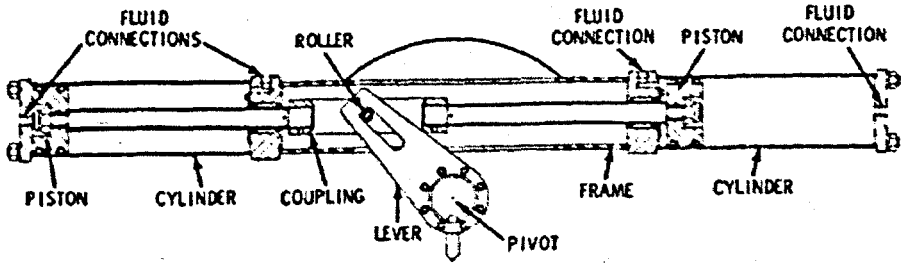

Fig.2-63 Drawing of a double action hydraulic actuator

pneumatic actuator, gas is simply exhausted through an outlet valve in the actuator. The control of pneumatic systems is very similar to hydraulics with some exceptions to gains and stiffness constants.

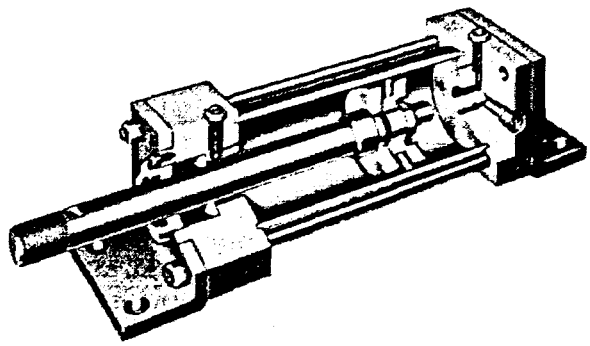

Fig.2-64 Cutaway view of a basic pneumatic actuator

The main advantage of hydraulic actuators is that they can deliver a great deal of power compared to their actuator inertia. Therefore, this type of actuator has a high power density, which is attractive to the micro devices. Other aspects, which make a hydraulic actuator useful, are the low compressibility of hydraulic fluids and, the high stiffness which leads to an associated high natural frequency and rapid response. As for this method of actuation, design characteristics are well known so the process of design is made easier due to this extent of knowledge.

However, the disadvantages of the hydraulic actuators are significant and some of them would be fatal for a micro system with high integration level. One of the larger concerns with hydraulic systems is the containment of the fluid within the actuation system. Not only is this because of the contamination of the surrounding environment, but the leakage can also contaminate the fluid and possibly lead to damage of interior surfaces. The degradation of the interior surfaces and the contamination of the fluid will result in a marked drop in the performance of the system. In addition, commonly used hydraulic fluids for industrial applications are also function as lubricants that are usually flammable and pressurised, so leaks could pose an extreme hazard to equipment and personnel. A safe and clean medium should be sought in micro applications. As a result, most existing miniature hydraulic actuators suffer from either leakage or high friction

and are restricted in the micro systems because of inherent sealing difficulties.

Pneumatic actuators have less force capability than hydraulic actuators. Since, in contrast, the system operates at a lower pressure than the hydraulics and may not require return lines for the fluid, the support structure of the actuator is simpler and lighter than the other system. Pneumatics is cleaner and non-flammable that makes its usage in certain environments (i.e. clean rooms, operating rooms) more desired.

A common drawback of the fluidic (hydraulic or pneumatic) actuators is that an extra driving source and relevant accessories are required to store and provide energy that can be transferred by the fluid. Hence, other types of actuators, e.g. electric machines, must be introduced, and they should be either integrated on board or linked with pipes or hoses for some applications with restricted space. A good example can be found in Fig.2-28.

Pneumatic actuators have been used for the locomotive mechanism in many of micro robotic designs, which have been described in section 2.1.5. Most of the applications are in-pipe microrobots or medical endoscopies. In addition, the traditional fluidic actuators have been evolved to many novel configurations for the micro systems, some of which are quite different from their ancestors to meet the requirement in micro systems. One of the attractive implementations of the concept of fluidic actuator is the so called "rubberuator" (a contraction of the term rubber actuator) [Dario 1992]. It was proposed originally in macro robotic applications for soft operation and safety, and it can be driven either by a pneumatic or by a hydraulic system. One of the designs of rubberuator for microrobots called FMA was presented in [Suzumori 1991], which is a fibber-reinforced silicon rubber micro actuator with one to three DOFs. The structure and working principle of the actuator is shown in Fig.2-65. The designed actuators are driven by adjusting the pressure in the three internal chambers of the rubber structure. When the internal chamber is pressurised, the actuator bends and can act as a micro leg or gripper.

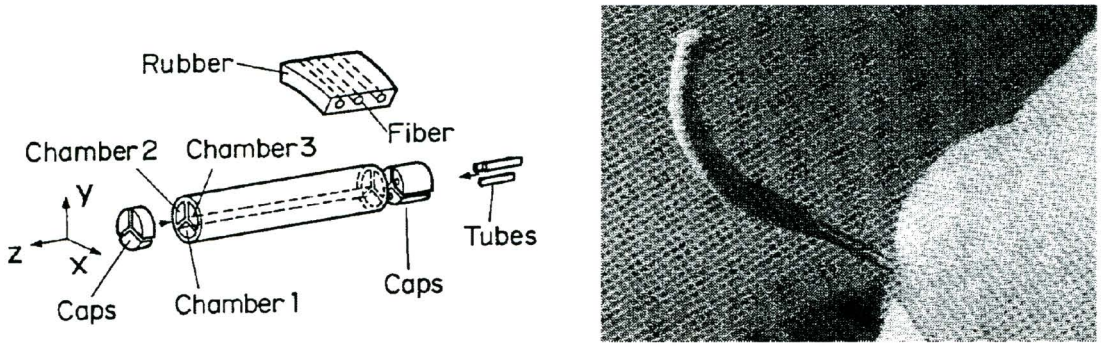

(a) (b)

Fig.2.65 (a) Flexible micro actuator developed by K. Suzumori
(b) Movement of a 1mm diameter FMA

In [Suzumori 1999], a pneumatic wobble motor was reported. The objective of the design is to generate relatively high torque for rotating the camera and the hands in an in-pipe inspection microrobot (Fig.2-31). Figs.2-66(a) and (b) show the prototype and its schematic structure, respectively. The motor consists of a wobble generator, a wobble ring, and a rotor. The wobble generator is made of silicone rubber and is structured with six chambers. The wobble ring and rotor are made of stainless steel, and the internal and external gears are fabricated on the wobble ring and on the rotor, respectively. Pressurising each chamber sequentially through pneumatic tubes causes periodic elastic deformations of the wobble generator, thereby achieving revolution of the wobble ring. The tooth number of the rotor is less than that of the wobble ring, and the external surface of the wobble ring is attached to the internal surface of the wobble generator to allow the wobble ring only to revolve but not to rotate. Thus, revolution of the wobble ring causes rotation of the rotor. A latest developed prototype is 6.6mm in diameter,

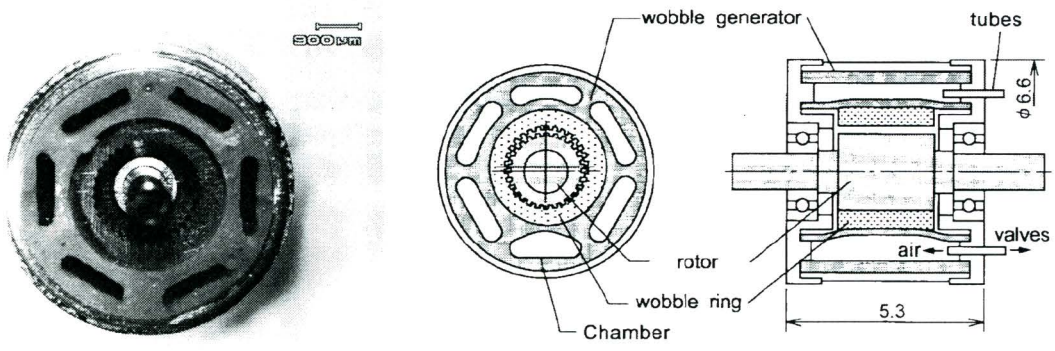

(a) (b)

Fig.2-66 Pneumatic wobble motor (a) Prototype, (b) Schematic structure

5.3mm in length, and can generates a torque of several mN·mm. In addition to the pneumatic wobble motor, they also developed a micro-handling device for the microrobot by adopting the previously developed pneumatic actuator FMA, which is describe in Fig.2-65. The designed micro hand can grasp an object of 1~3 g in weight and the response time is 0.5s.

In [Ikuta 2003], an active catheter using the hydraulic actuator was proposed, as shown in Fig.2-67. The system consists of hydraulic bellows as actuators at each joint and a drive tube to control the bellows. Each joint is designed to bend while a bellows is extended by fluid supply. The hydraulic fluid used is normal saline hence safety is ensured. In order to simplify the hydraulic control mechanism, a novel Band Pass Valve (BPV), which will be open only when the fluid pressure is within its specified range (Fig.2-67(b)), was invented so that a number of hydraulic bellows can be control by only one hydraulic input.

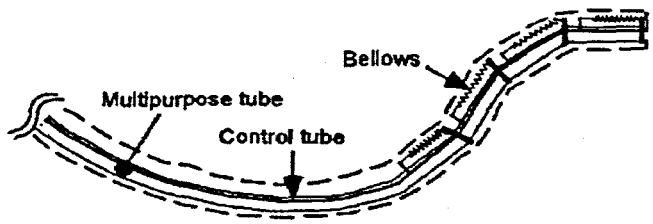

(a) Basic schematic structure

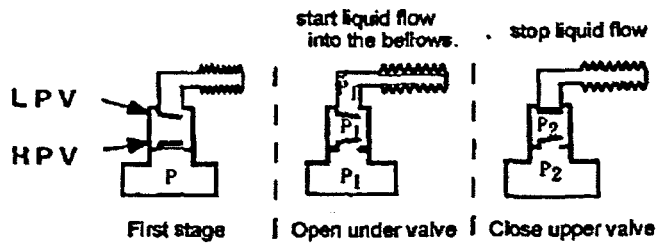

(b) Basic principle of Band Pass Valve

Fig.2-67 Micro hydraulic active catheter

2.3.2 Electromagnetic actuators

Electromagnetic actuator is the most commonly used driving source in the macro

domain. A general form of electromagnetic actuation is based on the Lorenz effect: a conductor of length l carrying a current of magnitude I in a magnetic field B experience a force F_{em} given by

$$F_{em} = \vec{l} \times \vec{B}, \tag{2.1}$$

and the force direction is determined by a vector production.

The electromagnetic actuators, especially the electric machines, have been in use for more than a hundred years. Of the three types of conventional actuators, the electromagnetic actuators have the largest variety of possible devices such as solenoid actuators and different types of electric machines including direct current (DC), alternate current (AC) motors (synchronous and induction), and their variants.

A simplest electromagnetic actuator could be a solenoid actuator. It usually consists of a solenoid electromagnet and a ferromagnetic moving component. An air gap is required between the two components. When a current is applied to the electromagnet, a magnetic force and movement are generated due to the Lorenz effect. A typical solenoid actuator is shown in Fig.2-68. The force generated by the solenoid is a function of the number of turns of the coil N_t, the current I, the pole area A, the air gap length g, and magnetic permeability of air μ_0 [Slocum 1992], and can be expressed as

$$F = \frac{\mu_0 N_t^2 I^2 A}{2g^2}. \tag{2.2}$$

By using a permanent magnet, a larger actuation force can be obtained, and

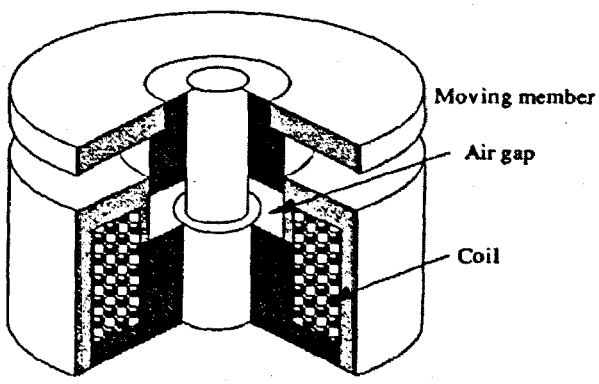

Fig.2-68 Basic structure of a solenoid actuator

bi-directional force and motion can be achieved by changing the polarity of the excitation current.

A DC motor is a device for converting DC electrical energy into rotary or linear mechanical energy. Generally, a DC motor has a rotor which is the inner part that rotates and a stator composed of two or more permanent magnet pole pieces. The rotor is composed of windings which are connected to a mechanical commutator. A schematic of a DC motor is illustrated in Fig.2-69. In a DC machine, the current in each winding of the rotor is alternating so that unidirectional torque or force can be produced continuously. Accordingly, a commutator is required to convert the input direct current into alternating current at appropriate times, as shown in the figure.

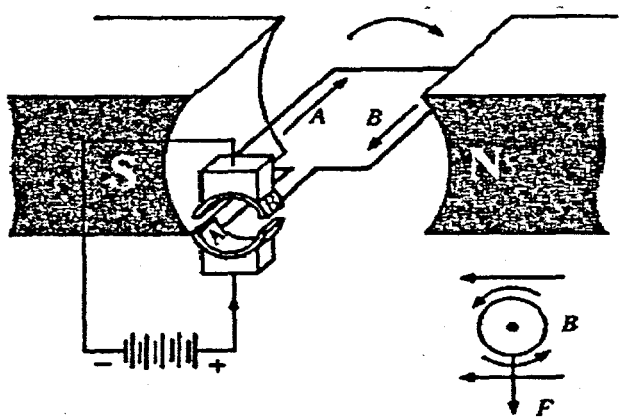

Fig.2-69 Schematic of a DC motor

AC motors use either single-phase or polyphase alternating current as their power source as opposed to the direct current of DC motors. The working principle of most AC motors is the rotating electromagnetic fields, as illustrated in Fig.2-70 [Henkenius 1991]. The magnetic field produced by the alternative stator current rotates in the air gap. The magnetic field in the rotor chases the electrically induced rotating magnetic field in the stator by being attracted and repelled by it. The interaction of two magnetic fields causes a continuous torque on the rotor and makes it rotate.

There are two basic types of AC motors that are in wide applications: synchronous and

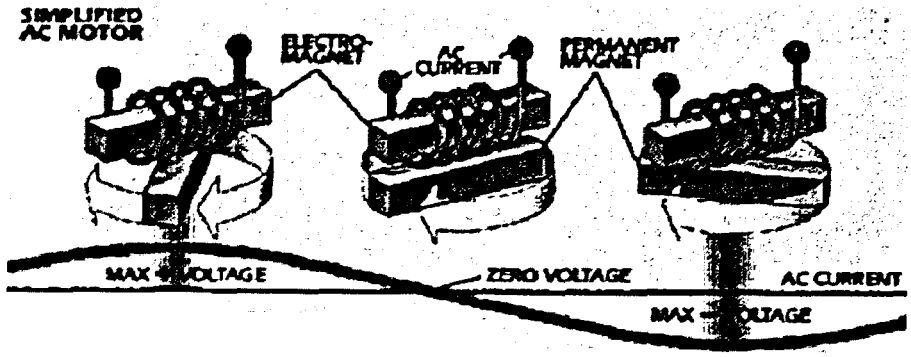

Fig.2-70 Basic principle of an AC motor

induction motors. AC synchronous motors are able to operate at a constant speed in absolute synchronism with the excitation frequency. The synchronous motor operates when polyphase (often 3-phase) alternative currents in the stator windings produce a rotating magnetic field around the rotor. The rotor is energised by direct current or permanent magnets that cause it to be attracted to the rotating magnetic field created by the stator currents. The rotor rotates at the same speed as that created by stator currents, known as synchronous speed, and a steady torque results.

The difference between an induction and synchronous motors is the rotor structure. The rotor winding of an induction motor is a multi phase short-circuited winding with no external excitation. When a rotating magnetic field is generated by the stator windings, currents will be inducted in the rotor windings and hence a torque is produced due to Lorenz effect. Since there must be a relative movement between the magnetic filed and rotor, the rotating speed of the rotor is always different from that of the magnetic field created by the stator currents. Therefore, this type of AC motor is also known as the asynchronous motor.

Nowadays, many modern types of electric machines have been developed, such as reluctance motors, stepping motors, and brushless DC motors, etc. In terms of the basic operational principle, these motors are the members of AC synchronous motor family.

Since the energy medium for electromagnetic actuators, i.e. electricity, can be easily

transmitted and stored, this makes the electromagnetic actuators the best choice when it comes to portability. Concurrently, electrical power is more adaptable to environments than hydraulics or pneumatics since volumetrically they take up less space. There are no hydraulic return lines, air lines, high pressure pumps, or reservoir tanks as used in the fluidic actuators. In tasking a robot to perform difficult manoeuvrers, the flexibility of control of the mechanical system with electromagnetic actuators is far greater because the energy medium can be used by both the control system and the manipulator directly.

Electromagnetic actuators have also some attractive features for applications in micro systems. Since electromagnetic devices have low input impedances, they are current rather than voltage driven. This and the fact that low voltages are involved make packaging feasible and affordable. Electromagnetic actuators are integrated circuit friendly. This term is used when the needed microelectronic control components are off-the-shelf items and/or can be co-fabricated [Guckel 1998].

The major disadvantage of the electromagnetic actuators is that they produce relatively small torques/force compared to their size and weight. Consequently, as in the application of micro robotic systems, the electromagnetic actuators seem to be not powerful enough compared to some other actuation principles. Another problem to the (non superconducting) electromagnetic actuation is the thermal dissipation in coils while maintaining a constant force or torque. Moreover, the fabrication and miniaturization of the complex magnetic structure are also critical problems for the micro electromagnetic actuators.

Nevertheless, thanks to the development of the micro-engineering technology, high performance magnetic materials have been successfully developed for micro applications and the manufacturing of micro machines with complicated structures is no longer a problem. The addition of permanent magnet technology to the present soft magnetic materials also produces an environment for many new devices.

Just as their macro counterparts, the integration of miniaturised coils and magnets are necessary for micro electromagnetic actuators. Among the possible miniature electromagnetic actuators, the solenoid actuator is perhaps the easiest that can be implemented in the micro systems due to its simple structure. This type of actuator has been used in the locomotion mechanisms of some microrobots, as previously described in Figs.2-20, 21, 38, and 57. The solenoid actuators are also used as the clamp device in some walking microrobots when large friction to the travelling surface is required (Figs.2-11 to 15). However, the force of the solenoid actuator will decrease dramatically when the air gap increase and this significantly limits the achievable stroke of the actuator.

For miniaturisation of electric machines, the synchronous machines are the earliest to be put into micro applications [Nicoud 1997]. In 1995, RMB Inc. (currently within Faulhaber Group, Switzerland) introduced a brushless DC micro motor – Smoovy, which is shown in Fig.2-71 [Jufer 1995]. The currently available diameters of Smoovy micro motors are 5mm and 3mm. In the same year, Mimimotors Inc. announced a 1.9mm diameter brushless DC motor, which was initially developed at the University Mainz [Lehr 1996]. Apart from those traditional tube-shaped micro motors, Faulhaber Group also produces planar brushless DC motor called Penny micro motors. The available smallest type is only 2mm thick and 12mm in diameter. However, all these

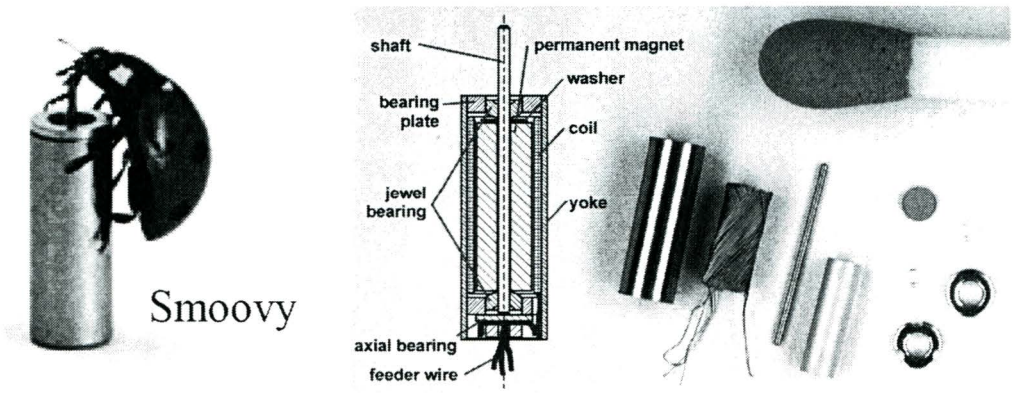

(a) (b)

Fig.2-71. (a) Smoovy micro motor produced by RMB
(b) 1.9mm brushless DC motor produced by Mini motors

types of micro motors rotate at a very high speed (>10,000rpm) and a reductor is usually needed for robotic actuation. Table 2-2 lists the main dimensions and performances of the above four types of micro motors.

Table 2-2 Key parameters of three types of micro motors*

Stator Dimensions (mm)	ϕ5×13.2	ϕ3×8	ϕ1.9×5.5	ϕ12×2
Torque (μNm)	70	18	12	114
Speed (rpm)	15,000	15,000	100,000	60,000
Current (A)	0.17	0.08	0.12	0.12
Max. Output power (mW)	110	6.3	130	170
Max. Efficiency	16.5%	16.5%	26.7%	32%

*from datasheets on Faulhaber Group website

The Smoovy micro motor has been used in some of the microrobot designs. Fig.2-72 shows an example of microrobot reported in [Nicoud 1997], which uses two 3mm Smooy micro motors as its wheel drives. Another design using Smoovy micro motor is the cricket microrobot described in Fig.2-28. The designers used the motor to drive an air compressor that supplies the compressed air to the Mckibben artificial muscles for the actuation of the legs.

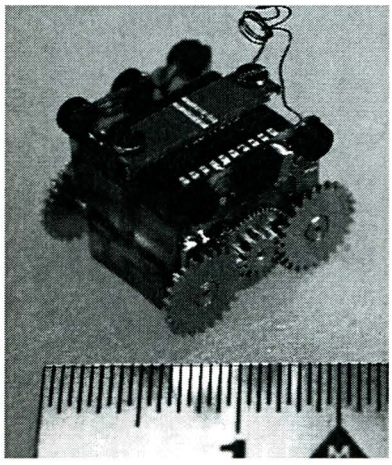

Fig.2-72 A 1cm^3 microrobot using 3mm Smoovy micro motor

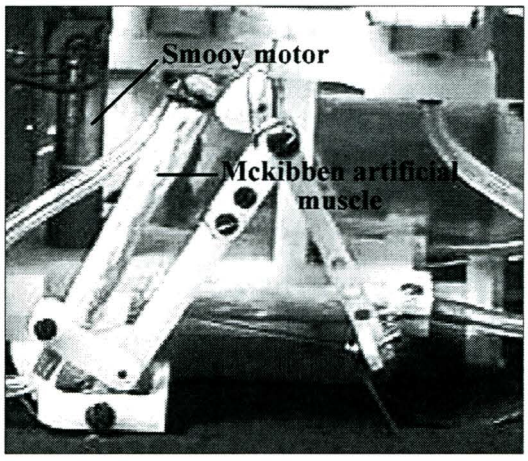

Fig.2-73 Actuation structure of the Mckibben artificial muscles in cricket microrobot

In 2000, P. -A. Gilles *et al.* presented a micro machined planer PM synchronous micro motor of which the diameter is less than 10mm [Gilles 2000]. The design was based on their 18mm prototypes developed in 1998. It adopts a twin stator structure as shown

inFig.2-74(a). Each stator is a double layer 3-phase coil made on a Si substrate (each coil with 20μm thickness) as illustrated in Fig.2-74 (b). The rotor is a SmCo disk with 0.5mm thickness and is magnetised into 15 pole pairs. Three different prototypes with 3, 5, and 8mm diameters were designed and analysed. Theoretical results show that a 3mm micro motor can achieve 10μNm torque under 0.3A phase current and the speed is up to 100,000rpm.

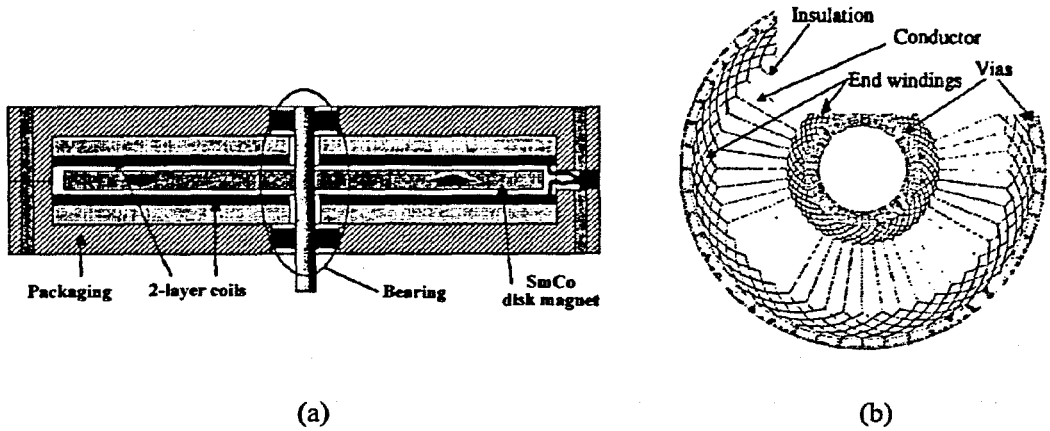

Fig.2-74 A planar type PM synchronous micro motor

The electromagnetic wobble micro motor presented by C. Stefanini *et al.* for their contest winning microrobot "Pollicino" is another application of electromagnetic actuator in microrobot [Stefanini 1996]. Although the operational principle of the proposed wobble motor is quite simple (Fig.2-25), some electromagnetic issues unique to micro systems should still be considered. For instance, if the rotor is made up of bare metal, the reluctances will be considerably different between the working stator poles, e.g. stator pole A (contact, extremely small reluctance) and C (air gap, very large reluctance) as shown in Fig.2-75. Hence, the magnetic force between the rotor and activated stator pole with air gap may not be sufficient to operate. A nonmagnetic film is therefore inserted between the rotor and stator to make the reluctances similar. The ratio between the thickness of the film and air gap is also optimised to achieve satisfactory torque and speed. Table 2-3 summarises the characteristics of the wobble micro motor and its theoretical mechanical performance is shown in Fig.2-76.

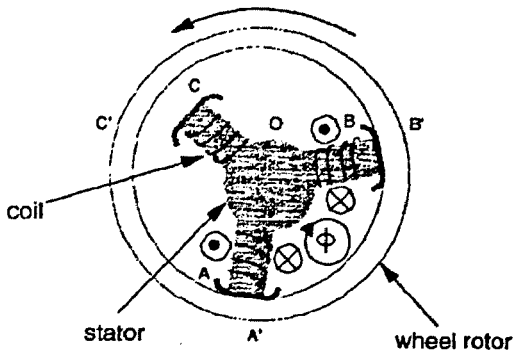

Fig.2-75 Schematic of the electromagnetic wobble micro motor

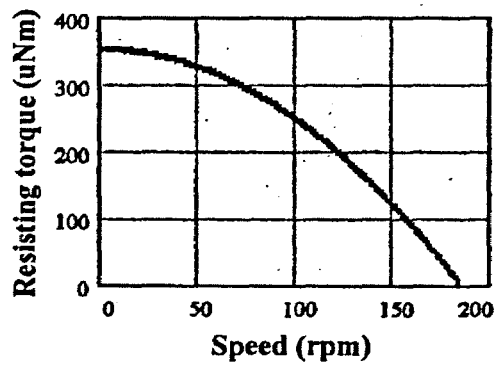

Fig.2-76 Theoretical mechanical performance of the wobble micro motor

Table 2-3 Characteristics of the wobble micro motor

Rotor Outer diameter	9.2 mm
Rotor inner diameter	8.2 mm
Axial length	2.5 mm
Airgap	0.08 mm
Max. torque (I = 140mA, zero speed)	350 μNm
Max. speed (I = 140mA, no load)	185 rpm

In addition, an electromagnetic wobble micro motor that can convert rotation into linear motion was described in [Iizuka 1996]. The micro motor was designed with threaded structure as shown in Fig.2-77. By sequentially energising the stator poles, the rotor is attracted consecutively to the poles and wobbles around. Then the rotational motion of the rotor is transfer to linear displacement by threads. When the rotor rotates 360 degrees, it will move linearly a screw pitch in the axial direction. The experimental force of a 6-pole prototype can be up to 1N with 230mA current and a 9mm/s speed can be achieved. However, despite the large force it can produce, the considerably big stator

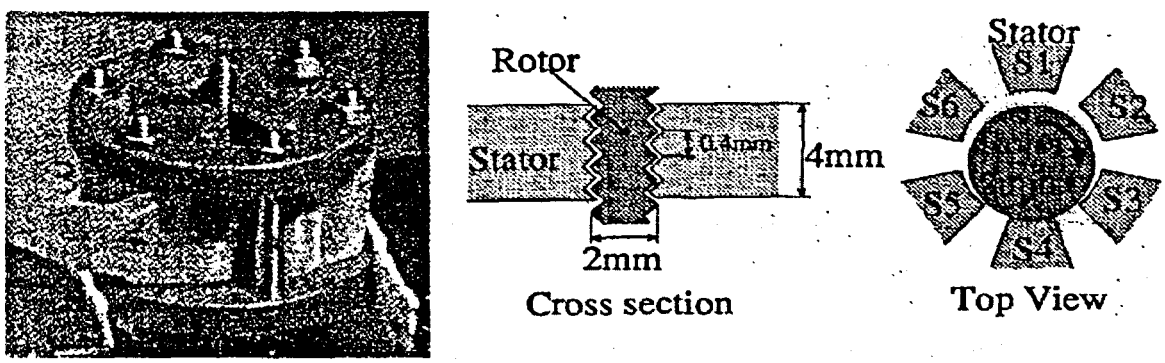

Fig.2-77 Structure of a threaded wobble micro motor

compared to its moving component implies that more compact stator should be developed in future to meet the requirement of micro systems.

In [Ahn 1993], a fully silicon-based micro motor was reported. The motor is based on variable reluctance principle and the schematic structure is shown in Fig.2-78. In contrast to conventional magnetic structure, a micro-machined magnetic circuit usually has a high reluctance due to the processing limitations on the achievable permeability and/or thickness of the magnetic core. Thus, the reduction of the reluctance of magnetic core is a major concern in realising a micro-machined magnetic circuit. The proposed magnetic structure makes all phases in pairs of opposite polarity to achieve adjacent pole paths. This arrangement greatly shortens the magnetic flux paths and provides an isolated magnetic core for the flux path of each phase. A prototype was demonstrated on a silicon wafer with a micro-machined nickel-iron rotor and a fully integrated stator. The predicted torque of the micro motor at 500mA current is approximately 3.3nNm.

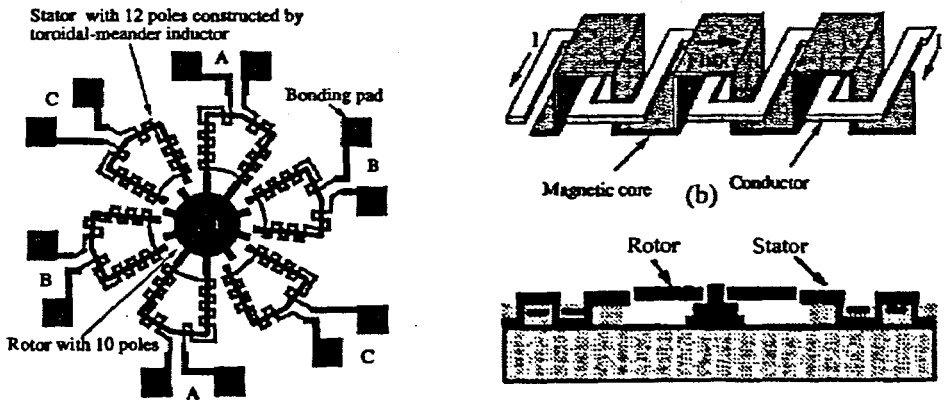

Fig.2-78 A silicon-based electromagnetic micro motor
(a) Structure, (b) Meander inductor, (c) Rotor and stator assembly

2.3.3 Piezoelectric actuators

Piezoelectricity is a property of insulating materials where an applied voltage generates an external stress and vice versa (Fig.2-79). The piezoelectric phenomenon was discovered by Pierre and Jacques Curie in 1880 [EDO 1998] in some crystalline materials that produce a voltage proportional to the applied pressure when compressed,

and when an electric field is applied across the material there is a corresponding change of shape. However, it took several decades to utilize the phenomenon after the discovery. The first commercial applications were the ultrasonic submarine detector developed during the World War I and the actuators using this effect became available just after 1970s.

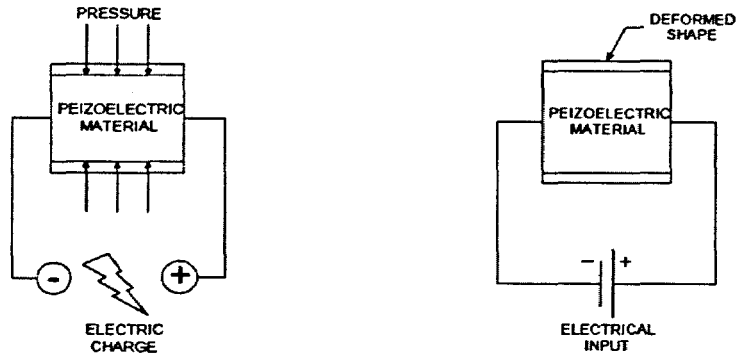

(a) Charge generated by applied pressure (b) Deformation when voltage is applied

Fig.2-79 Piezoelectric effect

Some natural materials possess piezoelectric characteristic property, such as quarts and tourmaline. Artificially produced piezoelectric crystals are Rochelle salt, ammonium dihydrogen phosphate (ADP) and lithium sulphate (LH). Another class of materials possessing these characteristics is synthetic ceramics. Barium titanate is the first synthetic piezoelectric material produced by Arthur von Hiffel in 1940 [Shields 1966]. The development of barium titanate then led to the discovery of other synthetic piezoelectric materials, such as lead titanate and lead zirconate titanate (PZT). Among these materials, PZT is the dominant piezoelectric ceramics that are commonly used in actuation and sensing applications due to its high force capability and working temperature.

As an actuator, the maximum expansion of the piezoelectric element depends on its material and length, the applied electric field and force. Generally, piezoelectric actuators can provide extremely fine resolution, very fast response, high output force, and low power consumption. Conventional piezoelectric actuator's resolution is typically below one micrometer, but even one nanometer is possible. This makes the piezoelectric actuator ideal for micro positioning systems. Another advantageous feature

of piezoelectric actuators is their mechanical durability.

However, the fractional stroke (displacement per unit length) of a piezoelectric actuator is considerably small, typically being around 0.1% when maximum durable voltage is applied. As a result, the speed and displacement of the piezoelectric actuator are severely limited. Moreover, the piezoelectric actuators usually require medium to high working voltages to achieve desirable displacement. Normally, the low-voltage piezoelectric element operates in the voltage range of 10 ~ 100V while the high-voltage type need an operating voltage up to 1000V.

Microrobots using piezoelectric actuators have been developed and experimentally demonstrated by many researchers. Among those proposed actuators, the bimorph, impact drive, inchworm, and ultrasonic motors are the main driving mechanisms.

The bimorph is similar to a bimetallic gauge, which two thin piezoelectric strips are connected together so that one of them contracts while the other expands. There are also designs where one ceramic strip and a steel strip are bonded together. Bimorphs are usually mounted as a cantilever. When a voltage is applied, the cantilever deforms. Though a bimorph actuator can generate large displacement, the output force is small. A developed locomotion mechanism utilising the piezoelectric bimorph vibration to move inside tubes or along wires was reported in [Aoshima 1989]. The designed piezo bimorphs are mounted on elastic fins, as illustrated in Fig.2-80. Some of the leg-based microrobot such as NanoWalk and MINIMAN are also based on such piezoelectric bimorph mechanism.

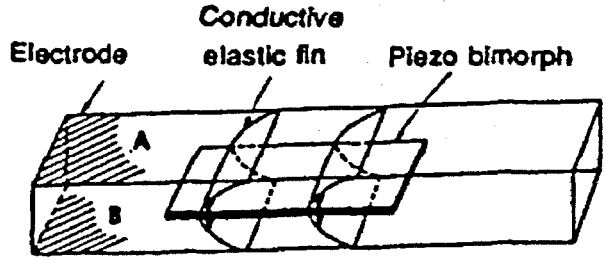

Fig.2-80 A microrobot with piezoelectric bimorph actuators

The impact drive mechanism (IDM) is to utilise the frictional force and inertial force by rapid deformation of the piezoelectric elements for robot locomotion. An early IDM actuator for robotic applications was proposed in [Higuchi 1990]. The actuator includes two parts: a main body held on a plane surface and a weight connected to the main body by a piezoelectric element between them. The robot locomotion can be realised by the steps illustrated in Fig.2-81: (1) the piezoelectric element makes a rapid extension by applying a steep rising voltage and the body will move forward while the weight moves backward; (2) the piezoelectric element contracts slowly to return the weight. While returning, the weight is speeded up by a constant acceleration that will not cause the main body moves backward; (3) a sudden stop is made once the piezoelectric element restores its initial length and the whole system will move forward due to the inertial force of the weight. An example using the IDM principle is an in-pipe microrobot described in Fig.2-35.

The above IDM actuator was improved by K. Ikuta *et al.*, who introduced so-called Cybernetic Actuator in [Ikuta 1991]. Figs.2-82 (a) and (b) show the first design of the linear type Cybernetic Actuator and the prototype with a tiny griper, respectively. The piezoelectric stack of the actuator is connected with a small mass to achieve impact driving while the other is used for locking the actuator to the travelling surface. By

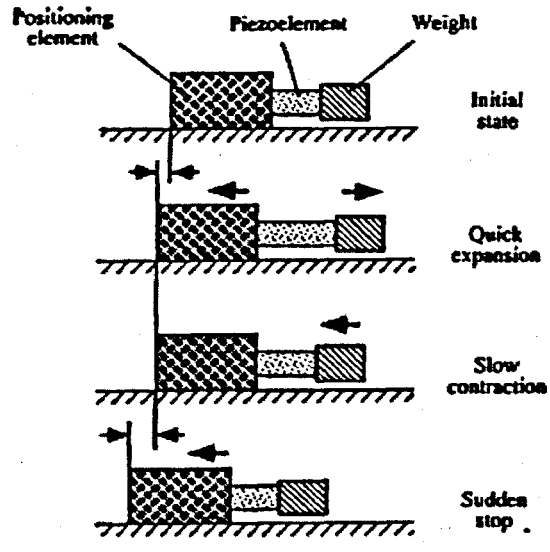

Fig.2-81 IDM mechanism using piezoelectric actuator

introducing the clamping mechanism in the prototype, the sliding of the main body is avoided during the contraction phase of the actuator. Therefore, quick contraction can be applied and a faster speed can be obtained.

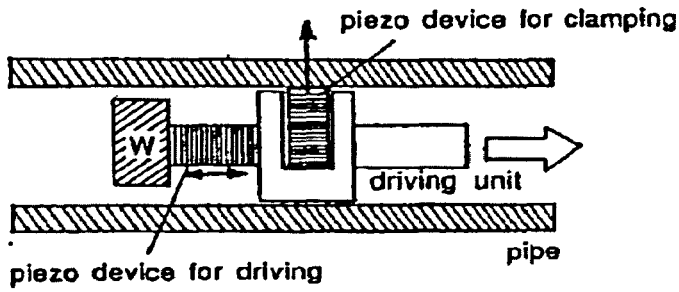

(a)

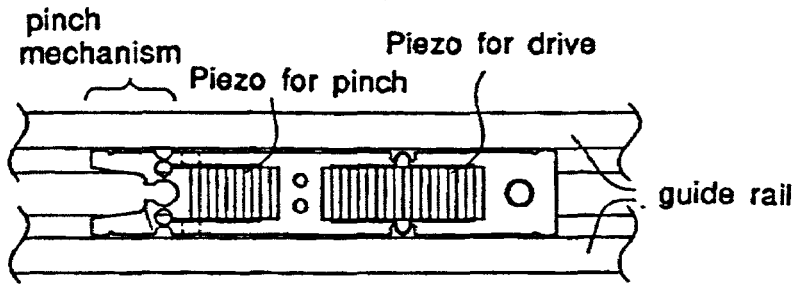

(b)

Fig.2-82 (a) First design of the linear Cybernetic Actuator
(b) Prototype of the linear Cybernetic Actuator

After the first design, they proposed a new design by combining two types of excitation principle in [Ikuta 1992]. As shown in Fig.2-83, the design uses an electromagnet to generate the clamping force, instead of the pinch mechanism in the first prototype. Hence, neither high precision machining nor fine gap adjustment between the actuator and travel surface is needed. In addition, the new actuator is much smaller ($5\times5\times12mm^3$) and only weights 1g. The prototype of the actuator can operate at a speed of 35 mm/s under an operation frequency of 37 kHz.

By using the designed linear Cybernetic Actuator, the research group developed an active laparoscope called "Hyper Endoscope" for MIS [Ikuta 1994]. The system was made up of a couple of "miniature active universal joints" driven by the Cybernetic Actuator, which are shown in Fig.2-84. Each joint segment is 10mm in diameter and 50mm in length and the total length of the presented prototype is 250mm with 10 DOFs.

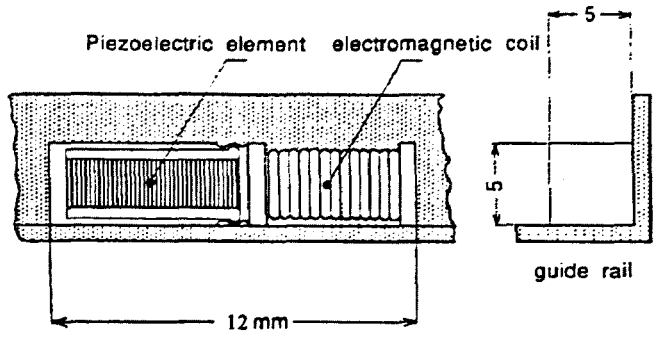

Fig.2-83 Second design of the linear Cybernetic Actuator

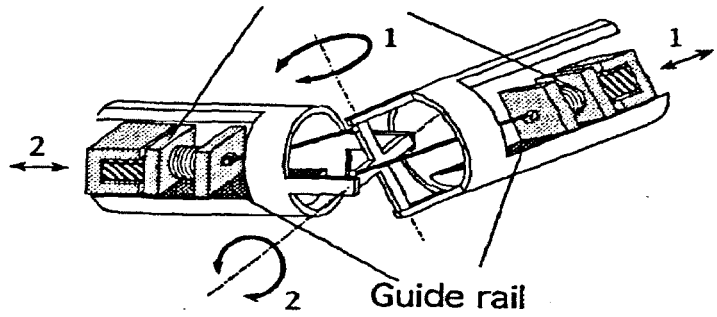

Fig.2-84 A universal joint with 2 DOF driven by Cybernetic Actuator

It was reported that a smooth inserted motion in three-dimensional space could be implemented.

Inchworm actuation is a locomotion technology that utilises small repetitive increments to produce large movements. Hence, inchworm mechanism would be an ideal choice for the piezoelectric actuator to realise large displacement by its tiny stroke under high working frequency. Generally, the inchworm actuator consists of two main components: an actuating module that can deform in the direction of travel and a mechanism that produces friction against the environment, such as grippers. The motion of the robot is realized by repeating a clamp-extend-clamp cycle through a series of actuator actions. An inchworm actuator using piezoelectric actuator for moving along a rod [Lind 1998] is described in Fig.2-85. Many developed microrobots have been adopted the inchworm actuator as their locomotion mechanisms, such as the Abalone microrobot and those developed by H. Aoyama and A. Torii, etc.

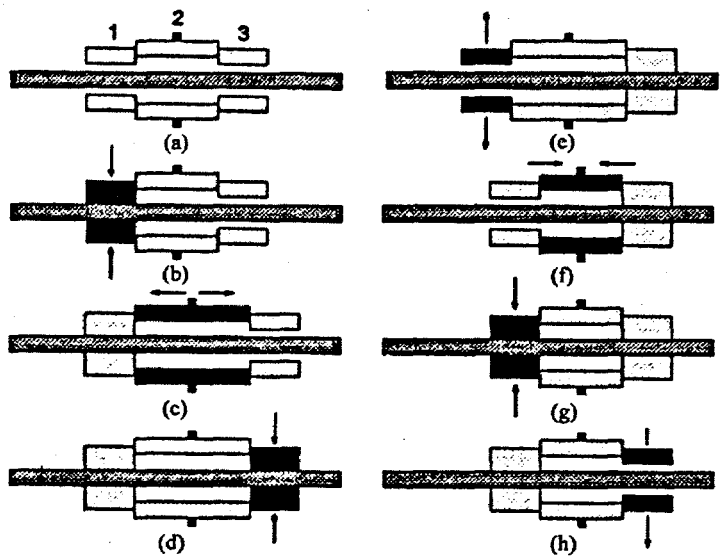

Fig.2-85 Operation of an inchworm actuator

A rotary type of piezoelectric actuator for the microrobots is the travelling wave ultrasonic motor, which has been used in many consumer electronic applications like the electronic focusing system in a camera. A schematic structure and operation principle is illustrated in Fig.2-86. In an ultrasonic motor, the elliptic motion of the stator surface induced by wave propagation in piezoelectric layer is converted in motion of the rotor by friction coupling.

The ultrasonic motor proposed in [Fleischer 1989] makes use of the longitudinal and flexural oscillations of a metallic resonator induced by piezoelectric ceramic elements. The driving action originates from the intermittent friction contact between the resonator and the rotor. The prototype with a diameter of a few centimetres can generate torques of 0.15Nm at 150rpm with a peak efficiency of 35%. A thin film ultrasonic

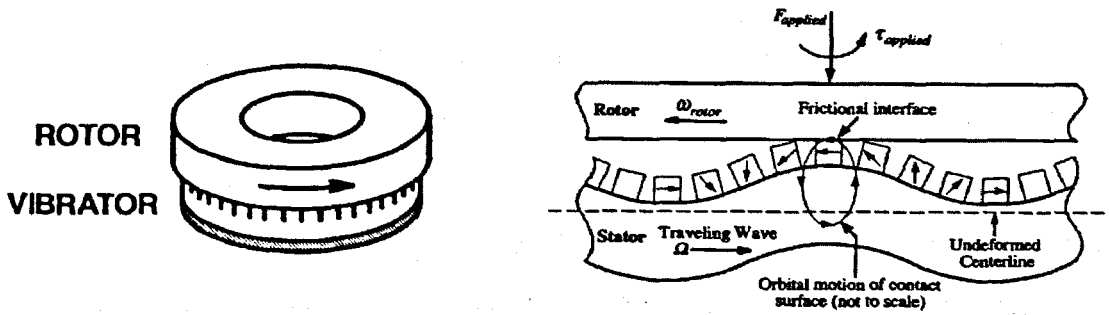

Fig. 2-86 Scheme and principle of a planar travelling wave type ultrasonic motor

micro motor was reported in [Flynn 1992]. The stator is made up of thin PZT film on a silicone substrate and the rotor is a small glass lens (ϕ1.5mm×1mm) placed on top of the stator. The experimental results show that the rotor could rotate at a speed of 100 to 300 rpm and the estimated torque is 0.041μNm. In 2003, Dong *et al.* developed a tubular piezoelectric ultrasonic micro motor with 1.5mm in diameter and 7mm in length [Dong 2003], as shown in Fig.2-87. The PZT stator generates wobble motions at its ends by combining bending vibration in the x- and y- directions and drives the two rotors pressed on its ends into a wobble motion through frictional force between them. The proposed motor can operate from hundreds to 2000 rpm in both directions and the maximum torque is 45μNm.

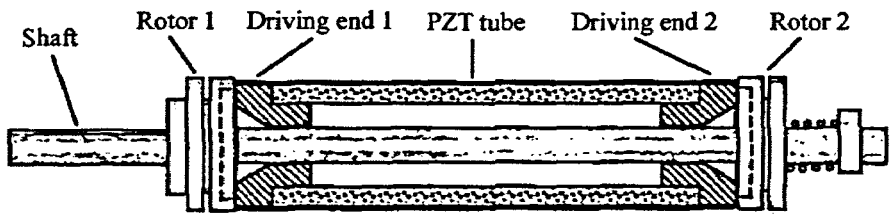

Fig.2-87 A tubular piezoelectric ultrasonic micro motor

2.3.4 Shape memory alloy actuators

In 1932, Swedish physicist Arne Ölander discovered a phenomenon that an alloy of gold (Au) and cadmium (Cd) could be plastically deformed when cool and then be heated to return to, or "remember", the original dimensional configuration and metallic strength. This phenomenon is known as the Shape Memory Effect (SME) and the alloys that exhibit the behaviour are called Shape Memory Alloys (SMA). In 1958, researchers Chang and Read demonstrated the mechanical work performed by an Au-Cd SMA at the Brussels World's Fair. Further research revealed other materials that demonstrate this phenomenon. In 1961, a group of U. S. Naval Ordnance Laboratory researchers lead by William Beuhler found that an alloy of Nickel (Ni) and Titanium (Ti) exhibited the SME. This was an important discovery in the field of SME and SMA because the Ni-Ti SMA proved to be significantly less expensive, easier to work with, and less dangerous (from

health standpoint) than previously discovered alloys. These factors refreshed interest and research in the SMA and its applications [Toki 1987; Grant 1997].

As a result, starting in the 1970's, commercial products began to appear. The early SMA devices functioned as fasteners and took advantage of a single shape memory dimensional change. Soon after, researchers started to propose SMA devices to perform dynamic tasks as actuators. In order to perform a dynamic task, the SMA must experience a cycle of heating, cooling, and deformation. Some of the researchers used SMA actuators in temperature regulation systems where the environmental temperature could be used for thermal actuation, such as greenhouses and air conditioners. Other researchers pursued electricity (resistive or joule heating) as a source of heat and thus actuation. In 1971, a team lead by Sawyer developed and tested an artificial heart powered by electrical actuation of SMA elements. In 1983, Honma *et al.* showed that SMA actuation could be controlled by resistive heating and proposed that SMA actuators could be used in micro robotics [Honma 1985].

Using SMA actuators provides an interesting alternative to other actuation methods in the applications of micro systems. Their advantages create a means to reduce the size, weight, and complexity of robotic systems. First of all, SMA actuators possess an extremely high force to weight ratio. A Ni-Ti actuator can apply an actuation stress of 500 MPa so a 150μm diameter Ni-Ti wire can apply a force of 8.8 N. Secondly, SMA have a large strain compared with piezoelectric materials. The maximum recovery strain of SMA is in the order of 8%, but should be below 5% to avoid lost of the "memory" effect if it is used more than a few cycles. Moreover, the strain can be detected by measuring the change of electric resistance of the actuator. SMA actuators are also compatible with integration circuit fabrication.

SMA actuators do have disadvantages which must be thoroughly considered and analysed prior to deciding to use SMA for an application. First and foremost, they operate with a very low efficiency. An SMA actuator is effectively a heat engine where

the material converts thermal energy directly into work. Therefore, the efficiency of the actuator cannot be greater than that of a Carnot cycle – not exceeding 10% in the temperatures where typical SMA actuators operate [Hirose 1984]. In fact, most SMA actuators operate at 5% efficiency or less [Wood 1998]. Secondly, SMA actuators operate at a low bandwidth, meaning they are relatively slow response. The cycling time is primarily dependent on the heat transfer characteristics of the SMA "cooling system". In addition, depending on the environment, heat dissipation can also be a problem. However, the heating and cooling rates increase when the size of the actuator decreases. Therefore, small sizes of the SMA actuators are preferable. The final disadvantage, and also a topic of many researches, is the difficulties in controlling SMA actuators due to their highly non-linear behaviour, narrow deflection temperature range and structural elasticity.

Because of the excellent bio-compatibility of the SMA materials, especially Ni-Ti alloy, SMA actuators have been used for some medical micro systems. As a first step towards his proposed "MEDIWORM" medical microrobot concept, K. Ikuta developed an active endoscope [Ikuta 1988b] that uses SMA actuators to guide the device around obstacles. The proposed endoscope consists of many segments that are made up of a number of The SMA coil spring and a skeleton of stainless steel coil spring, as shown in Fig.2-88. Each pair of SMA actuator capable of antagonistic motion is arranged in symmetry with respect to the axis so that they can bend in 3 dimensions. Each of the SMA coil spring is 1.0mm in diameter and made by 0.2mm Ti-Ni alloy wire.

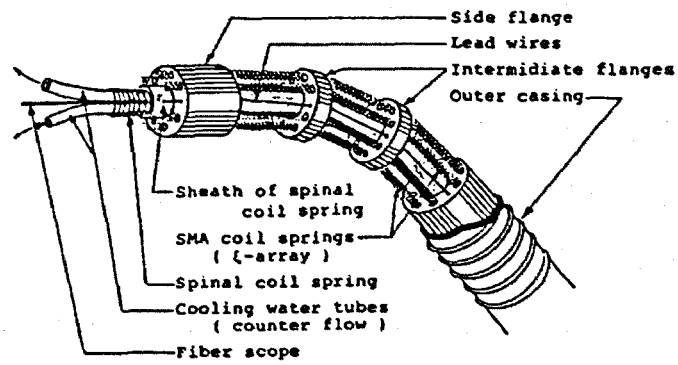

Fig.2-88 Active endoscope using SMA actuator developed by K. Ikuta

A similar design was presented in [Haga 1998]. The scientists used three SMA coils between two joints to form the elementary segment. The entire system is simplified by eliminating the solid joints and the diameter of the endoscope is down to only 1mm.

SMA actuator is also used for the locomotion of microrobots. In the design shown in Fig.2-40, An SMA coil spring is used between the legs to achieve inchworm locomotion. A passive spring is used to contract the SMA spring. It was reported that a 3mm stroke could be obtained in 5 seconds. The in-pipe microrobot illustrated in Fig.2-42 adopts the similar locomotion principle. The designed SMA spring actuator is 10mm in length and assembled together with a silicon bellows as a passive spring, as shown in Fig.2-89. The theoretical stroke per cycle is expected to 3.4mm and the experimental results show that a 2mm stroke is obtained in an 8 seconds cycle (2 second heating and 6 seconds cooling).

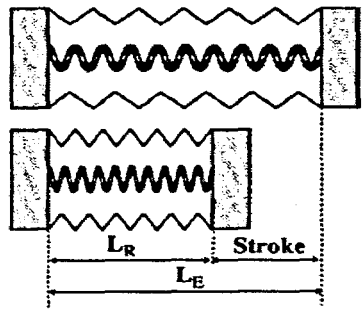

Fig.2-89 SMA actuator developed by B. Kim *et al.*

2.3.5 Electrostatic actuators

Electrostatic actuators make direct use of coulombic force to function. When a voltage is applied between a pair of electrodes, an attractive force is produced between the plates, and this is known as normal force actuator (Fig.2-90(a)). Electrostatic actuator also exploits the force parallel to the plates which tend to realign each other after a displacement has occurred with respect to each other, and so called tangential force actuator (Fig.2-90(b)). The forces produced by such electrostatic actuators are given by [Fearing 1998]

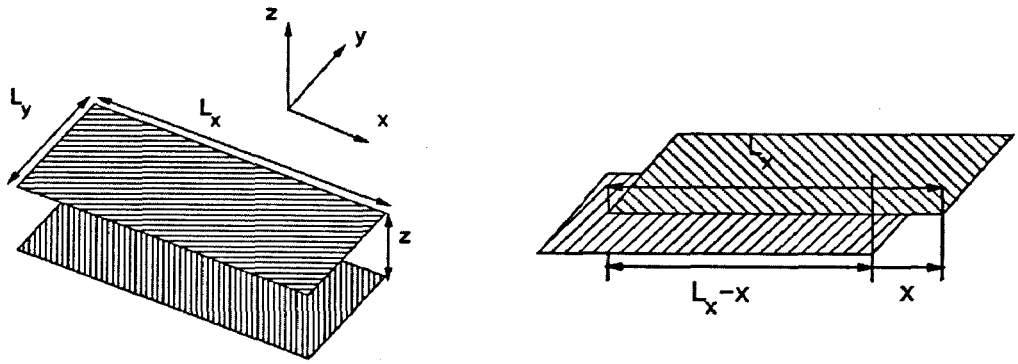

(a) normal force actuator (b) tangential force actuator

Fig.2-90 Basic principle of electrostatic actuators

$$F_z = \frac{1}{2} \cdot \varepsilon_r \cdot \varepsilon_0 \cdot \frac{L_x \cdot L_y \cdot}{z^2} \cdot U^2, \tag{2.3}$$

$$F_x = \frac{1}{2} \cdot \varepsilon_r \cdot \varepsilon_0 \cdot \frac{L_y}{z} \cdot U^2, \tag{2.4}$$

where L_x and L_y are lateral dimension of the electrodes, U is the applied voltage and z the gap between the electrodes. The force F_z is acting perpendicular to the plate and the force F_x is acting within the direction of the plate.

The electrostatic force is a surface force and it scales down with the size very favourably as the electrostatic forces increase when the gap shrinks. However, this reduces the maximum displacement perpendicular to the electrodes and may be a restrictive factor for some applications where displacements larger than some μm are required. On the other hand, one benefit for miniaturization can be discovered, that is, if all dimensions of the system (l, w, h) decrease uniformly ($l \cdot w/h^2$ = constant) and the electric field (U/h) also remains scale independent, the electrostatic force scales with the square of the scaling factor. This feature is superior to many other actuation principles. When the air gap is very small (< 5μm), the electrostatic actuation also profits from the increased breakdown field due to the Paschen effect. Another advantage of electrostatic actuators is that they can be fabricated easily by silicon micromachining technology and LIGA. The further features of electrostatic actuator are small power consumption, fast response and temperature independence.

Like other principles, electrostatic actuation has several disadvantages. One is the charge accumulation in the dielectric if the two charged surfaces make contact. This is possible if the driving voltage exceeds a certain value which is known as the pull-in voltage and the electrode will deflect all the way to touch the substrate. Another problem is that since electric fields interact with most materials, the electrostatic actuator may need greater environment isolation than other types of actuators. Hence, a dusty environment or a conductive fluid medium such as water are not acceptable for an electrostatic actuator.

Electrostatic actuators can be either linear or rotary. The first rotary electrostatic micro actuators with diameters of 60 to 120 μm were reported in [Fan 1989]. These actuators are called side-drive micro motors since they utilise the electrostatic force that acts between the edges of a rotor and a stator (Fig.2-91(a)). The working voltage of the actuator is up to 300V and the rotational speed is in the order of 500rpm. The torque is estimated to be a few pNm. The speed was relatively low because of the large frictional force on sliding surface. Later improvements described in [Mehregany 1990] enabled rotational speed up to 15,000rpm and the torque was about 10pNm. However, even for improved electrostatic micro motors, friction appears to be a major problem. One of the solutions is to replace the sliding contact at the centre axis of the device with a rolling contact. One type of micro motor, called a wobble motor [Mehregany 1990], was designed on this principle and was realized using surface micromachining. Its rotor is a smooth ring, and using electrostatic attraction to rotate eccentrically without slipping at the contact with the shaft, as shown in Fig.2-91(b). Since the circumferential distance of the rotor hole is slightly longer than that of the shaft, the rotor really revolves a fraction of a circle after one eccentric rotation. This results in two advantages for the motor, i.e., reduction of friction and higher torque at low speed. The reported speed is 300rpm and the estimated torque is up to 1nNm. An outer rotor design that permits easier extraction of motion is also possible (Fig.2-91(c)).

A type of surface-driven electrostatic actuator was presented in [Gao 1997]. The

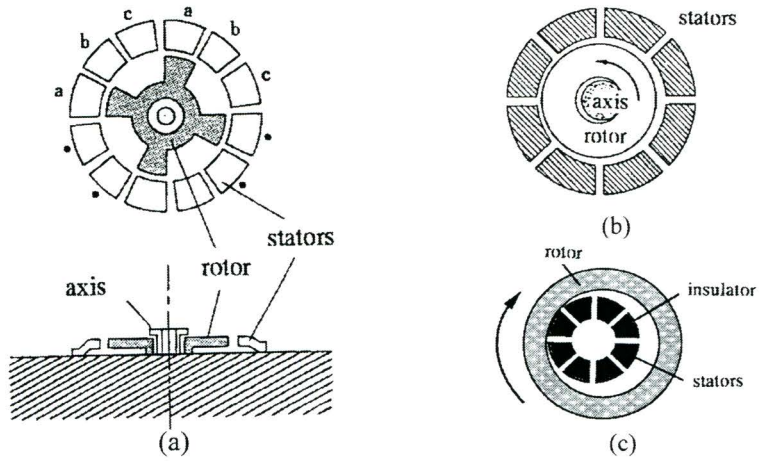

Fig. 2-91 Side-driven rotary electrostatic micro actuators

proposed actuators are of both rotary type and linear type with 8 to 40 mm in sizes. The designed rotary actuator is shown in Fig.2-92 and the linear actuator uses similar configuration. The experimental results showed that the designed linear actuator could generate a force of 47mN in $2cm^2$ driving surface when 380V voltage was applied. For the rotary actuator with 18mm in diameter could produce 76μNm under 380V excitation voltage and the speed was up to 500rpm.

An inchworm microrobot using a linear electrostatic actuator array was proposed in [Hollar 2003]. The actuator is made up of side driven comb actuator called gap closing actuator arrays, as shown in Fig.2-93(a). The entire actuation system consists of two clutch/drive actuator pairs. Through working in tandem, the mechanism translates the small displacements of the actuator arrays to large displacements of the shuttle and inchworm locomotion is realised. By reversing the working order, the system can

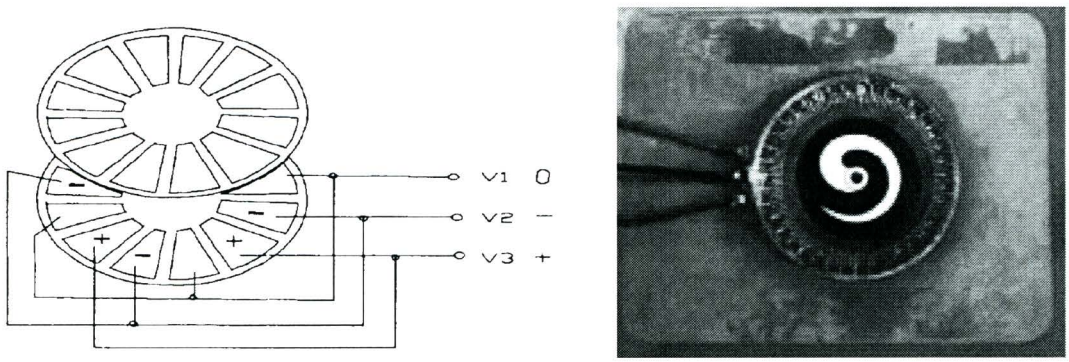

(a) schematic structure (b) prototype

Fig.2-92 Surface driven electrostatic actuator developed by X. Gao *et al.*

perform a bidirectional movement. The working voltage of the actuator is 40V to 50V and the leg driven by the actuator can generate 6μN to 33μN of vertical force, depending on the angle of the joints.

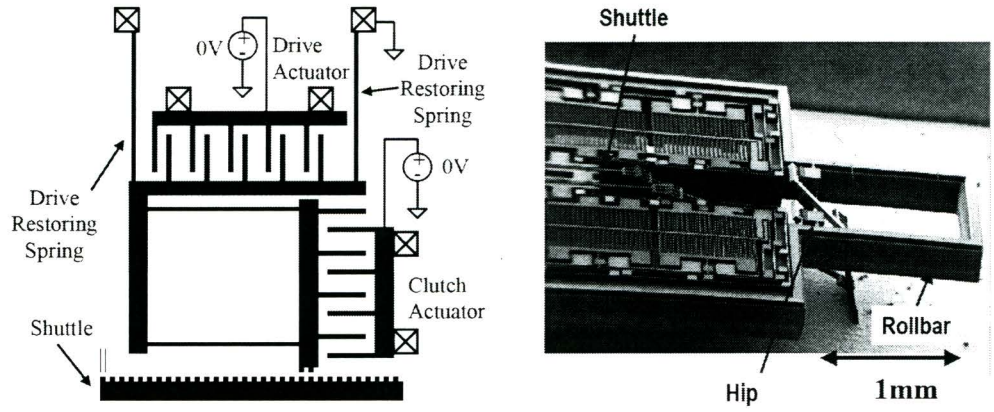

(a) Schematic layout of the actuator (b) Image of fabricated structure

Fig.2-93 A bidirectional inchworm electrostatic actuator for microrobot

Despite those researches conducted on micro electrostatic actuators that are supposed to be the preferable actuation method in the micro systems, their application in microrobots is still rare due to their restrictions in strokes and working environments.

2.3.6 Electrostrictive and magnetostrictive actuators

Electrostriction is an applied electric field effect and the response observed is dominated by electrostatic forces generated by free charges on the contact electrodes. An electrostrictive actuator can be considered of as an electrostatic device with a thin-film deformable material in place of the electrode air gap and the resultant electrostatic forces compress and stretch the film. The force generated by an electrostrictive actuator is similar to an electrostatic actuator but the electrostrictive force is affected by the variation of dielectric constant with strain. It is shown that the resultant electrostrictive force is several times larger than that by just considering the dimensions of the actuators [Anderson 1986]. In addition, a distinctive feature of electrostriction compared to other field-driven principles is that the strain does not change sign if the electric field is reversed.

The magnetostrictive effect is discovered in 1842 by Joule [Lind 1998]. It is a similar dimension change under the influence of a magnetic field. On application of a field, the magnetic domains of a magnetostrictive material orient themselves in the filed direction. The material thus expands in the direction, and contracts along the orthogonal axes. However, as the contraction is much less than the expansion, it is the latter that is taken as the strain direction.

The electrostrictive and magnetostrictive actuators are all with fast response, but the problem of small strokes is common to these actuators. Typical magnetostrictive materials promise fractional strokes comparable to piezoelectrics but with a much greater force. On the other hand, the electrostrictive actuators, in particular polymeric ones, have a larger fractional stroke of about 4%.

Magnetostrictive actuators have been used in several micro actuator designs, especially those based on GMM. GMM is a newly developed magnetic material with relatively larger magnetostrictive strain and higher output force. An in-pipe microrobot utilising GMM actuator has been described in Fig.2-29. In [Zhang 2004], a linear actuator based on the GMM actuator was presented. The proposed actuator is an inchworm type actuator. Fig.2-94 shows the schematic structure of the actuator. A GMM element with rectangular cross section is put in a channel with tight-fitting walls. A longitudinal magnetic field is applied to the GMM element from both sides of the walls. If the field is started from the right side as shown in Fig.2-95(b), the affected portion of GMM element expands to along the direction of magnetic field and the rest of the element is blocked by the channel walls. When the applied field moves to the middle of the element, the right portion of the element returns its original shape and locks against the channel wall as shown in (c). If the magnetic field continuously passes through the GMM element, the extended region propagates through the element and the GMM element can moved to the right as shown in (d). A prototype of the proposed actuator was built by the researchers but no experimental results were reported.

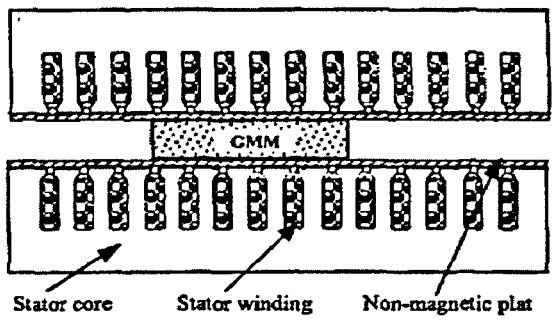

Fig.2-94 Schematic structure of a GMM linear actuator

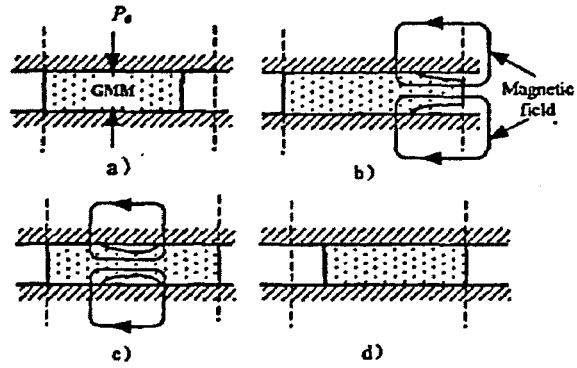

Fig.2-95 Operation principle of the GMM linear actuator

2.4 Conclusion

Microrobots are those highly application oriented systems. Various applications suggest the use of new actuation systems. As discussed in this chapter, many innovative mechanisms and actuators have been proposed and are being investigated. These actuators make use of different kinds of transducing materials and energy conversion principles to meet the requirement of micro robotic systems.

Although there are a number of actuation alternatives for the microrobots, it is difficult to find solutions that have small size, high resolution, large force and large displacement at the same time. Table 2-4 shows a comparison of the techniques that have been discussed, with some typical results obtained [Hollerbach 1992; Dario 1992; Robert 2004]. None of these principles has dominance over any other in the micro applications. For instance, the electrostatic actuators are usually preferable for micro systems, but other principles, such as piezoelectric, electromagnetic and SMA, bring other performances that can meet the design needs. Therefore, the best engineering solution is to select the appropriate actuator for each specific application. The choice of mechanism is a balance between many different factors, only some of which are related to the actuation benefit. Those of material properties, reproducibility, and process compatibility are all key issues.

Table 2-4 Comparison of actuation principles

Actuator	Maximum Strain (%)	Maximum Stress (MPa)	Driving Voltgae (V)	Maximum Efficiency (%)	Response
Hydraulic	50	20	–	High	fast
Pneumatic	50	0.7	–	High	medium
Electromagnetic	50	0.1	< 10V	Medium to high	fast
Piezoelectric	< 0.2	35	10V ~ 500V	High	fast
SMA	8	400	1V ~ 10V	Low	slow
Electrostatic	30	0.03	5V ~ 500V	High	fast
Magnetostrictive	0.2	70	–	Medium	fast
Electrostrictive	4	15	< 10V	Medium to high	fast

From the mobile microrobot's point of view, the energy supply is a critical issue. The existing of power cable, no matter electric lead or fluidic pipe, will greatly limit the moving area and freedom of a microrobot. Therefore, fluidic actuators are not suitable for the mobile robots. In order to eliminate the power leads, much of the advances in the past made in research of mobile microrobot have been in terms of the energy packed by batteries. However, because the energy of a battery is proportional to its volume, the energy of the battery becomes limited as the size of robot reduced. Recently, some researches on mobile microrobot with microwave wireless energy transmission have been conducted and several transmission methods were proposed [Shibata 1998; Mitumoto 2001; Basset 2001], but the voltage and power transmitted by this method are still limited. Hence, actuators with low conversion efficiency like SMA would not be a good choice either. Among these techniques listed in Table 2-4, the piezoelectric and electromagnetic actuators would to be the suitable candidates for mobile microrobots as they are of good force capability, high efficiency and they do not need an extreme energy supply.

In chapter 3, a detailed comparative study will be conducted towards the piezoelectric and electromagnetic actuators and a selection will be concluded for the desired application.

Chapter 3

PIEZOELECTRIC AND ELECTROMAGNETIC ACTUATORS – A COMPARATIVE STUDY

3.1 Introduction

With the development of micro and nano technologies, micro machines are interested by many scientists due to their great potential of application in the new century. The piezoelectric actuators are much attractive for micro applications because of their small sizes, simple structures and large force capability. They have been used successfully in the applications of precision machining. Many effectual designs for the micro robotics have been developed as well, such as inchworm actuators and ultrasonic micro motors, etc.

Electromagnetic actuators are dominant in the macro scale machines. Over a hundred years, they have been accomplished by those specialising in machinery, control and drives. However, because of complicated fabrication and miniaturisation, electromagnetic actuation has many restrictions when used in micro systems. Fortunately, advances in micro technologies such as LIGA and micro fabrication of permanent magnets enable the electromagnetic machines to extend more into the micro world [Lagorce 1996].

Since several actuation principles could be used in micro systems, the selection of actuation principles in a micro robotic system is an important issue that should be thought well of before the design of the micro machines. Accordingly, analysis and comparison of the performances of different actuation principles are necessary as they can provide a valuable guideline in design. In this chapter, some of the important features for evaluating an actuator in micro applications are discussed. The scaling effects of piezoelectric and electromagnetic actuators are firstly studied, followed by a comparison of their attainable energy density. The dynamic performances of the piezoelectric and electromagnetic actuators are then analysed and compared through a case study. Based upon the results obtained from the comparative study, a conclusion will be made to the actuation of the target application.

3.2 Scaling Effects

Scaling analysis is a significant issue concerned by many scientists since nineteenth century, when Froude and Reynolds derived indices of dynamic similarity to relate the performance of scale models to full sized vessels [Lewis 1988]. For more than a hundred years, many studies have been done in various scientific fields like biology and mechanics, and it is found that many natural creatures such as insects are good models for the micro machine designs. In 1942, D'Arcy Thompson derived scaling laws for biomorphology and showed, for instance, that the range of jumping heights for legged animals varies much less than the body mass of the animals (i.e. fleas and humans have about the same jumping height). Recently, some studies have been conducted on the scaling properties of electromagnetic actuators [Pelrine 1987, Wallace 1993, 1994].

Among geometrically similar objects, the scaling relationship between properties and sizes of an object can be expressed by a variable ξ with a power of a [Shimoyama 1995], say $[\xi^a]$, where ξ represents the characteristic size of the object. It is obvious that the

volume of an object is proportional to $[\xi^3]$.

The forces usually scale in one of the four ways: $[\xi^1]$, $[\xi^2]$, $[\xi^3]$, and $[\xi^4]$. For example, when the force scales as $[\xi^2]$, i.e. $F = [\xi^2]$, it means that when the size of the object is reduced by a factor of 10, the corresponding force will decrease by a factor of 100. For instance, inertia forces scale as the volume of an object, say $[\xi^3]$, and the forces scaling in $[\xi^1]$ and $[\xi^2]$ increase relative to the inertia forces as the size of the system is decreased. Therefore, a smaller value of a means a better scaling effect since the produced force of an object will not reduce too fast when the size gets smaller, and hence a better dynamic performance can be obtained for micro systems [Trimmer 1989].

3.2.1 Scaling of piezoelectric actuators

When analysing the behaviour of a piezoelectric material, the constitutive tensor equations are usually used by taking into account the changes of strain and electrical displacement in three orthogonal directions caused by the cross coupling effects due to applied electrical and mechanical stresses. Generally, the constitutive characteristics of piezoelectric materials are given by following two basic tensor equations [Jordan 2002]:

$$D_i = \varepsilon_{ik}^T E_k + d_{ikl} T_{kl}, \tag{3.1}$$

$$S_{ij} = d_{ijk} E_k + s_{ijkl}^E T_{kl}. \tag{3.2}$$

The state of strain is described by a second-rank tensor S_{ij}, and the state of stress is described by a second-rank tensor T_{kl}. The relationship relating the stress tensor to the strain tensor, the compliance coefficient s_{ijkl} of the piezoelectric material, is then a fourth-rank tensor. The relationship between the electric field E_k (first-rank tensor) and the electric displacement D_i (also a first-rank tensor) is the electrical permittivity of the material ε_{ik}, which is a second-rank tensor. d_{ijk} is the piezoelectric constant, a third-rank tensor. Superscripts ^{T} and ^{E} indicate that the electrical permittivity ε_{ik} and compliance coefficient s_{ijkl} are measured under conditions of constant stress and constant electrical field, respectively. The subscripts $i, j, k, l = 1, 2, 3$ are the orthogonal axis directions

shown in Fig.3-1(a).

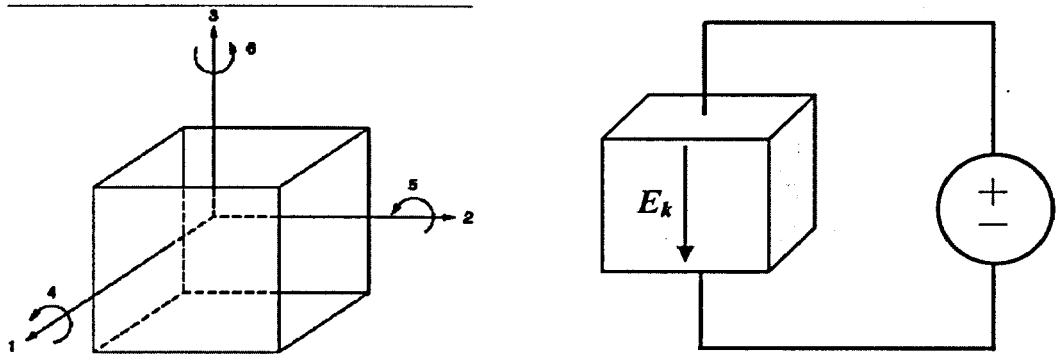

(a) coordinator system (b) a bulk of piezoelectric material with applying voltage

Fig.3-1 Piezoelectric actuator coordinator systems

Normally, a first-rank tensor has three components, a second-rank tensor has nine components, a third-rank tensor has twenty-seven components, and a fourth-rank tensor has eighty-one components. Not all of these tensor components are independent. The relationships derived from both equations depend on orientations and they describe a set of equations that relate these properties in different orientations of the material. The crystal symmetry and the choice of reference axes can reduce the number of independent components. A convenient way of describing them is to use axis directions as given by Fig.3-1(a). The convention is to define the poling directions as the 1, 2, and 3 axes; and the shear planes, which are perpendicular to directions 1, 2, and 3, as 4, 5, and 6, respectively. This simplifies the notations introduced before by replacing a 2-subscript tensor notation (i, j = 1, 2, 3) with a 1-subscript matrix notation (m = 1, 2, 3, 4, 5, 6), a 3-subscript tensor notation (i, j, k = 1, 2, 3) with a 2-subscript matrix notation (k = 1, 2, 3 and m = 1, 2, 3, 4, 5, 6), and a 4-subscript tensor notation (i, j, k, l = 1, 2, 3) with a 2-subscript matrix notation (m, n = 1, 2, 3, 4, 5, 6). Therefore, (3.1) and (3.2) can be rewritten as

$$D_i = \varepsilon^T{}_{ik} E_k + d_{in} T_n, \tag{3.3}$$

$$S_m = d_{mk} E_k + s^E_{mn} T_n. \tag{3.4}$$

Accordingly, a shear strain such as S_4 is a measure of the change of angle between the two initially orthogonal axes in the plane perpendicular to axis 1. One subscript of the

piezoelectric constant d gives the "electrical" direction (field or dielectric displacement), and the other gives the component of mechanical deformation or stress.

Equation (3.3) relates to the direct effect and (3.4) relates to the converse effect. Consider an application of actuation which employs the converse piezoelectric effect shown in Fig.3-1(b), if it is assumed that the actuator is rigidly held so as not to deform in any direction, i.e. $S_m = 0$, the tensor of stress is then given by

$$T_n = -\frac{d_{mk}}{s^E_{mn}} E_k . \tag{3.5}$$

Consequently, the piezoelectric force can be found as

$$F_n = T_n A_n = -\frac{d_{mk}}{s^E_{mn}} E_k A_n , \tag{3.6}$$

where A_n is the area of (kl) plane. Therefore, the force generated by piezoelectric actuator is proportional to the applied electrical field and the working area of the actuator. In case of the linear type actuators, when the electric field is kept constant, the scaling of the piezoelectric force will be [ξ^2].

A typical design of rotary actuator using piezoelectric material is the travelling wave ultrasonic motors. The basic structure and principle of a ring type travelling wave ultrasonic motors has been described in Fig.2-86. Since the ultrasonic motor is working via the friction coupling between the rotor and stator, there is a normal force F_N at the contact area during the operation.

To analyse the torque of an ultrasonic motor, a piezoelectric segment of the stator and related elastic rotor section shown in Fig.3-2 is considered [Bao 2000], and the stator drives the rotor through a thin friction layer in the rotor. If defining the thickness of the friction layer is h_d and the penetration of the stator into the friction layer is h_p, the normal pressure p developed in the contact area is given by

$$p = \frac{h_p}{h_d} Y , \tag{3.7}$$

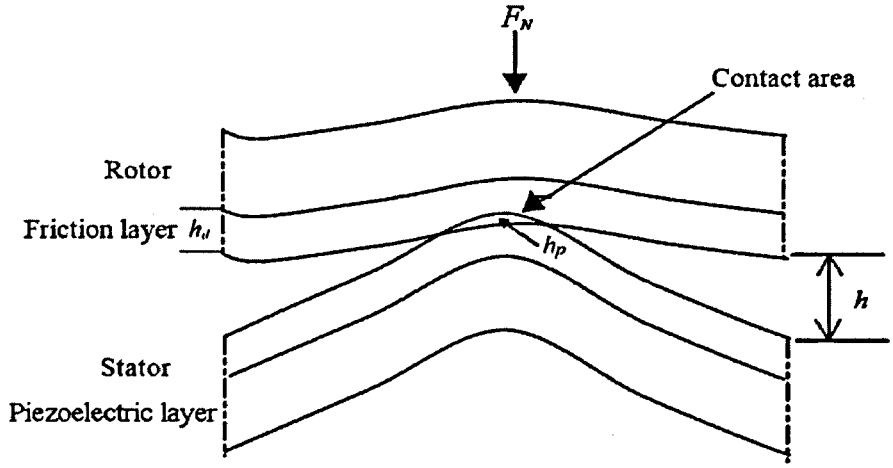

Fig.3-2 Interaction between the stator and rotor via friction layer

where Y is Young's Modulus of the material of the friction layer. Hence, the total normal force F_N is

$$F_N = \int pdA = \int \frac{h_p}{h_d} YdA\,. \tag{3.8}$$

Because the stator drives the rotor to rotate by the static frictional force, according to the Coulomb's law, the driving frictional force exerted on the rotor in the contact area is then expressed as

$$F_f = sign(v_s - v_r)\mu_f \int \frac{h_p}{h_d} YdA\,, \tag{3.9}$$

and the torque Γ is

$$\Gamma = F_f r_r\,, \tag{3.10}$$

where v_s is the velocity on the surface of the stator in tangent direction, v_r the rotor velocity due to rotation, r_r the effective radius of the rotor ring, and μ_f the frictional coefficient between the contacted surfaces.

Because the friction layer is usually designed with less stiffness than the stator material, the penetration h_p in the friction layer can be regraded proportional to the deformation of the piezoelectric segment layer. Under this assumption, the piezoelectric segment can be considered as unclamped, i.e. $T_n \approx 0$. and h_p can be expressed by the following relationship

$$h_p = k_d S_m h_s = k_d d_{mk} E_k h_s, \tag{3.11}$$

where k_d is the deformation coefficient of the friction layer which is determined by the dimensions of the motor, and h_s the thickness of the piezoelectric segment. Accordingly, the driving force can be expressed as

$$F_f = sign(v_s - v_r)\mu_f \int \frac{k_d d_{mk} E_k h_s}{h} YdA. \tag{3.12}$$

It can be seen that the driving force of ultrasonic motor is proportional to the applied electric field strength E_k and the contact area A_p, say,

$$F_f \propto E_k A_p. \tag{3.13}$$

Therefore, the scaling effect of the driving force of piezoelectric rotary actuator is the same as the linear type and the torque scales as $[\xi^3]$.

The energy density of the piezoelectric actuator is similar to that of a plate capacitor, whose electric energy density $[W_E]$ can be calculated by

$$[W_E] = \frac{1}{2}\varepsilon E^2. \tag{3.14}$$

where ε is the electrical permittivity of the piezoelectric material used for the actuator and E the applied electrical field. Therefore, the energy density of a piezoelectric actuator is only related to the dialectic property of the piezoelectric material and the applied voltage. If the applied electric field is kept constant, the energy density of the piezoelectric actuator will be independent to its scale sizes.

3.2.2 Scaling of electromagnetic actuators

To analyse an electromagnetic actuator, a simplest structure consisting of a current carrying conductor in a constant magnetic field is considered, as shown in Fig.3-3. In order to find out the electromagnetic force generated by the actuator, the magnetic co-energy of the magnetic system is firstly evaluated. According to the magnetostatic theory, the co-energy of the system is given by

$$W_M^{'} = \frac{1}{2} I_1^2 L_1 + \frac{1}{2} I_m^2 L_m + I_1 I_m L_{1m}, \tag{3.15}$$

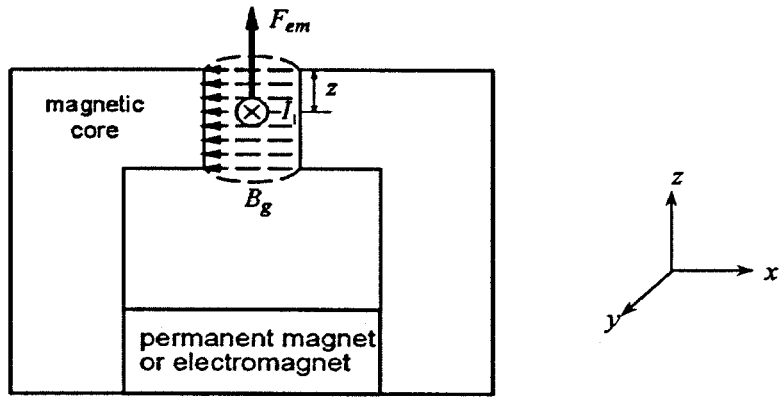

Fig.3-3 Electromagnetic force on a conductor in magnetic field

where I_1 and I_m are the current in the moving conductor and the equivalent field excitation current, L_1 and L_m the self inductances of the moving conductor and exciting coil, and L_{1m} is the mutual conductance between them. The electromagnetic force acting on the moving conductor, F_{em}, can be found by the derivative of W'_M with respect to z:

$$F_{em} = \frac{\partial W'_M}{\partial z} = \frac{1}{2} I_1^2 \frac{\partial L_1}{\partial z} + \frac{1}{2} I_m^2 \frac{\partial L_m}{\partial z} + I_1 I_m \frac{\partial L_{1m}}{\partial z}. \tag{3.16}$$

Normally, the magnetic field can be produced by either an electromagnet or a permanent magnet. This, however, will cause different scaling effects.

3.2.2.1 Actuator with electromagnet

Consider an actuator with electromagnet, in which the magnetic field is generated by the current in an excitation coil. Assume that the magnetic permeability of the magnetic core is infinite, and by the magnetic circuit analysis, the inductances in (3.15) can then be expressed as the following

$$L_1 = \frac{\mu_0 wz}{l}, \tag{3.17}$$

$$L_m = \frac{\mu_0 N_t^2 A_g}{l}, \tag{3.18}$$

$$\text{and} \quad L_{1m} = \frac{\lambda_{1m}}{I_m} = \frac{B_g}{I_m} wz, \tag{3.19}$$

where μ_0 is the magnetic permeability of free space, N_t the number of turns of the coil, z

the distance shown in Fig.3-3, $A_g=hw$ the cross sectional area of the air gap, and l, h, and w are the length, height and depth of the air gap, respectively. B_g is the flux density in the air gap, which is given by

$$B_g = \frac{\mu_0 N_t I_m}{l}. \tag{3.20}$$

By putting the formulation of inductances and flux density into (3.16), and noting that $\partial L_m/\partial z$ is zero, the electromagnetic force can then be obtained as

$$F_{em} = \frac{1}{2}\mu_0 I_1^2 \frac{w}{l} + \mu_0 N_t I_m I_1 \frac{w}{l}, \tag{3.21}$$

and the co-energy of the system is

$$W_M' = \frac{\mu_0}{2} I_1^2 \frac{wz}{l} + \frac{\mu_0}{2} N_t^2 I_m^2 \frac{A_g}{l} + \mu_0 N_t I_1 I_m \frac{wz}{l}. \tag{3.22}$$

From the above result, it can be seen that the electromagnetic force of the actuator consists of two components: the reluctance force (first term) and the Lorenz force (second term). It is shown that both force components vary with the productions of currents. In order to examine the scaling effects of these terms, three cases are discussed in the following: 1) constant current density, 2) constant heat flow through the surface of the conductor, and 3) constant temperature rise.

Constant current density

If the current density is assumed as an intensive variable, say, it does not change with the scale size, i.e. $J=[\xi^0]$, the current in the conductors I_1 will be

$$I_1 = \int \vec{J} \cdot d\vec{A} = JA_c, \tag{3.23}$$

where A_c is the cross sectional area of the conductor as shown in Fig.3-4. Hence, I_1 will scale as

$$I_1 = [\xi^0][\xi^2] = [\xi^2]. \tag{3.24}$$

The rule applies to the field current in excitation coils, too. Then, the scaling effect of the force can be found as

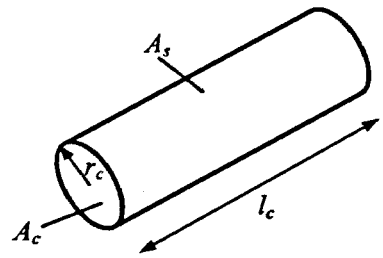

Fig.3-4 A conductor with surface area A_s and cross sectional area A_c

$$F_{em} = \frac{1}{2}\mu_0 I_1^2 \frac{w}{l} + \mu_0 N_t I_m I_1 \frac{w}{l} = [\xi^2][\xi^2]\frac{[\xi^1]}{[\xi^1]} = [\xi^4], \tag{3.25}$$

and the scaling effect of the energy density can be obtained based on (3.22) as

$$[W_M'] = \frac{W_M'}{V} = \frac{[\xi^2]^2 [\xi^2]/[\xi^1]}{[\xi^3]} = [\xi^2]. \tag{3.26}$$

Therefore, the electromagnetic force scales as $[\xi^4]$ while the system energy density scales as $[\xi^2]$ when keeping the current density unchanged. The results show that, in this case, the available force will decrease dramatically when the actuator size is getting smaller and the regime is obviously not preferable for the micro applications.

Constant heat flow through the surface of the conductors

Under this condition, there are two intensive variables, the heat flow out of the conductor per unit conductor surface area Q/A_s, and the resistivity ρ of the conductor. Because the heat flow out of the conductors must be equal to the power dissipation in the conductors,

$$Q = I^2 R t = I^2 \left(\frac{\rho l_c}{A_c}\right) t, \tag{3.27}$$

the heat flow per unit surface area is hence give by

$$\frac{Q}{A_s} = I^2 \frac{\rho l_c}{A_s A_c} t, \tag{3.28}$$

and

$$I^2 = \frac{Q}{A_s}\frac{A_s A_c}{\rho l_c}t, \tag{3.29}$$

where l_c is the length of the conductor. If the heat flow out of per unit surface area of the conductor is constant, i.e. $Q/A_s = [\xi^0]$, the following relationship can be obtained

$$I^2 = [\xi^0]\frac{[\xi^2][\xi^2]}{[\xi^1]} = [\xi^3] \text{ or } I = [\xi^{1.5}]. \tag{3.30}$$

Because the electromagnetic force is proportional to the production of the currents as shown in (3.21), the force will scale as $[\xi^3]$ in case of constant heat flow per unit surface area. The energy density, on the other hand, scales as $[\xi^1]$. Compare to the results under the constant current density condition, the scaling effect is improved. However, this benefit is achieved at the cost of the increase of resistive power dissipation. As per (3.30), the current density will scale as $[\xi^{-0.5}]$, meaning that it increases when the system is scaled down. According to Joule's law, the resistive power dissipation per volume is J^2/ρ, which therefore scales as $[\xi^{-1}]$.

Constant temperature rise in the conductors

There is a maximum temperature that the conductor and insulation can withstand. Under this condition, a maximum temperature rise between the conductor and the surrounding ambient is set, and it is independent to the scale size. Based on this assumption, the current density and the force scaling can be evaluated.

Fig.3-5 shows a section of a conductor with a radius of r_c and length of the section under consideration is l_c. According to the thermal theory, the relationship between the heat flow Q and temperature T is given by the equation of heat conduction

$$\frac{dQ}{dt} = -k_T A_T \frac{dT}{dx}, \tag{3.31}$$

where A_T is the area for heat exchange, x the distance, and k_T the thermal conductivity. Considering a cylinder of radius r_1 inside the conductor shown in Fig.3-5, dQ/dt is equal to the resistive heat dissipated within this cylinder and it can be found as

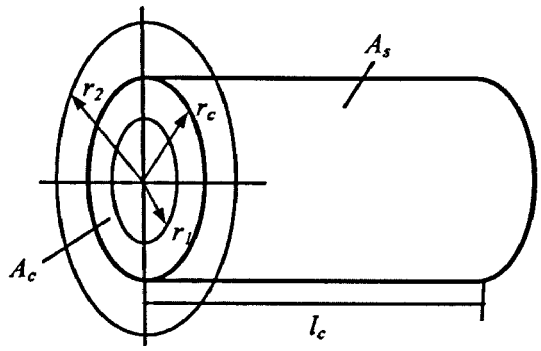

Fig.3-5 A conductor of radius r_c and length l_c

$$\frac{dQ}{dt} = I^2 \frac{\rho l_c}{A_{c1}} = J^2 \rho A_{c1} l_c = J^2 \rho \pi r_1^2 l_c, \tag{3.32}$$

where $A_{c1} = \pi r_1^2$.

Because the heat exchange area of the cylinder is the internal surface area $A_T = 2\pi r_1 l_c$, (3.31) can be rewritten as

$$\frac{dQ}{dt} = -2\pi r_1 l_c k_T \frac{dT}{dr_1}. \tag{3.33}$$

Combining (3.32) and (3.33), the following equation can be obtained,

$$J^2 \rho r_1 dr_1 = -2k_T dT. \tag{3.34}$$

By integrating the both sides of the above equation, one can obtain the following relationship:

$$J^2 = -\frac{4k_T \Delta T}{\rho r_1^2}. \tag{3.35}$$

As assumed, the temperature rise of the conductor ΔT is intensive, say, $\Delta T = [\xi^0]$, the scaling of current density can then be obtained as

$$J = \left[\frac{[\xi^0]}{[\xi^2]}\right]^{1/2} = [\xi^{-1}] \text{ and } I = \int J dA = [\xi^1]. \tag{3.36}$$

Considering the outside of the conductor, the total heat flux will be constant, and (3.31) becomes

$$\frac{dQ}{dt} = J^2 \rho \pi r_c^2 l_c, \tag{3.37}$$

and (3.33) becomes

$$\frac{dQ}{dt} = -2\pi r_2 l_c k_T \frac{dT}{dr_2}, \tag{3.38}$$

where r_2 is the radius outside the conductor. Therefore,

$$J^2 \rho r_c^2 \frac{1}{r_2} dr_2 = -2k_T dT. \tag{3.39}$$

Similarly, by integrating the both sides of the equation, the following relationship can be obtained:

$$J^2 = -\frac{2k_T \Delta T}{\rho r_c^2} \log_e [r_2/r_c]. \tag{3.40}$$

Equation (3.40) is similar to (3.35) except the term of $\log_e(r_2/r_c)$. If the ratio of r_2 to r_c remain unchanged when the system is scaled down, e.g. the distance to the heat sink scales with the entire system, the scaling of (3.40) is exactly the same as (3.35).

Resultantly, the scaling of the electromagnetic force of the actuator will be $[\xi^2]$ and the energy density will be constant, say, $[\xi^0]$. In this case, an electromagnetic actuator is comparable to a piezoelectric actuator. The resistive power dissipation per volume, on the other hand, will increase a great deal, resulting in a lower efficiency of the system.

In summary, the electromagnetic force produced by an electromagnet based actuator scales as $[\xi^2]$ to $[\xi^4]$ depending on the different current conditions. For both linear and rotary type electromagnetic actuators, the above scaling analysis is applicable as they employ the same force generation principle. However, in order to achieve a comparative performance as that of a piezoelectric actuator, the power dissipation will become a serious issue in this kind of electromagnetic actuators.

3.2.2.2 Actuator with permanent magnet

The permanent magnet (PM) materials have been greatly developed during the past

decades and PM with high magnetic energy product such as NdFeB can be readily obtained. The applications of PMs in the electromagnetic actuators are widely adopted to achieve higher force-to-volume ratios and efficiency.

If a PM is applied for generating the magnetic field instead of excitation coil in the actuator shown in Fig.3-3, and assuming that the PM and air gap have the same cross sectional area A_g, the magnetic flux in the air gap can be found by

$$\phi_g = \frac{H_c \tau_m}{l/\mu_0 A_g + \tau_m/\mu_m A_g}, \tag{3.41}$$

where H_c, μ_m are the coercive force and magnetic permeability of the PM material, respectively, and τ_m is the thickness of the PM along the magnetisation direction. Usually, the permeability of commonly used PM materials is close to that of air, μ_0. Hence, (3.41) can be simplified as

$$\phi_g = \frac{\mu_0 A_g}{l+\tau_m} H_c \tau_m . \tag{3.42}$$

The flux density in the air gap B_g is then given by

$$B_g = \frac{\phi_g}{A_g} = \frac{\mu_0 H_c \tau_m}{l+\tau_m} . \tag{3.43}$$

As a convention in magnetic field analysis containing PMs, the PM component is often treated as an electromagnet with a single turn coil and an equivalent exciting current $I_m = H_c \cdot \tau_m$. Thus, the inductances of the system shown in Fig.3-3 can be calculated by the following equations:

$$L_1 = \mu_0 \frac{(lh+(h-z)\tau_m)}{lh(l+\tau_m)} wz, \tag{3.44}$$

$$L_m = \frac{\mu_0 A_g}{l+\tau_m}, \tag{3.45}$$

$$\text{and} \quad L_{1m} = \frac{B_g}{I_m} wz . \tag{3.46}$$

The co-energy of the PM actuator will then be found as

$$W_M' = \frac{\mu_0}{2} I_1^2 \frac{(lh+(h-z)\tau_m)}{lh(l+\tau_m)} wz + \frac{\mu_0}{2} H_c^2 \frac{\tau_m^2}{l+\tau_m} A_g + \mu_0 H_c I_1 \frac{\tau_m}{l+\tau_m} wz, \quad (3.47)$$

and the electromagnetic force is

$$F_{em} = \frac{\mu_0}{2} I_1^2 \frac{(lh+(h-z)\tau_m)}{lh(l+\tau_m)} w + \mu_0 H_c I_1 \frac{\tau_m}{l+\tau_m} w. \quad (3.48)$$

Similar to the actuator using electromagnet, the electromagnetic force of a PM type actuator also consists of the reluctance force (first term) and the Lorenz force (second term). However, unlike the actuator with electromagnet, the scaling effects of these forces in a PM actuator may be different as they have different relationships with the currents and the sizes of the system. Following are the analysis of the scaling effects under the three conditions used for analysing of the scaling effect of actuator with electromagnet.

Constant current density

If the current density keeps constant, the current scales as $[\xi^2]$. The scaling of the force can be obtained as

$$F_{em} = [\xi^2]^2 + [\xi^2][\xi^1] = [\xi^4] + [\xi^3], \quad (3.49)$$

and the scaling effect of energy density of the system is found as

$$[W_M'] = \frac{[\xi^2]^2[\xi^1] + [\xi^3] + [\xi^2][\xi^2]}{[\xi^3]} = [\xi^2] + [\xi^0] + [\xi^1]. \quad (3.50)$$

Constant heat flow through the surface of the conductors

In case of constant heat flow per unit surface area of the conductor, the current scales as $[\xi^{1.5}]$ and the scaling of the force can be calculated as

$$F_{em} = [\xi^{1.5}]^2 + [\xi^{1.5}][\xi^1] = [\xi^3] + [\xi^{2.5}], \quad (3.51)$$

while the energy density scales as

$$[W_M'] = \frac{[\xi^{1.5}]^2[\xi^1]+[\xi^3]+[\xi^{1.5}][\xi^2]}{[\xi^3]} = [\xi^1]+[\xi^0]+[\xi^{0.5}]. \qquad (3.52)$$

Constant temperature rise in the conductors

When the temperature rise of the current carrying conductor is constant, the current will scale as $[\xi^1]$. As a result, the scaling of the force will become

$$F_{em} = [\xi^1]^2 + [\xi^1][\xi^1] = [\xi^2], \qquad (3.53)$$

and the scaling of energy density is

$$[W_M'] = \frac{[\xi^1]^2[\xi^1]+[\xi^3]+[\xi^1][\xi^2]}{[\xi^3]} = [\xi^0]. \qquad (3.54)$$

It can be seen that, in a PM actuator, the components in the electromagnetic force and energy density have different scaling effects and it seems difficult to use only one scaling effect to describe the whole scenario. Nevertheless, for most of the PM actuators, the magnetic field is dominated by that generated by the PM ($I_m \gg I_1$). The magnetic energy produced by the PM and the Lorenz force account for the majority of the energy and force in the actuator. Therefore, the other components can be neglected when analysing the scaling effect of the PM actuators. Accordingly, the energy density of a PM actuator is independent to the scale sizes and only determined by the property of the PM material used in the actuator. The electromagnetic force of the PM actuator, however, scales as: $[\xi^3]$ for the constant current density, $[\xi^{2.5}]$ for the constant heat flow and $[\xi^2]$ for the constant temperature rise.

Table 3-1 compares the scaling effects between the electromagnetic actuators with electromagnet and PM. The results show that the best scaling effect of the PM actuator is the same as that of the actuator using electromagnet. However, the PM actuators do not need exciting current for building up the magnetic field, so the resistive power dissipation as well as the required energy input is greatly reduced, and hence a much

higher efficiency can be achieved. Consequently, compare to the actuator with electromagnet, PM actuators are more feasible in the micro applications due to its simpler structure, higher energy density and less power consumption.

Table 3-1

Comparison of scaling effects between the electromagnetic actuators with electromagnet and PM

Actuator type \ Conditions		Constant current density	Constant heat flow	Constant temperature rise
Electromagnet	Energy density	$[\xi^2]$	$[\xi^1]$	$[\xi^0]$
	Force	$[\xi^4]$	$[\xi^3]$	$[\xi^2]$
PM	Energy density	$[\xi^0]$	$[\xi^0]$	$[\xi^0]$
	Force	$[\xi^3]$	$[\xi^{2.5}]$	$[\xi^2]$

3.3 Power Density Limitations

Attainable energy density is one of the important features concerned in the micro system design. As discussed in section 3.2.1, the energy density in a piezoelectric actuator can be obtained by finding the stored energy in the electrical field within the actuator. It is known that the energy density in an electric field at any point in a linear, isotropic region is given by (3.14). The assumption of linearity is applicable since the commonly used piezoelectric materials usually display a linear property in their application circumstances.

For a piezoelectric actuator, the permittivity of a typical piezoelectric material is about two or three orders of magnitude larger than that of free air. For example the relative permittivity of soft PZT material is about 1700 while the break down field strength is 11×10^6 V/m. The maximum energy density is then up to 900kJ/m^3. Table 3-2 [Jenkins 2001, Measurement 2006] shows the properties and attainable energy densities of some common piezoelectric materials.

Table 3-2 Properties and attainable energy density of some piezoelectric materials

Materials	Hard PZT	Soft PZT	PZT film	PVDF[1]
Electrical Permittivity ($\varepsilon/\varepsilon_0$)	1250	1700	1000	12
Breakdown Field (MV/m)	13	11	40	75
Energy density (kJ/m^3)	900	900	7000	300

$\varepsilon_0 = 8.85\times10^{-12}$ F/m

Although piezoelectric materials have favourable energy density because of their very high endurable breakdown voltage, the operational voltage of the piezoelectric actuator are usually much lower due to the capability and insulation limitations of the power suppliers (limited to several hundreds of volts per millimetre), or they are often fabricated with very thin structure with thickness down to several microns. Therefore, the available energy density could be much less than those expected shown in Table 3-2.

Likewise, when considering an electromagnetic actuator, the energy density stored in a magnetic field in a linear and isotropic region is given by

$$[W_M] = \frac{1}{2\mu} B^2, \tag{3.55}$$

where μ is the magnetic permeability of the material in the region and B the flux density in the region. Ferromagnetic materials ordinarily cannot exceed 1.5T before they saturate. The air gap flux density is usually effectively limited to 1T due to the magnetic structure configurations such as spaces required for conductors. Therefore, 1T will be taken as the maximum flux density to be considered. Moreover, most of the ferromagnetic materials for the magnetic core have very high permeability compared to the air so that the majority of magnetic energy is stored in the air gap. As a result, the attainable magnetic energy density stored in the air gap will be up to 400kJ/m^3, and this excellent energy density feature compared to other actuation principles is the reason why the electromagnetic actuators are far superior in the macro scale as well known.

Nonetheless, 1T field strength limit is questionable when supposing that the magnetic

[1] PVDF: Polyvinylidene fluoride

field must be produced by current carrying conductors in micro scale. The thermal restrictions will result in a maximum current density in the conductor and the available energy density is limited by the case. As a result, the energy density produced by exciting conductors is much smaller than expected when current density and number of turns is restricted in the micro scale applications [Chapman 2001].

The use of PMs can considerably improve the competence of electromagnetic actuators. In this case, a favourable flux density could be achieved with small air gaps and independent to thermal limitations. Approximately, the flux density produced by PM in the air gap can be estimated by (3.43). As an example, when the thickness τ_m of the PM material is designed close to the length of air gap g in micro systems (in large-scale systems, g could be designed much smaller than τ_m), the flux density in the air gap would be $\mu_0 H_c/2$. The flux density in the air gap could reach about 0.6T if using high magnetic energy product rare earth PM materials such as NdFeB, and the energy density could be 230kJ/m^3. Accordingly, electromagnetic actuators using PM materials are favoured in micro systems.

In general, the piezoelectric actuators and the PM type electromagnetic actuators can have similar energy densities. For the high power applications and those scale large than hundreds of micrometers, both of them could be the preferable candidate for the actuation.

3.4 Performance Analysis - A Case Study

In the analysis conducted in sections 3.2 and 3.3, the scaling effect and the energy density of both the piezoelectric and electromagnetic actuators are studied. To the best conditions, both types of the actuators can have the similar indices in these features. A further comparative study is hence required to examine the advantages and drawbacks

of these actuators. In this section, detailed studies on the dynamic actuation performances of the both types of actuators are performed. Since the PM actuators have superior scaling effect and energy density than those with electromagnet, the analysis of the electromagnetic actuators will be only conducted on the PM types.

3.4.1 Structures of the actuators for comparison

In order to make a comparison between electromagnetic and piezoelectric actuators, linear type actuators with comparable structures and volumes are considered. As shown in Fig.3-6, the electromagnetic actuator used for performance analysis consists of a pair of poles of PMs and a current-carrying moving coil. The coil could move along the gap between the PMs and the supporting frame due to the Lorenz force when it is excited by a current. For convenience, the magnetic permeability of the soft magnetic frame for the magnetic flux circulation at the top and bottom of the actuator is assumed infinity so that their thicknesses could be small enough to be neglected during the analysis. In addition, the length of the air gaps between the coil and the fixed parts of the actuator (PMs and frame) and the fringing effects are ignored for simplifying the analysis. These assumptions would not lead to much error to the results.

The piezoelectric actuator used for analysis is rather simple. It is a piezoelectric beam as shown in Fig.3-7. When supplying an alternative voltage, the actuator can extend or

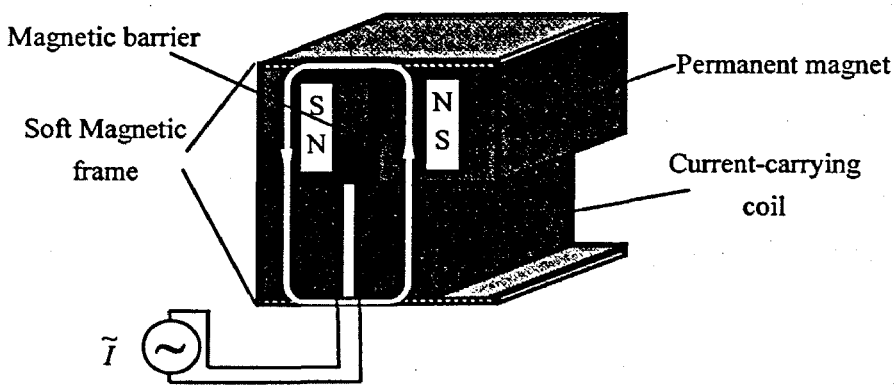

Fig.3-6 An electromagnetic linear actuator

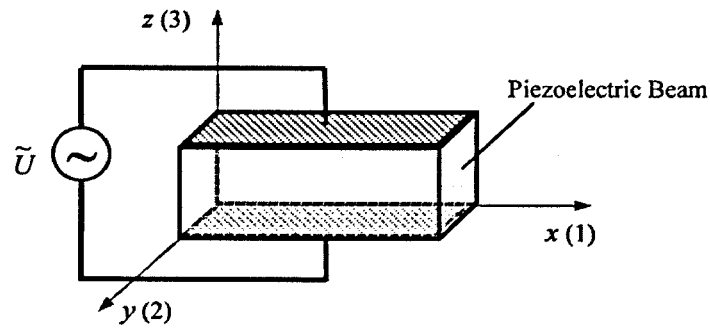

Fig.3-7 A piezoelectric linear actuator

constrict in the x (1) direction.

3.4.2 Analytical study of the piezoelectric actuator

Piezoelectricity can be regarded as a linear interaction between electrical and mechanical systems. The empirical equivalent circuit model based on the electromechanical constants in terms of impedance or admittance constitutes a powerful theoretical approach for analysing the performance of piezoelectric devices, and thereby avoiding the complexity during analysis and the discrepancy between theoretical linear and practical nonlinear problems [Ghouti 2000].

3.4.2.1 Equivalent circuit model for a T-effect transducer

Consider a piezoelectric beam with cross sectional area of $A_c = hw$ and length of l, as shown in Fig.3-8. When it is driven by an alternating voltage, the beam will be subjected to a transverse type (T-effect) deformation. If the power dissipation in the piezoelectric material is not taken into account, by the constitutive relationships of piezoelectricity and kinetic laws, the forces at each end of the piezoelectric beam and the input voltage/current can be given by the following equations in terms of complex notation,

$$\hat{I} = -\Phi\dot{\hat{x}}_0 + \Phi\dot{\hat{x}}_l + j\omega C_d\hat{U}\,, \tag{3.56}$$

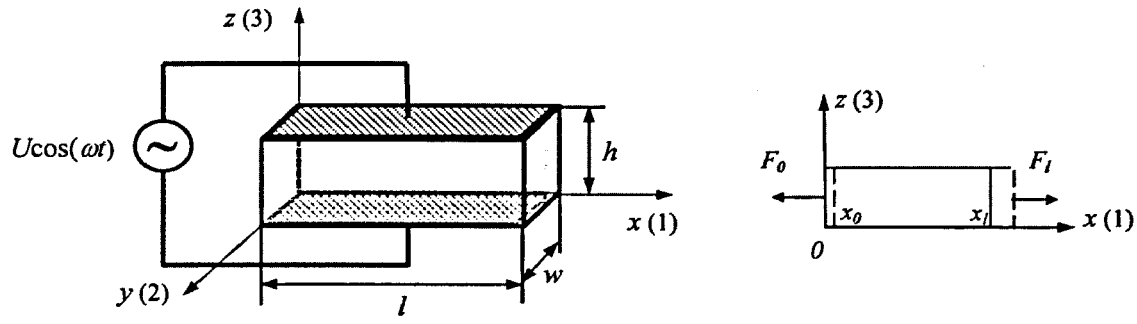

Fig.3-8 Piezoelectric transducer of T-effect

$$\hat{F}_0 = (Z + Z_0)\hat{\dot{x}}_0 - Z\hat{\dot{x}}_l + \Phi\hat{U}\,, \tag{3.57}$$

$$\hat{F}_l = Z\hat{\dot{x}}_0 - (Z + Z_0)\hat{\dot{x}}_l + \Phi\hat{U}\,, \tag{3.58}$$

where:

U, I: the input voltage and current, and $\hat{U} = Ue^{j\omega t}$, ω is the angular frequency;

F_0, F_l: the forces at the position of $x = 0$ and $x = l$;

$\dot{x}_0$, $\dot{x}_l$: the velocities at the position of $x = 0$ and $x = l$;

Z, Z_0: the elastic impedances of the piezoelectric actuator, and

$$Z = \frac{\rho_m A_c v_{ph}}{j\sin(k_v l)},$$

$$Z_0 = j\rho_m A_c v_{ph}\tan(k_v l/2),$$

where $v_{ph} = \dfrac{1}{\sqrt{\rho_m s_{11}^E}}$ is the phase velocity, $k_v = \omega/v_{ph}$ the wave number, and ρ_m the mass density of the piezoelectric material;

C_d: the clamped capacitance of the actuator, and

$$C_d = \varepsilon_{33}^S \frac{wl}{h}\,, \qquad \varepsilon_{33}^S = \varepsilon_{33}^T\left(1 - \frac{d_{31}^2}{s_{11}^E \varepsilon_{33}^T}\right);$$

Φ: the electromechanical coupling factor of the piezoelectric beam, and

$$\Phi = w\frac{d_{31}}{s_{11}^E}.$$

Based on the above equations, an equivalent circuit of a piezoelectric transducer, known

as Mason's equivalent circuit model, can be drawn as shown in Fig.3-9.

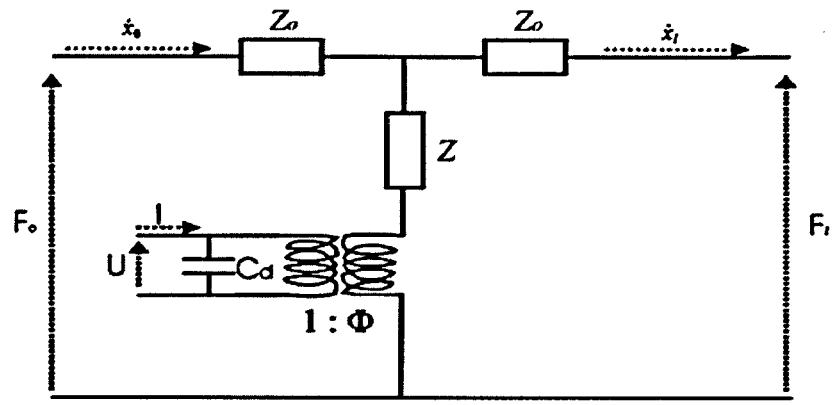

Fig.3-9 Mason's equivalent circuit model of piezoelectric transducer

3.4.2.2 Dynamic performance of the actuator

Based on the equivalent circuit model and its equations, an analytical study can be conducted on the piezoelectric actuator shown in Fig.3-7. In the following part, the dynamic performances with and without load are discussed respectively, and the corresponding models are established.

3.4.2.2.1 Actuator with no load

In case of no load, the piezoelectric beam is unclamped and each side of the actuator is free. Therefore, the external force on each end will be zero, say, $F_0 = F_l = 0$. Equations (3.57) and (3.58) will become

$$\hat{F}_0 = (Z + Z_0)\hat{\dot{x}}_0 - Z\hat{\dot{x}}_l + \Phi\hat{U} = 0, \tag{3.59}$$

$$\hat{F}_l = Z\hat{\dot{x}}_0 - (Z + Z_0)\hat{\dot{x}}_l + \Phi\hat{U} = 0. \tag{3.60}$$

By solving (3.59) and (3.60), $\hat{\dot{x}}_0$ and $\hat{\dot{x}}_l$ can be obtained as

$$\hat{\dot{x}}_l = -\hat{\dot{x}}_0 = \frac{\Phi}{2Z + Z_0}\hat{U}.$$

Considering that

$$
\begin{aligned}
2Z + Z_0 &= 2\frac{\rho_m A_c v_{ph}}{j\sin(k_v l)} + j\rho_m A_c v_{ph}\tan(k_v l/2) \\
&= j\rho_m A_c v_{ph}\left[-\frac{2}{\sin(k_v l)} + \tan(k_v l/2)\right] \\
&= j\rho_m A_c v_{ph}\left[-\frac{1+\tan^2(k_v l/2)}{\tan(k_v l/2)} + \tan(k_v l/2)\right] \\
&= \frac{\rho_m A_c v_{ph}}{j\tan(k_v l/2)}
\end{aligned}, \tag{3.61}
$$

the velocities $\dot{x}_0$ and $\dot{x}_l$ can be found as

$$
\hat{\dot{x}}_l = -\hat{\dot{x}}_0 = \frac{\Phi}{2Z + Z_0}\hat{U} = j\frac{\Phi\tan(k_v l/2)}{\rho_m A_c v_{ph}}\hat{U}. \tag{3.62}
$$

By combining (3.56) and (3.62), the input current can be solved as

$$
\hat{I} = \left(j\frac{2\Phi^2\tan(k_v l/2)}{\rho_m A_c v_{ph}} + j\omega C_d\right)\hat{U}. \tag{3.63}
$$

If defining $C_{mp} = \Phi^2\frac{\tan(k_v l/2)}{\omega\rho_m A_c v_{ph}}$, the above equations can be further expressed as

$$
\hat{\dot{x}}_l = -\hat{\dot{x}}_0 = \frac{1}{\Phi}j\omega C_{mp}\hat{U}, \tag{3.64}
$$

$$
\hat{I} = \hat{I}_{m0} + \hat{I}_{ml} + j\omega C_d\hat{U}, \tag{3.65}
$$

$$
\hat{I}_{m0} = \hat{I}_{ml} = j\omega C_{mp}\hat{U}, \tag{3.66}
$$

Based on the above equations, an equivalent circuit of the piezoelectric actuator can be derived as shown in Fig.3-10. C_{mp} in the circuit can be regarded as an electrical device in the actuator that transfers electrical energy into mechanical energy.

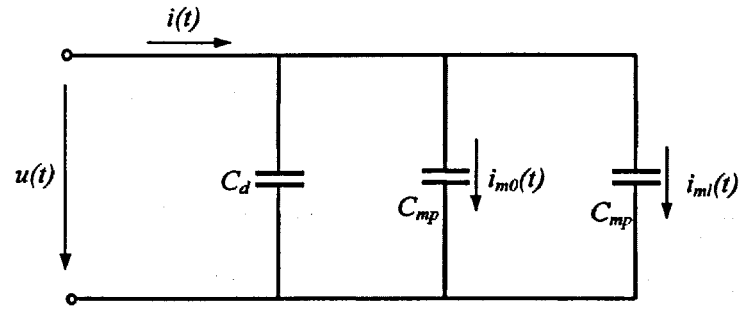

Fig.3-10 Equivalent circuit of the piezoelectric actuator with no load

If the actuator is fixed at the position of x=0, say, the velocity $\dot{x}_0$ is zero, the velocity at $x=l$ is then given by

$$\hat{\dot{x}}_l = \frac{1}{\Phi} j2\omega C_{mp}\hat{U}. \tag{3.67}$$

In this case, only the properties at $x=l$ will be considered. Thus, (3.65) can be rewritten as

$$\hat{I} = \hat{I}_m + j\omega C_d \hat{U}, \tag{3.68}$$

$$\hat{I}_m = j2\omega C_{mp}\hat{U}. \tag{3.69}$$

The equivalent circuit can therefore be simplified as the one shown in Fig.3-11. In the time domain, the velocity of the actuator at $x=l$ can be expressed as,

$$\dot{x}_l = \frac{2C_{mp}}{\Phi}\frac{du(t)}{dt}, \tag{3.70}$$

and the corresponding displacement is given by

$$x_l = \frac{2C_{mp}}{\Phi}u(t) + l. \tag{3.71}$$

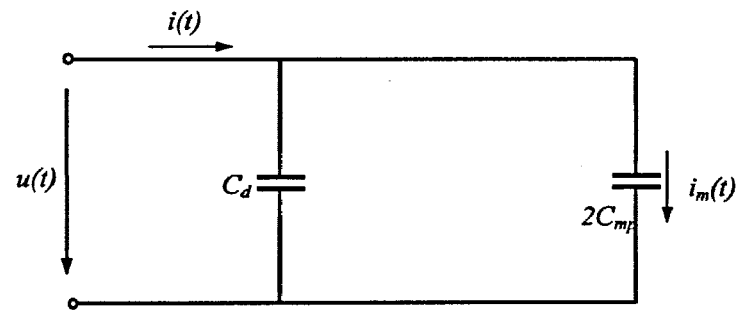

Fig.3-11Simplified equivalent circuit of the piezoelectric actuator with no load

3.4.2.2.2 Actuator with external load

If the actuator is applied with an external force F as shown in Fig.3-12, according to Newton's law, the force at the both sides of the actuator will be $F_0 = F_l = F$. As a result, the equations for Mason's equivalent circuit model become

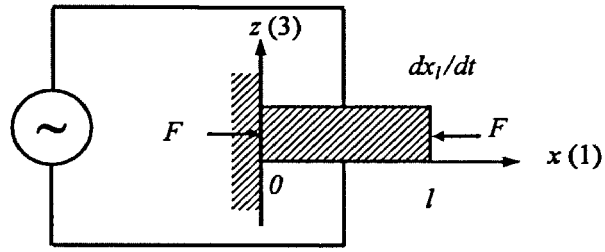

Fig.3-12 A piezoelectric actuator with external load

$$\hat{I} = -\Phi\hat{\dot{x}}_0 + \Phi\hat{\dot{x}}_l + j\omega C_d\hat{U}\,, \tag{3.72}$$

$$\hat{F} = (Z + Z_0)\hat{\dot{x}}_0 - Z\hat{\dot{x}}_l + \Phi\hat{U}\,, \tag{3.73}$$

$$\hat{F} = Z\hat{\dot{x}}_0 - (Z + Z_0)\hat{\dot{x}}_l + \Phi\hat{U}\,. \tag{3.74}$$

By solving above equations, following relations can be derived:

$$\hat{I} = \frac{-2\Phi}{2Z + Z_0}\hat{F} + (\frac{2\Phi^2}{2Z + Z_0} + j\omega C_d)\hat{U}\,, \tag{3.75}$$

$$\hat{\dot{x}}_0 = \frac{1}{2Z + Z_0}\hat{F} - \frac{\Phi}{2Z + Z_0}\hat{U}\,, \tag{3.76}$$

$$\hat{\dot{x}}_l = -\frac{1}{2Z + Z_0}\hat{F} + \frac{\Phi}{2Z + Z_0}\hat{U}\,. \tag{3.77}$$

If denoting the actuation velocity of the beam as

$$\hat{\dot{x}} = \hat{\dot{x}}_l - \hat{\dot{x}}_0\,, \tag{3.78}$$

Equations (3.72), (3.73) and (3.74) can be rewritten in the following forms

$$\hat{I} = -\frac{2\Phi}{2Z + Z_0}\hat{F} + (\frac{2\Phi^2}{2Z + Z_0} + j\omega C_d)\hat{U}\,, \tag{3.79}$$

$$\hat{\dot{x}} = -\frac{2}{2Z + Z_0}\hat{F} + \frac{2\Phi}{2Z + Z_0}\hat{U}\,. \tag{3.80}$$

Because

$$\frac{\Phi}{2Z + Z_0} = \frac{1}{\Phi}j\omega C_{mp}\,, \tag{3.81}$$

(3.79) and (3.80) can then be expressed as

$$\hat{I} = j2\omega C_{mp}(-\frac{1}{\Phi}\hat{F} + \hat{U}) + j\omega C_d \hat{U} = j2\omega C_{mp}(-\hat{U}_m + \hat{U}) + j\omega C_d \hat{U}, \quad (3.82)$$

$$\hat{\dot{x}} = \frac{1}{\Phi} j2\omega C_{mp}(-\hat{U}_m + \hat{U}). \quad (3.83)$$

where $\hat{U}_m = \hat{F}/\Phi$. Compare to the no load case, the input current and the velocity are affected by the external force, and the corresponding components are given by the terms associated to F, as shown in the equations. As a result, the derived equivalent circuit in no load case can be modified to the one shown in Fig.3-13.

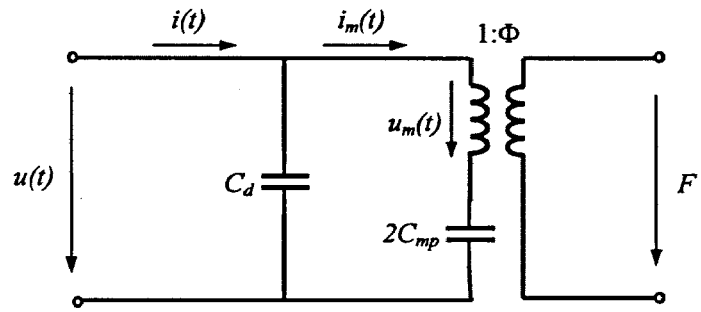

Fig.3-13 Equivalent circuit of the piezoelectric actuator with external load

3.4.2.2.3 Attainable force and displacement

From the derived dynamic model of the piezoelectric actuator, the actuation force and displacement will vary at different strain conditions of the actuator. The maximum force occurs when actuator is clamped at both sides and no deformation is observed. Under this condition, the velocity $\hat{\dot{x}}$ will be zero, and the maximum driving force is achieved, which is given by:

$$\hat{F}_{\max} = \Phi \hat{U} \quad (3.84)$$

When excited by low frequency or DC voltage, the unloaded actuator can reach its maximum strain. According to (3.67), the velocity can be found by

$$\hat{\dot{x}}_l = j\frac{2\Phi}{\rho_m A_c v_{ph}} \tan(k_v l/2)\hat{U}. \quad (3.85)$$

When operational frequency of the actuator is far below the resonant frequency of the

piezoelectric beam, $k_v l$ would be a small value and $\tan(k_v l/2)$ could be replaced by $k_v l/2$. Hence, (3.85) cab be rewritten as

$$\hat{\dot{x}}_l \approx j\frac{(k_v l)}{\rho_m A_c v_{ph}}\Phi\hat{U} = j\frac{\omega l}{\rho_m A_c v_{ph}^2}\Phi\hat{U}. \tag{3.86}$$

The displacement of the actuator can be obtained by the integration of (3.86) as

$$\begin{aligned}\hat{x} &= \int\hat{\dot{x}}dt = \frac{l}{\rho_m A_c v_{ph}^2}\Phi\hat{U} + l = d_{31}\frac{\hat{U}}{h}l + l \\ &= d_{31}\hat{E}_3 l + l = \Delta\hat{x} + l\end{aligned}. \tag{3.87}$$

It can be seen that the result consists with that derived directly from the constitutive equations of piezoelectric materials when $T_1 = T_2 = T_3 = 0$,

$$\Delta\hat{x} = \hat{S}_1 l = d_{31}\hat{E}_3 l. \tag{3.88}$$

3.4.3 Analytical study of the PM type electromagnetic actuator

The dimensions of the PM type electromagnetic actuator shown in Fig.3-6 are defined in Fig.3-14. Without losing the universality, the current carrying coil is specified as one turn with a width of $l/4$ so that it can have a space to move within the magnetic field region. Other dimensions of the actuator could also be pre-assumed except the height of the PM h_m, which should be determined carefully before the further study can be conducted.

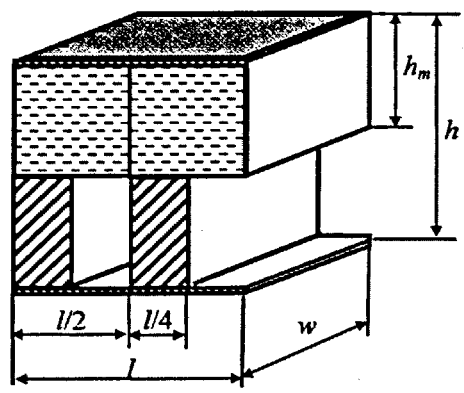

Fig.3-14 Dimensions of the linear electromagnetic actuator

3.4.3.1 Thickness of the permanent magnet

The criteria used for determining the thickness of the PMs is that the selected dimension can result in a maximum output force of the actuator. Based on the magnetic circuit analysis, the magnetic flux density B_g in the coil area is given by

$$B_g = \mu_0 H_c \frac{h_m}{h}, \tag{3.89}$$

and the electromagnetic force F_{em} can be found as

$$F_{em} = 2B_g Iw = 2B_g (JA_c)w, \tag{3.90}$$

where I is the current in the coil and A_c the cross sectional area of the coil, $A_c=(h-h_m)l/4$. Rewriting (3.90) by using (3.89) and A_c yields

$$F_{em} = 2\mu_0 H_c \left(J(h-h_m)\frac{l}{4} \right) \frac{h_m}{h} w = \frac{1}{2}\mu_0 H_c J \frac{wl}{h}(h-h_m)h_m. \tag{3.91}$$

It can be seen that a maximum force can be achieved by selecting h_m properly if the current density J is kept constant. The optimal value of h_m can be obtained by solving the equation of $dF_{em}/dh_m = 0$, and the result is $h_m = h/2$. This means that, to obtain a maximum force output for the actuator, the thickness of the PMs should be the same as that of the current carrying coil.

3.4.3.2 Dynamic performance of the actuator

Assume that there are no load and damper associated with the moving coil, and the displacement of the coil will not exceed the range of $l/4$ (refer to Fig.3-14) so that the coil will remain in the constant flux density region. The electromagnetic force acting on the coil can be expressed as

$$F_{em} = K_f I, \tag{3.92}$$

where $K_f = 2B_g w$ is the force coefficient of the actuator. When the coil is excited by a sinusoidal current with an angular frequency ω, as shown in Fig.3-15, (3.92) can be rewritten using complex notation as

$$\hat{F}_{em} = K_f I e^{j\omega t} = K_f \hat{I}\,. \tag{3.93}$$

According to Newton's law, under the conditions of no load and damper, the kinetic equations of the moving coil can be expressed as

$$d\hat{\dot{x}}/dt = \hat{F}_{em}/m_a\,, \tag{3.94}$$

and $$d\hat{x}/dt = \hat{\dot{x}}\,, \tag{3.95}$$

where $\hat{\dot{x}}$ and $\hat{x}$ are the velocity and displacement of the moving coil in complex notation, respectively, and m_a is the mass of the moving coil.

By solving simultaneously (3.94) and (3.95) with (3.93), the velocity and displacement of the moving coil can be obtained as

$$\hat{\dot{x}} = \frac{K_f}{j\omega m_a}\hat{I} + C_1\,, \tag{3.96}$$

$$\hat{x} = -\frac{K_f}{\omega^2 m_a}\hat{I} + C_1 t + C_2\,, \tag{3.97}$$

where C_1 and C_2 are the constants depending on the initial conditions. If the initial conditions are set as

$$\hat{\dot{x}}(0) = \frac{K_f I}{j\omega m_a} \quad \text{and} \quad \hat{x}(0) = 0\,,$$

these two constants will be

$$C_1 = 0 \quad \text{and} \quad C_2 = \frac{K_f I}{\omega^2 m_a}.$$

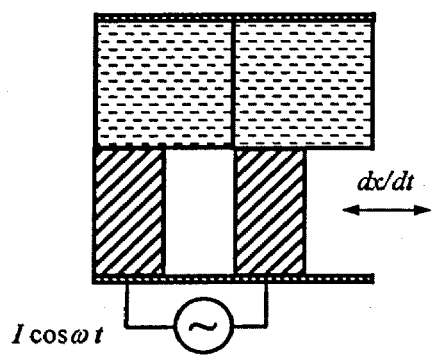

Fig.3-15 Movement of the electromagnetic actuator under sinusoidal excitation

Consequently, (3.96) and (3.97) can be simplified as

$$\hat{\dot{x}} = \frac{K_f}{j\omega m_a}\hat{I}, \tag{3.98}$$

$$\hat{x} = \frac{K_f}{\omega^2 m_a}(I - \hat{I}). \tag{3.99}$$

Equations (3.98) and (3.99) are the kinetic equations of the electromagnetic actuator under the sinusoidal excitation current. In addition, a back electromotive force (EMF) will be generated in the coil when it moves in the magnetic field, and it is given by

$$\hat{E}_m = K_e\hat{\dot{x}} = \frac{K_e K_f}{j\omega m_a}\hat{I}, \tag{3.100}$$

where $K_e = 2B_g w$ is the back EMF coefficient and the supply voltage U can be expressed as

$$\hat{U} = \hat{E}_m + R_a\hat{I} + j\omega L\hat{I} = (\frac{K_e K_f}{j\omega m} + R_a + j\omega L)\hat{I} = (\frac{1}{j\omega C_{me}} + R_a + j\omega L)\hat{I}, \tag{3.101}$$

where R_a and L are the resistance and self inductance of the moving coil, respectively, and $C_{me} = m_a/K_e K_f$.

Similar to the analysis of the piezoelectric actuator, (3.101) can be illustrated by an equivalent circuit, which is shown in Fig.3-16. Constant C_{me} can be regarded as an electrical device that transfers the energy and K_e as electromechanical coupling factor. Thus, the velocity of coil can be further expressed as

$$\hat{\dot{x}} = \frac{1}{K_e}\frac{1}{j\omega C_{me}}\hat{I}. \tag{3.102}$$

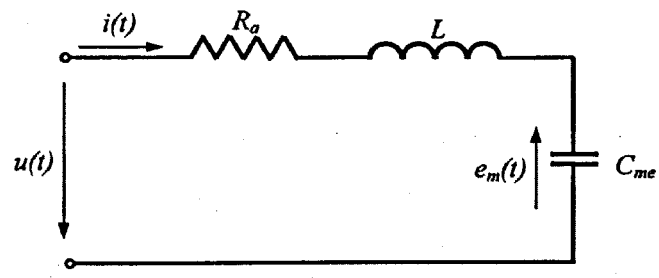

Fig.3-16 Equivalent circuit of the electromagnetic actuator

3.4.4 Quantitative comparison with specified dimensions

In order to look into more intuitively the performances of the actuators for an easier comparison, the dimensions of the actuators are specified for a quantitative comparison. Both types of the actuators will be given the same volume of 125mm^3. The electromagnetic actuator is chosen as a cubic structure, which is $l \times w \times h$ = 5×5×5 mm^3, while the piezoelectric actuator is a beam with $l \times w \times h$ = 25×2.5×2 mm^3 so that it can meet the requirements of the T-effect operation of the piezoelectric materials. Based on the results obtained in the analytical analysis of the actuators, the quantitative comparison can be conducted as follows.

3.4.4.1 Electromagnetic actuator

Assume that the PM material used in the actuator is NdFeB, the typical coercive force of which is 900kA/m. Copper wires can usually allow a current density of 6A/mm in *rms* value. Thus, for the given dimensions, the maximum coil peak current I could be 26.5A ($I = \sqrt{2} J \cdot A_c$). As a result, the attainable force can be 0.15N. The driving range is limited to a quarter of the length of the actuator because the actuator cannot operate beyond the magnetic field region. As a result, the driving range will be 1.25mm. By this driving range, a minimum operation frequency of about 587rad/s is required, which can be obtained from (3.99). However, this is subject to the actuator's dimensions rather than the electromagnetic actuation principle.

3.4.4.2 Piezoelectric actuator

The characteristics of the piezoelectric material used for the evaluation is shown in Table 3-3 and the actuator is fixed at one side. The maximum operation voltage of the material is set as 200VAC/mm, and the applied voltage of the actuator will be 400VAC. Therefore, according to the equations obtained in the analytical analysis, the actuator

can produce a maximum force of 10N while the maximum driving range will be only 0.86μm. However, as an actuator, the piezoelectric beam will not operate at a load equal to its maximum attainable force. Otherwise, no displacement will be obtained. On the other hand, if a load is applied to the actuator, the driving range will accordingly decrease as well.

Table 3-3 Properties of the piezoelectric material for evaluation

Density (g/cm^3)	Relative Dielectric Constant (ε^T_{33})	Electric Charge Constant ($\times10^{-12}m/N$)		Elastic Constant ($\times10^{-12}m^2/N$)		Dielectric Loss $\tan\delta$ ($\times10^{-3}$)	Maximum Voltage (V/mm)
7.75	1730	d_{31}	-170	s^E_{11}	16.4	4	200
		d_{33}	374	s^E_{33}	18.8		

Consider that the piezoelectric actuator generates the same force and frequency as the electromagnetic actuator. The operational status can be calculated according to the equations derived in section 3.4.2. The results are shown in Table 3-4. The data of the electromagnetic actuator operating under the same conditions are also listed in the table for comparison. It should be noted that the low velocity of the piezoelectric is due to the limited operational frequency. In fact, the piezoelectric actuator can operate under much higher frequency.

Table 3-4 Comparison of the piezoelectric and electromagnetic actuators

	Piezoelectric	Electromagnetic
Force (N)	0.15	0.15
Velocity (m/s)	0.49×10^{-3}	0.73
Displacement (mm)	0.84×10^{-3}	1.25

3.4.5 Piezoelectric actuator vs. Electromagnetic actuator

Through the analytical and quantitative studies of the both types of actuators, some interesting facts could be noted. For the sake of comparison, some of the important relationships of both types of actuators are listed in Table 3-5.

Table 3-5 Characteristic equations of the piezoelectric and electromagnetic actuators

Piezoelectric Actuator	Electromagnetic Actuator
$\hat{I}_m = \Phi\hat{\dot{x}}$	$\hat{E}_m = K_e\hat{\dot{x}}$
$\hat{I} = \hat{I}_m + j\omega C_d\hat{U}$	$\hat{U} = \hat{E}_m + (R_a + j\omega L)\hat{I}$
$\hat{F} = \Phi\hat{U}_m$	$\hat{F} = K_f\hat{I}$

From the table, it is shown that the piezoelectric actuator is a voltage source device while the electromagnetic actuator is a current source device. The relationships in electrical and mechanical characteristics are similar to some extent and there exits reciprocality between them.

The quantitative comparison shows that a piezoelectric actuator can generate large force while the attainable driving range is considerably small. In addition, the drive range and the force are also affected by the load conditions. The electromagnetic actuator, on the contrary, generates relatively smaller force but a much larger driving stoke. The force of the electromagnetic actuator is only determined by the excitation current and hence can be easily controlled.

3.5 Actuator for an In-pipe/Endoscopic Microrobot

The scope of the thesis is to develop a suitable actuator for the locomotion of a mobile microrobot that can effectively travel in the narrow tract, such as an in-pipe mobile microrobot or medical endoscopic microrobot. According to the former comparative studies, the electromagnetic actuators can provide moderate force output but very large stroke. Meanwhile, since the electromagnetic actuator is a current source driven device that could be operated at low voltages, they are suitable for electrochemical batteries, wireless power and those biomedical preferred power supplies. Moreover, they are compatible with the microelectronic technology and can be integrated with the

electronic control logics and semiconductor driving devices. Therefore, a PM type electromagnetic actuator will be selected as the actuation source for the locomotion of the microrobot. In addition, because the locomotion of robot is a kind of linear motion, a linear PM actuator would be appropriate for the application. Compared to the rotary machine based mechanisms, the direct linear drive schemes can greatly simplify the drive mechanisms, which is crucial for micro systems.

Based on the comprehensive survey on the actuation techniques for the microrobots, several actuation mechanisms could be employed for the locomotion of in-pipe or endoscopic microrobots. Among these methods, inchworm mechanism is a compact design option that can generate large displacement by accumulating a number of small steps since the single stroke of the microrobot is usually limited by the dimensions of the embedded actuator. In particular, this kind of locomotion scheme is thought to be useful in travelling and conducting tasks in narrow and highly constrained environments [Fukuda 1993b], such as pipes and conduits in industrial plants, or slender vessels and intestines in human body.

Generally, an inchworm mechanism consists of two main components [Zhang 1997]: an actuating module that can deform in the direction of travel and a mechanism that produces friction against the environment. The motion of the robot is realized by repeating a stick-slip or clamp-extend-clamp cycle through a series of actuator actions. One of the commonly used elongation actuator in an inchworm mechanism is piezoelectric actuator. The actuator performs a quick expansion and contraction by energizing and de-energizing the piezoelectric elements. Some of piezoelectric based inchworm actuation mechanisms have been shown in chapter 2. As mentioned in the comparative studies, the piezoelectric actuator has large force capability, but their factional stroke is extremely limited. In addition, a powerful voltage supply is necessary for the operation of such a piezoelectric actuator. The electromagnetic actuators are also employed in many designs. One of the good design examples, which is utilising the stick-slip principle by controlling the electromagnetic force between a solenoid and a

PM material, has been demonstrated in Fig.2-57 of chapter 2.

A frictional mechanism is usually required for the motion of the inchworm robot. Some of the design use electromagnet for the attachment of the robot to the travel surface as shown in Figs.2-11 to 13. However, this type of friction generation is effective only on the ferrite surface. Some of the designs use inclining legs outside the body to produce frictional force for the locomotion such as those shown in Figs.2-36 to 38. Another effective but quite simple scheme is the IDM method which utilises the frictional force and inertial force of the robot body via controlling the expansion and contraction of the actuator. The basic principle of the method has been discussed in chapter 2 with Fig.2-81. The advantage of this frictional mechanism is that it does not require complex mechanical structure and hence is suitable for the micro applications.

Fig.3-17 illustrates the schematic structure of the mobile microrobot proposed in the thesis utilising the IDM principle. It is made up of an extendable tubular main body and a locomotive actuator is installed within the main body. The main body contains two parts: front (main body) and rear unit (movable unit). The stator of the actuator will be attached to the front unit of the robot and the movable component of the actuator is connected to the rear unit to allow the body of the robot longitudinally extend or contract. An elastic bellows is employed as a joint between the front and rear unit and it can function as a spring between the main body and movable unit of the mechanism for

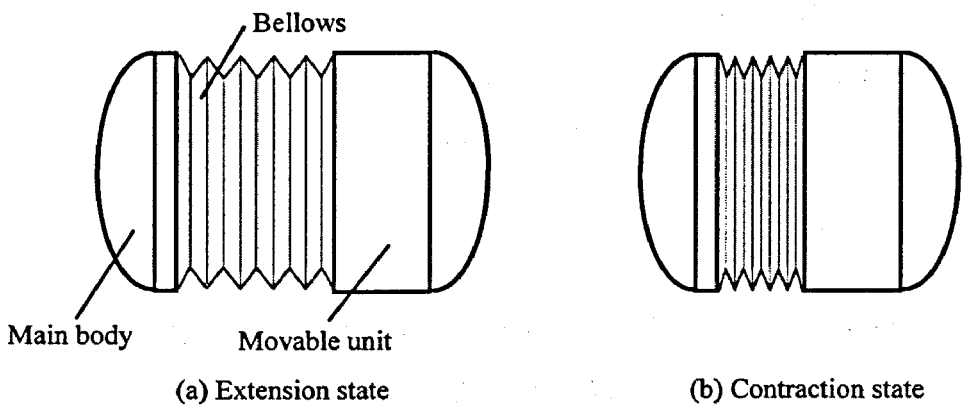

Fig.3-17 Schematic of the proposed micro mobile robot

the restoration of the starting position of the movable unit. In addition, the application of the elastic force can also reduce the power consumption of the actuator. The gross dimension of the microrobot is based on the typical sizes of a medical capsule.

3.6 Conclusion

A comparative study of the actuators operated in piezoelectric and electromagnetic principles is conducted in this chapter. Two important issues concerned mostly in micro applications, the scaling effect and power density, are analysed on both types of actuators. Moreover, the analytical dynamic models of the both kinds of actuator are derived and studied. The results show that both types of actuator can have the similar scaling effects and energy densities. The electromagnetic actuator is a kind of current source device while the piezoelectric actuator is a kind of voltage source device. The relationships in electrical and mechanical characteristics are similar to some extent and there is certain reciprocity between them. More detailed performance study indicates that the piezoelectric actuator has a favorable force capability while the electromagnetic actuator has a larger driving range.

With the consideration of the actuation requirements in the target application of this thesis, a PM type linear electromagnetic actuator will be employed for the locomotion of the proposed microrobot. The selection is based on a set of benefits that an electromagnetic actuator can provide, such as moderate force output with quite large fractional stroke, low voltage operation capability with wireless powered potential, and silicon technology compatibility.

In the following chapters, the design and analyses of the linear electromagnetic actuator for the proposed microrobot will be conducted and presented in detail.

Chapter 4

DESIGN METHODOLOGY AND THE FIRST ATTEMPT – A MOVING-COIL LINEAR ACTUATOR

4.1 Introduction

The scope of this chapter is to present the design methodology for the electromagnetic actuator and its application to the development of linear actuator for the proposed microrobot. Based on the understanding of the basic methods for designing the electromagnetic actuators and the special considerations of linear actuator, a moving-coil linear actuator is proposed as the first attempt for the project. Through magnetic circuit analysis and 3D numerical magnetic field solutions, the electromagnetic force and machine parameters of the linear actuator are predicted. According to the results from the field analysis, the dynamic model of the actuation system is established and used for the performance analysis of the actuation system. The predicted dynamic performances show that the proposed design has limited driving capabilities and further improvements are required. However, the applied design and analysis methods become the key tools for the development of the actuator reported in the thesis.

4.2 Linear Electromagnetic Machines – A Brief Overview

As discussed in chapter 3, a linear electromagnetic machine is chosen as the actuator for the proposed microrobot in the thesis. In order to have a good understanding of the principles and configurations of the linear type electromagnetic actuator, a brief review of the linear electromagnetic machines is conducted in this section.

4.2.1 General concept of linear electromagnetic machines

A linear machine produces motion in a straight line directly, without the use of a crank shaft or any other mechanisms for converting rotary motion to linear motion. The history of linear machines goes back as far as the last decade of the nineteenth century, but the machines were practically forgotten for half a century until Eric Laithwaite published papers about the theory and application of linear machines later in 1950s [Laithwaite 1971]. In spite of these first steps it took still more than 20 years to find a growing interest in machine engineering to understand the advantages of the linear drives.

Although linear machines dispense with the need for ball-screw, gears, belts, etc., which are necessary to obtain linear motion from their rotary counterparts, the latter are still preferred because of the wide range of speed and thrust that can be obtained with the help of gearing at an economic cost. As a result, many linearly moving parts in mechanical systems are driven by a rotary machine with those mechanical rotary-to-linear converters.

However, the rotary-to-linear driving mechanism has some weak points, such as low acceleration performance, backlash, mechanical complexity and a low impact load capacity. While linear machines may present a solution to these problems, they were restricted by high cost and large size compared to their output power [Bang 2003].

Thanks to the development of the PM materials and power electronics, the drawbacks of the linear machines become less serious compared to its attractive performances in those drive applications such as high speed transport, propulsion and machine tools. Moreover, linear machines also play a key role in micro robotic systems when linear motion is required. Compared to the rotary-machine based drives, linear machines show significant advantages in terms of efficiency, thrust control, position accuracy, and system volume [Bianchi 2001]. Particularly, linear machines can greatly simplify the drive mechanisms, and this is crucial for micro systems. By using high magnetic energy product PMs in linear machines, much higher force-to-volume ratios and hence better drive performance can be obtained [Lu 2005].

4.2.2 Types of linear electromagnetic machines

Like the rotary electromagnetic machines, there are basically two types of linear machine, depending upon the mode of excitation: alternating current (AC) and direct current (DC). The two different types of machines have different advantages. For example, AC linear machines can be used for movement over a long distance, whereas DC linear machines can be used, without much auxiliary equipment, for precise movement over a short distance.

4.2.2.1 AC linear machines

Generally, AC linear machines can be subdivided into three main groups: 1) linear induction, b) linear synchronous, and c) linear reluctance machines. These types of machines have been thoroughly investigated during the last sixty years.

Linear induction machines

Linear induction machines (LIMs) are the best known and most frequently used linear machines, since their secondary member (rotor) is, in its simplest form, only a strip of

conductive material which does not require an electrical supply. The principle of operation of the linear induction machine can be best understood by considering a rotary induction machine with a squirrel-cage rotor; as shown in Fig.4-1. If the squirrel-cage rotor of rotary machine is cut along a radial plane and then unrolls it, a flat configuration is obtained (Fig.4-1(c)). This type of linear machine is known as an open-sided or single-sided machine as illustrated in Fig.4-2(a). If another unrolled stator winding is placed on the other side (the open side) of the single-sided machine, a double-sided linear machine is obtained, which is shown in Fig.4-2(b).

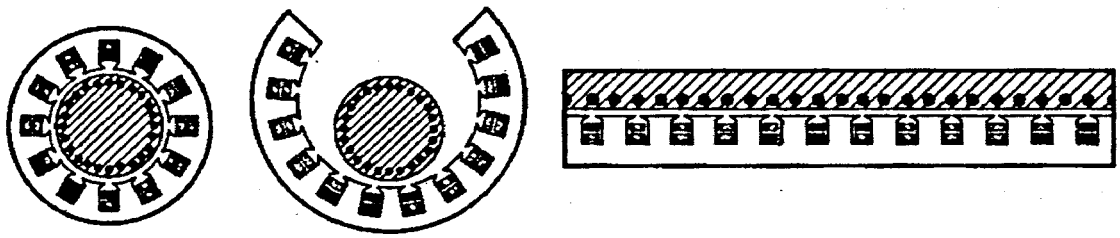

(a) (b) (c)

Fig.4-1 Imaginary process of unrolling a conventional induction machine to obtain a linear induction machine

The LIMs can also be classified into two main groups, short-stator (or short primary) and short-rotor (or short secondary) machines, depending on whether the rotor or stator is extended to the full length of the machine, which are described in Fig.4-2, too.

The LIMs have been developed for three particular applications: (1) oscillating

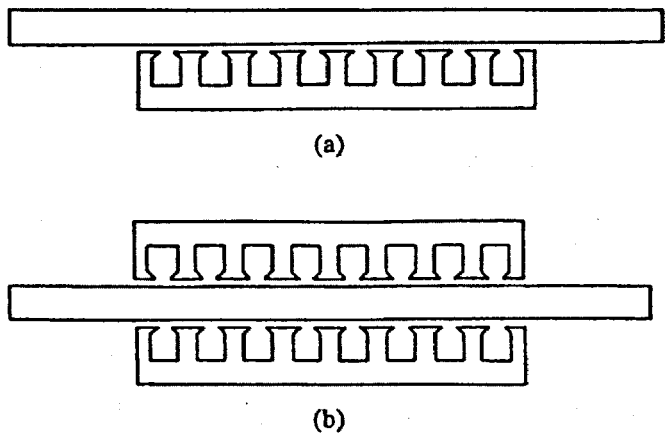

(a)

(b)

Fig.4-2 (a) A single sided machine, and (b) a double sided machine

machines, which can be used in the textile industry; (2) the movement of conductive liquids, and (3) transportation.

Linear synchronous machines

Like the linear induction machines, the linear synchronous machines (LSMs) are similar in principle to its rotary counterparts. The LSM came into prominence in the 1960s as a propulsion device for high-speed ground transportation. As in a conventional synchronous machine, the LSM has poly-phase armature excitation and DC field excitation. The field excitation may be of a conventional type (Fig.4-3), or a superconducting field winding. Although in principle it is irrelevant whether the LSM has a moving armature or a moving field winding, it appears that the latter is more practical.

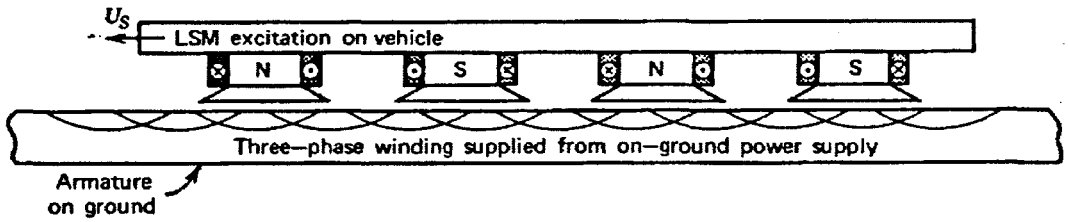

Fig.4-3 A salient-pole linear synchronous machine

Linear reluctance machines

The linear reluctance machine (LRM) is similar to a synchronous machine but does not have any field winding. The stator or primary of the reluctance machine is similar to that of a synchronous machine. However, there are two common types of rotor or secondary configurations: (a) the conventional LRM (Fig.4-4(a)) and the LRM with segmented secondary which is made of blocks of ferromagnetic material, embedded in a nonmagnetic material (Fig.4-4(b)). The thrust produced by the LRM is similar to the torque due to saliency in a rotary salient-pole synchronous machine.

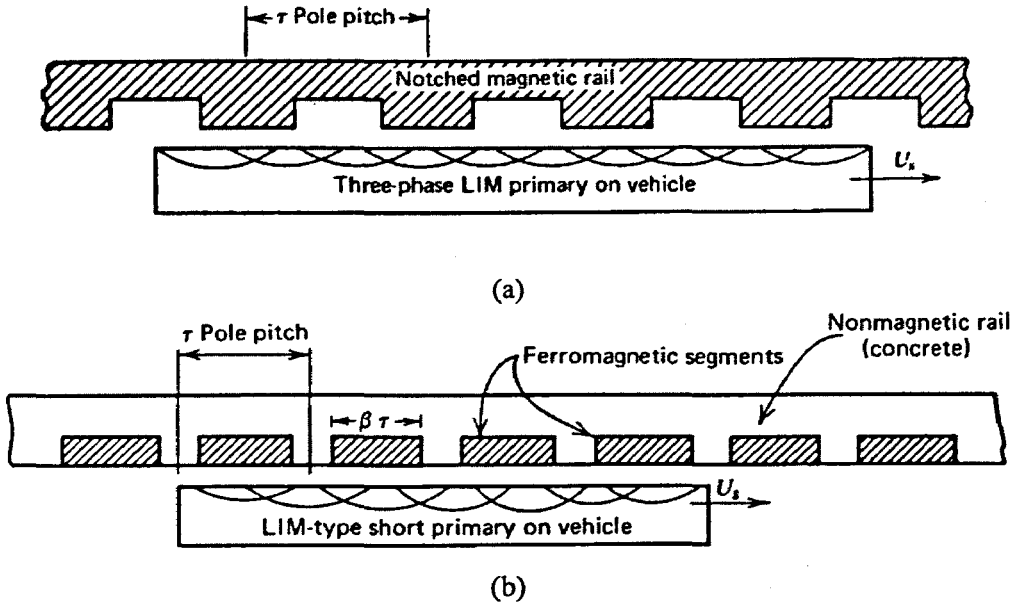

Fig.4-4 Linear reluctance machines

4.2.2.2 DC linear machines

Compared to AC linear machines, DC linear machines have been comparatively neglected in the past but have been greatly developed recently, and they are envisaged more applications in the future.

Generally, DC linear machines are similar to the rotating DC machines since they all have an armature and a field system. In most cases, the armature of the DC linear machine is stationary and the field is the moving part, whereas in some applications, moving armature is preferred. For instance, a voice coil actuator is a special type of DC linear machine with moving armature. The basic principles of those DC linear machines are similar in essence. However, they differ widely in their construction and performance.

Like the conventional rotary DC machines, the DC linear machines can also be divided into two basic forms by their field unit structures. One type is the DC linear machine with field windings and two different field winding structures is used in the design of such linear machines. The first type has a multi-pole-piece field assembly, whereas the

second configuration is based on a cylindrical field unit.

Fig.4-5 shows an example of DC linear machine with multi-pole-piece field unit. A number of mild-steel pole pieces, each of which has a surrounding field winding, are placed around the armature at equal intervals as shown in Fig.4-5(a). The armature is a mild-steel round rod with a surface winding. The flux produced by the field unit completes its path via the end plates, pole shoes, air gap, and armature core, as shown in Fig.4-5(b).

The typical structure of DC linear machine with cylindrical field unit is shown in Fig.4-6. As the entire device looks similar to a segment of tube, this type of DC linear machine is also called tubular linear machine. The armature of the machine, which is supported at each side by a linear bearing to be free to move over a limited displacement in the longitudinal direction, has a single layer surface winding. The direction of the

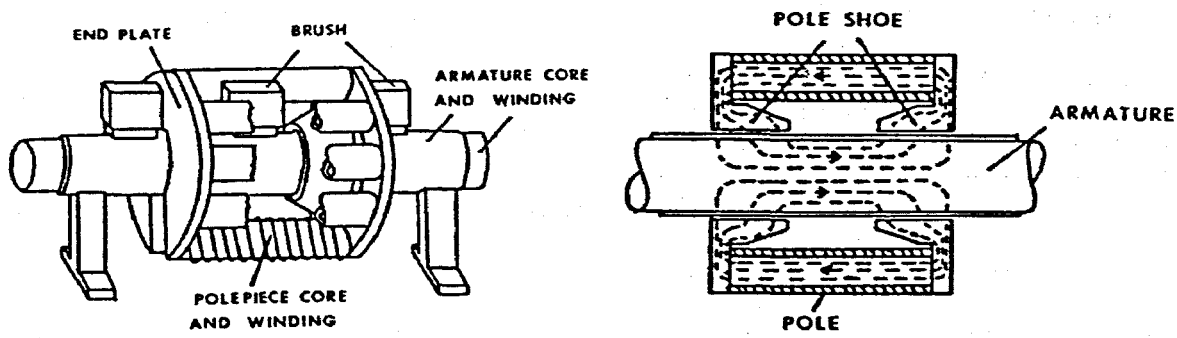

Fig.4-5 A multi-pole-piece DC linear machine
(a) construction, and (b) the flux path

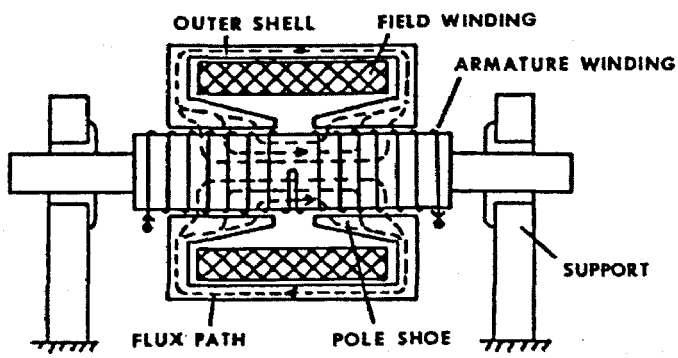

Fig.4-6 A two-pole DC linear machine with cylindrical field unit

winding is reversed at the mid-point so that neither brushes nor a commutator are required. The field winding is embedded in the cylindrical mild-steel outer shell encircling the armature. The main flux completes its path through the armature core via the air gap, pole shoes, end plates and outer shell. Detailed comparative analysis [Nasar 1976] shows that more air gap flux can be obtained under the same input field power when using cylindrical field unit due to its more compact structure.

In general, the DC linear machine with multi-pole-piece field unit is most suitable when there is a wide range of displacement, while the latter may be used for more restricted ranges of displacement.

4.2.3 PM Linear machines

PM machines have been used for linear motion for many years, such as the voice coil actuators used in speakers and hard-disk drive readers, exhibiting high force-to-volume ratios and high positioning speed [Basak 1996]. The use of new powerful rare-earth magnet materials, such as SmCo or NdFeB magnets, greatly improves the performance of electrical machines, including linear machines.

As rotary PM brushless machines are increasingly applied in drive systems, linear PM machines are also designed and driven in brushless mode. According to the structures employed, the PM linear machines can be moving-magnet, moving-armature, or moving-coil machines. Although there are several differences between these types of linear machine, they are all of the same principle and provide essentially the same basic linear motion.

4.2.3.1 Moving-magnet machines

In their simplest form, moving-magnet machines consist of a movable assembly containing magnets and a support member which serves as a magnetic flux return path.

Laminated steel stampings can be used in the stator, with windings inserted as in the rotary type machines. Fig.4-7 shows the schematic diagram of a moving-magnet machine. This type of machine is useful when high linear force levels are required or where mechanical simplicity is desired. As mentioned in AC LIM, the machine shown in the figure is a single-sided type, which has a strong magnetic attraction force between the magnet assembly and the stator. This force is orthogonal to the linear force direction and can cause strong bias loading of the linear bearing system. The problem can be solved by either a double-sided stator design or a tubular (cylindrical linear) structure.

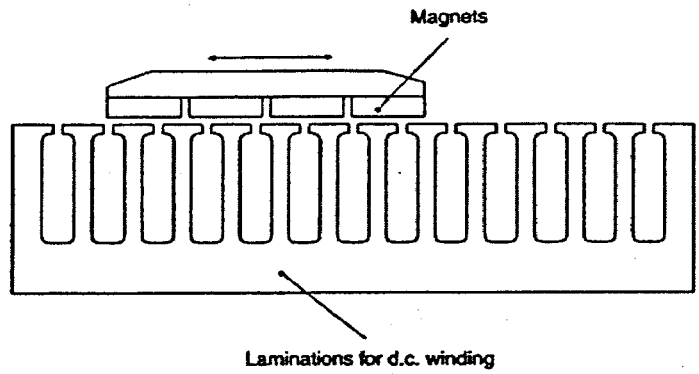

Fig.4-7 A moving-magnet linear machine

4.2.3.2 Moving-armature machines

Moving-armature machines have a moving lamination and winding assembly which is shorter than the stator. The stator consists of long group of magnets mounted on a magnetically permeable surface. Because all the windings interface with the adjacent magnets, the moving-armature machines are more efficient but at the cost of more magnets. In addition, moving-armature machines require flexible cables for the windings, which increase the complexity and difficulty in manufacturing the devices. Fig.4-8 shows the schematic of a moving-armature machine.

4.2.3.3 Moving-coil machines

Moving-coil machines, shown in Fig.4-9, are similar to the moving-armature type,

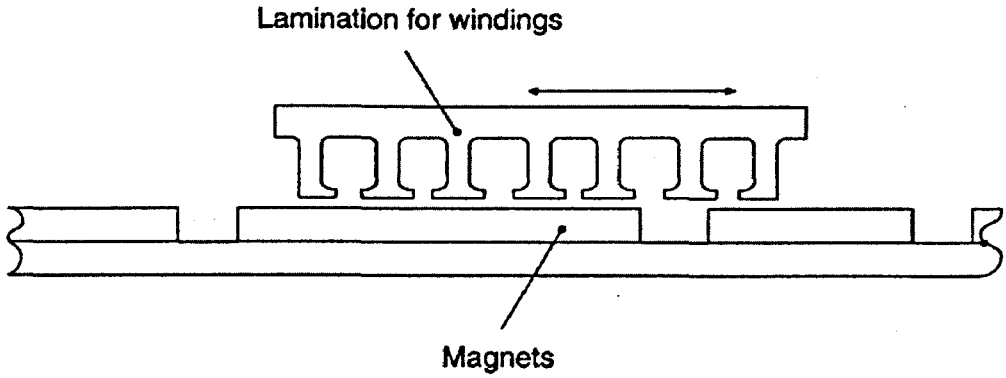

Fig.4-8 A moving-armature linear machine

except that the iron is removed from the moving part and only the conductors and their support structure remain. The magnet structure can be the balance type as shown in the figure or a structure with magnets on one side and a flux return path on the other side. This type of linear machine, with its light-weight armature, has the highest force-to-inertia ratio and allows incremental motion with extremely high acceleration and deceleration rate. However, the thermal resistance between the armature and ambient air is higher than the other models, and therefore, cooling of the coil could be a problem in the moving-coil machines. Moreover, the demand of flexible cables for the armature is also an issue to be concerned.

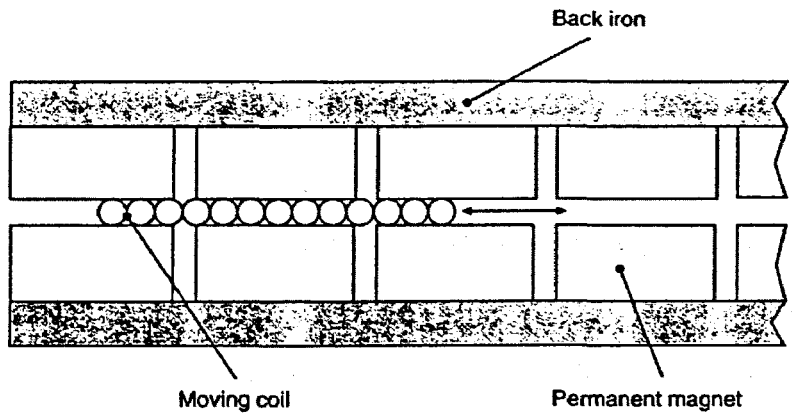

Fig.4-9 A moving-coil linear machine

4.2.3.4 Comparison of PM linear machines

The most prominent features of the three types of PM linear machines mentioned above

are listed in Table 4-1 for comparison. Although these features should not be taken as absolute, the moving-coil and moving-magnet linear machine could still be regraded as the preferred structures in micro applications because of their simpler mechanical structures, and lighter moving mass. Therefore, these two types of PM linear machines would be considered as the candidates for micro robotic applications. As the first attempt of the actuator design, the moving-coil PM linear machine will be analysed in this chapter as this type of actuator has the best force-to-inertia ratio and simplest configuration.

Table 4-1 Comparison of PM linear machines

Linear machine type	Moving-magnet	Moving-armature	Moving-coil
Weight of moving unit	Medium	Heavy	Light
End effects	Present	Present	Absent
Power loss	High	Medium	Low
Moment of inertia	Medium	High	Low
Reluctance clogging	Moderate	Moderate	None
Volume of magnets	Low	Medium	High
Cost	Moderate	Low	High

4.3 General Design Methodology of the Electric Machines

Design is perhaps the most important stage in the development of a new application. For a new electric machine, an appropriate design methodology can significantly reduce the time and cost during the development cycle. By using accurate modelling techniques, developers can effectively predict the performances and parameters of the new design before it becomes a prototype, and also can effectively reduce the number of prototyping iterations. Moreover, various methods can be used to optimise the machine performance for the most effective use of the materials and available space so as to achieve the optimal performance under a minimised cost.

4.3.1 Basic procedure of machine design

The basic design procedure of an electric machine usually consists of several stages. The determination of the machine specifications and constraints can be considered as the first step of the design. By analysing the requirements and conditions of the machine application, a number of issues are decided, such as the type and topology of the machine, power supply (type, voltage, etc), outline dimensions, output torque or force, and the electronic drive scheme if necessary.

Due to the differences of applications, the importance of these issues can be different. For conventional machine design, the rated torque and speed are often taken as the first considerations during the design. In micro applications, however, due to the limited space, the outer dimensions are usually considered as the most important constraint, and the force or torque of the actuator should be optimally designed within the available space.

After the determination of the basic specifications and machine type, the materials and the dimensions of all components of the machine are to be determined according to the specifications and constraints. Then, the machines performances are evaluated. By the aid of analytical and numerical techniques in addition to the designer's expertise, characteristics of the newly designed machine are checked whether or not satisfying the defined specifications, such as the torque/force, speed, current, power, efficiency, temperature rise, and etc. During this stage, the following general steps can be followed [Guo 2003]:

(1) Determination of the machine topology and possible drive scheme for the best system performance
(2) Determination of dimensions of the components of the machine, such as diameter, length of the stator and rotor, the number of poles, the number of turns of the windings, etc.

(3) Mechanical design. Care should be taken to avoid structures that are mechanically too weak or too complicated to fabricate. Especially for the micro applications, much concern should be taken during the mechanical design as micro components require high precision and tolerance demand during the fabrication.

(4) First order calculation of the machine characteristics by analytical approach, empirical formula and data. The results can be used as the preliminary verification of the design.

(5) Refine the electromagnetic design by conducting more accurate parameter calculation and performance prediction. The commonly used numerical solutions such as 2D and 3D finite element method (FEM) can be used for the analysis of the electromagnetic and thermal performance of the machine.

(6) Theoretical machine performance appraisal. If any of the performance indicator, such as the output torque/force, speed, efficiency and temperature rise, etc. does not satisfy the predefined specifications, adjustment to the machine dimensions and electromagnetic design should be performed until a valid design is achieved. Sometime, the original specifications are required to be reconsidered to avoid any impractical demand.

(7) System performance evaluation. This is specially required by the actuator design for a robotic system. Only evaluating the machine performance itself is not enough for validating the entire system. A combined analysis should be conducted by putting the designed machine into the robotic system. To perform the analysis, an electro-mechanical system model is usually required, which can be derived based on the results from the machine performance and parameter analysis. If any of performance of the system is not satisfactory, adjustment of the machine and/or system design is required.

(8) Prototype fabrication and experimental verification. If the experimental performance of the prototype is not as good as expected in the theoretical analysis, the design needs to be adjusted. However, before a modification is made, the causes of the unsatisfied performance should be considered carefully

as some of them may arise from fabrication. This issue is especially importance for the micro application as they usually require a high precision manufacturing and assembling.

The electromagnetic design performed in step (2) and (4) to (6) is the most important work during the electric machine design. The goal of the electromagnetic design is to determine theoretically the major dimensions and parameters base on the machine specifications and constraints. The performance of the design can be evaluated theoretically in this stage and some iteration may be required before a satisfactory design is obtained.

4.3.2 Advanced design and analysis techniques

The rapid development of the computational technology enhanced the techniques of the electric machine design and analysis. A number of powerful numerical computer aided design (CAD) tools are available for the electromagnetic computation and system analysis.

4.3.2.1 Numerical electromagnetic field analysis

Numerical solutions for the electromagnetic field can be retrospected to 1954, when the machine designers used punched cards to solving field distribution of AC machines [Saunders 1954]. Since then, the CAD techniques have been increasingly used in the electric machine design.

Among various numerical methods, the FEM is perhaps the most commonly used method. The FEM was firstly applied to the analysis of electromagnetic fields in electric machine design in early 1970s [Hammons 2000] and it experienced several stages during the last decades of evolution. The 2D techniques were developed for solving the field problems of electric machines in 1980s and 3D FEM solutions were developed and

applied in the machine designs since 1990s. Nowadays, the FEM including 2D and 3D solutions are being used routinely in designing the electric machines and it represents the state-of-the-art in the numerical magnetic field computation relating to electric machines. The long computation time suffered in the past is no longer a problem as the development of modern computers and parallel computing techniques. The advanced non-linear solutions and effective numerical computation techniques provided by the FEM make the prediction of machine characteristics more accurate and efficient. Many powerful software packages are now available such as ANSYS and ANSOFT, etc.

4.3.2.2 Combined field-circuit simulation

The numerical analysis of electromagnetic fields has become a standard in electrical machine design. However, the amount of electronics coupled with electrical machines has greatly increased, such as variable speed drives, servo systems and robotics. The design of electronic control systems and electrical machines were used to be carried out separately, but the demands for increased performance and efficiency at lower cost push the development activities towards a combined design process. In the electronic controlled machine drive systems, both the machine and controller must be individually tailored to work together and thereby guarantee the best possible performance for the application. In such a task, a combined simulation environment, where the magnetic field analysis of the electric machine is coupled with a detailed model of the electronic controller and converter is required for the system analysis [Kanerva 2005].

The electronic controller models are generally composed of electrical circuits and a control system with varying complexity. The electronic circuits usually contain passive circuit elements, such as resistors, inductors and capacitors, and switching components. The control systems, on the other hand, are based on complex estimators and feedback loops, and they are typically implemented by micro processors and digital signal processors. Generally, the simulation of the electronic control system is usually carried out in system simulators like MATLAB/SIMULINK. However, only general and simple

analytical models for the electric machines can be available in these system simulators.

In order to achieve the desired system simulation environment for the electric machine and corresponding electronic control system, the FEM computation should be coupled with the circuit and control simulation. Normally, the numerical solution of the coupled problem can be accomplished directly or indirectly. The difference lies in whether the field and circuit equations are solved simultaneously or sequentially. One of the benefits and applicability of indirect coupling procedures is that, when the time constants in the sub-domains differ significantly from each other, it is advantageous to decouple the domains and utilize different time steps. Another major advantage is that the decoupled models can be constructed separately by the experts in different fields. On the other hand, for the systems with strong physically coupling between magnetic fields and electrical circuits, they can still be analysed indirectly in the case of different time constants without causing a significant error in the analysis.

In this thesis, the performance analysis of the robotic system is carried out by the combination of the FEM software ANSYS and the powerful engineering computational software MATLAB/SIMULINK indirectly. The magnetic behaviour and machine parameters are predicted by the FEM non-linear analysis in advance. Based on the FEM results and the machine theory, the circuit model of the machine is established and combined with the electronic control system. Then, by using the system simulator provided by the MATLAB/SIMULINK environment, the dynamic performance of the entire robotic system can be analysed.

4.4 Design of a Moving-coil Linear Actuator

As the first attempt of the actuator design for the locomotion of the proposed mobile microrobot, the moving-coil PM linear machine is considered and analysed.

4.4.1 Structure, materials and dimensions

The schematic structure of PM moving-coil linear actuator for the proposed mobile microrobot is illustrated in Fig.4-10. It is made up of a cylindrical stator core and a circular moving coil. One cylindrical magnet and three bow-shaped magnets tile are attached on the inner walls of the stator core to build up the magnetic field. At each side of the stator core, a soft magnetic disk is used for the circulation of the magnetic flux. A 3D model of the actuator is also shown in the figure. In order to let the moving coil connect to the power supply and movable unit of the robot, three notches are made on the outer core.

When being installed into the microrobot, the stator core of the actuator is attached to the front unit (main body) of the robot and the moving coil is connected with the rear unit (movable unit) as shown in Fig.4-11. If the elastic force of the bellows cannot

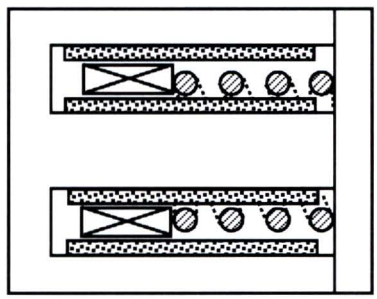

(a) Schematic structure of the actuator

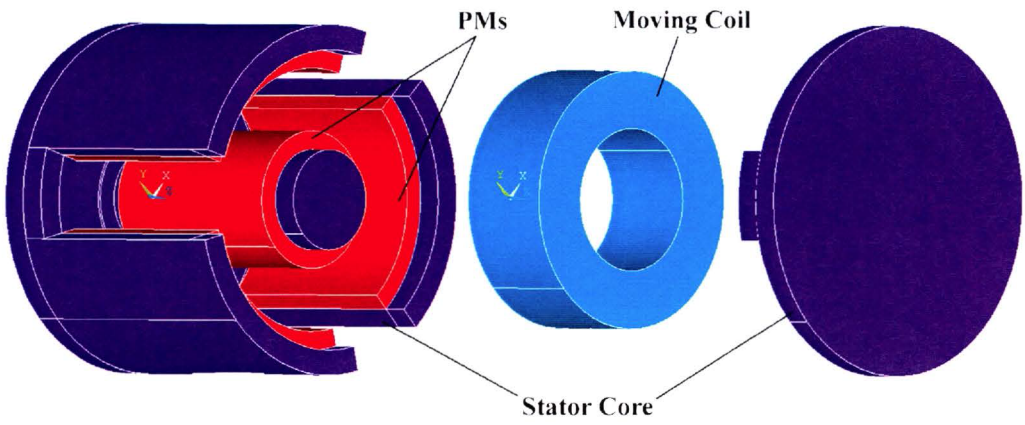

(b) 3D model of the actuator

Fig.4-10 Proposed moving-coil linear actuator

provide enough restoration force for the movable unit, a spring can be used between the moving coil and the stator to help the movable unit return to its original position. When the coil is excited by a current, it will move forward or backward due to the Lorenz force. By applying a proper driving scheme and moving gait activated by the actuator, the robot can move forward continuously.

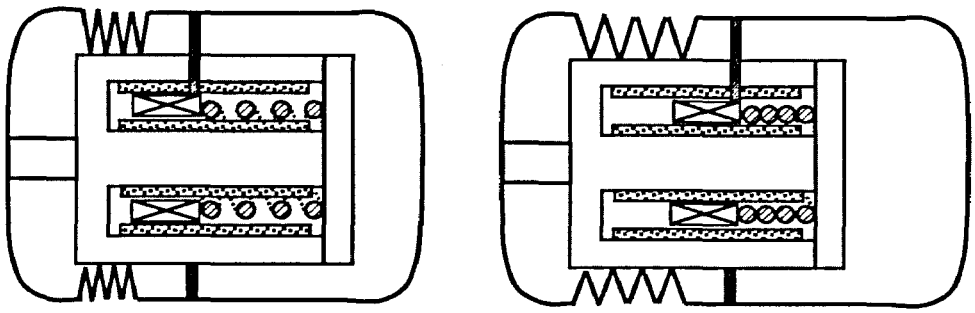

Fig.4-11 Micro moving robot using the moving-coil linear actuator

The soft magnetic material used for the stator core of the actuator is the amorphous alloy 2605SA1 manufactured by METGLAS Inc. The alloy is a thin ribbon made by rapidly quenched based on the transition metals Fe, Co and Ni. It features very high permeability and extremely low core loss. The core loss of the material is typically less than 0.2W/kg at 60Hz/1.4T, which is only 30% of the core loss of grade M-2 electrical steel. Table 4-2 list the main properties of the materials and Fig.4-12 show the typical DC hysterisis loop and average B/H curve of the material [Matglas 2004].

Table 4-2 General properties and characteristics of 2605SA1

Electromagnetic		Physical	
Saturation induction (as cast) (T)	1.56	Thickness (mm)	0.0254
Maximum DC Permeability (as cast) (μ_r)	45000	Density (as cast) (g/cm^3)	7.19
Saturation magnetostriction (ppm)	27	Lamination factor	> 0.79
Electrical resistivity (μΩ-cm)	130	Thermal expansion (ppm/°C)	2 - 7
Curie temperature (°C)	395	Continuous service Temp. (°C)	150

As previously mentioned, the dimensions of the actuator are based on the size of a typical medical capsule or pills, which are usually limited to 10mm in diameter and 15mm in length. By considering the accessories required for the microrobot, such as

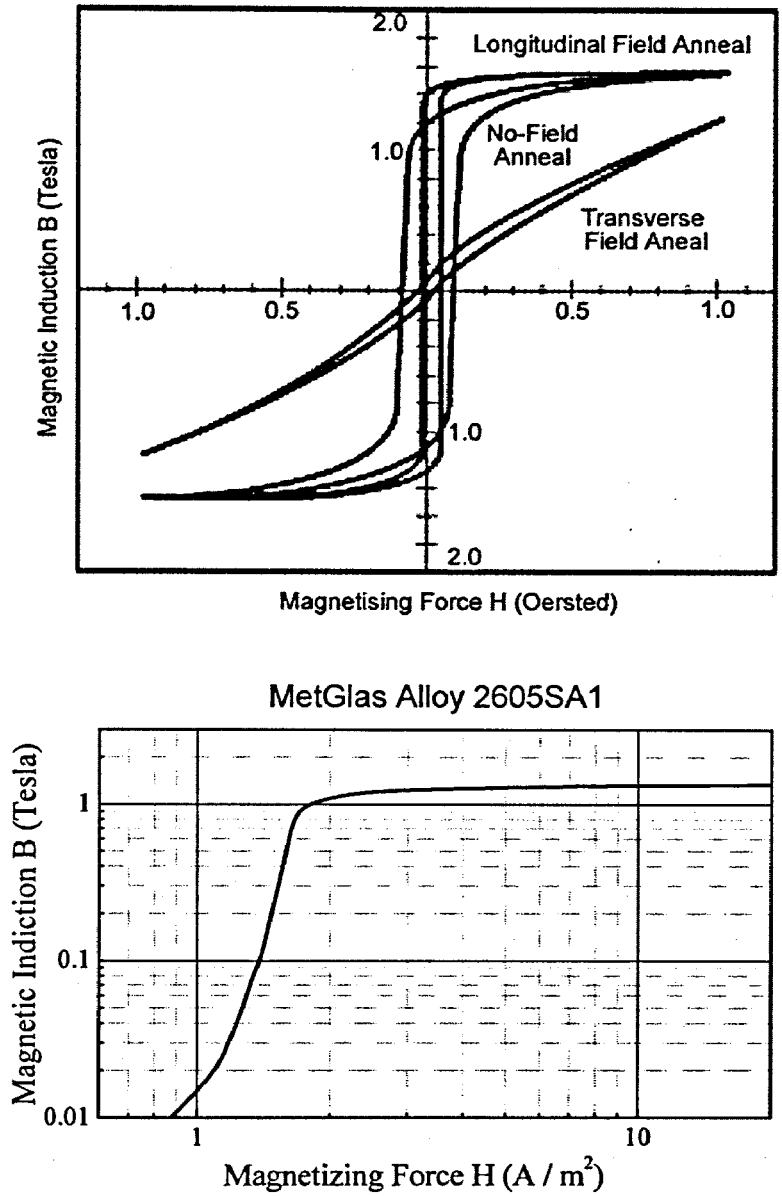

Fig.4-12 Typical DC hysterisis loop and average B/H curve of 2605SA1

mechanical components and joints, control and wiring units, the proposed linear actuator is designed with 7mm in diameter and 6mm in length. The net axial space within the actuator is designed to be 5mm and the length of the magnets are 4mm so that there is 0.5mm gap between the core and magnets to reduce the fringing flux.

In addition, in order to avoid over saturation in the inner core of the stator, the inner radius of the stator core is designed larger than the thickness of the outer core so that a similar cross sectional area can be achieved. The key dimensions of the linear actuator

shown in Fig.4-13 are listed in Table 4-3. Among these dimensions, the thicknesses of the magnets and moving coil are required to be further determined by considering the optimal force output of the actuator.

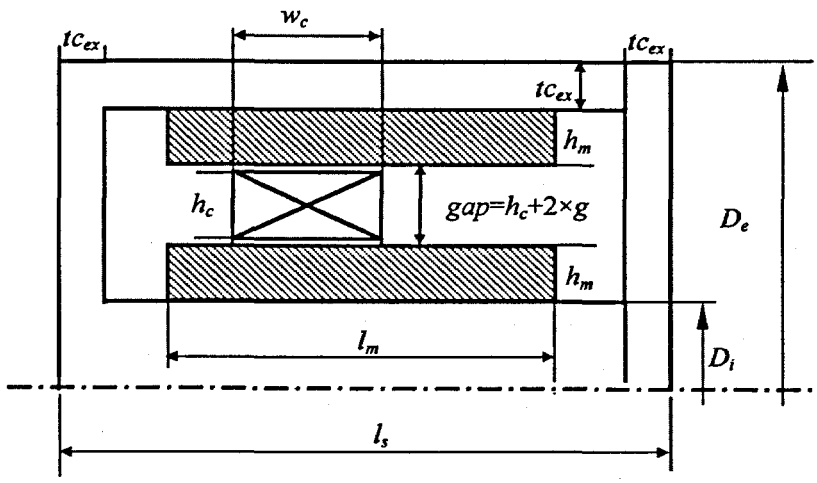

Fig.4-13 Dimensions of the moving-coil linear actuator

Table 4-3 Key dimensions of the moving-coil linear actuator unit: mm

Dimensions	Symbols	Quantities
Total length	l_s	6
Out core diameter	D_e	7
Out core thickness	tc_{ex}	0.5
Inner core diameter	D_i	2
Air gap	g	0.05
PM length	l_m	4
PM thickness	h_m	To be determined
Moving coil width	w_c	2
Moving coil height	h_c	To be determined

4.4.2 Determination of the magnet thickness

As mentioned above, the magnet thickness should be carefully determined by considering the output force of the actuator. According to the analytical performance study of the electromagnetic actuator conducted in chapter 3, the thickness of the magnet should be equal to the total air gap occupied by the moving coil. However, this result is derived by assuming that the magnetic permeability of the stator core is infinite

and the thickness of the core can be neglected. Hence, the thickness of the magnets determined by this method may not be accurate enough in practice.

4.4.2.1 2D FE model of the actuator

In order to find out the proper thickness of the magnets, 2D finite element (FE) analysis is performed. A 2D FE model of the moving-coil linear actuator is built based on the dimensions shown in Table 4-3. Fig.4-14 shows the implemented model in ANSYS.

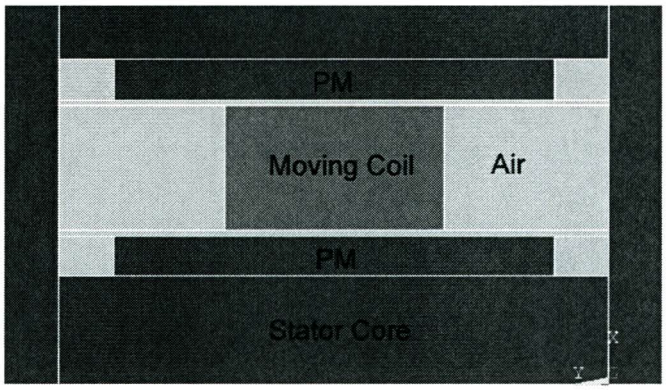

Fig.4-14 2D FE model of the moving-coil linear actuator

During the analysis, the stator core is considered in two cases: linear and non-linear. In linear case, the stator core is set with a relative permeability of 5000, which is the typical value of mild steel. For non-linear analysis, the stator core is set according to the properties of MATGLAS 2605SA1 shown in Fig.4-12.

The magnet used in the model is grade N38 NdFeB material. The typical coercive force and remanence of the magnet are 880kA/m and 1.2T at room temperature. The magnetic permeability of the material is hence very close to that of free air and its relative permeability of the magnets in the actuator is set as 1.

The relative permeability of the moving coil is regarded as the same as air, i.e. μ_r=1. A current density is applied within the moving coil as the excitation current. If a copper wire with nominal diameter 0.1mm is used for the coil, the maximum current of the

copper wire can be set to 6A/mm^2. However, the actual current density within the coil region will be much less than that due to the fill factor when constructing the coil. The fill factor of the coil k_{ff} can be estimated by the following method.

Consider that a round wire is put into a square container as shown in Fig.4-15, the ratio of the effective area to the gross area k_{rs} can be found by

$$k_{rs} = A_{round} / A_{square} = \pi r^2 / 4r^2 = \pi / 4 . \quad (4.1)$$

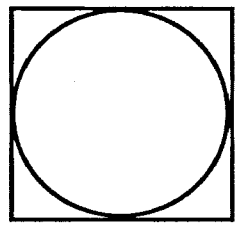

Fig.4-15 Round wire in a square region

In addition, the copper wire contains insulation layer and the outer diameter of the copper wire is larger than the nominal diameter of the wire and the ratio of pure copper cross sectional area to the gross area is usually 0.6 to 0.8 based on the nominal diameter of the wire. For estimation, an average ratio of 0.7 is used. Therefore, the fill factor of the moving coil k_{ff} can be estimated as

$$k_{ff} = 0.7 k_{rs} = 0.55 , \quad (4.2)$$

and the effective current density of the moving coil will be

$$J_s = k_{ff} J . \quad (4.3)$$

The boundary conditions of the 2D FE model for the field analysis are set as follows:

(1) the outer surface of the stator core is supposed to be flux-parallel, namely, no flux leakage out of the stator surface;
(2) the flux along the axis of the centre stator core is set to be flux-parallel due to the axisymmetric structure of the actuator;
(3) the element used for the FE analysis is set with axisymmetric property.

4.4.2.2 The electromagnetic field solutions

It is well known that the magnetic field is governed by the Maxwell's equations [Guru 1998],

$$\nabla \times \vec{H} = \vec{J}, \tag{4.4}$$

$$\nabla \cdot \vec{B} = 0. \tag{4.5}$$

The above field equations are supplemented by the constitutive relation that describes the behaviour of electromagnetic materials. For problems considering saturable material with PMs, the constitutive relation for the magnetic fields is

$$\vec{B} = \mu \vec{H} + \mu_0 \vec{M}, \tag{4.6}$$

where $\vec{M}$ is the remnant intrinsic magnetisation vector of the PM material. By introducing (4.6) to (4.4), one can obtain

$$\nabla \times (\frac{1}{\mu}(\vec{B} - \mu_0 \vec{M})) = \vec{J}. \tag{4.7}$$

Because the magnetic flux density is always continuous, a vector whose divergence is zero can be expressed in terms of the curl of another vector quantity as

$$\vec{B} = \nabla \times \vec{A}, \tag{4.8}$$

where $\vec{A}$ is the *magnetic vector potential*. Quite often, it is expedient to work with the magnetic vector potential to obtain the flux density in the electromagnetic field solutions. By using the magnetic vector potential, (4.7) can be further expressed as

$$\nabla \times (\frac{1}{\mu}(\nabla \times \vec{A} - \mu_0 \vec{M})) = \vec{J}. \tag{4.9}$$

Defining the Laplacian operator of a vector field as

$$\nabla^2 \vec{A} = \nabla(\nabla \cdot \vec{A}) - \nabla \times (\nabla \times \vec{A}), \tag{4.10}$$

one can obtain

$$\nabla(\nabla \cdot \vec{A}) - \nabla^2 \vec{A} = \mu \vec{J} + \mu_0 \vec{M}. \tag{4.11}$$

Because $\Delta \cdot \vec{A} = 0$, the above equation can be simplified as

$$\nabla^2 \vec{A} = -(\mu \vec{J} + \mu_0 \vec{M}) \tag{4.12}$$

Equation (4.12) is the formulation that can be used for the solutions of 2D and 3D static magnetic fields. Moreover, in 3D field solutions, a scalar potential $\mathscr{F}$ can be introduced to reduce the number of unknown variables. In a source-free region, i.e. a region void of current, the scalar potential is defined as

$$\vec{H} = -\nabla \mathscr{F}, \tag{4.13}$$

and (4.4) can be rewritten as

$$\nabla^2 \mathscr{F} = 0. \tag{4.14}$$

Equation (4.14) is the Laplace's equation for the magnetic scalar potential and can be used to solve the problems in 3D current-free magnetic fields.

4.4.2.3 Linear 2D FE magnetic field analysis

A linear 2D FE analysis is firstly conducted by setting the stator core with linear magnetic property as mentioned in section 4.4.2.1. Because the magnetic field generated by the current in the moving coil is considerably small compared to that produced by the magnets ($I_m >> N_t I$), the position of the moving coil will not affect the magnetic field very much within the actuator. Hence, the position of moving coil will always be put in the middle of the actuator during the analysis. Fig.4-16 shows the flux contour and the flux density distribution obtained from the linear analysis.

Based on the results from the FE analysis, the flux density within the moving coil can be readily obtained by averaging the flux densities of the elements in the moving coil region. Since the actuation force of the actuator is only related to the radial component of the flux density, only the radial component will be considered during the force calculation. Once the flux density within the coil is known, the electromagnetic force acting on the moving coil can be found by

$$F_{em} = B_{gr} J_s A_c l_c, \tag{4.15}$$

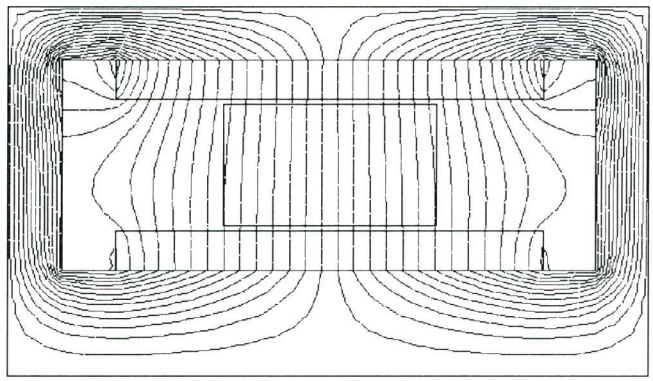

(a)

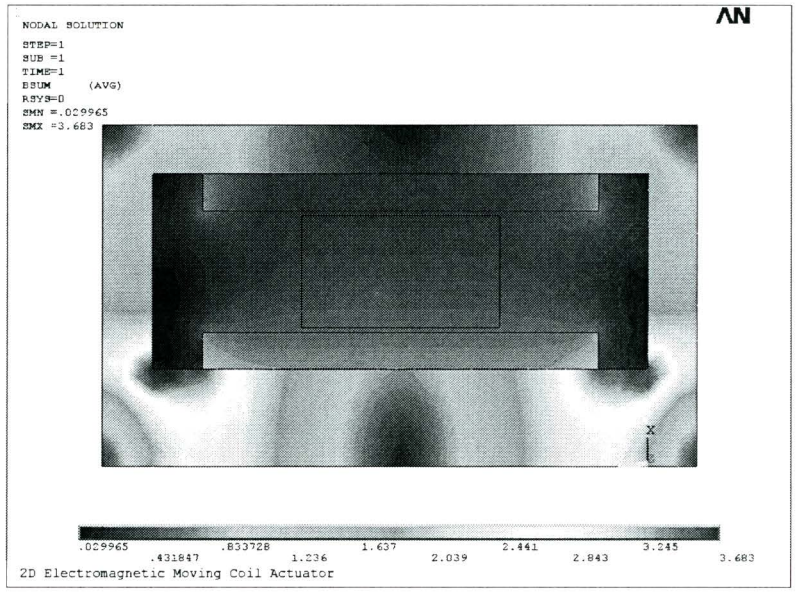

(b)

Fig.4-16 Linear 2D FE analysis results (a) flux contour, (b) flux density distribution

where B_{gr} is the radial component of the flux density in the coil, A_c and l_c are the cross sectional area and mean circumference of the coil. Table 4-4 shows results of the radial flux densities within moving coil and the generated forces under the preset current condition when different ratios of the thickness of magnets to the total air gap $2h_m/gap$ are applied. The results shown with bold font in the table are the optimal values.

Table 4-4 Radial flux densities within the moving coil and the generated forces in linear case

$2h_m/gap$	Radial flux density in moving coil B_{gr} (T)	Electromagnetic force F_{em} (N)
3/5	0.38	0.038
1	**0.53**	**0.041**
5/3	0.66	0.037

It can be seen that in linear case, the maximum force output of a moving-coil actuator can be achieved by designing the thickness of magnets equal to that of the moving coil. Although a higher flux density can be obtained by increase the thickness of magnets, the reduction of current in the coil will cause the decrease of the force. This agrees with the result derived from the analytical analysis in chapter 3.

However, it is shown that, without considering the saturation effect, the highest flux density in the stator core will be over 3T and this is not possible for most of the magnetic materials. Therefore, non-linear property and saturation effect must be taken into account during the analysis and the thickness of the magnets should be re-evaluated.

4.4.2.4 Non-linear 2D FE magnetic field analysis

During the non-linear FE analysis of the actuator, the properties of Matglas 2605SA1 is applied to the stator core of the FE model. With the non-linear characteristics of the materials, the maximum flux density of the core will be restricted to its saturated value. Fig.4-17 show the flux density distribution obtained from the non-linear analysis.

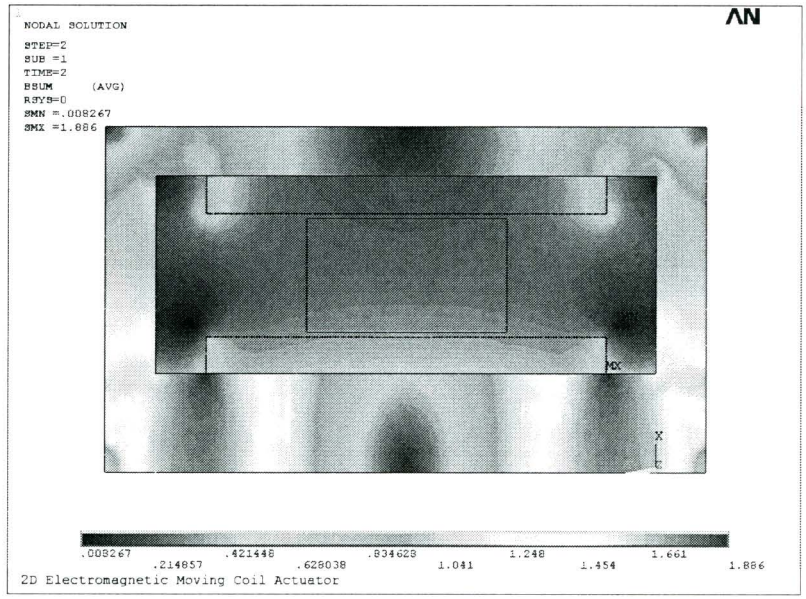

Fig.4-17 Flux density distribution obtained from non-linear 2D FE analysis

Table 4-5 lists the results of the radial flux densities and the corresponding forces under different ratios of the thickness of magnets to the total air gap under non-linear condition. It can be seen that the attainable flux density in the moving coil is much less than that in linear case due to the saturation of the stator core, and the output force of the actuator deceases as well. In this case, application of the thickness of magnets and coil obtained by linear analysis cannot achieve the maximum force and the proper optimal ratio of $2h_m/gap$ becomes 3/5.

Table 4-5 Radial flux densities within the moving coil and the generated forces in non-linear case

$2h_m/gap$	Radial flux density in moving coil B_{gr} (T)	Electromagnetic force F_{em} (N)
1/3	0.21	0.026
3/5	**0.28**	**0.027**
1	0.33	0.025
5/3	0.38	0.021

Consequently, the final selection of the thickness of the magnets h_m is 0.375mm and therefore, the height of the coil h_c will be 1.15mm.

4.4.3 3D magnetic field analysis of the actuator

Because there are three notches on the outer surface of the stator core, the entire magnetic system of the moving-coil actuator is not a truly axisymmetric structure. The 2D axisymmetric model cannot accurately reproduce the reality of the actuator. Therefore, 3D FE analysis should be employed for the accurate performance prediction of the actuator. The 3D FE model built in the ANSYS environment is shown in Fig.4-18. In the model, the thickness of the magnets and moving coil is set based on the results obtained from the 2D non-linear analysis.

The solution used for the 3D magnetic field analysis is the non-linear magnetic scalar potential method. It is one of the two nodal-based methods for 3D magnetic field analyses which the ANSYS supports and it is recommended for most 3D static analysis

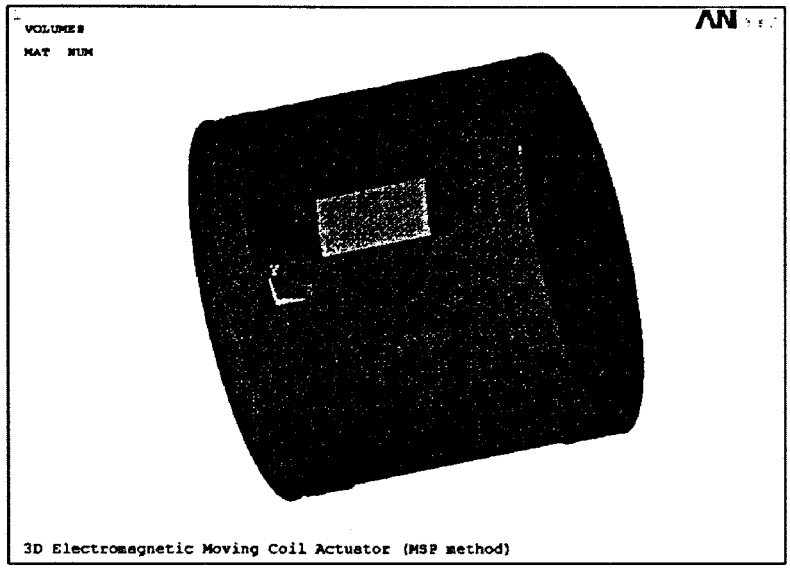

Fig.4-18 3D model of the actuator for FE analysis

applications. In the scalar potential approach, current sources can be modelled as primitives rather than elements. Hence, the current sources do not need to be part of the finite element mesh and it is easier and quicker to solve magnetic fields for the numerical solution.

By setting the boundary condition as parallel on the outside surface of the stator core, the 3D magnetic field of the designed actuator is solved and Fig.4-19 plots the flux density vectors in the stator core and moving coil. The magnitude of the flux densities is shown by colour and proportional to the line lengths.

Due to the notches on the outer surface of the stator core, the flux densities within the moving coil are deceased near these positions and the produced electromagnetic force is affected. Based on the flux densities obtained from the 3D non-linear FE analysis, when the moving coil is in the middle of the actuator, the average radial flux density in the moving coil is found to be 0.25T and the electromagnetic force of the actuator is 0.024N, which is 11% less than those obtained by the 2D FE analysis due to the notches on the stator core. The calculated radial flux densities B_{gr} and forces of the actuator when the moving coil is at different positions within the actuator are plotted in Fig.4-20 and 21, respectively. It can be seen that the flux and force decease when the moving coil is close

to the ends of the actuator due to the fringing effect.

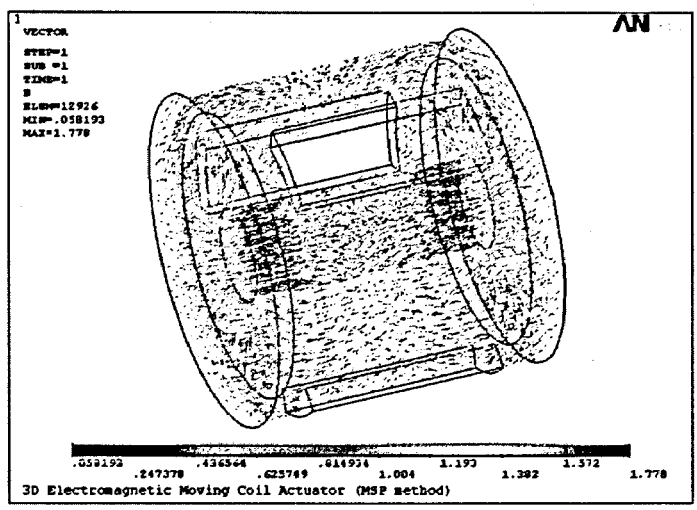

(a) The flux density vectors in the stator core

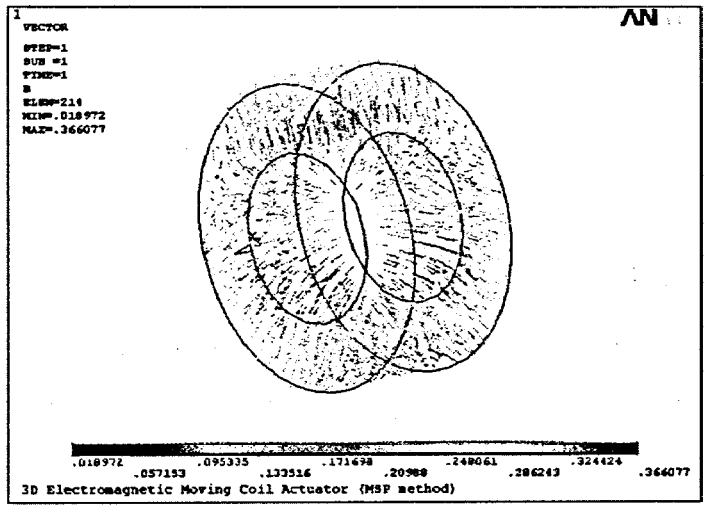

(b) The flux density vectors in the moving coil

Fig.4-19 3D flux density vectors of the moving-coil linear actuator

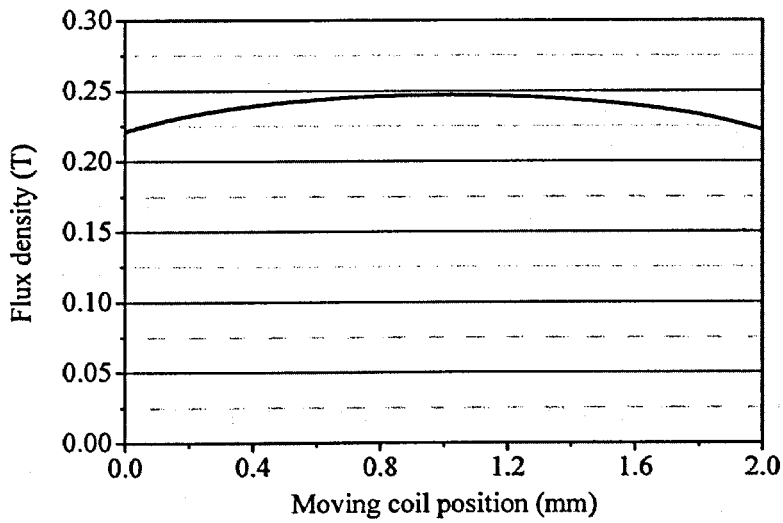

Fig.4-20 Radial flux densities B_{gr} within the moving coil

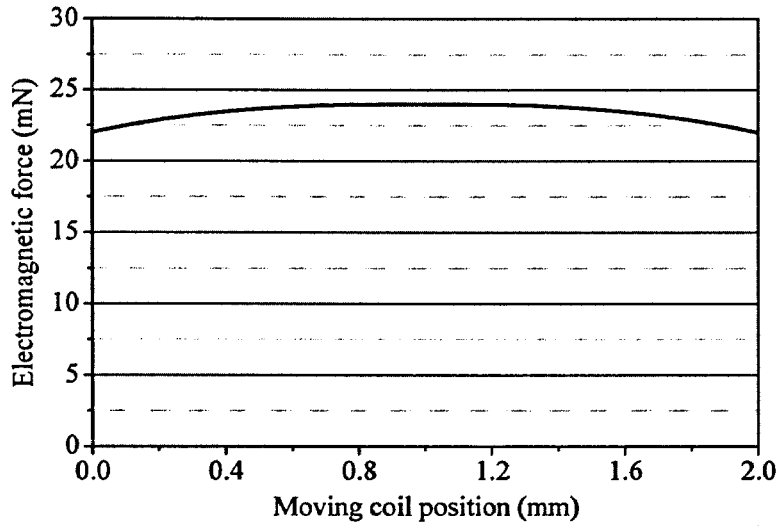

Fig.4-21 Electromagnetic force of the moving-coil linear actuator

4.5 Calculation of Machine Parameters

The machine parameters, including winding resistances and inductances, are important for the system modelling, performance simulation and controller design. Therefore, the resistance and self-inductance of the moving coil of the actuator are required to be calculated.

4.5.1 Calculation of coil resistance

As mentioned in section 4.4.2.1, the moving coil is made up of enamelled copper wire with nominal diameter of 0.1mm. According to the IEC standard No. 60317, the 0.1mm copper wire has a resistance of 2.18 Ω per metre at 20°C[1]. Hence, the resistance of the coil can be estimated by

$$R_a = 2.18 N_t l_c, \tag{4.16}$$

where N_t is the number of turns of the coil. According to the cross sectional area of the

[1] For simplicity, only the resistance under room temperature will be considered in this thesis. Because of low resistance of the coil, change of the resistance due to temperature rise will not lead to much error during the analysis.

moving coil, the number of turns of the moving coil N_t can be 144. The mean circumference of the moving coil l_c is 12.57mm. As a result, the resistance of the moving coil is calculated as 4.95Ω at 20°C. Moreover, according the number of turns of the coil, the rated current for achieving the desired current density is found as

$$I_{rated} = J_s \times A_c / N_t = 54\text{mA}.$$

4.5.2 Calculation of coil inductance

Normally, there are two ways to work out the coil inductance L_a via magnetic field analysis. One of the methods is based on the definition of the inductance, $L = N_t\phi / I$. By this method, the flux linked to the coil that generated by the corresponding current should be found and this can be achieved by $\phi = \int_{A_{cl}} \vec{B} \cdot d\vec{s}$, where $\vec{B}$ is the flux density vector passing through the enclosed area of the coil A_{cl}. For the structure of the proposed moving-coil actuator, only the self inductance of the coil will be considered and the flux linkage of the moving coil can be found by defining the enclosed area in the middle of the coil, as shown in Fig.4-22.

The magnetic field generated by the current of the moving coil can be solved by the 3D magnetic field analysis. During the inductance calculation, the flux generated by the magnets should be excluded and this can be achieved by "switching off" the magnets

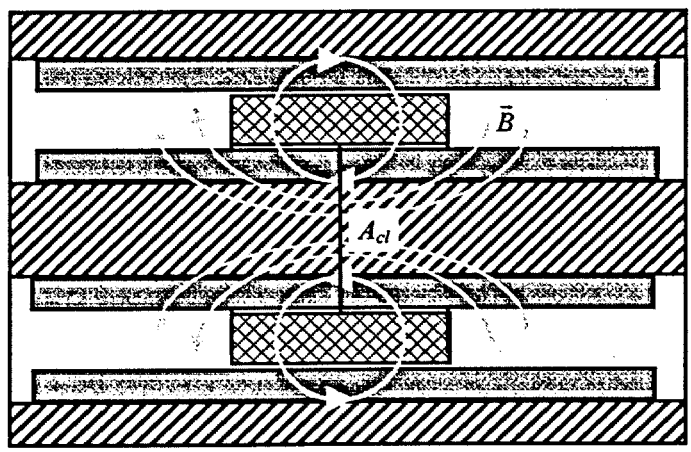

Fig.4-22 Flux linkage of the moving coil generated by the current in the coil

during the computation. However, the saturation of the stator core must be considered when analysing the magnetic field solely produced by the coil current since this is the operational condition of the magnetic system of the actuator. Otherwise, the obtained inductance will be inaccurate. To do this, the average permeability of the stator core under the operational condition set by the PMs is worked out firstly by performing the static field analysis incorporating the magnets and the acquired magnetic permeability of the stator core is then used as the operational permeability of the stator core during the inductance calculation.

The method can be realised by two steps: (1) Obtaining the average operational permeability of the stator core via the non-linear magnetic field solution with magnets; (2) Performing the linear magnetic field analysis by using the average operational permeability of the stator core and excluding the magnets. The linear method can be used for the inductance calculation because the magnetic field generated by the coil current is considerably small that the stator core can be regarded as a linear material near the operational point. By this method, the flux linkage of the coil that generated by the coil current under the operational condition can be worked out.

Fig.4-23 plots the flux density vector generated by the current in the moving coil by utilising the method described above. After the flux density distribution is obtained, the flux linkage of the moving coil can be readily obtained by $\phi = \int_{A_d} \vec{B} \cdot d\vec{s}$. For example, when the moving coil is at the middle of the actuator, the flux linkage is found as 2.3×10^{-8} Wb when the coil current is 54mA, the self-inductance can be calculated by using $L = N_t\phi/I$ and the result is 0.061mH.

An alternative method is based on the magnetic co-energy, $W'_M = LI^2/2$. The magnetic co-energy of the model can be worked out by the embedded function in ANSYS so that the inductance can be found by $L = 2W'_M/I^2$. Same procedure as used in the flux method could be followed to eliminate the effects of the PMs, and the co-energy generated by

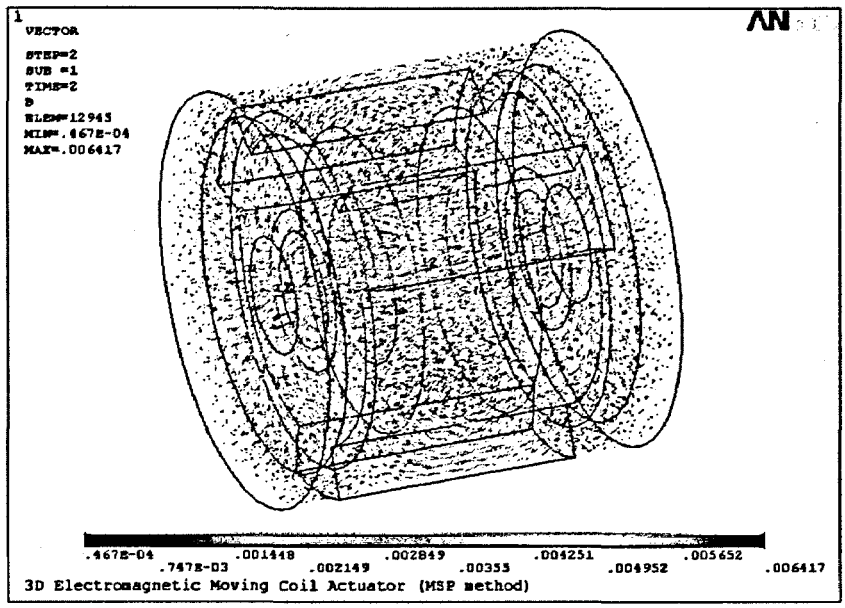

Fig.4-23 Flux density vectors generated by the coil current

the current in moving coil can be calculated. For instance, the magnetic co-energy when the moving coil is in the middle of the actuator is found to be 8.4×10^{-8} J. As a result, the self inductance of the moving coil at the position can be calculated as

$$L_a = 2W_M^{'} / I^2 = 0.058 \text{ mH}.$$

Fig.4-24 shows the calculated inductances by the both methods when the moving coil is at different positions. It can be seen that the results obtained by the two methods are very close to each other. The fringing effect can be seen from the variation of the inductances. Because the caps of the actuator are made of soft magnetic material, the

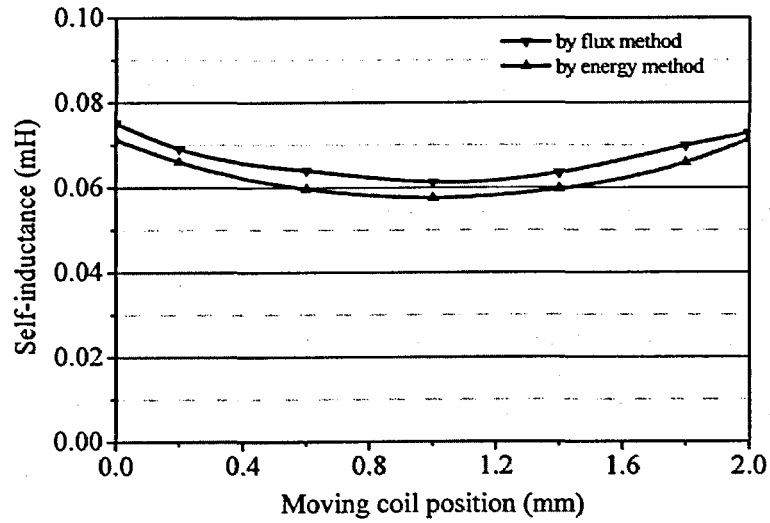

Fig.4-24 Calculated inductances under different moving coil positions

reluctances will reduce when the moving coil is closed to the sides of the actuator. Hence the resultant inductances increase.

Both methods can be used for the calculation of the coil inductance in the electromagnetic system. However, the energy method might be more preferable because the enclosed area required for the flux calculation is difficult to be found in many cases.

4.6 System Modelling and Performance Analysis

Dynamic analysis is an important step in designing an actuation system. The analysis can provide elementary performances of the system including the forces, velocities and displacements. The results from the dynamic analysis can be used for examination of the effectiveness of the actuator design.

Generally, a dynamic analysis of an actuation system can be realised through the solutions of a set of differential and output equations that can adequately describe the electrical and mechanical behaviour of the system. These equations form the dynamic model of the system. Together with the magnetic field analysis, the coupled field-circuit analysis/simulation, as mentioned in section 4.3.2.2, can be implemented.

4.6.1 Dynamic modelling of the moving-coil linear actuator

The circuit model of the moving-coil linear actuator is quite simple. According to the magnetic field analysis conducted in section 4.5, the magnetic flux density and the inductance of the moving coil can be regarded as constants as they do not change much throughout the motion range of the moving coil. Accordingly, the electrical equation of the actuator can be expressed as

$$u = R_a i + L_a \frac{di}{dt} + e_m, \tag{4.17}$$

where u and i are the voltage and current applied to the moving coil, and e_m is the induced back EMF due to the magnetic field of PMs. The induced back EMF can be obtained by the following equation

$$e_m = B_{gr} N_t l_c v = K_e v, \tag{4.18}$$

where v is the velocity of the moving coil with respect to the stator and $K_e = B_{gr} N_t l_c$ the back EMF coefficient. The output equation of the actuator is the force equation, which is

$$F_{em} = B_{gr} N_t l_c i = K_f i, \tag{4.19}$$

where K_f is the force coefficient and $K_f = B_{gr} N_t l_c$.

Equations (4.17), (4.18), and (4.19) build up the dynamic model of the moving-coil actuator and can be used for the dynamic analysis of the actuator. The constants in the model can be readily obtained from the magnetic field analysis performed in the previous section.

4.6.2 Kinetic modelling of the robotic system

Only the dynamic model of the actuator is not enough for the analysis of the actuation performance of the robotic system. A kinetic model of the system must be derived before a system analysis can be carried out.

According to the proposed structure and locomotion principle, the mechanical system of the microrobot can be described by the model illustrated in Fig.4-25. In the figure, x_s and x_a are the displacements of the main body and the movable unit. l_{sa} is the initial distance between the main body and the movable unit. An equivalent spring is used to represent the elastic force produced by the elastic bellows and the spring installed inside of the actuator if necessary.

The forces acting on each component are analysed, as shown in Fig.4-26. m_s, m_a, v_s and

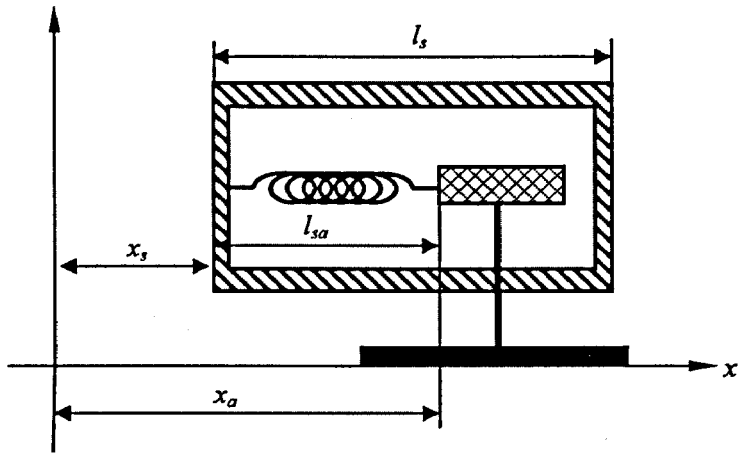

Fig.4-25 Mechanical model of the proposed microrobot

v_a are the masses and velocities of the main body and movable unit, respectively. F_{em} is the electromagnetic force produced by the actuator, F_{sp} the elastic force of the spring, F_{ma} the frictional force between the movable unit and main body, and F_{mg} the frictional force between the movable unit and the travelling surface.

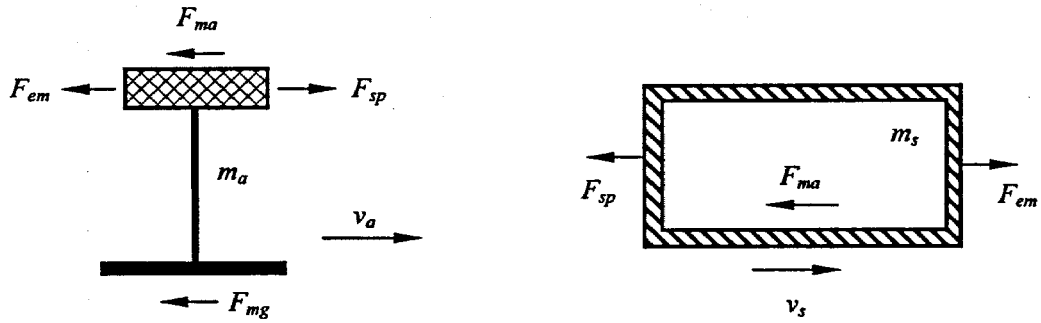

Movable unit assembly Main body

Fig.4-26 Forces in the system

According to the forces shown in the figure, the kinetic equations of the movable unit and main body can be derived based on the Newton's laws as follows:

$$F_{sp} - F_{em} - F_{ma}sign(v_a - v_s) - F_{mg}sign(v_a) = m_a \frac{dv_a}{dt}, \qquad (4.20)$$

$$F_{em} - F_{sp} - F_{ma}sign(v_s - v_a) = m_s \frac{dv_s}{dt}. \qquad (4.21)$$

The elastic force F_{sp} can be found according to Hooke's law by knowing the elastic constant K_{sp} of the equivalent spring as

$$F_{sp} = K_{sp}\Delta l_{sp}, \tag{4.22}$$

where Δl_{sp} is the strain of the spring and can be obtained by

$$\Delta l_{sp} = x_s + l_{sa} - x_a. \tag{4.23}$$

4.6.3 Dynamic model of the microrobot

By combining the dynamic model of the actuator and the kinetic model of the mechanical system of the robot, the dynamic model of the whole robotic system can be achieved. The derived dynamic model of the robot, which is expressed in the form of a set of differential and output equations, is as the following,

a. Differential equations

$$\begin{cases} \dfrac{di}{dt} = \dfrac{1}{L_a}(u - R_a i - e_m) \\ \dfrac{dv_a}{dt} = \dfrac{1}{m_a}\left(F_{sp} - F_{em} - F_{ma}sign(v_a - v_s) - F_{mg}sign(v_a)\right) \\ \dfrac{dv_s}{dt} = \dfrac{1}{m_s}\left(F_{em} - F_{sp} - F_{ma}sign(v_s - v_a)\right) \\ \dfrac{dx_a}{dt} = v_a \\ \dfrac{dx_s}{dt} = v_s \end{cases} \tag{4.24}$$

b. Output equations

$$\begin{cases} e_m = K_e(v_a - v_s) \\ F_{em} = K_f i \\ F_{sp} = K_{sp}\left(x_s + l_{sa} - x_a\right) \end{cases} \tag{4.25}$$

4.6.4 Locomotion control of the microrobot

According to the operational principle of the moving-coil linear actuator, the locomotion control of the microrobot is determined by the input voltage u. Because the inductance of the moving coil is very small, the drive force of the actuator is chiefly

proportional to the input voltage. For the proposed microrobot, the IDM method, which is adopted in many piezoelectric actuator based microrobots, is applied. The basic principle of IDM is to utilize the difference of the inertia of the different parts of the robot. Consider a microrobot moving on a plane surface as shown in Fig.4-11, the movable unit is designed with less weight than that of the main body as it contains the stator core of the actuator and other working components. During the locomotion, a slow expansion of the robot is firstly activated by the linear actuator and the main body of the robot is pushed forward. Then, a rapid contraction is performed by the actuator and movable unit will move ahead against the friction. The main body of the robot, however, will just move slightly due to its large inertia. Hence, a net displacement of the robot can be achieved. Fig.4-27 illustrates the locomotive principle. By repeating the above actuation cycle, continuous movement of the robot can be accomplished. The suitable excitation voltage used for the IDM is shown in Fig.4-28.

4.6.5 Locomotive performance analysis

To examine the effectiveness of the proposed drive control method, a performance simulation is conducted based on the derived dynamic model of the robotic system. The simulation is implemented in the MATLAB environment and the model of the system is described by m scripts provided by the MATLAB.

4.6.5.1 Masses of the microrobot

Before the simulation can be performed, the masses of the components of the microrobot should be determined first. The mass of the moving coil can be estimated by knowing the volume and density of the coil. According to the IEC-60317, the 0.1mm enamelled copper wire weights 7.5×10^{-5} kg per metre. Based on the dimensions of the actuator, the mass of the moving coil is calculated as 0.15g. Considering other mechanical parts used for the movable unit, the mass of the movable unit is estimated as 0.4g. The total volume of the stator core is $105mm^3$ according to its dimensions.

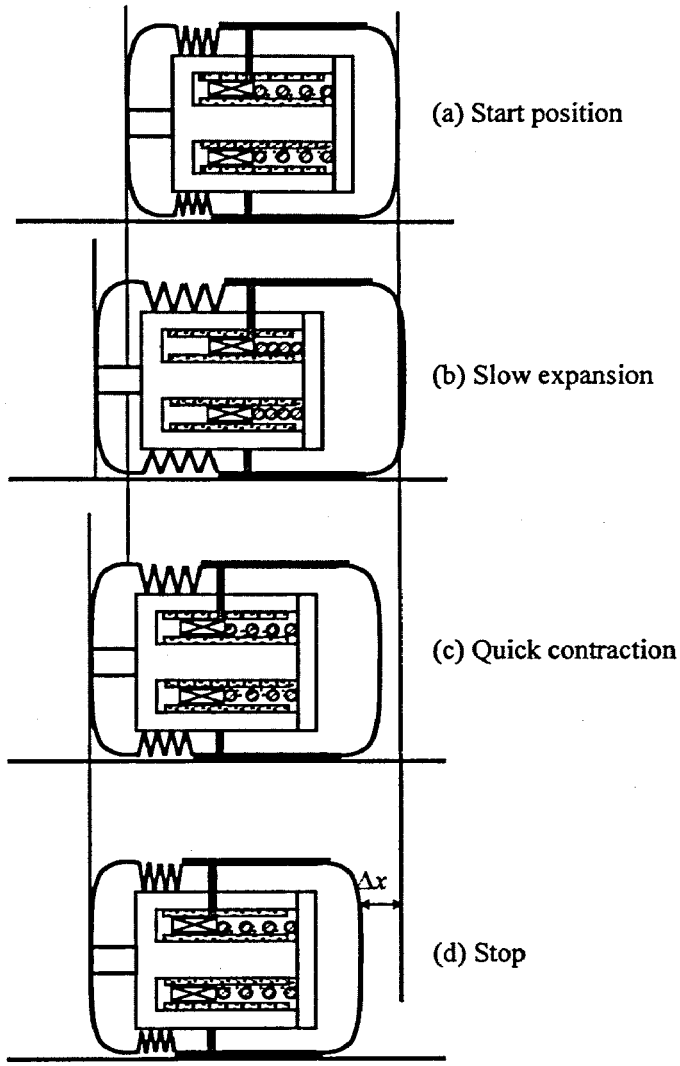

Fig.4-27 Locomotion principle of the microrobot

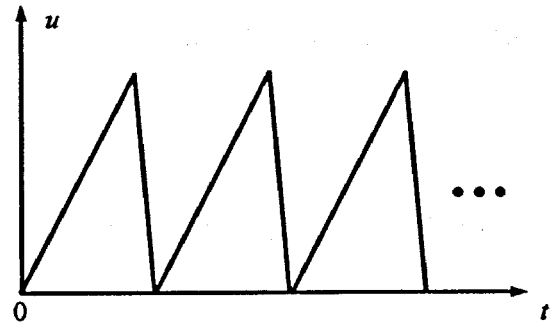

Fig.4-28 Excitation voltage for the actuator

Therefore, the mass of the stator core can be found as 0.76g. In order to meet the requirement of the IDM principle, the main body of the robot is designed to be 7g by including the mechanical components, control units and power supply.

4.6.5.2 Elastic constant of the equivalent spring

The elastic constant of the equivalent spring is an important parameter in the mechanical system of the robot. The selection of the elastic constant will greatly influence the dynamic behaviour of the system.

According to the structure of the moving-coil actuator, the moving coil can have a maximum 2mm moving range within the actuator. By taking into account the minimum length of the elastic bellows or the internal spring, the stroke of the linear actuator is designed as 1.5mm. Hence, the maximum strain of the equivalent spring is 1.5mm. When the elastic force of the spring at its maximum strain is designed equal to the average electromagnetic force of the actuator, say 0.023N, the elastic constant will be 15N/m. If considering a 20% excess to avoid collision between the stator and moving coil, an elastic constant of 18N/m is applied in the design.

4.6.5.3 Simulated locomotive performance

By applying the masses of the components of the robot and the electrical/mechanical parameters derived in the design, the locomotion performance of the microrobot can be solved by using the MATLAB. Figs.4-29 and 30 shows the simulated force of the actuator and the displacement of the robot.

From the simulation results, it is seen that the microrobot can operate as the expected. By applying the designed saw-shaped voltage, the movable unit and the main body of the robot move alternatively and the whole system can move forward continuously.

The speeds of the both the movable unit and the main body are shown in Fig.4-31. The locomotion speed of the robot is the speed of the main body, which the peak speed can reach 45mm/s and the average locomotion speed is 15mm/s at 10Hz driving frequency. The deformation of the equivalent spring is shown in Fig.4-32. It can be seen that the

moving coil is operating within the space of the actuator and the results show that the mechanical system of the robotic system is designed properly.

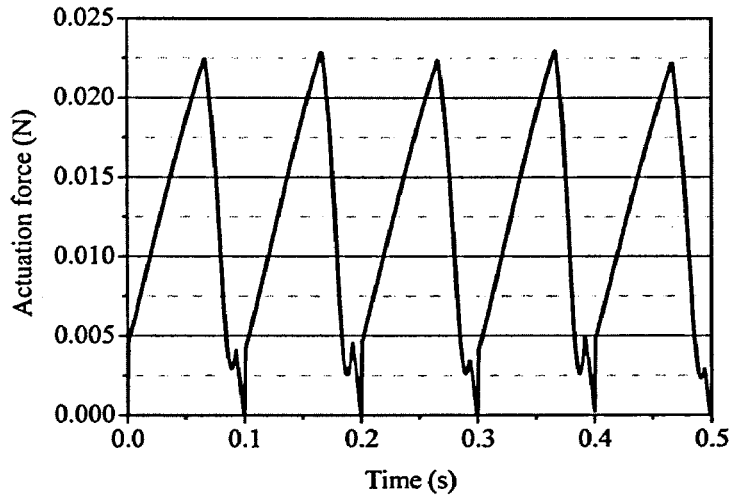

Fig.4-29 Actuation force of the actuator

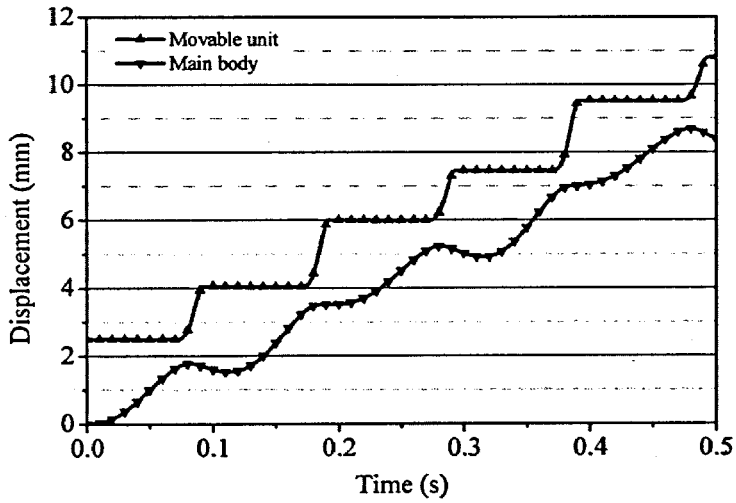

Fig.4-30 Displacements of the microrobot

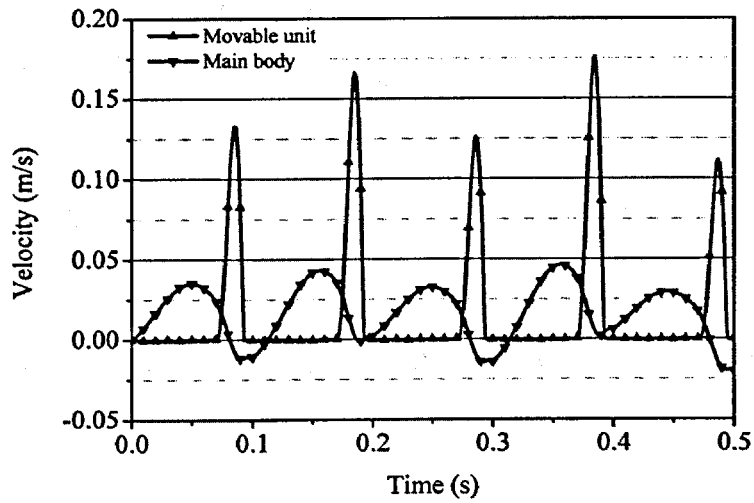

Fig.4-31 Velocities of the microrobot

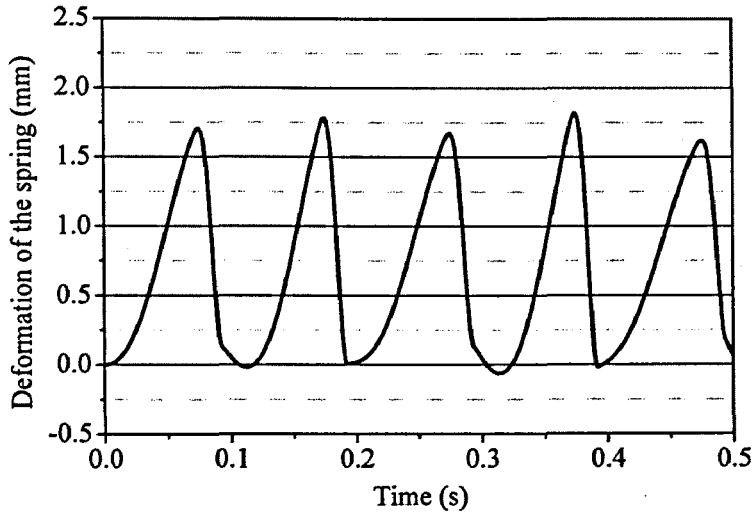

Fig.4-32 Deformation of the equivalent spring during the locomotion

During the performance analysis, it is found that the dynamic performance of the robot is associated with the ratio of the masses between the movable unit and main body of the robot due to the IDM principle. Figs.4-33 and 34 show the dynamic performance when the mass of the main body is reduced to 2g. It can be seen that the performance is degraded and the locomotion speed is markedly decreased. The oscillation during the movement also becomes significant.

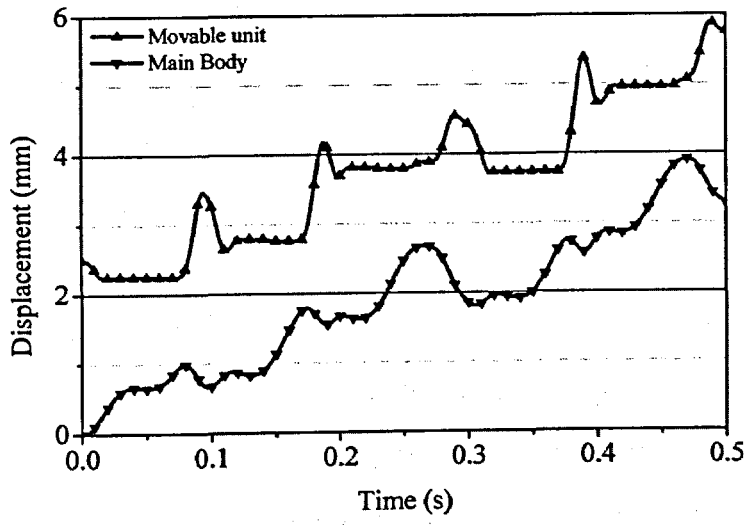

Fig.4-33 The displacement of the robot when the mass of the main body is 2g

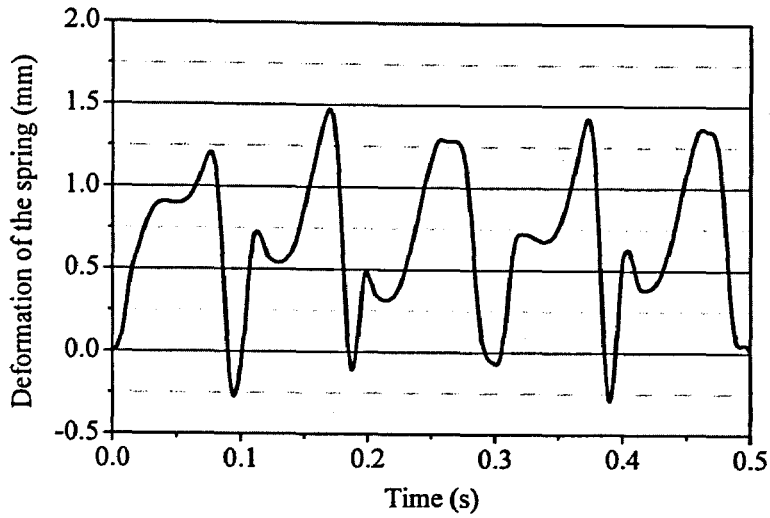

Fig.4-34 Deformation of the equivalent spring during the locomotion when the mass of the main body is 2g

4.7 Conclusion and Discussion

In this chapter, a PM moving-coil linear actuator for the locomotion of the proposed micro mobile robot is designed and analysed based on the study on the principles, topologies and performances of the various types of linear electromagnetic machines. The structure and dimensions of the moving-coil actuator is deliberately designed according the application requirements. In particular, the sizes of the magnets and moving coil of the actuator are carefully selected for an optimal force output within the limited dimensions based on the numerical magnetic field analysis.

The characteristics and parameters of the designed actuator is analysed and calculated by the 3D FE magnetic field analysis implemented in ANSYS. Based on the results obtained by the field analysis, the dynamic model of the actuator is derived. Through the analysis of the mechanical system of the microrobot, the kinetic model of the robotic system is also developed. By combining the models of the electrical and mechanical systems of the microrobot, the system model is established and used for the dynamic performance analysis.

Through the simulation conducted in the MATLAB, the dynamic performances are estimated and analysed. By proper designing the mechanical parameters of the microrobot and applying appropriate drive control scheme, the expected operation of the microrobot can be achieved.

However, through the analysis of the characteristics of the actuator and the locomotion system, some limitations of the design are found as follows:

(1) Although the PM material used in the moving-coil linear actuator is more than that in other types of the PM linear machine, the flux density in the air gap (moving coil) is quite low (0.23T) and the stator core of the actuator is heavily saturated. Therefore, the utilisation of PM material is inefficient. Moreover, low flux density in the PM (about 0.3-04T) makes it vulnerable to demagnetisation.

(2) Due to the low flux density in the air gap, a higher current is required to produce desired electromagnetic force. Hence, the resistive power dissipation in the moving coil is large and results in low efficiency of the actuator.

(3) According to the dynamic analysis, a satisfied actuation performance can only be achieved by designing the mechanical system and the control scheme very carefully. These requirements result in difficulties in the fabrication of the actuator and the robotic system.

(4) The structure of the whole system is somewhat complicated due to the connection of the moving coil and movable unit of the robot. In addition, the flexible cables required for the moving coil is also a very vulnerable component in the system.

Due to the above restrictions, the designed moving-coil linear actuator appears to be less practical for the proposed application, and a new design of the linear actuator is required. In the following chapters, a new PM linear actuator using the moving-magnet structure will be proposed and analysed.

Chapter 5

DESIGN AND ANALYSIS OF THE MOVING-MAGNET TUBULAR LINEAR ACTUATOR

5.1 Introduction

In chapter 4, a moving-coil linear actuator was designed and studied. The performance analysis shows that it has some limitations in application of the proposed microrobot. Hence, an improved design should be conceived and analysed. Based on the comparison shown in section 4.2.3, the moving-magnet PM linear machines could be an alternative option to the moving-coil actuator in miniature or micro applications. Accordingly, the moving-magnet tubular linear actuator is to be discussed in this chapter.

Firstly, important design considerations of the moving-magnet tubular linear actuator are examined so that a proper topology of the actuator can be employed. After the determination of the structure of the linear actuator, detailed design and analysis of the actuator, including the selection of the dimensions, analysis of the electromagnetic characteristics, which are similar to those in designing the moving-coil linear actuator, is performed. Finally, the dynamic model of the designed actuator is derived based on the results obtained from the magnetic field analysis, which is essential for the evaluation of the system performance, and a coupled field-circuit analysis is carried out to study the validity of the machine model.

5.2 General Structure of Moving-magnet Tubular Linear Actuators

For every rotary electric machine, a linear counter part may be found in principle. The moving-magnet linear actuator can be regarded as the counter part of the brushless PM machines, and the moving-magnet tubular linear actuator (TLA) is one of the designs with cylindrical structure by rolling up the stator and rotor about their longitudinal axes [Boldea 1997], as shown in Fig.5-1.

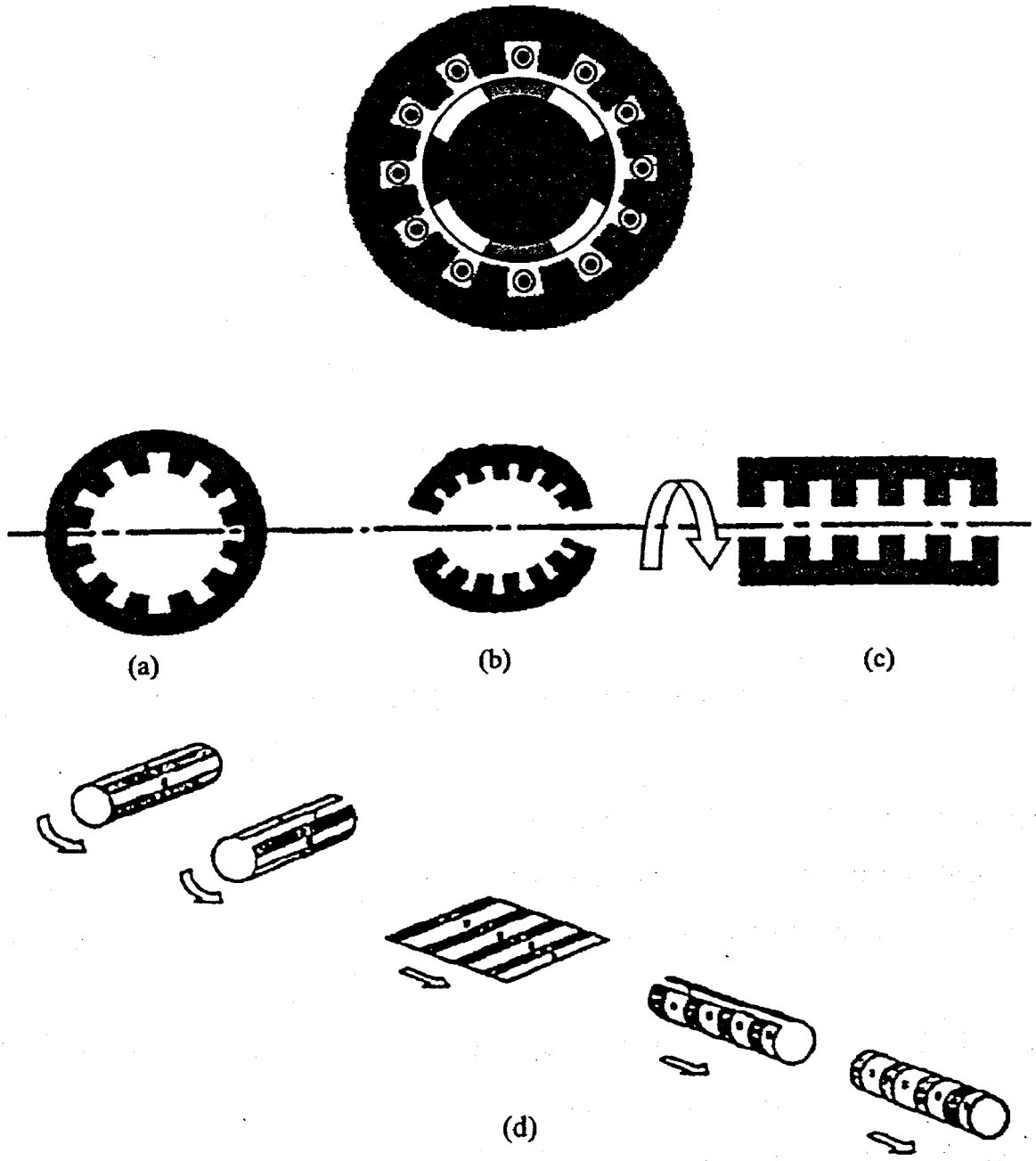

Fig.5-1 From a rotary brushless PM machine to a moving-magnet tubular linear actuator

Fig.5-2 shows an example of moving-magnet TLA [Eastham 1990]. The PMs are in the form of cylindrical shells, whereas the stator windings are constructed from simple circular coils.

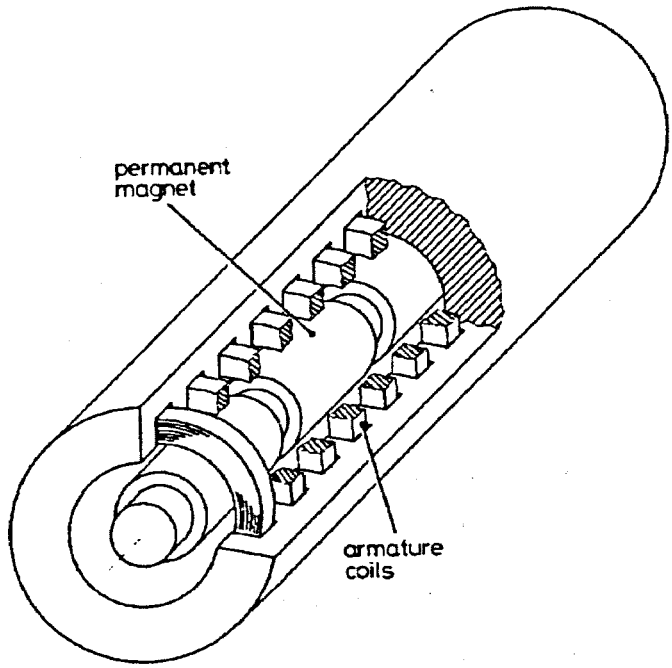

Fig.5-2 An example of moving-magnet TLA

5.3 Design Considerations of PM Tubular Linear Actuators

Different from the moving-coil linear actuator, the windings of the moving-magnet linear actuator can be more complex in structure, such as polyphase and/or distributed windings, for better performance because they are the stationary components.

The application of different winding configurations results in various options of the machine topologies, such as the structure and installation of magnets, number of poles, and slot topologies for windings, etc. These options are of different characteristics that can meet different application requirements. Thus, an appropriate topology and structure

for the specified application should be considered carefully during the design of the actuators. In this section, some importance design considerations are discussed and the results constitute the basis of the actuator design.

5.3.1 Number of poles

The number of poles is one of the most important parameters that can greatly affect the machine configuration and performances. An impropriate setting of the number poles could result in poor performance of the actuator and waste of materials and spaces. Hence, it should be carefully considered during the design of the linear actuator.

The optimum number of poles for a PM TLA has been investigated by some researchers. One of the studies can be found in [Lesquesne 1992], which the work was based on the moving-armature actuators, but from the point of view of magnetic force production, the study applies equally to the moving-armature and moving-magnet configuration.

Based on the conducted study, as the number of poles is increased, the saturation in the magnetic core diminishes and the reluctance will decrease, resulting in higher air gap flux densities and higher force production of the actuator. Although multi-pole configuration requires the current flow direction to match the polarities of the magnets, electronic commutation with/without position sensor can be used. Detailed field calculations show that a 4-pole design would be preferable as it features a high air gap flux and a good acceleration-per-ampere-turns[1] ratio. The number of poles more than this value will not contribute much to the force production but reduces the available stroke of the actuator. Fig.5-3 shows the proposed configuration for the analysis of multi-pole actuator in the Lequensne's study.

[1] acceleration-per-ampere-turns: $F_{em}/(mN_t i)$, m is the moving mass

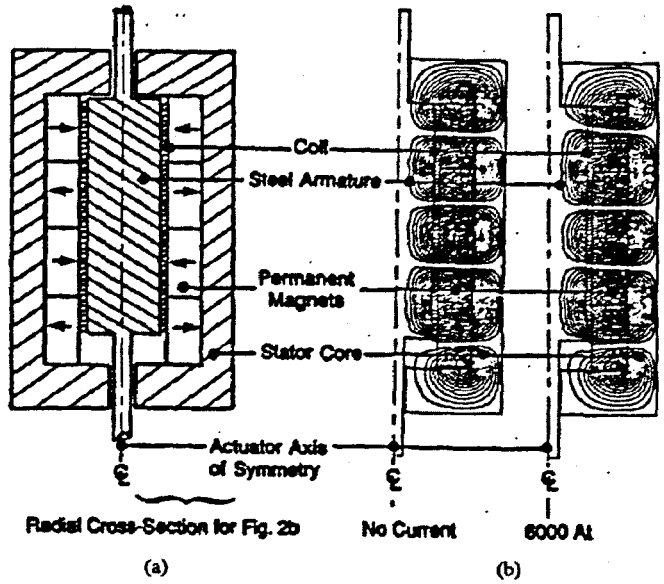

Fig.5-3 Multi-pole configuration studied by Bruno Lequensne
(a) actuator layout, (b) flux plots

5.3.2 Surface mounted and interior mounted magnets

Similar to the rotary PM machines, the tubular PM linear actuators also have two major different configurations due to the magnet construction: surface mounted and interior mounted. A TLA with surface mounted magnets is illustrated in Fig.5-4(a). By this structure, the radially magnetised PMs are made in the form of cylindrical shell and are mounted along the ferromagnetic shaft. Apart from the radially magnetisation, the surface mounted magnets can also be Halbach magnetised (Fig.5-4(b)) to achieve an improved performance. By Halbach configuration, the shaft can be either ferromagnetic or nonmagnetic material as the magnetic field in shaft region is considerably weak.

On the other hand, the interior mounted structure is constructed by stacking the axially magnetised PM discs and the associated pole pieces, and they are accommodated into a tube made by non-magnetic material, as shown in Fig.5-4(c). Due to the magnetising direction of the magnets, this type of linear actuator is also called axially magnetised PM TLA.

Studies on PM TLA with different topologies show that the interior mounted structure has a higher force capability than other topologies, but requires more PM material [Wang 2001; Bianchi 2003]. Another advantage of the interior mounted topology is that axially anisotropic magnets are easily manufactured and widely available.

Recently, an improved structure for the interior mounted PM TLA was proposed [Wang 2004], in which the magnets and the associated pole pieces are annular shaped and supported by a nonmagnetic shaft instead of the nonmagnetic tube. Fig.5-5 shows the

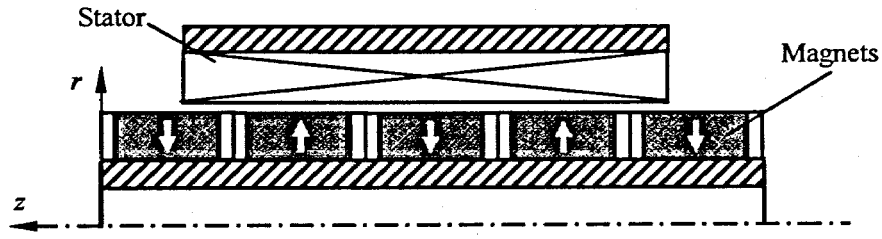

(a) TLA with radially magnetised magnets

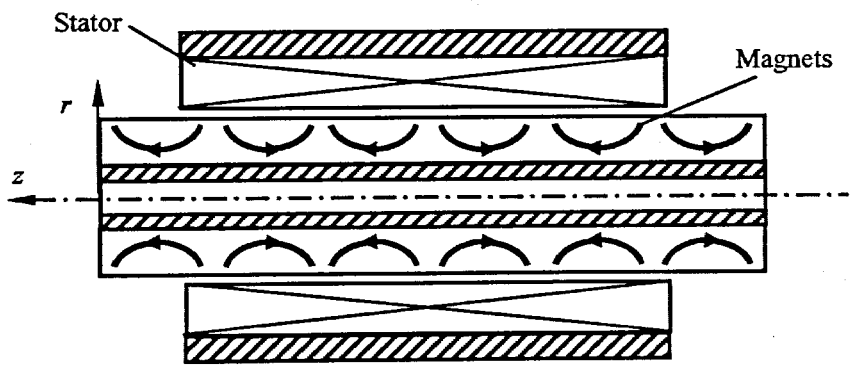

(b) TLA with Halbach magnetised magnets

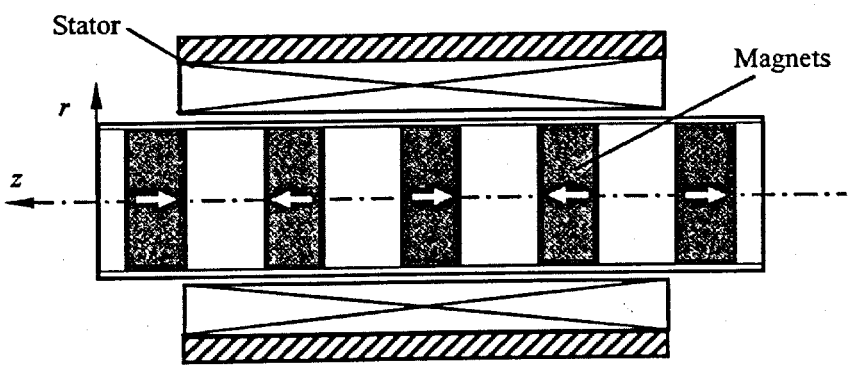

(c) TLA with axially magnetised magnets

Fig.5-4 Different topologies for PM TLA

schematic structure of the machine. The new configuration offers several advantages over the conventional topology. Firstly, it eliminates the need for a nonmagnetic tube to contain the magnets and the pole pieces, so that the effective air gap between the stator and moving magnet is reduced. In addition, it reduces the volume of the PM material and hence a lighter moving mass is achieved. Although the application of the nonmagnetic shaft will result in some leakage flux in the shaft, the affect on the force production is proved to be fairly small.

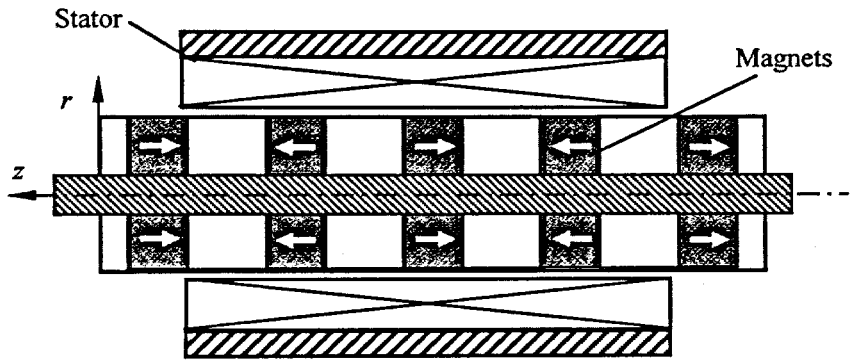

Fig.5-5 Improved interior mounted topology

5.3.3 Slot and slotless magnetic core

Using slots in the armature core for containing the armature windings is a common design for most of the electric machines. Slot structure can reduce the effective air gap of the machine and hence achieve higher flux density in the air gap. However, heavily saturation in the slot region of the armature magnetic core is a problem that can offset the benefit.

Thanks to the advances in PM materials, the slotless structure becomes interesting in the machine designs due to the availability of the high magnetic energy magnets. Although the attainable flux density in the air gap is somewhat less than that in the slot design, the slotless structure can have the following attractive features:

(1) the cogging force due to the tooth of the slotted magnetic core is totally

eliminated;

(2) the radial attraction force is effectively reduced due to the relatively large air gap between the armature and magnets

(3) the slotless design could be lighter than the slotted magnetic core that can result in a better force/mass ratio;

(4) the slotless design is more compact and can greatly reduce the complexity of the armature assembly in the fabrication, which are essential for the micro applications.

Detailed performances comparison [Bianchi 2001] also shows that the slotless structure is much favoured in the designs that the outer diameters of the actuator are less than 40mm as the slotless structure can achieve a better force-to-volume ratio than the slotted one.

5.4 Design of the PM Tubular Linear Actuator

5.4.1 Basic structure

Based on the analysis and discussion conducted in section 5.3, the proposed moving-magnet PM TLA will adopt the interior mounted topology with slotless windings since the configuration could achieve high force capability, less force ripple and relatively simple structure. Fig.5-6 shows the schematic structure of the designed PM TLA.

The stator core of the actuator is a cylindrical tube stacked by glassy metal METGLAS 2605SA1 thin film. Two caps are attached at each side of the stator core acting as the supporter and guide for the moving magnet assembly. The caps are made of nonmagnetic material such as aluminium to reduce the fringing flux as well as the mass

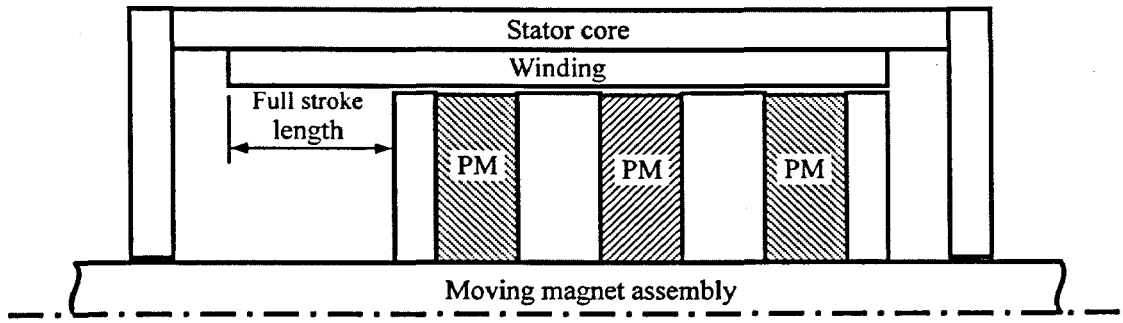

Fig.5-6 Proposed slotless interior mounted PM TLA

of the actuator.

The moving magnet assembly (hereafter called "translator") contains the NdFeB magnets, the associated pole pieces, and the supporting shaft. The magnets and the pole-pieces are assembled alternatively along the shaft, as shown in Fig.5-7. As mentioned before, the shaft of the translator can be made of nonmagnetic materials. The number of magnets used on the translator is set as three and this number of poles is determined based on the trade-off between the flux density in the air gap and the saturation of the magnetic core, as discussed in section 5.3. The available thickness of the PM disc and the limit of total length of the actuator are also taken into account when deciding the number of magnets used. As a result, there are totally three poles on the translator according to its magnetic topology. Through a comparison illustrated in Fig.5-8, it can be seen that the proposed three-pole design for the interior mounted configuration has the comparative flux distribution to a four-pole surface mounted

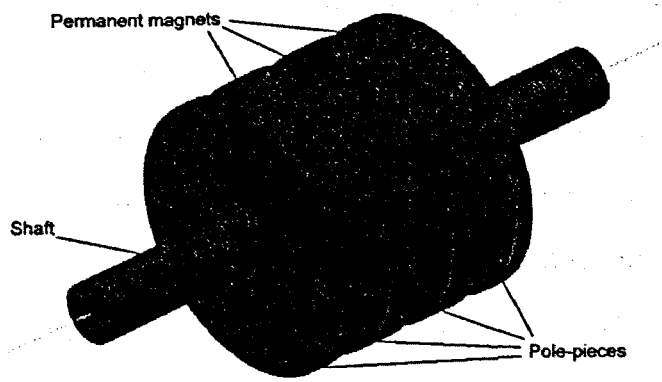

Fig.5-7 3D view of moving magnet assembly (translator)

topology, except there are some leakage flux at ends of the moving magnets in the surface mounted topology.

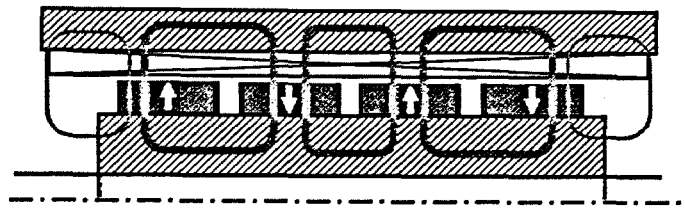

(a)

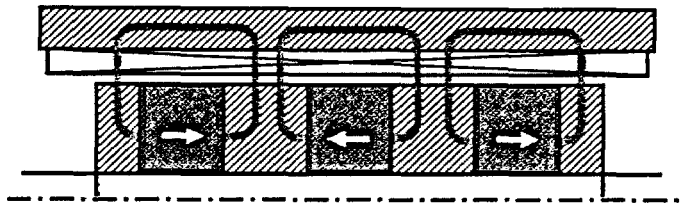

(b)

Fig.5-8 Flux density distribution (a) Surface mounted, (b) Interior mounted

The slotless windings are composed of a series of circular concentrated coils that are mounted inside the wall of the stator core. As a commonly used configuration for the small sized electric machines, the concentrated three phase windings are adopted for the proposed actuator. Hence, there will be three coils under each pole and each coil belongs to a phase. Considering that extra windings are required for the linear motion of the moving magnet, the stator windings containing the coils for four poles are therefore used so that the actuator can have a stroke length equal to one pole pitch. As a result, the stator windings compose of twelve phase coils that are arranged as *A-C-B* under each pole along the axial direction. The polarities of the coil of each phase are arranged alternatively so that a proper electromagnetic force can be generated by applied phase currents. Fig.5-9 illustrates the detailed construction of the stator windings. The coils in each phase can be connected either in series or in parallel. In order to have the actuator operating in an easily obtained voltage level, series connection is used in the design. Fig.5-10 illustrates the overall 3D configuration of designed linear actuator with stator, windings and translator, while different components and phase coils are shown in different colour.

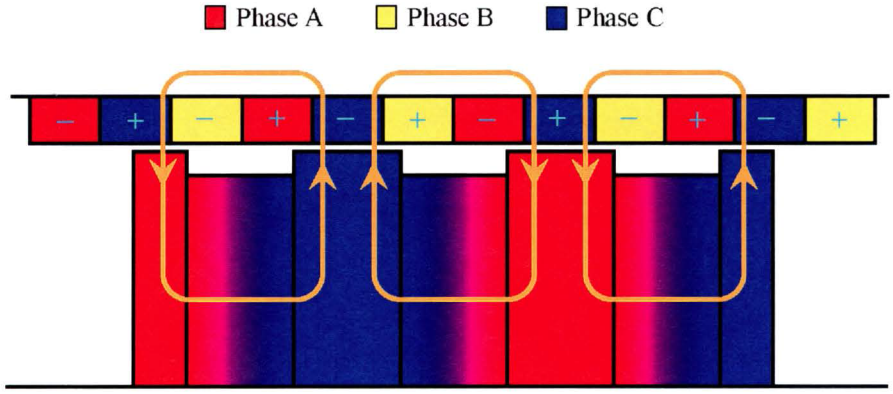

Fig.5-9 Stator windings of the PM TLA

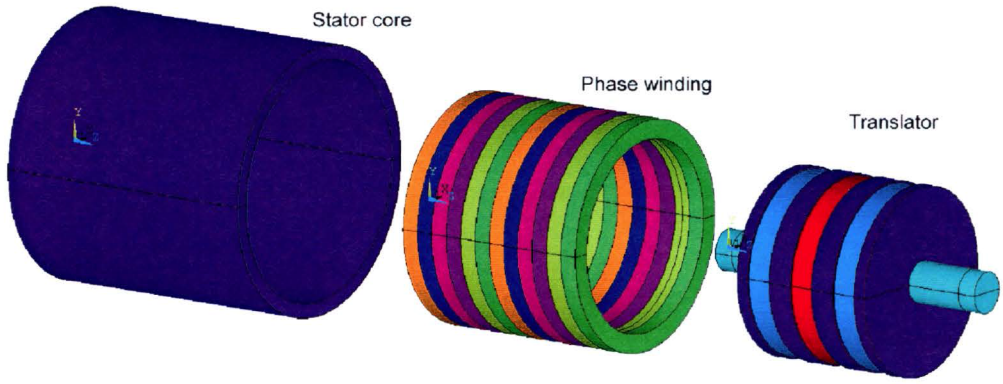

Fig.5-10. 3D configuration of the PM TLA

5.4.2 Major dimensions

Table 5-1 lists the major dimensions of the actuator and Fig.5-11 illustrates the meaning of these dimensions. Same as the design of the moving-coil linear actuator, the outlines of the proposed moving-magnet TM PLA are based on the typical size of medical capsules. The outer diameter of the stator, D_e, is designed as 6.4mm and same value applies to the stator length L_s. The thickness of the stator core and the end caps are designed to be the same, namely, 0.45mm. As a result, the inner diameter of the stator core D_o will be 5.5mm. The diameter of the translator shaft is designed as 1mm so that it can withstand the stress of the system. Moreover, 1mm diameter can also make it easier to find suitable magnets from the available commercial products. The air gap

between stator windings and translator is designed as 0.05mm.

Table 5-1 Major dimensions of the PM TLA

Dimensions	Symbol
Outer diameter of stator core	D_e
Inner diameter of stator core	D_o
Thickness of stator core	tc_{ex}
Length of stator core	l_s
Diameter of translator	D_a
Length of translator	l_m
Diameter of translator shaft	D_s
Pole pitch	τ
Thickness of pole-pieces	τ_c
Thickness of magnets	τ_m
Height of magnets	h_m
Height of the stator winding	h_c
Air gap	g
Clearance between winding and stator core edge	g_d

Among the rest of the dimensions, the thickness and height of the magnets are the most important for the actuator. Other dimensions can only be introduced after the sizes of magnets are determined as the gross space occupied by the magnets, pole-pieces, and stator windings are fixed by D_o. However, τ_m and h_m cannot be simply designated and should be designed carefully so that an optimum force capability of the actuator can be achieved.

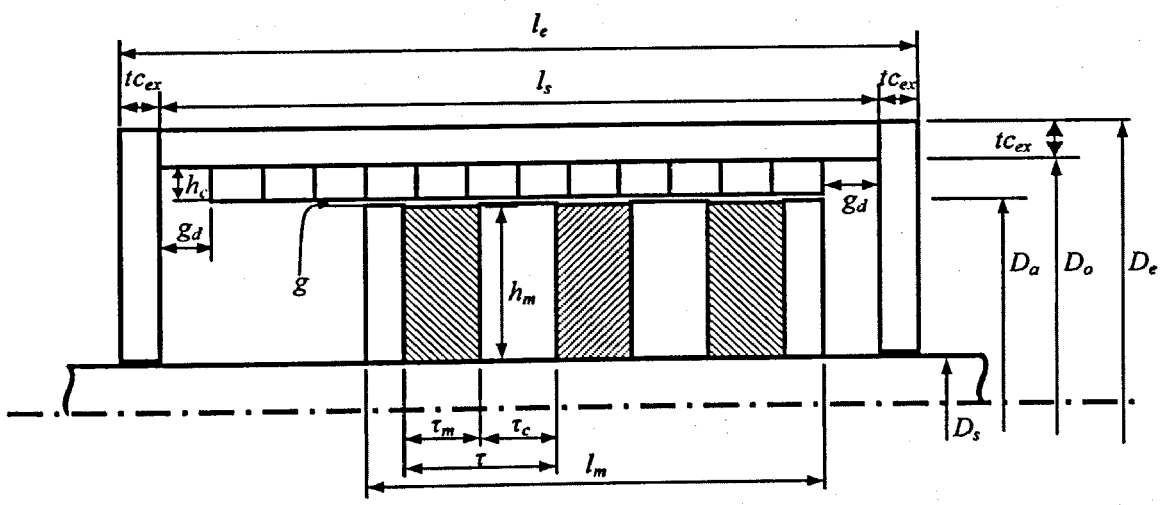

Fig.5-11 Major dimensions of the PM TLA

5.4.3 Optimal design by magnetic circuit method

In order to determine the suitable thickness and height of the magnets, an optimal design is conducted by means of an analytical magnetic analysis based on the magnetic circuit method. The optimisation of the dimensions aims at obtaining the highest force capability within the desired device volume, which is an importance feature for the micro applications.

5.4.3.1 Equivalent magnetic circuit model

Although the designed PM TLA has multiple poles, only one pole is necessary to be considered when analysing the performance of the machine by the analytical method due to symmetric distribution of the magnetic field. Fig.5-12 shows the structure of one pole in the actuator and the corresponding magnetic flux path. For simplicity, the following assumptions are made during the analysis:

(1) The magnetic permeability of the magnetic core is considered as infinite;

(2) The leakage flux in the air gap and the shaft is ignored;

(3) The flux produced by the winding currents is negligible compared with the flux produced by the magnets.

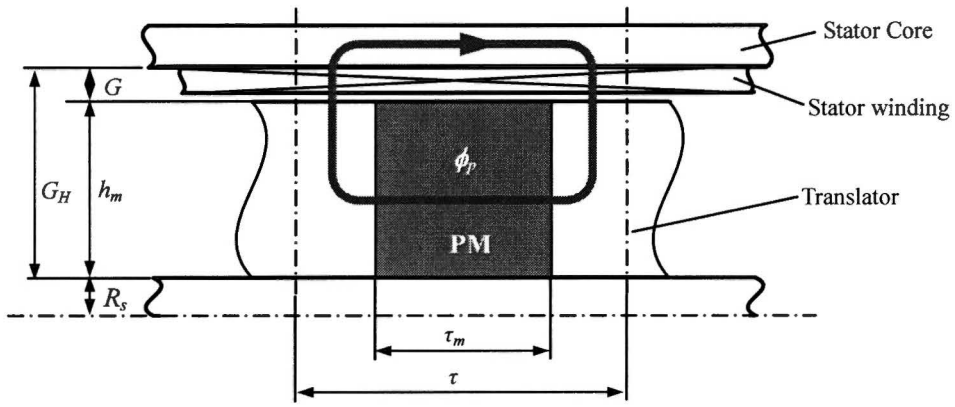

Fig.5-12 Magnetic circuit model of the PM TLA

Accordingly, a magnetic circuit shown in Fig.5-13 can be used to analyse the behaviour of the magnetic system shown in Fig.5-12. In Fig.5-13, $\Re_g$ and $\Re_m$ are the reluctances

of the air gap and the magnet, and F_{mm} is the magnetomotive force (MMF) generated by the magnet and $F_{mm}=H_c \cdot \tau_m$.

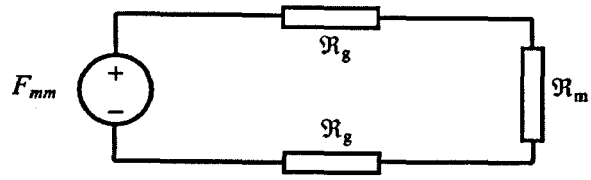

Fig.5-13 Equivalent magnetic circuit for the analytical analysis

5.4.3.2 Electromagnetic force per pole

According to Lenz's law, the electromagnetic force produced by a current i interacting with a magnetic field B is given by

$$F_{em} = i\vec{l} \times \vec{B}, \tag{5.1}$$

where $\vec{l}$ is the length vector of the conductor exposed to the magnetic field. Considering one pole of the actuator shown in Fig.5-12, the electromagnetic force generated by the stator windings under one pole can be given by

$$F_{emp} = 2\int_0^{w_c} B_{gr}(x) J_s h_c l_c dx, \tag{5.2}$$

where $B_{gr}(x)$ is the radial component of the flux density in the air gap along the axial direction x, J_s the effective current density in the winding, and h_c, w_c and l_c are the height, effective width and mean perimeter of the winding under one pole, respectively. The integration $\int_0^{w_c} B_{gr}(x) l_c dx$ gives the magnetic flux per pole, ϕ_p. Because the phase coils are concentrated, the current density J_s in the corresponding coils will be constant at a given time instant. Therefore, (5.2) can be expressed as

$$F_{emp} = 2\phi_p J_s h_c. \tag{5.3}$$

It can be seen that the force per pole is proportional to the magnetic flux per pole ϕ_p and the height of the stator winding. Since the dimensions of stator winding are related to the sizes of magnets as the total space that they can occupy in the actuator is fixed, an

optimal design based on the attainable electromagnetic force could be considered by the analysis of ϕ_p and suitable selection of the size of the magnet, which can make the best utilization of the actuator volume.

5.4.3.3 Maximum flux design

Based on the magnetic structure shown in Fig.5-12, the reluctances in the magnetic circuit can be derived as follows,

$$\Re_g = \frac{1}{\mu_0} \frac{G}{2\pi(h_m + R_s + G/2)\cdot(\tau - \tau_m)/2} = \frac{2G}{\pi\mu_0(2h_m + D_s + G)(\tau - \tau_m)}, \quad (5.4)$$

$$\Re_m = \frac{1}{\mu_m} \frac{\tau_m}{\pi((h_m + R_s)^2 - R_s^2)} = \frac{\tau_m}{\mu_m \pi h_m (h_m + D_s)}, \quad (5.5)$$

where R_s=D_s/2 is the radius of the translator shaft and G=h_c+g the gross air gap between the translator and stator core, as shown in Fig.5-12. Therefore, the magnetic flux per pole can be calculated as

$$\phi_p = \frac{F_{mm}}{\sum \Re} = \frac{H_c \tau_m}{2\Re_g + \Re_m}. \quad (5.6)$$

By introducing (5.4) and (5.5) to (5.6) and knowing that the permeability of NdFeB is the same as that of free air, the flux per pole can be further obtained as

$$\phi_p = \mu_0 \pi H_c \frac{\tau_m}{\frac{4G}{(2h_m + D_s + G)(\tau - \tau_m)} + \frac{\tau_m}{h_m(h_m + D_s)}}. \quad (5.7)$$

If both the numerator and denominator in (5.7) are divided by τ_m, the equation becomes

$$\phi_p = \mu_0 \pi H_c \frac{1}{\frac{4G}{(2h_m + D_s + G)(\tau_m \tau - \tau_m^2)} + \frac{1}{h_m(h_m + D_s)}}. \quad (5.8)$$

Furthermore, the radial flux density in the air gap can be obtained by

$$\begin{aligned} B_{gr} &= \frac{\phi_p}{2\pi(h_m + R_s + G/2)\cdot(\tau - \tau_m)/2} \\ &= 2\mu_0 H_c \frac{\tau_m h_m (h_m + D_s)}{4G h_m (h_m + D_s) + (\tau_m \tau - \tau_m^2)(2h_m + D_s + G)} \end{aligned}. \quad (5.9)$$

From (5.8) and (5.9), it can be seen that ϕ_p and B_{gr} are functions of τ_m. When considering the term $(\tau_m\tau-\tau_m^2)$ in (5.8), it can be easily known that it can have a maximum value when $\tau_m= \tau/2$ and hence the flux per pole ϕ_p will reach its maximum value if keeping other variables as constants. Accordingly, for obtaining a maximum magnetic flux per pole, the magnets and pole-pieces should be designed with the same thickness. Therefore, based on the desired length of the actuator, NdFeB discs with 0.6mm thickness, which can be commercially available from the manufacturer, is selected as the magnets for the translator.

The design is verified by a numerical magnetic field solution considering the saturation effect of the magnetic core, which is implemented in ANSYS. Both the analytical and numerical results of produced flux and flux densities in the air gap are plotted in Fig.5-14. It is shown that the results agree well. The reason why the results from the numerical solution are less than that from the analytical method is because of the saturation effect and fringing flux. However, the non-linear property of the magnetic core does not have much influence on the design criterion because the interior mounted topology uses less PM material and will not cause heavy saturation in the magnetic core like the moving-coil linear actuator.

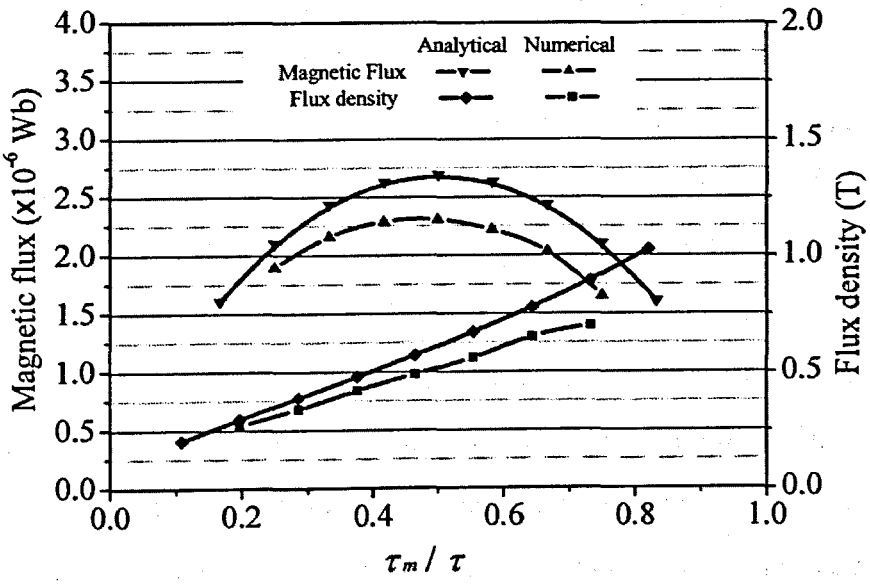

Fig.5-14 Flux and flux density per pole obtained by analytical and numerical methods

5.4.3.4 Maximum force design

Once the magnetic flux is obtained, the generated electromagnetic force of the actuator can be calculated based on (5.3). By using (5.8) and $\tau_m=\tau/2$, the force per pole can be given by

$$F_{emp} = 2\mu_0 \pi H_c J_s \frac{h_c}{\frac{16G}{(2h_m + D_s + G)\tau^2} + \frac{1}{h_m(h_m + D_s)}}. \qquad (5.10)$$

Considering $h_c >> g$ and $G \approx h_c$, one can rewrite (5.10) as

$$\begin{aligned} F_{emp} &= 2\mu_0 \pi H_c J_s \frac{G}{\frac{16G}{(2h_m + D_s + G)\tau^2} + \frac{1}{h_m(h_m + D_s)}} \\ &= 2\mu_0 \pi H_c J_s \frac{\tau^2 h_m G(h_m + D_s)(2h_m + D_s + G)}{16h_m G(h_m + D_s) + (2h_m + D_s + G)\tau^2} \end{aligned} . \qquad (5.11)$$

By defining the gap between the stator core and translator shaft as G_H, as shown in Fig.5-11, G can be replaced by $(G_H - h_m)$ and the above equation can be expressed as

$$F_{emp} = 2\mu_0 \pi H_c J_s \frac{\tau^2 h_m (G_H - h_m)(D_s + h_m)(D_s + G_H + h_m)}{16h_m (G_H - h_m)(D_s + h_m) + \tau^2 (G_H + D_s + h_m)}. \qquad (5.12)$$

By introducing the magnetic occupation ratio $k_m = h_m/G_H$, the equation of the force per pole becomes

$$F_{emp} = 2\mu_0 \pi H_c J_s \frac{\tau^2 k_m (1-k_m)(k_s + k_m)(1 + k_s + k_m) G_H}{16k_m (1-k_m)(k_s + k_m) G_H + \tau^2 (1 + k_s + k_m)}, \qquad (5.13)$$

where $k_s = D_s/G_H$. It can be seen that the electromagnetic force per pole is a complicated function related to several variables. If the dimensions of the stator and translator shaft are defined, G_H and k_s will be constants and F_{emp} varies with k_m and the pole pitch τ. Fig.5-15 shows the variation of the force per pole with k_m based on the known dimensions of the PM TLA. In addition, the variations of force at those pole pitches other than the designed value are also computed and plotted for an extensive comparison of the relationship between the generated electromagnetic force and machine pole pitch. The current density J_s used for the analysis is the same as that used in the analysis conducted in chapter 4.

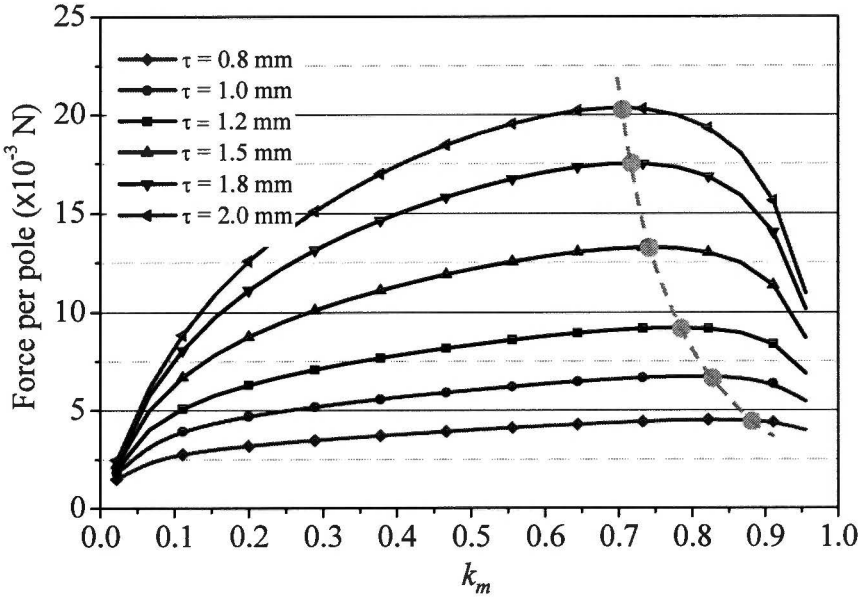

Fig.5-15 Variation of force vs. k_m obtained by analytical analysis

From the results, it can be noted that there exist a series of optimal values of k_m that can make the electromagnetic force achieve its maximum value at different pole pitches, and they can be found by applying $dF_{emp}/dk_m = 0$ to (5.13). However, since there is no universal solution that can be derived from the equation, a proper value of k_m should be determined in conjunction with the sizes and the number of poles of the actuator for every design cases. For the pole pitch used for the proposed actuator, namely 1.2mm, the optimum value of k_m is found as 0.776. As a result, the height of the magnets will be 1.7mm and the height of the stator winding is therefore 0.45mm.

Like the analysis of flux, numerical method is also applied to validate the above analytical result. Via a 2D non-linear FE analysis, the variation of the electromagnetic force produced in the stator winding is calculated by using the dimensions acquired by the above analytical method. By applying different k_m values, the forces are computed and plotted in Fig.5-16. Meanwhile, the result obtained by the analytical method is also plotted for comparison. It can be seen that both methods give the similar value of k_m when the maximum force occurs. Additionally, the saturation effect of the magnetic core can be observed in the numerical result. When k_m continues to increase after the force reaches its maximum value, the electromagnetic force will decrease faster than that

obtained by the analytical method because of the saturation of the magnetic core caused by the increased amount of PM material and smaller air gap.

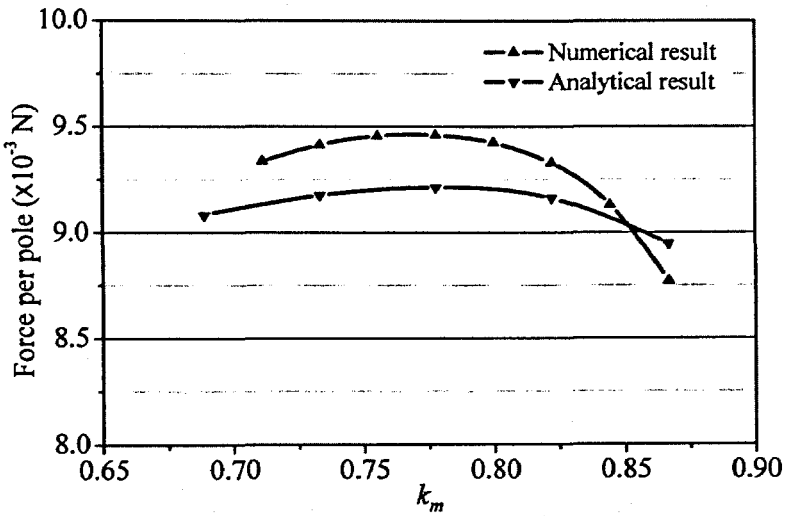

Fig.5-16 Comparison of F_{em} vs. k_m obtained by numerical and analytical solutions

5.4.4 Design summary

The major dimensions of the proposed moving-magnet PM TLA are analysed and determined in this section. By the analysis conducted, the important dimensions of the actuator are determined based on the optimal force capability of the machine. With the designed dimensions of magnets, number of poles and pole pitch, the proposed actuator acquires optimum force-to-volume ratio. Although the design is based on the analytical method, the validity of the results is verified by the numerical solutions with considering the non-linear property of the magnetic material used in the actuator.

Moreover, some of the dimensions are case dependant, such as the magnetic occupation ratio k_m. The results are not the common values for the actuator designs and required to be re-evaluated based on the optimal rules if the key dimensions of the actuator are changed.

5.5 Characteristic Analysis of the Actuator

The topology and major dimensions of the PM TLA have been confirmed during the previous analysis. The analysis of the characteristics of the actuator, including the induced flux density in the air gap, electromagnetic force under rated current condition will then be performed. As in the analysis of moving-coil actuator, the entire analysis will be carried out by using the FEM in ANSYS environment.

5.5.1 2D FE modal for the actuator

Because the designed moving-magnet PM TLA has an axisymmetric structure, a 2D FE model with axisymmetric element property can be used for the magnetic field analysis with enough accuracy and it is time-efficient. Fig.5-17 shows the 2D model of the actuator implemented in the ANSYS environment.

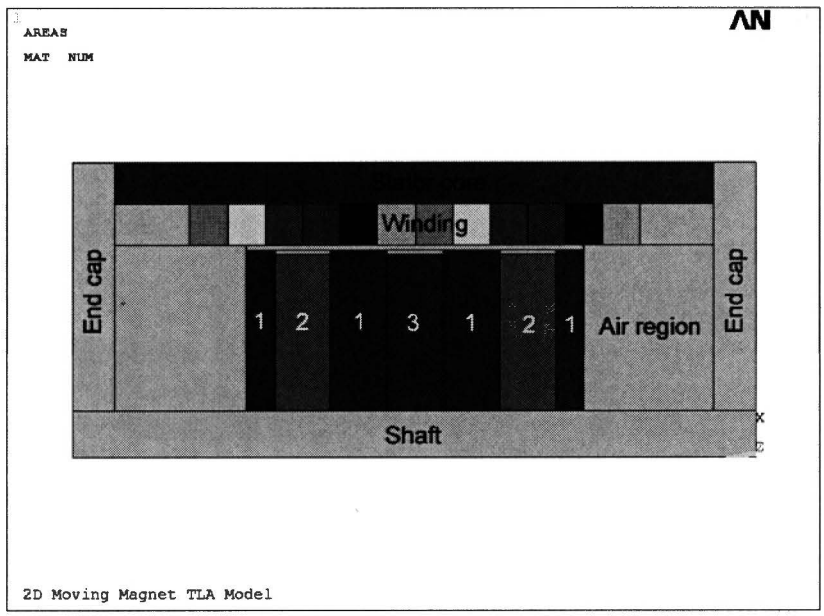

Fig.5-17 2D FE model of the PM TLA
1 - pole pieces, 2,3 - magnets with opposite magnetisation directions

In the model shown in the figure, the translator is in the middle of the actuator. However, the translator can be set at different positions within the stator length. The stator winding composes of twelve areas representing the coils used in the winding so that the

current in each phase coil can be independently defined. Fig.5-18 shows the meshed model for the FE analysis. Because the air gap between the translator and stator winging is considerably small and it is also the most concerned area, the finest meshing are therefore applied in this region.

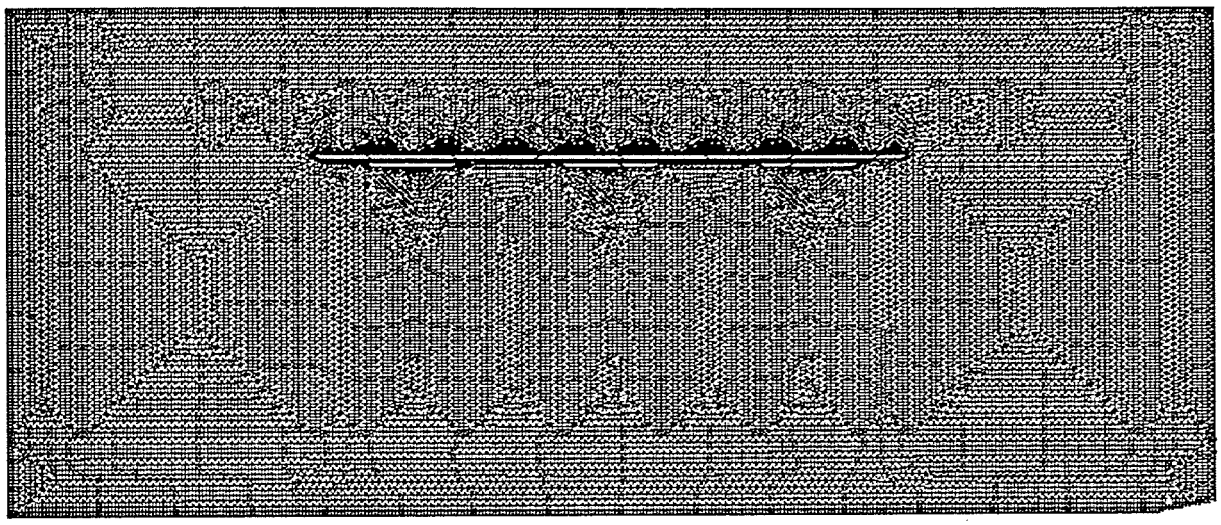

Fig.5-18 Finite element mesh for the actuator model

The setting of the material properties is similar to those in the analysis of the moving-coil linear actuator and the non-linear solution is applied for the field analysis. The boundary conditions used for the analysis are set as follows:

(1) the outer surface of the stator core and the side caps are supposed to be flux-parallel, namely, no flux leakage out of the stator surface;

(2) the flux along the axis of the translator shaft is set to be flux-parallel due to the axisymmetric structure of the actuator; and

(3) the element used for the FE analysis is set with axisymmetric property.

5.5.2 Flux density distribution

Since the translator of the PM TLA is deliberately designed shorter than the stator so that it can move back and forth within the range of the stator windings, the distribution of the resultant flux density in the air gap varies with the position of the translator. As an

example, two flux contour plots of the actuator obtained by the FE analysis when the translator is at the right hand side and in the middle of the stator winding, respectively, are shown in Fig.5-19.

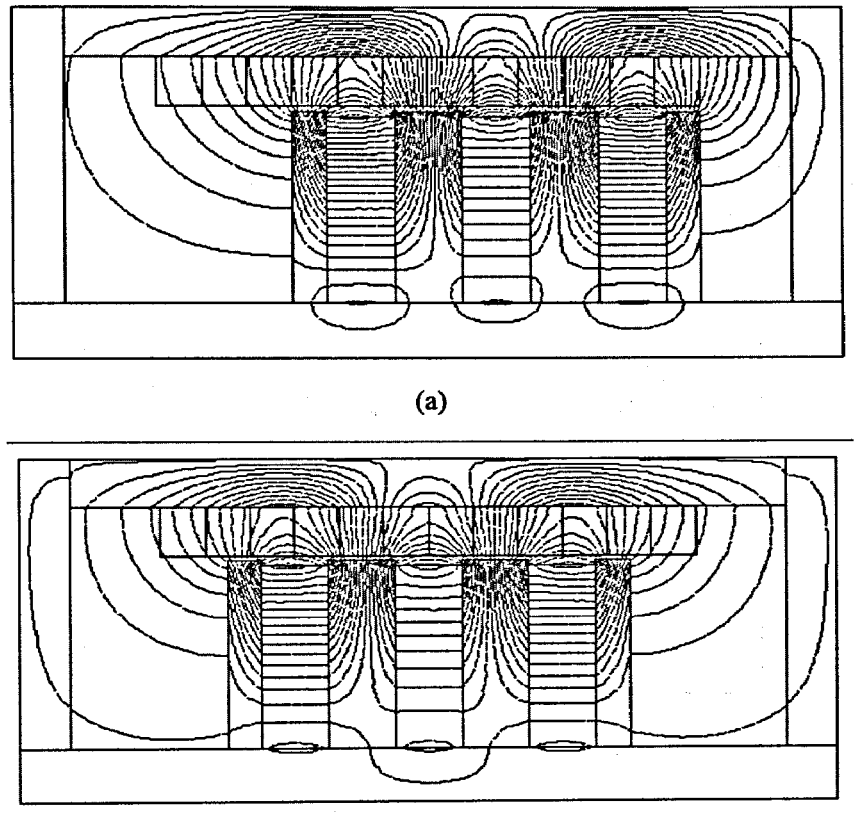

Fig.5-19 Flux contour distribution in the actuator: (a) right hand side, (b) middle

Variation of the magnetic field distribution in the air gap causes the flux densities corresponding to each of phase coils of the stator winding varies with the translator positions as well. Through the FE analysis, the radial flux densities in each coil of the stator winding at different translator positions are computed and the results are shown in Fig.5-20. During the computation, the magnetic field generated by the winding currents is also considered. However, the field produced by the currents is considerably small compared to the flux generated by the magnets and its influences to the profiles of the flux densities within the winding coils are almost invisible.

(a)

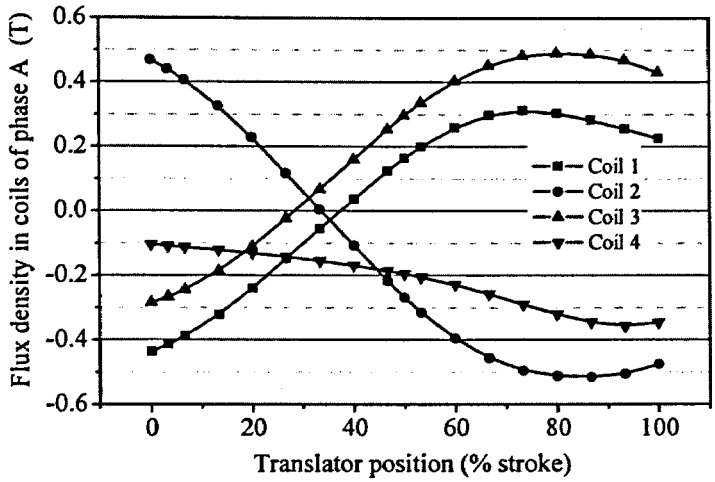

(b)

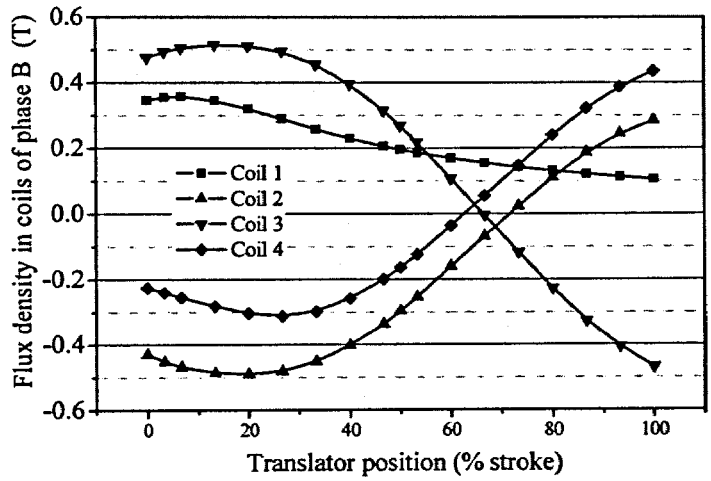

(c)

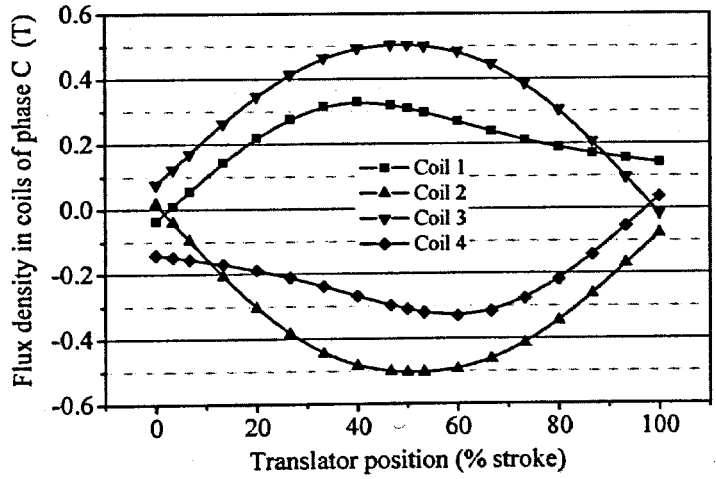

Fig.5-20 Flux densities in phase coils (a) phase *A*, (b) phase *B*, (c) phase *C*

From the results, it is shown that most of the variations of the flux density within the stator coils are close to the sinusoidal waveforms. However, the fringing effect is remarkable when the translator is near the extremities of the stator windings. For those coils near to the sides of the actuator, such as the 4th coil in phase *A*, the 1st coil in phase

B and the 2nd and 3rd coils in phase *C*, the flux densities in these coils no longer vary as sinusoidal and are also smaller than others. This effect will affect the attainable force when the translator is operating near the sides of the actuator.

It can be also noticed that the maximum flux density in the stator winding is much higher than that in the previously designed moving-coil actuator. Although the moving-magnet actuator uses less PM materials, the effective air gap is relatively smaller than that in the moving-coil actuator.

5.5.3 Electromagnetic force of the actuator

The electromagnetic force of the designed actuator can be produced properly by applying suitable excitation currents. Different force characteristics can be obtained by various excitation schemes. In applications of PM electric machines, conventional three-phase AC sinusoidal excitation and 2-phase DC excitation, which is widely employed in the brushless DC drives, are the commonly used driving method. According to the design of the PM TLA, either 3-phase sinusoidal or the 2-phase DC excitation can be used for the force generation. Hence, the electromagnetic forces under the both methods are analysed. The current density used for the force prediction is the same as that used in the analysis of the moving-coil actuator.

5.5.3.1 Sinusoidal excitation

Based on the obtained flux densities in the winding coils, the electromagnetic force can be calculated by using (5.1) via the FE solutions. For the 3-phase sinusoidal excitation, the excitation currents in three phases are set as follows:

$$\begin{cases} I_a = \sqrt{2} I_0 \sin\left((\pi/\tau)\cdot x_{sm} - \pi/3\right) \\ I_b = \sqrt{2} I_0 \sin\left((\pi/\tau)\cdot x_{sm} + \pi/3\right), \\ I_c = \sqrt{2} I_0 \sin\left((\pi/\tau)\cdot x_{sm} - \pi\right) \end{cases} \tag{5.14}$$

where x_{sm} is the translator position with respect to the stator windings, and I_0 the *rms* value of the phase current for the desired current density. The variations and phase shifts selected for the phase currents are based on the configuration of stator windings and the desired translator movement direction. By this translator position based current setting, one can also achieve a maximum attainable force provided by the actuator, known as field-oriented control method that is commonly used in the servo control of rotary PM machines. However, this maximum force/torque feature can only be obtained by the controller with rotor/translator position sensing technology implemented by either mechanical sensors or complicated sensorless algorithms.

The calculated electromagnetic force under 3-phase sinusoidal currents is shown in Fig.5-21. The maximum force can be achieved when the translator is in the middle of the stator windings, which is around 34mN. The salient effect caused by the translator structure is visible throughout the force curve. The force reduces when the translator is close to the extremities of the actuator due to the fringing effect of the magnetic field. When the translator is at the ends of the stator windings, the attained force will be down to about 31mN, about 10% drop from its maximum attainable force.

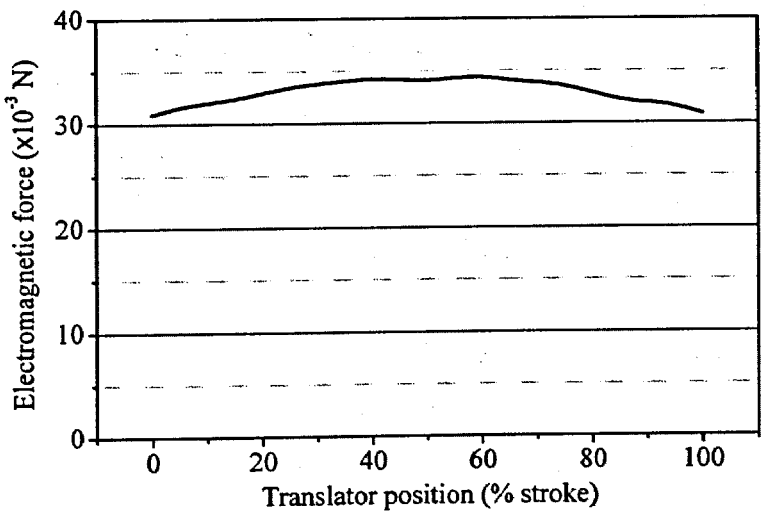

Fig.5-21 Electromagnetic force under sinusoidal excitation

5.5.3.2 2-phase DC excitation

The 2-phase DC excitation, generally known as the brushless DC drive method, are widely used in the PM brushless machine drives due to its simple implementation and very good control performance. Moreover, the brushless DC drives without the mechanical position sensors can also be easily realised by phase voltage detection technique. These features are attractive for the micro systems that do not allow complex system structure and large volume.

The excitations of the brushless DC drive method are the direct currents imposed to the phase windings according to the translator positions. The phase currents are required to be commutated between phases at specified translator positions to achieve the optimal force output. In our application, the conventional 120° square wave of energisation, as shown in Fig.5-22, is adopted for the current commutation. A proper switching sequence as well as a set of commutation positions can be found by comparing the produced forces under different commutation schemes. By this method, an appropriate switching sequence is obtained and is shown in Table 5-2.

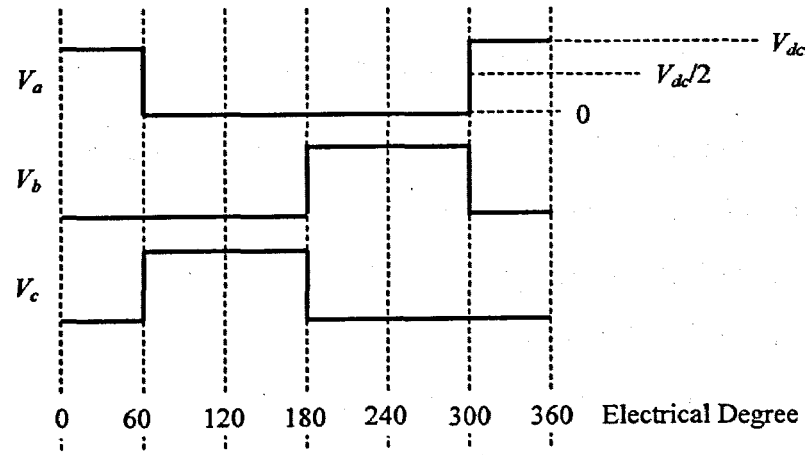

Fig.5-22 Conventional 120° energisation

Table 5-2 Switching sequence for the PM TLA

Stroke	0 – 13.3%	13.3 – 50%	50 – 86.7%	86.7 – 100%
Energisation Sequence	$\overline{A}B$	$B\overline{C}$	$A\overline{C}$	$A\overline{B}$

Based on the obtained switching sequence, the electromagnetic force was computed at different translator positions with the predefined excitation phases and the results are illustrated in Fig.5-23. The maximum force produced by the brushless DC drive method is about 28mN. Similar to the most of brushless DC rotary drives, the output force of the PM TLA has large ripples due to the DC phase currents interacting with sinusoidal magnetic field and the current commutations. The force ripples can be up to 20% with the average force of 25mN. The influence of the fringing effect on the electromagnetic force can also be clearly seen from the results. Fortunately, in the locomotion of robotics, the force ripples during the operation will not be a severe problem.

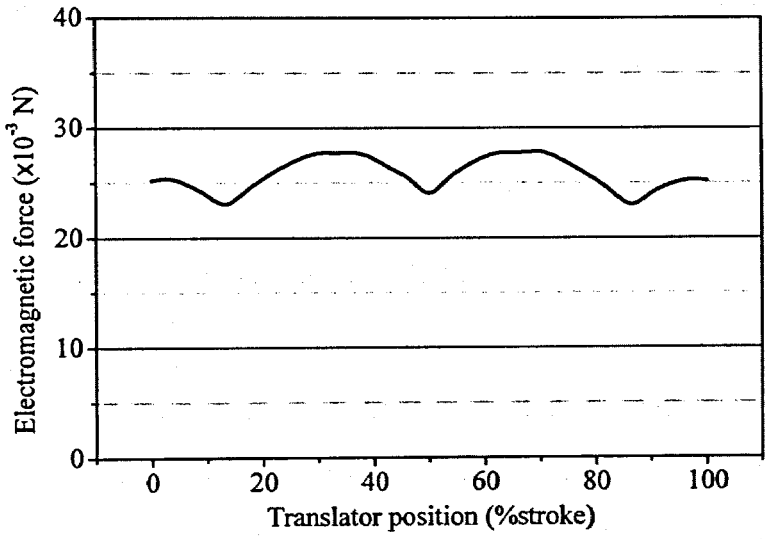

Fig.5-23 Electromagnetic force generated by brushless DC drive method

From the force outputs obtained by different drive methods (Figs.5-21 and 5-23), it can be seen that the balanced three phase sinusoidal excitation has the favourable mechanical power output under less electrical power input. However, an optimal performance under three phase excitation requires complex hardware such as the position sensors, three sinusoidal waveform generators, and complicated control algorithms. On the contrary, the force obtained by the brushless DC drive method is about 20% less than that produced by the three-phase energized scheme, but its control method is much simple and can be easily realised by less hardware (DC power supply and simple electronic converter) compared to the three phase drive method. This feature is preferred for the compact systems, especially micro systems. Moreover, the

sensorless control can be readily implemented in the brushless DC drive method by detecting the back EMF in the unexcited phase of the machine. This attribute is also essential for the miniature or micro applications that the installation of mechanical position sensors is not feasible.

5.5.4 Summary of the characteristic analysis

According to the results of characteristic analysis of the designed PM TLA, the attainable flux densities and force are satisfactory with the designed topology and dimensions. Compared to the previously designed moving-coil linear actuator, the new design has higher air gap flux density and better force capability.

5.6 Calculation of Machine Parameters

Just like the design of the moving-coil linear actuator, the parameters of the PM TLA are also required to be extracted for the performance analysis. The inductances of the PM TLA will be discussed in more detail as the new design contains more complex winding configuration. Because the flux distribution is much complicated within the PM TLA, only the energy method will be considered in the computation of the winding inductances.

5.6.1 Calculation of phase resistance

Each of the phase windings of the actuator consists of four series connected coils. Therefore, the phase resistance will be the sum of the resistance of the four coils. According the actuator design, there are three winding coils under one pole pitch. Hence, the cross sectional area of each coil will be 0.4(*width*)×0.45(*height*) mm.

Because of the limited space provided by each of the coils, a 0.05mm enamelled copper wire will be used for the fabrication of the coils. According to IEC standard No. 60317, the enamelled copper wire with nominal diameter of 0.05mm will have a nominal outer diameter of 0.06mm. Accordingly, each coil can have 6(*column*)×7(*row*), i.e. 42 turns in theoretical. Therefore, the resistance of each coil can be estimated as

$$R_{coil} = \rho_e \cdot N_t \cdot l_c = 8.706 \times 42 \times 15.88 \times 10^{-3} = 5.8\ \Omega,$$

where ρ_e is the resistance per meter of the enamelled wire that can be obtained from IEC standard, N_t the number of turns and l_c the mean perimeter of the coil, which can be calculated based on the actuator dimensions. For the series connected configuration, the resistance of the phase winding will be

$$R_{ph} = 4 \times R_{coil} = 23.2\ \Omega$$

In addition, Based on the number of turns of the phase coil, the rated current for achieving the desired current density can be found as

$$I_{rated} = J_s \times A_c / N_t = 15\text{mA}.$$

5.6.2 Calculation of phase inductances

Different from the moving-coil linear actuator, the stator windings of the PM TLA contain multiple phases with distributed configuration, the self inductances and mutual inductances are to be considered during the calculation. In addition, salient multi-pole structure and non-linear property of the magnetic core will result in the corresponding variations of the phase inductances. Therefore, detailed discussion and analysis on the phase inductances will be conducted in the following.

5.6.2.1 Apparent inductance vs. Differential inductance

Usually, the windings in an electric machine can be considered as a set of N discrete, coupled windings, shown in Fig.5-24. The flux linkage of each winding is a complicated function of the machine geometry, materials, and angle, θ, between the stationary and moving windings [Demerdash 1999]. Mathematically, for the j-th winding, the flux

linkage can be represented as follows:

$$\lambda_j = \lambda_j(i_1, i_2, \ldots, i_j, \ldots i_N, \theta). \tag{5.15}$$

In general, the j-th flux linkage, λ_j, is related to the k-th current, i_k, where, $k = 1, 2, \ldots, N$, through two types of coefficients. One coefficient is known as the *apparent inductance*, which is defined as

$$L_{jk}^{app} = \lambda_{jk} / i_k , \tag{5.16}$$

where λ_{jk} is the k-th component of λ_j, L_{jk}^{app} is the apparent inductance between windings j and k, and

$$L_{jk}^{app} = L_{kj}^{app} . \tag{5.17}$$

When $k = j$, L_{jj}^{app} is the apparent self inductance of the winding j, namely

$$L_{jj}^{app} = \lambda_{jj} / i_j . \tag{5.18}$$

Another type of coefficient is known as the *differential inductance*. It is defined as the partial derivative of the flux linkage with respect to the corresponding current for the mutual inductance between the winding j and k:

$$L_{jk}^{diff} = \partial \lambda_j / \partial i_k . \tag{5.19}$$

Similarly, the differential self inductance can be expressed as:

$$L_{jj}^{diff} = \partial \lambda_j / \partial i_j \tag{5.20}$$

It can be seen that the apparent inductance and differential inductance are identical only under linear condition.

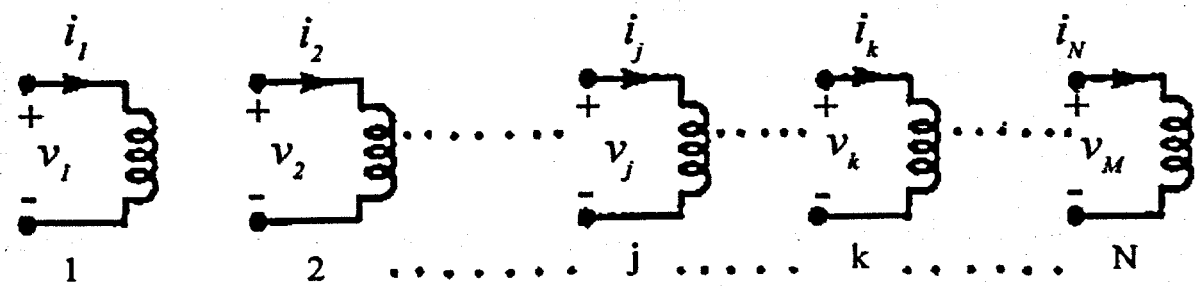

Fig.5-24 An electrical device with N windings

5.6.2.2 Inductances in dynamic machine model

The following equation is commonly used for analysing the dynamic performance of a multi-phase electromagnetic device:

$$u_j = R_j i_j + d\lambda_j / dt \ , \quad j = 1,2,...,N \ , \tag{5.21}$$

where R_j is the resistance of phase j, and u_j the phase voltage. According to (5.15), the derivative of the flux linkage in (5.21) can be expressed as

$$d\lambda_j / dt = \sum_{k=1}^{N} \frac{\partial \lambda_j}{\partial i_k} \frac{di_k}{dt} + \omega \frac{\partial \lambda_j}{\partial \theta} = \sum_{k=1}^{N} L_{jk}^{diff} \frac{di_k}{dt} + \omega \frac{\partial \lambda_j}{\partial \theta}, \tag{5.22}$$

where $\omega = d\theta/dt$ is the angular speed of the rotary component of the device. It can be seen that the differential inductances should be employed in the dynamic model of an electromagnetic device. Consequently, the method previously used for the inductance calculation of the moving-coil linear actuator is inaccurate when the device contains the non-linear magnetic material, since it is the solution for apparent inductance.

5.6.2.3 Calculation of differential inductances

5.6.2.3.1 Energy and current perturbation

One of the methods for computing the differential inductances is to use the numerical magnetic field solutions in conjunction with energy and current (E/C) perturbation technique.

Considering a conservative magnetic system with N windings as shown in Fig.5-24, the sum of the magnetic energy W_M, and co-energy, W_M', of the system is given by

$$W_M + W_M' = \lambda_1 i_1 + \lambda_2 i_2 + \cdots + \lambda_N i_N . \tag{5.23}$$

Accordingly, the change in the stored magnetic energy due to an infinitesimal change in flux linkage at a fixed set of currents can be obtained by

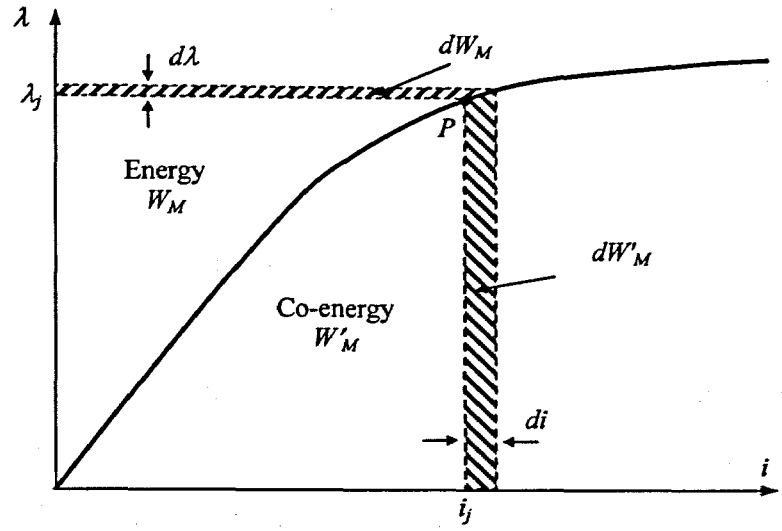

Fig.5-25 Magnetic energy and co-energy for a single coil

$$dW_M = i_1 d\lambda_1 + i_2 d\lambda_2 + \cdots + i_N d\lambda_N . \tag{5.24}$$

This differential of the magnetic energy is illustrated in Fig.5-25 for a single coil. The λ-i curve in the figure is the magnetization characteristic of the non-linear magnetic material in the system and P is the magnetic operational point of the material. If fixing the flux linkages while simultaneously introducing an infinitesimal change in the winding currents that produce a corresponding change in the co-energy, as shown in Fig.5-25, following change of the co-energy can be obtained

$$dW_M' = \lambda_1 di_1 + \lambda_2 di_2 + \cdots + \lambda_N di_N . \tag{5.25}$$

This differential may also be written as

$$dW_M' = \frac{\partial W_M'}{\partial i_1} di_1 + \frac{\partial W_M'}{\partial i_2} di_2 + \cdots + \frac{\partial W_M'}{\partial i_N} di_N = \sum_{j=1}^{N} \frac{\partial W_M'}{\partial i_j} di_j . \tag{5.26}$$

Comparing the corresponding terms of (5.25) and (5.26), reveals that:

$$\lambda_j = \partial W_M' / \partial i_j , \quad j = 1, 2, \ldots, N . \tag{5.27}$$

Differentiating both sides of (5.27) with respect to the k-th winding current yields the differential inductance as follows

$$L_{jk}^{diff} = \partial \lambda_j / \partial i_k = \partial^2 W_M' / \partial i_j \partial i_k \big|_P , \quad j, k = 1, 2, \ldots, N . \tag{5.28}$$

When $j = k$, the self differential inductance of winding j is given by

$$L_{jj}^{diff} = \partial\lambda_j / \partial i_j = \partial^2 W_M^{'} / \partial^2 i_j \big|_p, \quad j = 1,2,\ldots,N. \tag{5.29}$$

Consequently, the differential inductances can be found by applying (5.28) and (5.29) under the specified current conditions.

5.6.2.3.2 Numerical solution for E/C perturbation

In order to make the E/C technique usable in the numerical solutions, discretisation of the above method is required. By applying the central divided difference to (5.28) and (5.29), the following relationships can be yielded (refer to Appendix B),

$$\begin{aligned} L_{jk}^{diff} &= \partial^2 W_M^{'} / \partial i_j \partial i_k \\ &\cong [W_M^{'}(i_j + \Delta i_j, i_k + \Delta i_k) - W_M^{'}(i_j - \Delta i_j, i_k + \Delta i_k) \\ &\quad - W_M^{'}(i_j + \Delta i_j, i_k - \Delta i_k) + W_M^{'}(i_j - \Delta i_j, i_k - \Delta i_k)] / 4\Delta i_j \Delta i_k \end{aligned} \tag{5.30}$$

$$\begin{aligned} L_{jj}^{diff} &= \partial^2 W_M^{'} / \partial i_j^2 \\ &\cong [W_M^{'}(i_j + \Delta i_j) - 2W_M^{'}(i_j) + W_M^{'}(i_j - \Delta i_j)] / (\Delta i_j)^2 \end{aligned} \tag{5.31}$$

By using (5.30) and (5.31), the differential inductances can be readily obtained by computing the co-energy of the magnetic system under the specified current conditions. Nonetheless, accuracy problem will arise when dealing with the electromagnetic devices containing the PMs, and this will lead to the method not to be directly applicable in the numerical solutions.

It is known that the magnetic field is dominated by the magnets in a PM machine and the operational point of the non-linear magnetic material is hence determined. The magnetic field produced by the winding currents, on the other hand, only accounts for a very small amount, normally less than 10%. Consequently, compared to that generated by the PMs, the magnetic energy produced by the winding current is considerably small, especially in case of a small current perturbation. During numerical computation, the incremental energy generated by the current perturbation, or the differences between the co-energies, e.g. $W'_M(i+\Delta i)$ and $W'_M(i-\Delta i)$, are overwhelmed by the numerical computational errors and are not able to be used for the inductances calculation.

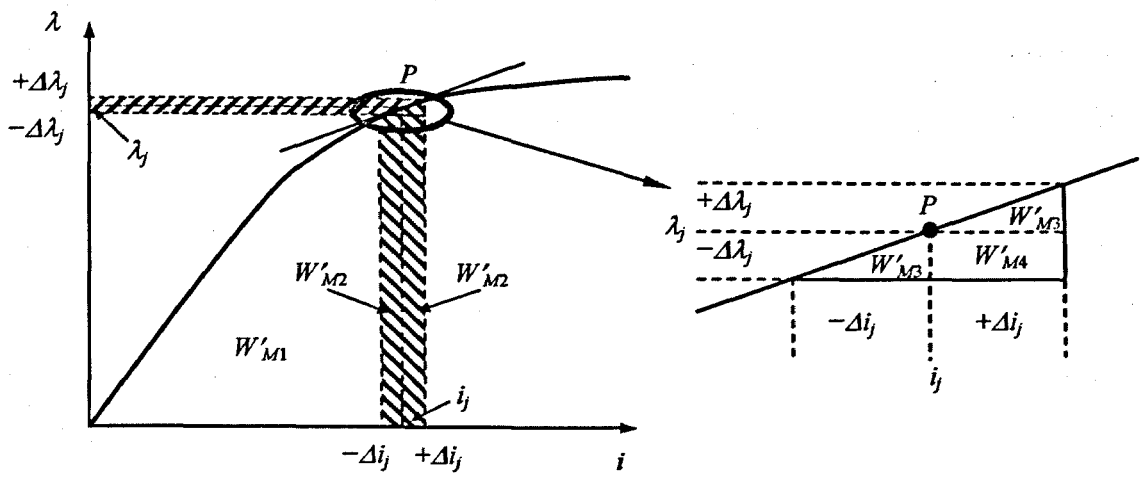

Fig.5-26 Numerical solution for E/C perturbation

One of the possible resolutions is to eliminate the huge co-energy produced by the PMs before the calculation of the co-energy caused by current perturbations. Considering a current perturbation in a single coil shown in Fig.5-26(a), due to the small value of current perturbation, the non-linear λ-i curve can be piece wisely linearised near the operational point P, as shown in the figure, and the slope of the tangent of the λ–i curve at point P is known as the differential permeability of the magnetic material at the operational point. Considering the magnetic co-energies in (5.31), one can obtain the following relationships based on the analysis illustrated in Fig.5-26:

$$W_M'(i_j - \Delta i_j) = W_{M1}', \tag{5.32}$$

$$W_M'(i_j) = W_{M1}' + W_{M2}' + W_{M3}', \tag{5.33}$$

$$W_M'(i_j + \Delta i_j) = W_{M1}' + 2W_{M2}' + 2W_{M3}' + W_{M4}'. \tag{5.34}$$

Substituting (5.32), (5.33) and (5.34) into (5.31), one can obtain the differential self inductance as

$$L_{jj}^{diff} = \frac{W_{M1}' - 2(W_{M1}' + W_{M2}' + W_{M3}') + W_{M1}' + 2W_{M2}' + 2W_{M3}' + W_{M4}'}{\Delta i_j^2} = \frac{W_{M4}'}{\Delta i_j^2}. \tag{5.35}$$

According to Fig.5-26(b), it is known that $W'_{M4} = \Delta\lambda_j \cdot \Delta i_j = 2W'_{M3}$, and (5.35) can be further expressed as

$$L_{jj}^{diff} = \Delta\lambda_j / \Delta i_j = 2W_{M3}' / \Delta i_j^2 \tag{5.36}$$

Consequently, a linear electromagnetic system without the PMs can be configured, in which the linear magnetic material possesses a constant permeability equal to the differential permeability of the non-linear magnetic material at the operational point P, as shown in Fig.5-27. As a result, W'_{M3} in the non-linear system shown in Fig.5-26 can be obtained by finding the co-energy in the newly configured linear system when applying a current perturbation Δi_j to the corresponding winding. Then, the differential self inductance can be worked out by solving the co-energy of such a linear electromagnetic system.

As discussed above, the reconfigured linear magnetic system can be obtained by means of linearising the magnetic core of the electromagnetic device by define its permeability with the differential permeability at the operational point. Therefore, the PMs in the device can be eliminated and only the co-energy generated by the winding current is to be calculated during the numerical solution. However, the saturation conditions can be quite different within the different regions of the magnetic core due to the uneven distribution of the magnetic field in the device. For instance, the pole pieces of the proposed linear actuator are much saturated in the regions near the air gap, especially the corners of the pole pieces. For higher accuracy, the non-linear magnetic core of the device should be discretised into a number of small regions with similar saturation conditions and each region is linearised with the corresponding differential permeabilties at its own operational point. Hence, the re-configured linear model will contain a number of different linear magnetic materials during the numerical solution.

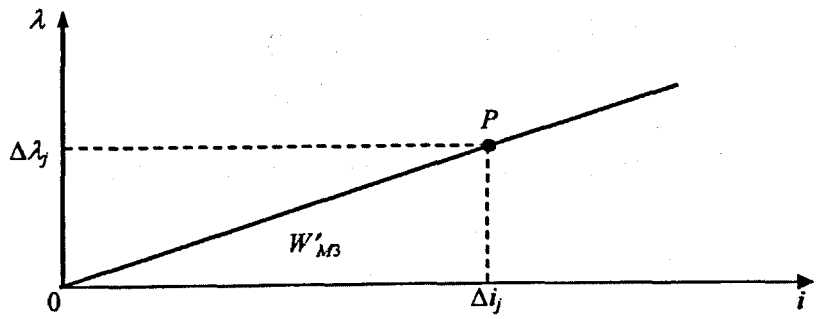

Fig.5-27 Linear system with the permeability equal to
the differential permeability at operational point P of the non-linear system

To apply the method in FEM, the non-linear magnetic field solution is firstly applied to the non-linear model with the PMs and winding currents to find the magnetic operational point of the device. The corresponding differential permeability in each of the predefined non-linear regions of the magnetic core is found by the solution. For the best computational accuracy, each element generated in the FE analysis is regarded as an independent region and the corresponding differential permeability can be worked out by FE analysis. Afterwards, the non-linear FE model is re-configured to a linear system by re-defining all the elements in the model as the linear materials with the obtained differential permeabilities and "switching off" the PMs (setting the coercive force to zero) in the model. Therefore, in the re-configured linear FE model, there will be equivalent amount of elements and materials. Finally, a linear solution is performed to obtain the co-energy produced by a current perturbation and then the differential self inductances of the winding can be computed by using (5.36). Due to the linearity of the model, the amplitude of the current perturbation is no longer relevant to the inductances and can be set as any value.

The differential mutual inductances can be found via the co-energy after all the differential self inductances have been obtained. For a linear electromagnetic system without PMs, the co-energy of the system with N coils is given by

$$W_M' = \frac{1}{2}\sum_{j=1}^{N}\sum_{k=1}^{N} L_{jk}^{diff} i_j i_k \,. \tag{5.37}$$

Thus, the differential mutual inductance between any two windings j and k can be calculated by

$$L_{jk}^{diff} = \frac{W_{M(jk)}' - \frac{1}{2} L_{jj}^{diff} \Delta i_j^2 - \frac{1}{2} L_{kk}^{diff} \Delta i_k^2}{\Delta i_j \Delta i_k}, \tag{5.38}$$

where $W'_{M(jk)}$ is the co-energy of the system when the winding j and k are excited with currents Δi_j and Δi_k.

The method can be used in either 2D or 3D FE solutions. However, due to the large number of materials in the linear FE model, the computational tasks could be huge.

Thanks to the axisymmetric structure of the designed tubular actuator, 2D FE analysis can be used and much less computation can be expected.

5.6.2.4 Inductances of the PM TLA

ANSYS electromagnetic field solution has embedded a macro for computing the differential inductances of *N*-coil system. However, as it is a general purpose solution, it is lack of flexibility and requires many predefined conditions. Hence, an ANSYS script is developed based on the above numerical E/C method for the calculation of differential inductances of the proposed PM TLA.

Fig.5-28 describes the flow chart of entire computation procedure. It consists of two major steps: the non-linear analysis for obtaining the operational point and the linear analysis for the inductance computation. During the first step, all the model information, such as the positions and indices of all the nodes and elements in the FE model, is stored for the reconstruction of the FE model in the second step. The calculated permeabilities in all the elements are stored as well for building up the material properties in second step.

In the second step, the FE model is re-constructed based on the previously stored model information. Each element in the model is defined as a material with the permeability obtained in the first step. For every translator position, six linear solutions will be performed for the three self inductances and three mutual inductances. By repeating the two-step solution at different translator positions, the results of all the inductances under different translator positions can be achieved.

Fig.5-29 shows the computed self and mutual inductances of the three phases. For comparison, the inductances without considering the non-linear property of the magnetic core are also computed and plotted in Fig.5-30. From the results, it is shown that the inductances vary with respect to the position of the translator and the variation

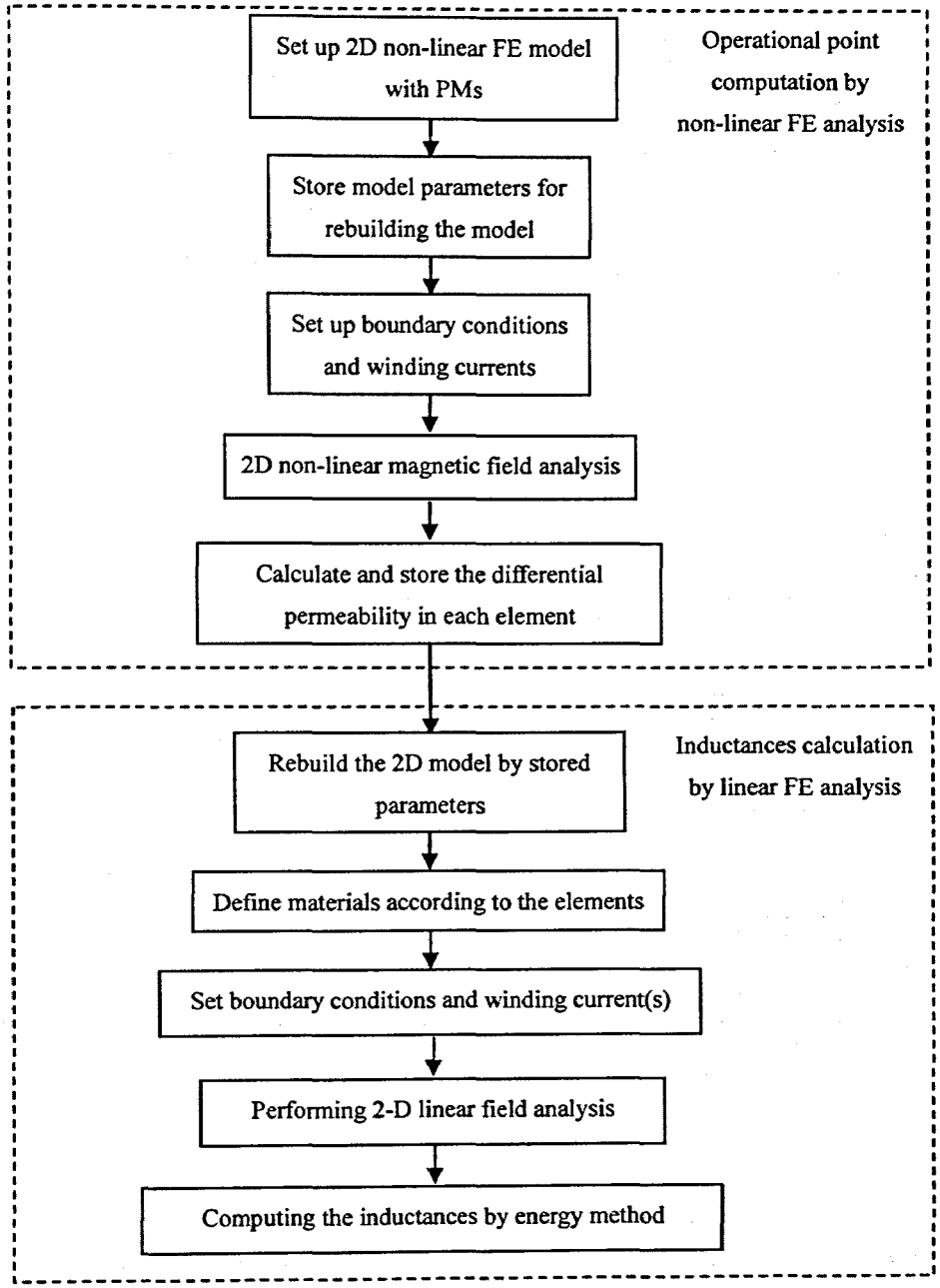

Fig.5-28 Flow chart of 2D differential inductances computation

of the inductances are also determined by the distribution the phase windings within the stator. Although the variations of the inductances are not very significant, the influences of the translator positions and the saturation effect on the magnetic core can still be clearly seen.

If the saturation effect of the magnetic core is not considered, the inductances increase when the translator moves to those positions that result in less reluctance associating

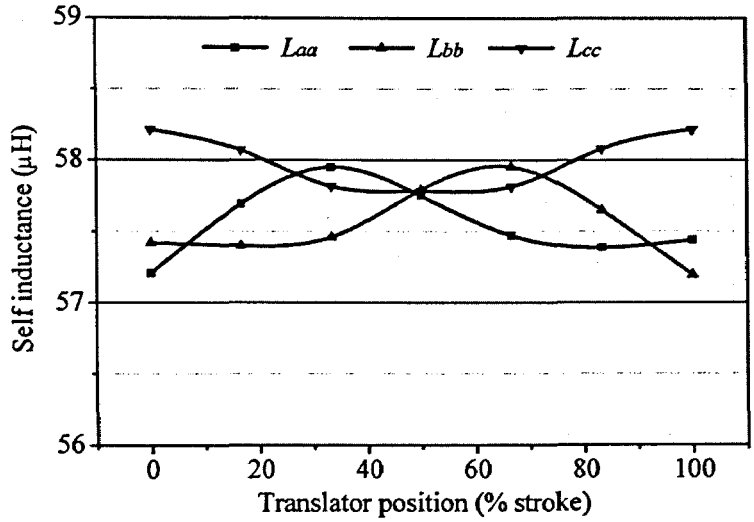

(a) Differential self inductances

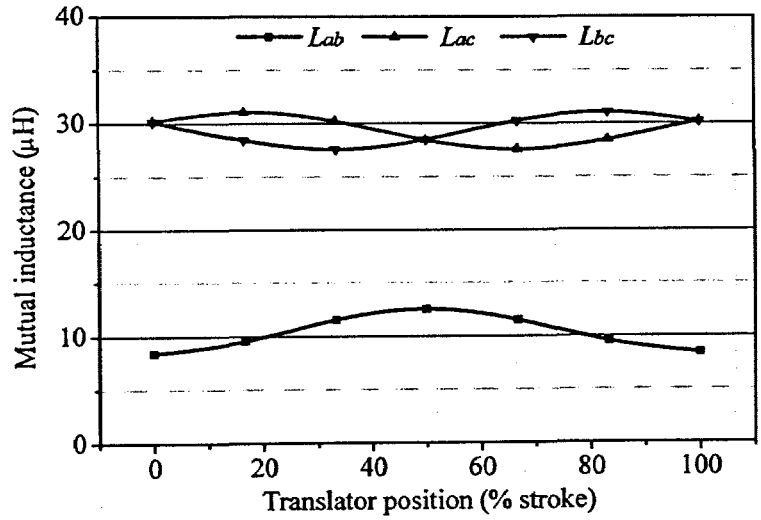

(b) Differential mutual inductances

Fig.5-29 Calculated phase inductances of the PM TLA

with the specified phase windings, as shown in Fig.5-30. The saturation of the magnetic core, however, increases the reluctances of the entire magnetic system and hence the inductances of the phase windings, including self and mutual inductances, decrease. Moreover, the saturation of the stator core caused by the approaching of the magnets offsets the reduction of the reluctances due to the mechanical geometry and the resultant reluctances become even greater because of the dramatic decrease of the permeability in the corresponding stator core. Accordingly, the self inductances at those positions that would be larger under the linear or less saturated conditions become even smaller. This can be explained schematically by an illustration shown in Fig.5-31 by using phase *A* as an example.

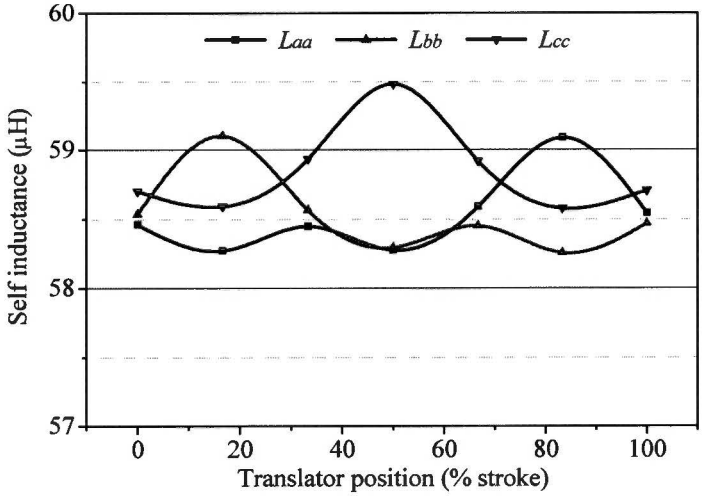

(a) Differential self inductances

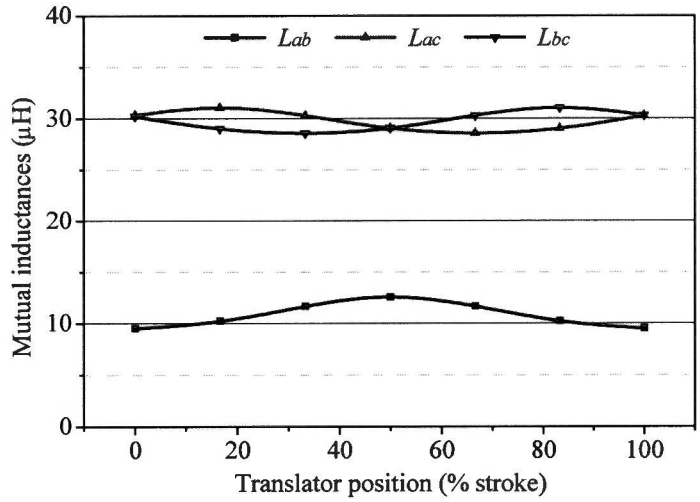

(b) Differential mutual inductances

Fig.5-30 Calculated inductances without considering the saturation effect

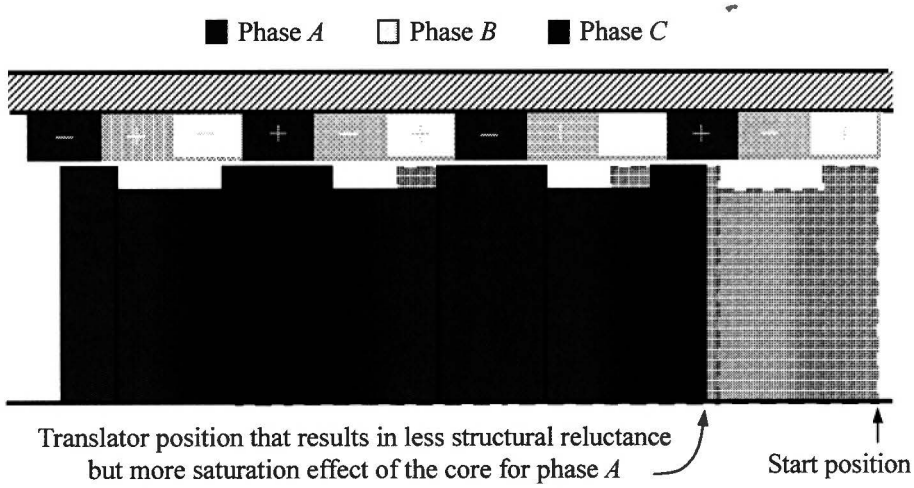

Fig.5-31 Principle of the variation of self inductances

The mutual inductances, on the other hand, are less affected by the saturation of the stator core, since two phase windings will associate more stator core region and the overall decrease of the permeability is not as significant as that in case of self inductances. Another matter that should be noticed is that, the mutual inductance between phases A and B is much smaller than the other two mutual inductances. This is due to the unsymmetrical distribution of the phase windings, which makes the coupling effect between phases A and B is less than that of others.

5.7 Dynamic Modelling of the Actuator

As discussed in chapter 4, the dynamic model is essential for the system performance analysis. The following content presents the detailed modelling of the proposed PM TLA based on the machine topology and magnetic field analysis.

5.7.1 Flux linkages of the phase windings

5.7.1.1 Flux linkage and back EMF of an enclosed coil pair

In order to analyse the flux linkage and back EMF in the phase windings of PM TLA, the flux linkage and back EMF in an enclosed cylindrical coil pair is discussed in advance. Fig.5-32 shows the structure of such an enclosed cylindrical coil pair and x is the centre axis of the coil pair. The polarity of the coils in the coil pair is in the opposite direction. When the coil pair is put into an external axisymmetric radial magnetic field, as shown in Fig.5-32(b), the flux linkage of the coil pair related to the external field is given by the following surface integration

$$\lambda_m = N_t\phi = N_t \int_{A_s} \vec{B}(x)\cdot d\vec{s} = N_t \int_{A_s} B_r(x)ds\,, \tag{5.39}$$

where N_t is the number of turns of the coil, r_c the mean radius of the coil, A_s the cylindrical surface area formed by the coil pair, and $\vec{B}(x)$ and $B_r(x)$ are the flux density

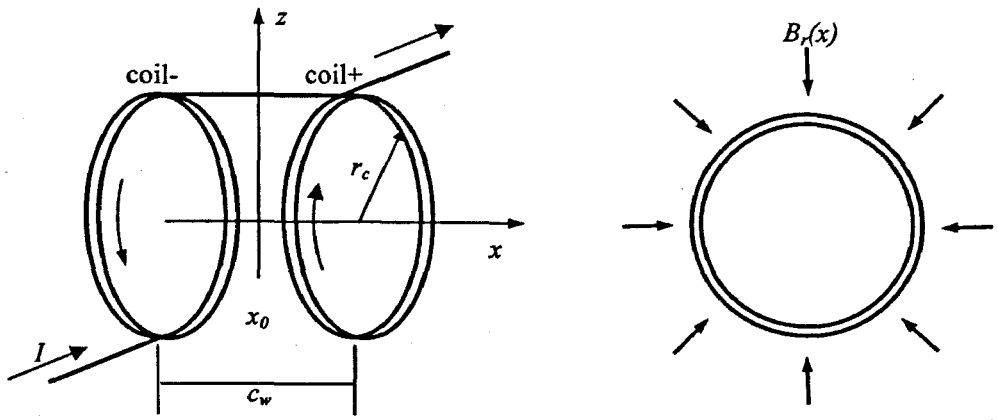

Fig.5-32 Flux linkage of an enclosed cylindrical coil pair

vector and its radial component of the magnetic field within the coils. Since $ds = 2\pi r_c dx$, (5.39) can be further written as

$$\lambda_m = 2\pi r_c N_t \int_{x_0-c_w/2}^{x_0+c_w/2} B_r(x)dx, \tag{5.40}$$

where x_0 is the centre of the coil pair and c_w the span between the two coils of the coil pair. If there is a relative movement between the coil pair and external magnetic field, a back EMF will be induced in the coil and it can be found by Faraday's law as

$$e_m = d\lambda_m/dt = 2\pi r_c N_t \frac{d}{dt}\left(\int_{x_0-c_w/2}^{x_0+c_w/2} B_r(x)dx \right). \tag{5.41}$$

By introducing $d\mathbb{B}_r(x)/dx = B_r(x)$, one can rewrite (5.41) as

$$\begin{aligned} e_m &= 2\pi r_c N_t \frac{d}{dt}\left(\mathbb{B}_r(x)\Big|_{x_0-c_w/2}^{x_0+c_w/2} \right) \\ &= 2\pi r_c N_t \frac{d}{dt}\left(\mathbb{B}_r(x_0+c_w/2) - \mathbb{B}_r(x_0-c_w/2) \right) \\ &= 2\pi r_c N_t \frac{d\left(\mathbb{B}_r(x_0+c_w/2) - \mathbb{B}_r(x_0-c_w/2) \right)}{dx}\frac{dx}{dt}, \\ &= 2\pi r_c N_t (B_r|_{x_0+c_w/2} - B_r|_{x_0-c_w/2})v_x \\ &= 2\pi r_c N_t (B_r|_{x_{0+}} - B_r|_{x_{0-}})v_x \end{aligned} \tag{5.42}$$

where v_x is the velocity in axial direction x between the coil and external field and $B_r|_{x0+}$ and $B_r|_{x0-}$ are the radial flux densities in coil + and coil –, respectively.

5.7.1.2 Flux linkages of the actuator

If the non-linear magnetic material is piece wisely linearised near the operational point, the flux linkage of each phase of the PM TLA can be expressed as follows:

$$\lambda_a = \lambda_{aa} + \lambda_{ab} + \lambda_{ac} + \lambda_{am}, \tag{5.43}$$

$$\lambda_b = \lambda_{ba} + \lambda_{bb} + \lambda_{bc} + \lambda_{bm}, \tag{5.44}$$

$$\lambda_c = \lambda_{ca} + \lambda_{cb} + \lambda_{cc} + \lambda_{cm}, \tag{5.45}$$

where λ_{am}, λ_{am}, and λ_{am} are the magnetising flux linkage produced by the PMs on the translator and λ_{ij} is the flux linkage of phase i that is corresponding to the current in phase j, and $i, j \in a$, b or c. According to the analysis of inductances in section 5.6, λ_{ij} can be given by $L_{ij}^{diff} \cdot i_j$ under the condition of piecewise linearization. For convenience, the subscript ^{diff} for the differential inductance will be omitted in the rest of the thesis and all the inductances hereinafter will refer to the differential inductances unless otherwise stated. Consequently, (5.43) to (5.45) can be rewritten as

$$\lambda_a = L_{aa} i_a + L_{ab} i_b + L_{ac} i_c + \lambda_{am}, \tag{5.46}$$

$$\lambda_b = L_{ba} i_a + L_{bb} i_b + L_{bc} i_c + \lambda_{bm}, \tag{5.47}$$

$$\lambda_c = L_{ca} i_a + L_{cb} i_b + L_{cc} i_c + \lambda_{cm}. \tag{5.48}$$

The magnetising flux linkage of each phase generated by the magnets can be worked out based on the analysis of the flux linkage of enclosed cylindrical coil pair. Since each phase winding of the designed actuator contains two enclosed cylindrical coil pairs, the magnetising flux linkages of these cylindrical coil pairs in three phases are

$$\lambda_{am1} = 2\pi r_c N_t \int_{x_{a01}-c_w/2}^{x_{a01}+c_w/2} B_r(x)dx, \tag{5.49}$$

$$\lambda_{am2} = 2\pi r_c N_t \int_{x_{a02}-c_w/2}^{x_{a02}+c_w/2} B_r(x)dx, \tag{5.50}$$

$$\lambda_{bm1} = 2\pi r_c N_t \int_{x_{b01}-c_w/2}^{x_{b01}+c_w/2} B_r(x)dx, \tag{5.51}$$

$$\lambda_{bm2} = 2\pi r_c N_t \int_{x_{b02}-c_w/2}^{x_{b02}+c_w/2} B_r(x)dx, \tag{5.52}$$

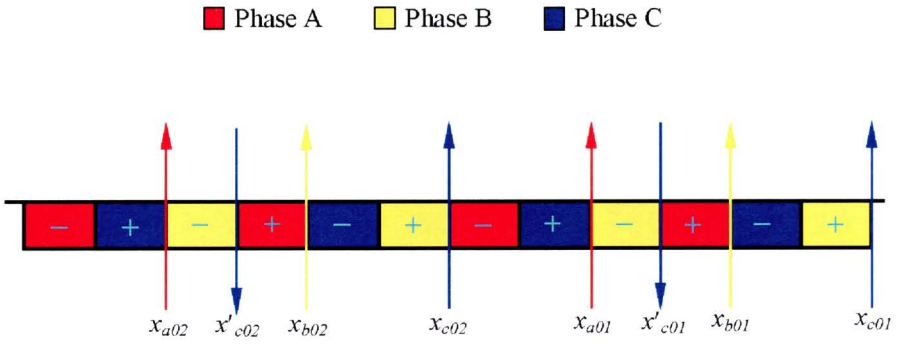

Fig.5-33 Axes and centre positions of the coil pairs in stator windings

$$\lambda_{cm1} = 2\pi r_c N_t \int_{x_{c01}-c_w/2}^{x_{c01}+c_w/2} B_r(x)dx, \tag{5.53}$$

$$\lambda_{cm2} = 2\pi r_c N_t \int_{x_{c02}-c_w/2}^{x_{c02}+c_w/2} B_r(x)dx, \tag{5.54}$$

and

$$\lambda_{am} = \lambda_{am1} + \lambda_{am2}, \tag{5.55}$$

$$\lambda_{bm} = \lambda_{bm1} + \lambda_{bm2}, \tag{5.56}$$

$$\lambda_{cm} = \lambda_{cm1} + \lambda_{cm2}. \tag{5.57}$$

According to the winding structure of the actuator, the total length of the stator windings can be found as $4c_w$, and the centre axes of the coil pairs in the phase winding are illustrated in Fig.5-33 and the centre positions are listed in Table 5-3.

Table 5-3 Centre positions of the coil pairs in the phase windings

Phase A		Phase B		Phase C	
x_{a01}	x_{a02}	x_{b01}	x_{b02}	x_{c01}	x_{c02}
$4/3c_w$	$10/3c_w$	$2/3c_w$	$8/3c_w$	0	$2c_w$

Because x_{c01} is zero, the position will be negative when calculating the magnetising flux linkage in (5.53). In order to avoid this problem, alternative centre axes, x'_{c01} and x'_{c02}, are use for the coil pairs in phase C, as shown in Fig.5-33. As a result, $x'_{c01}=c_w$ and $x'_{c02}=3c_w$, and the flux linkages of phase C will become

$$\lambda_{cm1} = -2\pi r_c N_t \int_{x'_{c01}-c_w/2}^{x'_{c01}+c_w/2} B_r(x)dx, \tag{5.58}$$

$$\lambda_{cm2} = -2\pi r_c N_t \int_{x_{c02}-c_w/2}^{x_{c02}+c_w/2} B_r(x)dx . \tag{5.59}$$

5.7.2 Electrical equations of the actuator

The electrical circuit equation of each phase of the actuator can be expressed as

$$u_a = R_a i_a + d\lambda_a/dt , \tag{5.60}$$

$$u_b = R_b i_b + d\lambda_b/dt , \tag{5.61}$$

$$u_c = R_c i_c + d\lambda_c/dt . \tag{5.62}$$

From (5.46), (5.47) and (5.48), the differentials of the flux linkages in the above equations can be derived as

$$\begin{aligned} \frac{d\lambda_a}{dt} &= \frac{d(L_{aa}i_a)}{dt} + \frac{d(L_{ab}i_b)}{dt} + \frac{d(L_{ac}i_c)}{dt} + \frac{d\lambda_{am}}{dt} \\ &= L_{aa}\frac{di_a}{dt} + i_a\frac{dL_{aa}}{dt} + L_{ab}\frac{di_b}{dt} + i_b\frac{dL_{ab}}{dt} + L_{ac}\frac{di_c}{dt} + i_c\frac{dL_{ac}}{dt} + \frac{d\lambda_{am}}{dt} \end{aligned} , \tag{5.63}$$

$$\begin{aligned} \frac{d\lambda_b}{dt} &= \frac{d(L_{ba}i_a)}{dt} + \frac{d(L_{bb}i_b)}{dt} + \frac{d(L_{bc}i_c)}{dt} + \frac{d\lambda_{bm}}{dt} \\ &= L_{ba}\frac{di_a}{dt} + i_a\frac{dL_{ba}}{dt} + L_{bb}\frac{di_b}{dt} + i_b\frac{dL_{bb}}{dt} + L_{bc}\frac{di_c}{dt} + i_c\frac{dL_{bc}}{dt} + \frac{d\lambda_{bm}}{dt} \end{aligned} , \tag{5.64}$$

$$\begin{aligned} \frac{d\lambda_c}{dt} &= \frac{d(L_{ca}i_a)}{dt} + \frac{d(L_{cb}i_b)}{dt} + \frac{d(L_{cc}i_c)}{dt} + \frac{d\lambda_{cm}}{dt} \\ &= L_{ca}\frac{di_a}{dt} + i_a\frac{dL_{ca}}{dt} + L_{cb}\frac{di_b}{dt} + i_b\frac{dL_{cb}}{dt} + L_{cc}\frac{di_c}{dt} + i_c\frac{dL_{cc}}{dt} + \frac{d\lambda_{cm}}{dt} \end{aligned} . \tag{5.65}$$

Generally, the inductances of the actuator are the functions of corresponding currents and translator position with respect to the stator, x_{sm}. As a result, the differentials of inductances in the equations can be derived as

$$\frac{dL_{aa}(i_a, x_{sm})}{dt} = \frac{\partial L_{aa}(i_a, x_{sm})}{\partial i_a}\frac{di_a}{dt} + \frac{\partial L_{aa}(i_a, x_{sm})}{\partial x_{sm}}v_{sm} , \tag{5.66}$$

$$\frac{dL_{bb}(i_b, x_{sm})}{dt} = \frac{\partial L_{bb}(i_b, x_{sm})}{\partial i_b}\frac{di_b}{dt} + \frac{\partial L_{bb}(i_b, x_{sm})}{\partial x_{sm}}v_{sm} , \tag{5.67}$$

$$\frac{dL_{cc}(i_c,x_{sm})}{dt}=\frac{\partial L_{cc}(i_a,x_{sm})}{\partial i_c}\frac{di_c}{dt}+\frac{\partial L_{cc}(i_c,x_{sm})}{\partial x_{sm}}v_{sm}, \tag{5.68}$$

$$\frac{dL_{ab}(i_b,x_{sm})}{dt}=\frac{\partial L_{ab}(i_b,x_{sm})}{\partial i_b}\frac{di_b}{dt}+\frac{\partial L_{ab}(i_b,x_{sm})}{\partial x_{sm}}v_{sm}, \tag{5.69}$$

$$\frac{dL_{ac}(i_c,x_{sm})}{dt}=\frac{\partial L_{ac}(i_a,x_{sm})}{\partial i_c}\frac{di_c}{dt}+\frac{\partial L_{ac}(i_c,x_{sm})}{\partial x_{sm}}v_{sm}, \tag{5.70}$$

$$\frac{dL_{ba}(i_a,x_{sm})}{dt}=\frac{\partial L_{ba}(i_a,x_{sm})}{\partial i_a}\frac{di_a}{dt}+\frac{\partial L_{ba}(i_a,x_{sm})}{\partial x_{sm}}v_{sm}, \tag{5.71}$$

$$\frac{dL_{bc}(i_c,x_{sm})}{dt}=\frac{\partial L_{bc}(i_a,x_{sm})}{\partial i_c}\frac{di_c}{dt}+\frac{\partial L_{bc}(i_c,x_{sm})}{\partial x_{sm}}v_{sm}, \tag{5.72}$$

$$\frac{dL_{ca}(i_a,x_{sm})}{dt}=\frac{\partial L_{ca}(i_a,x_{sm})}{\partial i_a}\frac{di_a}{dt}+\frac{\partial L_{ca}(i_a,x_{sm})}{\partial x_{sm}}v_{sm}, \tag{5.73}$$

$$\frac{dL_{cb}(i_b,x_{sm})}{dt}=\frac{\partial L_{cb}(i_b,x_{sm})}{\partial i_b}\frac{di_b}{dt}+\frac{\partial L_{cb}(i_b,x_{sm})}{\partial x_{sm}}v_{sm}, \tag{5.74}$$

where $v_{sm}=dx_{sm}/dt$ is the relative velocity between the translator and stator. The derivatives of λ_{am}, λ_{bm}, and λ_{cm} are the back EMFs due to the PMs. Based on the previous analysis of the magnetizing flux linkage in each phase winding, these EMFs can be further expressed as

$$\begin{aligned} e_{am}&=\frac{d\lambda_{am}}{dt}=\frac{d\lambda_{am1}}{dt}+\frac{d\lambda_{am2}}{dt}\\ &=2\pi r_c N_t(B_r|_{x_{a01+}}+B_r|_{x_{a02+}}-B_r|_{x_{a01-}}-B_r|_{x_{a02-}})v_{sm}\end{aligned}, \tag{5.75}$$

$$\begin{aligned} e_{bm}&=\frac{d\lambda_{bm}}{dt}=\frac{d\lambda_{bm1}}{dt}+\frac{d\lambda_{bm2}}{dt}\\ &=2\pi r_c N_t(B_r|_{x_{b01+}}+B_r|_{x_{b02+}}-B_r|_{x_{b01-}}-B_r|_{x_{b02-}})v_{sm}\end{aligned}, \tag{5.76}$$

$$\begin{aligned} e_{cm}&=\frac{d\lambda_{cm}}{dt}=\frac{d\lambda_{cm1}}{dt}+\frac{d\lambda_{cm2}}{dt}\\ &=2\pi r_c N_t(B_r|_{x_{c01+}}+B_r|_{x_{c02+}}-B_r|_{x_{c01-}}-B_r|_{x_{c02-}})v_{sm}\end{aligned}. \tag{5.77}$$

Substituting the above results into (5.63), (5.64), and (5.65), one obtains the following expressions of the derivatives of the flux linkages in each phase

$$\begin{aligned}\frac{d\lambda_a}{dt} &= \left(L_{aa}+i_a\frac{\partial L_{aa}}{\partial i_a}\right)\frac{di_a}{dt}+\left(L_{ab}+i_b\frac{\partial L_{ab}}{\partial i_b}\right)\frac{di_b}{dt}+\left(L_{ac}+i_c\frac{\partial L_{ac}}{\partial i_c}\right)\frac{di_c}{dt}\\ &\quad+\left(i_a\frac{\partial L_{aa}}{\partial x}+i_b\frac{\partial L_{ab}}{\partial x}+i_c\frac{\partial L_{ac}}{\partial x}\right)v_{sm}+e_{am}\\ &= L_{aa}^{'}\frac{di_a}{dt}+L_{ab}^{'}\frac{di_b}{dt}+L_{ac}^{'}\frac{di_c}{dt}+e_{as}+e_{am}\end{aligned}, \quad (5.78)$$

$$\begin{aligned}\frac{d\lambda_b}{dt} &= \left(L_{ba}+i_a\frac{\partial L_{ba}}{\partial i_a}\right)\frac{di_a}{dt}+\left(L_{bb}+i_b\frac{\partial L_{bb}}{\partial i_b}\right)\frac{di_b}{dt}+\left(L_{bc}+i_c\frac{\partial L_{bc}}{\partial i_c}\right)\frac{di_c}{dt}\\ &\quad+\left(i_a\frac{\partial L_{ba}}{\partial x}+i_b\frac{\partial L_{bb}}{\partial x}+i_c\frac{\partial L_{bc}}{\partial x}\right)v_{sm}+e_{bm}\\ &= L_{ba}^{'}\frac{di_a}{dt}+L_{bb}^{'}\frac{di_b}{dt}+L_{bc}^{'}\frac{di_c}{dt}+e_{bs}+e_{bm}\end{aligned}, \quad (5.79)$$

$$\begin{aligned}\frac{d\lambda_c}{dt} &= \left(L_{ca}+i_a\frac{\partial L_{ca}}{\partial i_a}\right)\frac{di_a}{dt}+\left(L_{cb}+i_b\frac{\partial L_{cb}}{\partial i_b}\right)\frac{di_b}{dt}+\left(L_{cc}+i_c\frac{\partial L_{cc}}{\partial i_c}\right)\frac{di_c}{dt}\\ &\quad+\left(i_a\frac{\partial L_{ca}}{\partial x}+i_b\frac{\partial L_{cb}}{\partial x}+i_c\frac{\partial L_{cc}}{\partial x}\right)v_{sm}+e_{cm}\\ &= L_{ca}^{'}\frac{di_a}{dt}+L_{cb}^{'}\frac{di_b}{dt}+L_{cc}^{'}\frac{di_c}{dt}+e_{cs}+e_{cm}\end{aligned}, \quad (5.80)$$

where

$$L_{ij}^{'}=L_{ij}+i_j\frac{\partial L_{ij}}{\partial i_j},\quad i,j=a,b,c \quad (5.81)$$

are the dynamic inductances of the machine, and

$$\begin{aligned}e_{as} &= \left(i_a\frac{\partial L_{aa}}{\partial x}+i_b\frac{\partial L_{ab}}{\partial x}+i_c\frac{\partial L_{ac}}{\partial x}\right)v_{sm}\\ e_{bs} &= \left(i_a\frac{\partial L_{ba}}{\partial x}+i_b\frac{\partial L_{bb}}{\partial x}+i_c\frac{\partial L_{bc}}{\partial x}\right)v_{sm}\\ e_{cs} &= \left(i_a\frac{\partial L_{ca}}{\partial x}+i_b\frac{\partial L_{cb}}{\partial x}+i_c\frac{\partial L_{cc}}{\partial x}\right)v_{sm}\end{aligned} \quad (5.82)$$

the back EMFs due to the machine saliencies. It can be seen that the dynamic inductance of the machine is a combination of the differential inductance and the variation of the inductance caused by the phase current. In the inductance computation it has been found that the influence of the phase currents to the inductances is considerable small because the magnetic field generated by the phase currents can hardly affect the operational point of the magnetic core. Therefore, the variation of the inductance due to the phase current can be ignored. As a result, we have $L'_{ij} \approx L_{ij}$ and

$L_{ij}=L_{ji}$. Hence, the electrical equations of the actuator become

$$u_a = R_a i_a + L_{aa}\frac{di_a}{dt} + L_{ab}\frac{di_b}{dt} + L_{ac}\frac{di_c}{dt} + e_{as} + e_{am}, \tag{5.83}$$

$$u_b = R_b i_b + L_{ab}\frac{di_a}{dt} + L_{bb}\frac{di_b}{dt} + L_{bc}\frac{di_c}{dt} + e_{bs} + e_{bm}, \tag{5.84}$$

$$u_c = R_c i_c + L_{ac}\frac{di_a}{dt} + L_{bc}\frac{di_b}{dt} + L_{cc}\frac{di_c}{dt} + e_{cs} + e_{cm}. \tag{5.85}$$

5.7.3 Electromagnetic force of the actuator

The electromagnetic force of the actuator can be obtained by taking the derivative of the system magnetic co-energy with respect to the displacement, i.e. $F_{em}=\partial W'_M/\partial x$. According to the flux linkages derived in the previous analysis, the contributed magnetic co-energy of each phase of the actuator can be found by the following integrations:

$$W'_{Ma} = \int_0^{i_a} \lambda_a di_a = \int_0^{i_a} (L_{aa}i_a + L_{ab}i_b + L_{ac}i_c + \lambda_{am}) di_a, \tag{5.86}$$

$$W'_{Mb} = \int_0^{i_b} \lambda_b di_b = \int_0^{i_b} (L_{ba}i_a + L_{bb}i_b + L_{bc}i_c + \lambda_{bm}) di_b, \tag{5.87}$$

$$W'_{Mc} = \int_0^{i_c} \lambda_c di_c = \int_0^{i_c} (L_{ca}i_a + L_{cb}i_b + L_{cc}i_c + \lambda_{cm}) di_c. \tag{5.88}$$

Since the inductances are considered free of the influences of phase currents, the co-energy of each phase can be further expressed as

$$W'_{Ma} = 1/2\, L_{aa}i_a^2 + L_{ab}i_b i_a + L_{ac}i_c i_a + \lambda_{am}i_a, \tag{5.89}$$

$$W'_{Mb} = L_{ba}i_a i_b + 1/2\, L_{bb}i_b^2 + L_{bc}i_c i_b + \lambda_{bm}i_b, \tag{5.90}$$

$$W'_{Mc} = L_{ca}i_a i_c + L_{cb}i_b i_c + 1/2\, L_{cc}i_c^2 + \lambda_{cm}i_c, \tag{5.91}$$

and the total magnetic co-energy of the actuator will be

$$\begin{aligned} W'_M = {} & 1/2\, L_{aa}i_a^2 + 1/2\, L_{bb}i_b^2 + 1/2\, L_{cc}i_c^2 + 2L_{ab}i_b i_a + 2L_{ac}i_c i_a + 2L_{bc}i_c i_b \\ & + \lambda_{am}i_a + \lambda_{bm}i_b + \lambda_{cm}i_c \end{aligned}. \tag{5.92}$$

Consequently, the electromagnetic force of the actuator can be found as

$$
\begin{aligned}
F_{em} &= \partial W_M' / \partial x \\
&= \frac{1}{2}\frac{\partial L_{aa}}{\partial x} i_a^2 + \frac{1}{2}\frac{\partial L_{bb}}{\partial x} i_b^2 + \frac{1}{2}\frac{\partial L_{cc}}{\partial x} i_c^2 + 2\frac{\partial L_{ab}}{\partial x} i_b i_a + 2\frac{\partial L_{ac}}{\partial x} i_c i_a + 2\frac{\partial L_{bc}}{\partial x} i_c i_b \\
&+ \frac{\partial \lambda_{am}}{\partial x} i_a + \frac{\partial \lambda_{bm}}{\partial x} i_b + \frac{\partial \lambda_{cm}}{\partial x} i_c \\
&= F_{ems} + F_{emm}
\end{aligned}
\tag{5.93}
$$

where

$$
F_{emm} = \frac{\partial \lambda_{am}}{\partial x} i_a + \frac{\partial \lambda_{bm}}{\partial x} i_b + \frac{\partial \lambda_{cm}}{\partial x} i_c \tag{5.94}
$$

is the force generated by the magnets, and

$$
F_{ems} = \frac{1}{2}\frac{\partial L_{aa}}{\partial x} i_a^2 + \frac{1}{2}\frac{\partial L_{bb}}{\partial x} i_b^2 + \frac{1}{2}\frac{\partial L_{cc}}{\partial x} i_c^2 + 2\frac{\partial L_{ab}}{\partial x} i_b i_a + 2\frac{\partial L_{ac}}{\partial x} i_c i_a + 2\frac{\partial L_{bc}}{\partial x} i_c i_b \tag{5.95}
$$

the force caused by the machine saliencies. According to the equations of the flux linkages, F_{emm} can be further expressed as

$$
\begin{aligned}
F_{emm} = {} & 2\pi r_c N_t (B_r|_{x_{a01+}} + B_r|_{x_{a02+}} - B_r|_{x_{a01-}} - B_r|_{x_{a02-}}) i_a \\
& + 2\pi r_c N_t (B_r|_{x_{b01+}} + B_r|_{x_{b02+}} - B_r|_{x_{b01-}} - B_r|_{x_{b02-}}) i_b \\
& + 2\pi r_c N_t (B_r|_{x_{c01+}} + B_r|_{x_{c02+}} - B_r|_{x_{c01-}} - B_r|_{x_{c02-}}) i_c
\end{aligned}
\tag{5.96}
$$

5.7.4 Dynamic model of the actuator

Equations (5.83), (5.84), (5.85), and (5.93) form the electrical dynamic model of the PM TLA. By using the parameters and the coil flux densities obtained by the numerical magnetic field analysis, the dynamic performances of the actuator can be readily achieved by solving the above and the kinetic equations of the actuator that expressed as

$$
dv_{sm} / dt = (F_{em} - F_{load}) / m_a , \tag{5.97}
$$

$$
dx_{sm} / dt = v_{sm} , \tag{5.98}
$$

where m_a is the mass of the translator, and F_{load} the external load force. Combination of the electrical equations with the above kinetic equations constitutes the

electromechanical model of the actuator and the comprehensive dynamic performances can be analysed based on the model.

5.7.5 Application of the dynamic model

For verification, the developed dynamic electromechanical model of the actuator is applied to predict the dynamic behaviour when the actuator is powered by a balanced three phase sinusoidal excitation. The amplitude of the phase voltage is set according to the rated current required for the actuator. The initial phase angle of the excitation voltage is defined according to the initial position of the translator. If the initial position of the translator is at the right hand side of the stator windings and a maximum starting force is desired, the initial phase shift of phase *A*, *B* and *C* voltage should be -π/3, π/3 and - π electrical degrees, respectively, based on the flux densities of the phase coils. Thus, the three-phase voltage will be as follows

$$\begin{cases} u_a = \sqrt{2}U_0 \sin\left(2\pi ft - \pi/3\right) \\ u_b = \sqrt{2}U_0 \sin\left(2\pi ft + \pi/3\right), \\ u_c = \sqrt{2}U_0 \sin\left(2\pi ft - \pi\right) \end{cases} \tag{5.99}$$

where U_0 is the *rms* value of the input phase voltage.

The numerical solution for the dynamic model of the actuator is implemented by using the m-script provided by the MATLAB and can be executed directly in the MATLAB environment. During the solution, the phase inductances and coil flux densities obtained by the FE analysis are inputted into the program for the simulation. Because the data points are limited, the inductances and coil flux densities at arbitrary translator positions are obtained by the linear interpolation. In addition, during the analysis, the masses of the stator and translator are assumed to be 0.9g and 0.5g according the actuator material and dimensions. During the simulation, the actuator is running without any load.

Figs.5-34 to 36 show the electrical and mechanical results obtained from the simulation

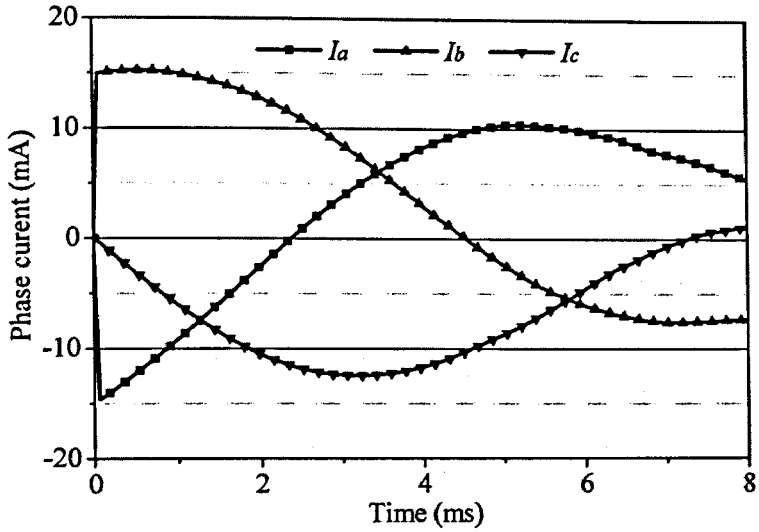

Fig.5-34 Phase currents of the actuator

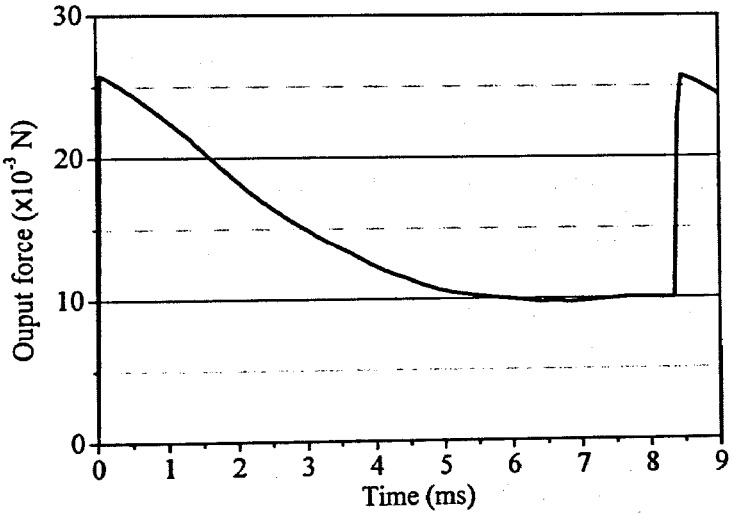

Fig.5-35 Output force of the actuator

when the actuator is running at 60Hz. It is shown that the translator can run smoothly throughout the entire stroke. However, the output force cannot be always at the actuator's maximum attainable value during the operation because the translator is not able to strictly follow the phase of the excitation current without the help of a position sensor. Therefore, in such an open-loop driving system, it is essential to keep the frequency of the applied voltage at a particular value (60 Hz in this case), which is determined by the mechanical constant of the actuator system, for stable operation of the actuator.

The back EMFs and the force caused by the machine saliencies are also plotted in Figs.5-37 and 38. It is interesting to see that the force caused by the machine saliencies

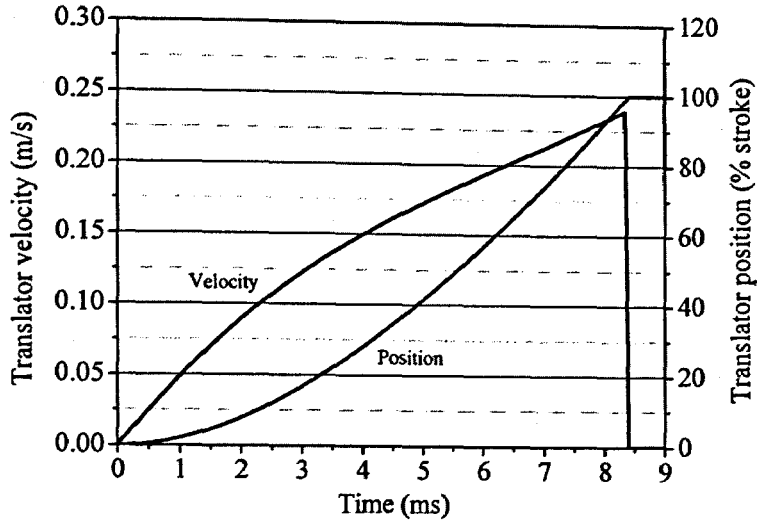

Fig.5-36 Translator velocity and position during the operation

is not always against the motion of the translator. It can help the operation under certain conditions. However, because the saliencies in the actuator are rather small, the influences can hardly be seen in the overall force and currents of the actuator. The saw-shape fluctuation appeared in the figures is not true in practice and is caused by the linear interpolation of the inductances employed in the numerical computation.

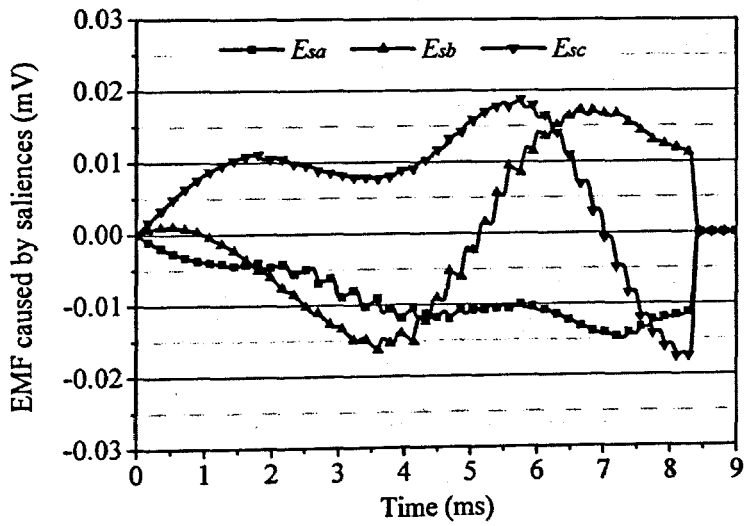

Fig.5-37 EMFs caused by the machine saliencies

If the frequency of the applied voltage is too low or too high compared to the natural frequency of the actuator system, the operation of the actuator can be unstable. Fig.5-39 shows the velocity and position of the translator when actuator is running at 10Hz. Because the translator travels faster, it is running out of the phase with the excitation

current and the negative force will be generated when the translator position and phase currents are mismatching. As a result, the operation of the actuator fluctuates. This is unacceptable in practice. Therefore, in order to achieve a satisfactory operational performance, a closed-loop driving control with the help of translator position information should be applied.

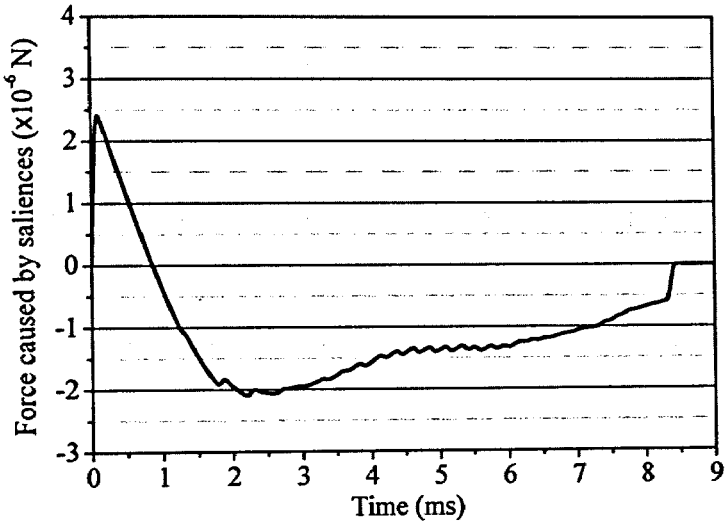

Fig.5-38 Force caused by the machine saliencies

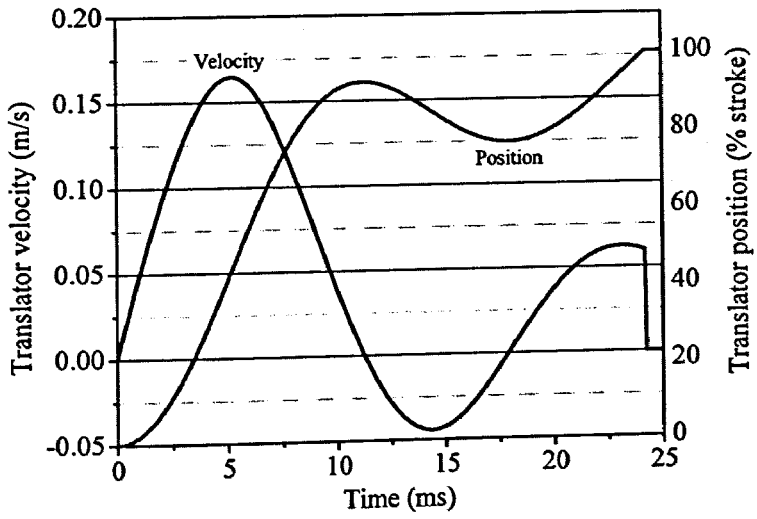

Fig.5-39 Translator velocity and position during the operation

5.8 Conclusion

The detailed design and analysis of a moving-magnet PM TLA are presented in this

chapter. Through the analysis of different possible topologies and dimensions of the PM TLA, an appropriate design of the actuator is implemented. The numerical magnetic field solutions are used for the design verification, characteristics prediction and machine parameters calculation. The results reveal that the proposed PM TLA has higher air gap flux density, better force capability, and higher efficiency compared to the moving-coil linear actuator proposed in chapter 4.

A comprehensive dynamic model of the actuator is developed by using the results from the magnetic field analysis. The application of the model for prediction of the actuator performance under three-phase excitation shows the validity and effectiveness of the model. The developed model will be a crucial tool for the design and analysis of the actuation control for the proposed microrobot.

Chapter 6

PROTOTYPE FABRICATION AND EVALUATION

6.1 Introduction

Two different scaled laboratory prototypes of the proposed moving-magnet PM TLA are fabricated to verify the design. One is five times larger than the designed dimensions and the other is made with the designed size. The large sized prototype is to be used for the verification of the design and analysis conducted in chapter 5 as its dimensions with desired machining precision can be easily achieved. The small sized prototype with the designed dimensions, on the other hand, which may be of limited performance due to the difficulties in construction, is used to examine the fabrication techniques when the size of the actuator is getting smaller.

The performances and parameters of the prototypes are re-examined by modifying the FE model according to the construction and actual dimensions of the prototypes. The forces and phase inductances are measured by a specially designed test bench and the results are compared with the predicted values.

6.2 Construction of the Prototypes

6.2.1 Basics of laser cutting technology

Since the proposed actuator contains many miniature components with high precision, the conventional methods such as punching, nibbling, acid etching or normal electrical discharge machining (EDM) are no longer able to meet the machining requirements. The precision laser cutting technology is therefore employed for the machining of the key components of the designed actuator.

The precision laser cutting technology can be applied to almost any metals and alloys, and many non-metal materials. The basic principle of the laser cutting is illustrated in Fig.6-1 [Andrew 2002]. During the machining process, a pulsed high quality laser beam is focused on the material being processed. The high energy applied by the laser beam melts down or evaporates the material along the cutting edge and the desired shape of the component can be obtained. Usually, two methods are predominately used in the precision cutting of metals. In exothermic laser cutting, either oxygen or air is used as the process gas. The material is burned by the oxygen and blown downwards out of the

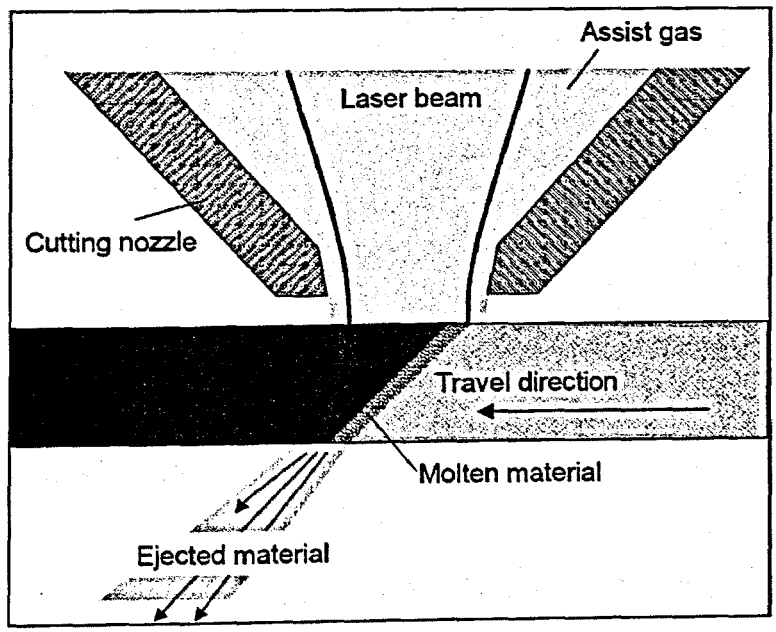

Fig.6-1 Operating principle of laser cutting

cut by the assist gas jet that does not react. In endothermic laser cutting, an inert gas such as nitrogen is used. The material that is melted by the laser beam is driven downwards out of the cut by the gas pressure and the frictional force of the gas alone. For this reason, a higher gas pressure is generally required in the endothermic laser cutting process.

The laser cutting technology offers several advantages. Firstly, laser cut edges have a small kerf width, low roughness, and high accuracy. In addition, the high precision at which parts can be made results in less need for subsequent machining. Moreover, the facility of changing contours offers flexibility in products. Fig.6-2 shows a photo of the laser cutting equipment in the Laser Micromachining Solutions of Macquarie University in New South Wales. With the help of their precision technology, the fabrication of the components for the designed actuator, such as stator cores and pole pieces, is accomplished.

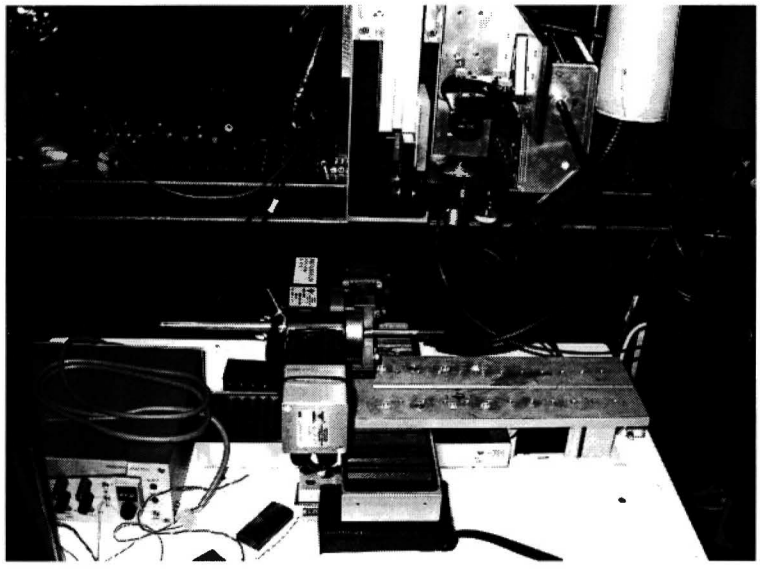

Fig.6-2 The laser cutting equipment used for the fabrication of designed actuator

6.2.2 Fabrication of stators

The stator core of the actuator is made by rolling the METGLAS 2605SA1 thin-film ribbon. The thickness of the ribbon is 1 mil (0.0254mm). Because of the short length of

the stator core, it would be convenient to firstly construct a cylinder tube using the raw material of the METGLAS ribbon and then cut it into the desired length. The fabrication procedure is illustrated in Fig.6-3. There are two slots made on the opposite sides of the stator core that are used for the lead wires of the stator windings coming out of the actuator. The use of two slots is to minimise the structural influence on the stator core.

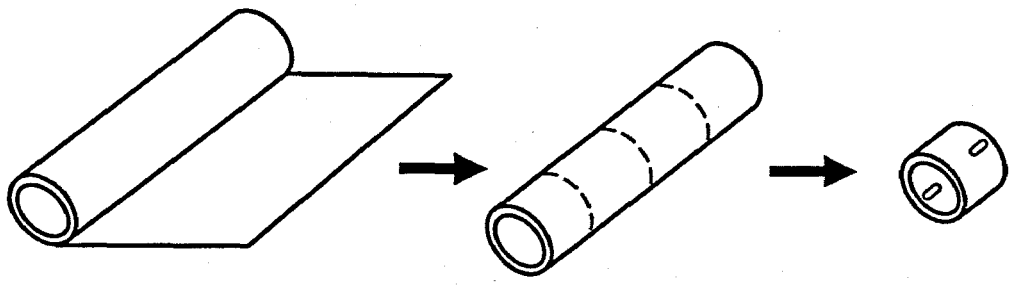

Raw material rolled long tube completed stator core

Fig.6-3 Fabrication of the stator core

The methods for cutting the stator core of the large-sized and small-sized prototypes are different. Because the large sized stator core is too thick, the laser beam produced by the laser machine can not burn through the wall of cylinder tube. If high power laser beam is applied for machining, the surface of the stator core will be burnt out. Hence, laser cutting is not suitable for large sized stator core. Instead, the EDM method is employed for the fabrication of the large sized stator core. Fig.6-4 shows a photo of the completed large sized stator core obtained by the EDM technique.

For the small sized stator core, the EDM method can not be used as the component can not withstand the stress produced during the machining. In order to solve the thickness problem during the laser cutting, the fabrication procedure of the small sized stator core is prepared as follows: (1) The stator core with desired dimensions is divided into several thinner cylinder tubes with different diameters so that the tubes with smaller diameters can be just fitted into the tube with larger ones; (2) The thickness of each tube is small enough that can be cut through by the proper laser beam without damaging the material surface; (3) The stator core is then obtained by assembling these tubes as a whole. Fig.6-5(a) shows a photo of the three tubes with step down diameters machined

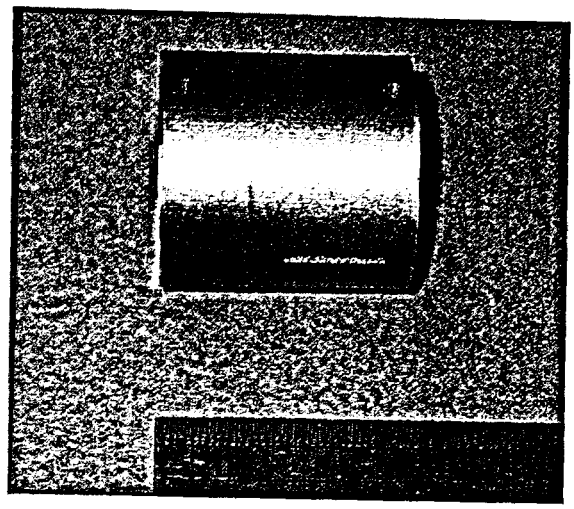

Fig.6-4 The completed large sized stator core

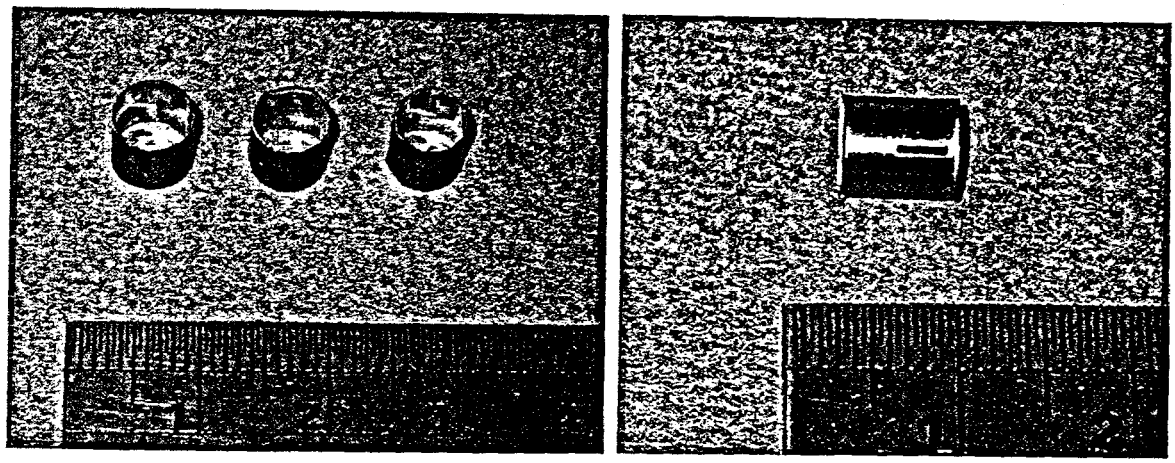

(a) (b)

Fig.6-5 Fabrication of the small sized stator core
(a) three different sized tubes, (b) completed stator core

by precision laser cutting and Fig.6-5(b) the final stator core assembled by the three different sized tubes.

As mentioned in the chapter 5, the stator windings are made up of a number of annular coils. Fig.6-6 shows a photo of the coils used for the different sized prototypes. These coils are constructed by 0.2mm and 0.05mm copper wires, respectively, for the large and small sized prototypes. The large coil has 71 turns while the small ones 45 turns. These coils are assembled carefully inside the stator core and connected into three phases based on the predefined polarities. As an example, Fig.6-7 shows a photo of the assembled stator for the small prototype.

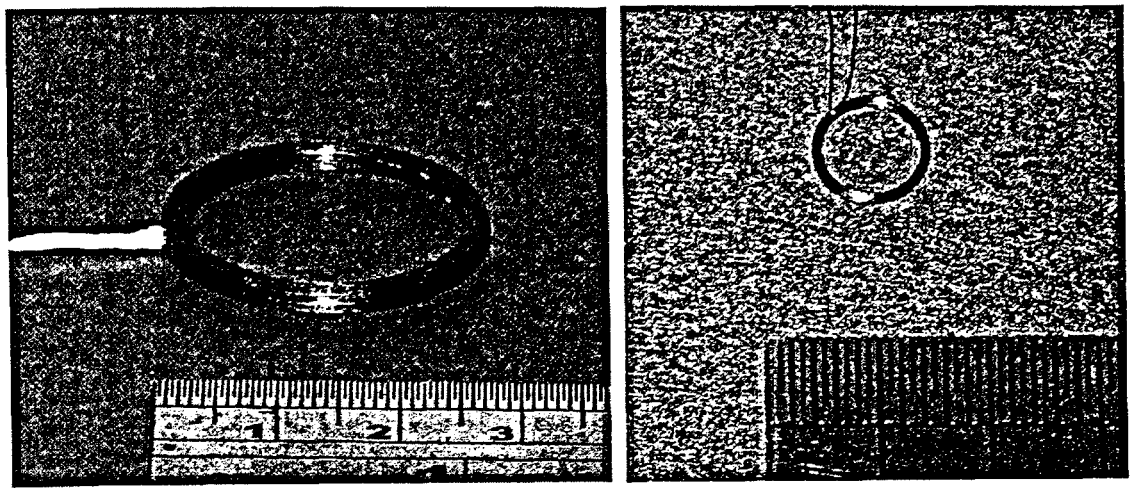

(a) (b)

Fig.6-6 Phase coils for the prototypes
(a) large sized coil, (b) small sized coil

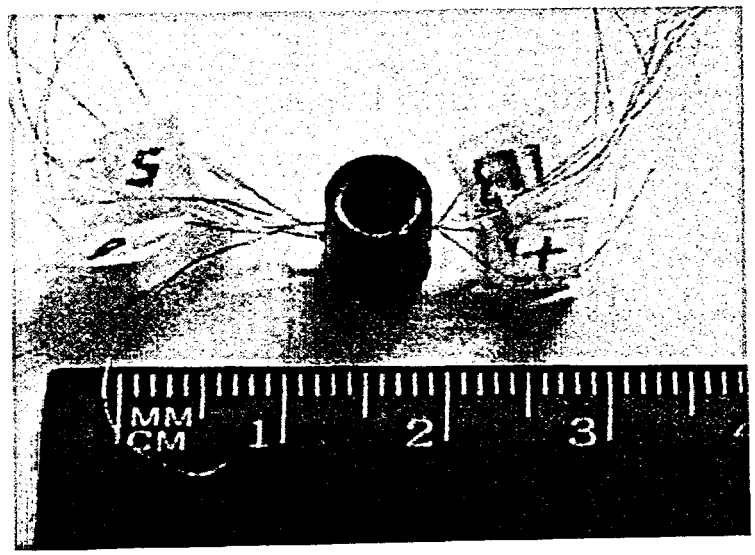

Fig.6-7 Assembled stator for the small prototype

6.2.3 Fabrication of pole pieces

The pole pieces of the actuator are stacked by a number of round-shaped sheets cut from the METGLAS thin-film ribbon. During the laser cutting, the applied power of the laser beam plays a very important role to the quality of the cutting result. The appropriate power of the laser beam is dependent on the material property, size of the raw material

and size of the component. If the applied power is insufficient, the laser beam cannot cut through the material and only snicks remain on the material. On the contrary, if the laser power is too high, the edge of the component will be burnt out and the component becomes fragile, and the entire pole piece sheet will lose its shape due to the high temperature acting on the material during the machining. Fig.6-8 shows an example of pole piece sheet cut by an over powered laser beam.

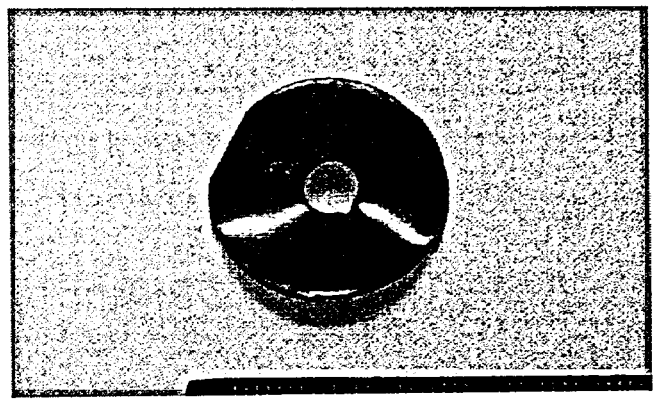

Fig.6-8 Pole piece sheet cut by over powered laser beam

To obtaining a satisfactory result, a raw material sheet with suitable size should be prepared in advance. The size of raw material sheet is mainly determined based on the clamping tools of the laser machine. According to the size of raw sheet, several trials were carried out to determine a proper laser power used in the machining. Fig.6-9 shows the pole piece sheets of the both sizes obtained by a proper setting of laser power.

By stacking the pole piece sheets obtained by the laser cutting, the pole pieces of the actuator can be constructed. According to the design, two types of pole pieces with different thickness will be used for the actuator. The thickness of the pole pieces in the middle of the translator is equal to the thickness of the magnets and the thickness of the pole pieces at the sides of the translator equals half of it. For the large sized prototype, totally 84 and 40 pole piece sheets are used for the middle and side pole pieces, respectively. For the small sized prototype, the numbers of sheets for the pole pieces are 15 and 7, respectively. Fig.6-10 shows the constructed pole pieces for the small sized prototype.

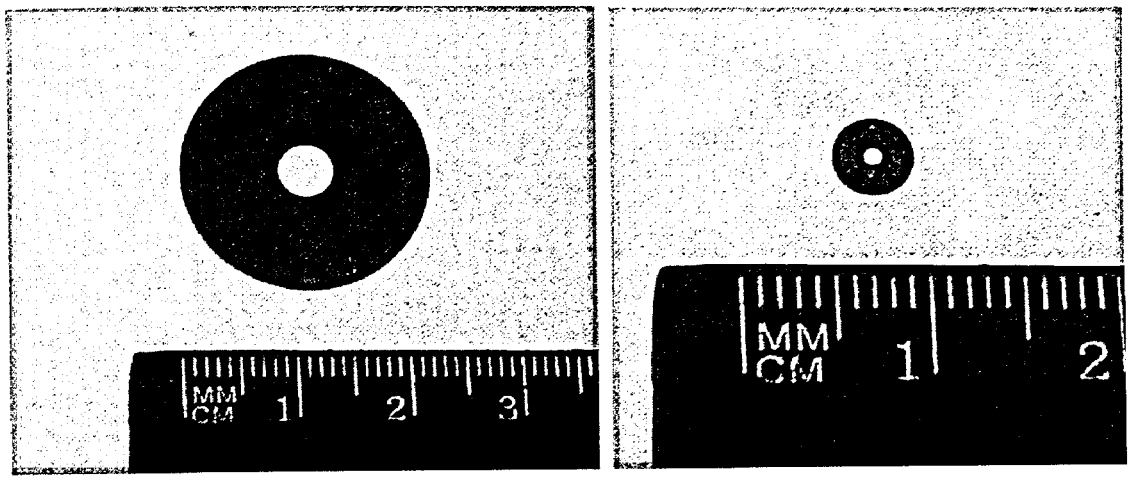

(a) Large sized pole piece sheet (b) Small sized pole piece sheet

Fig.6-9 Pole piece sheets obtained by the proper setting of the laser power

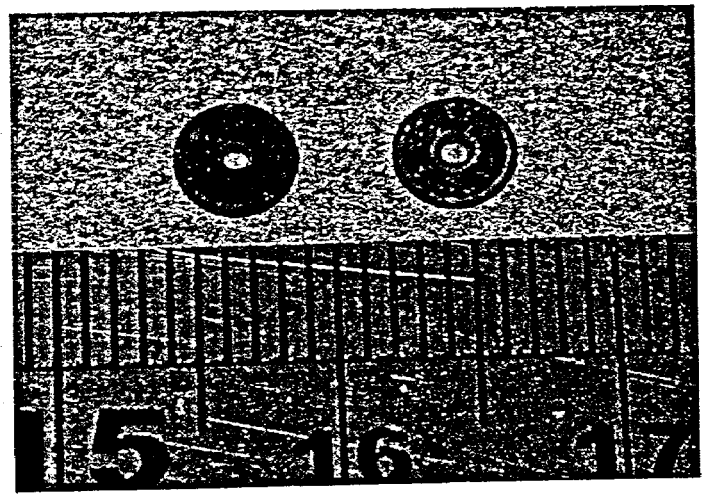

Fig.6-10 The constructed pole pieces for the small sized prototype

6.2.4 Construction of the translators

The translator of the actuator is constructed by alternatively stacking the pole pieces and magnets along the translator shaft. In order to counteract the repulsive forces between the magnets, the translator shaft is designed with two parts as shown in Fig.6-11. They are made up of stainless steel and the thin discs on each part of the shaft are used for firmly holding the pole pieces and magnets within the translator. This structure can also avoid the disassembly of the pole pieces and magnets during the operation of the actuator. The completed assemblies of the translators for the both sized actuators are

shown in Figs.6-12 and 13, respectively

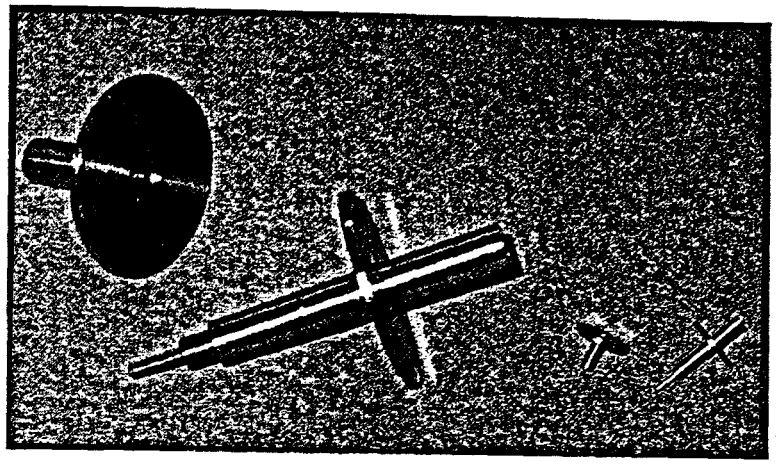

Fig.6-11 Translator shafts for the prototypes

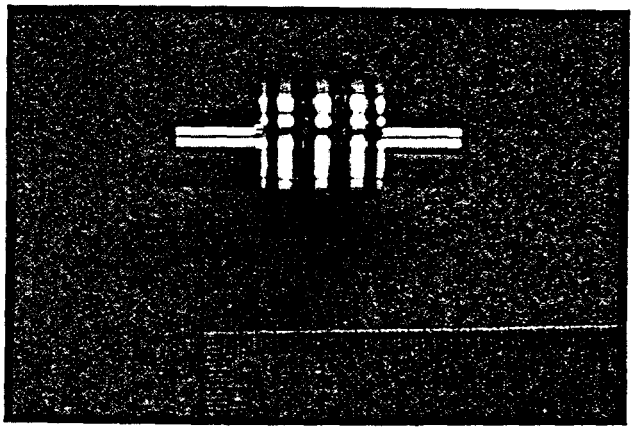

Fig.6-12 Assembly of the translator for large sized prototypes

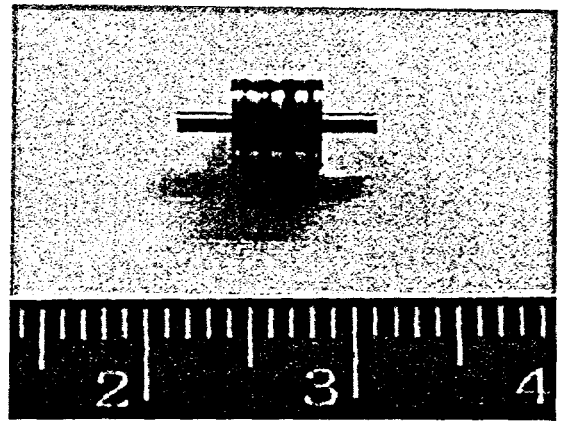

Fig.6-13 Assembly of the translator for small sized prototypes

6.2.5 Assembly of the prototypes

The final stage of the prototype fabrication is assembling of the prototypes. However, due to the small air gap, the large attracting force between the translator and stator core makes assembling a very difficult job, especially for the large sized prototype. Any collision between the translator and stator will cause damage to the insulation of stator windings. Therefore, a special mechanical tool is designed to safely insert the translator into the stator. The tool utilises the designed test bench (will be explained later). Two holders with clamping blocks are constructed and mounted on the stage of the test bench. One used for gripping the translator is attached to the screw of the test bench and

the other for holding the stator is fixed on the stage. With the help of the tools, the translator and stator are adjusted to align to the same horizontal axis. When pushing the translator along the stage by turning the screw, the translator can be safely inserted into the stator without any contact with the stator windings. Fig.6-14 shows the assembling process of the large prototype.

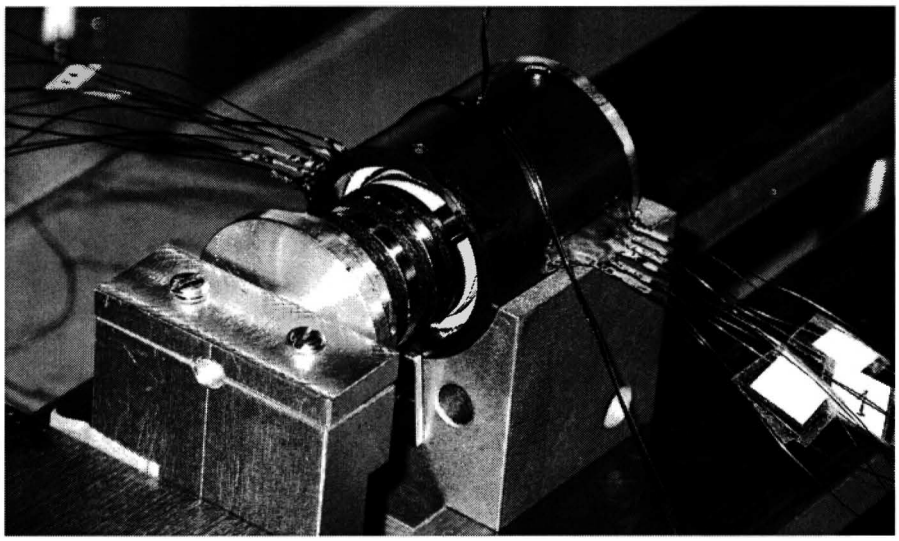

Fig.6-14 Assembling process of the large prototype

The end caps for the prototypes shown in the figure are made up of aluminium for reducing the whole mass of the actuator. Two Teflon sleeves are made and installed in the middle holes of the caps acting as the linear bearings. Fig.6-15 shows the completed prototypes.

6.2.6 Design of the test bench

A special test bench is designed for testing the prototypes. The schematic diagram of the test bench is illustrated in Fig.6-16. It consists of a force gauge, a micro position meter, a tool set used for clamping the actuator, and a supporting stage with a screw. The position of the translator of the actuator can be preset by the micrometer before the testing. The force gauge is attached to a sliding block with a screw so that it can move accurately by turning the screw. The combination of the micro meter and the force gauge can be used for clamping the translator at a certain position with a preload

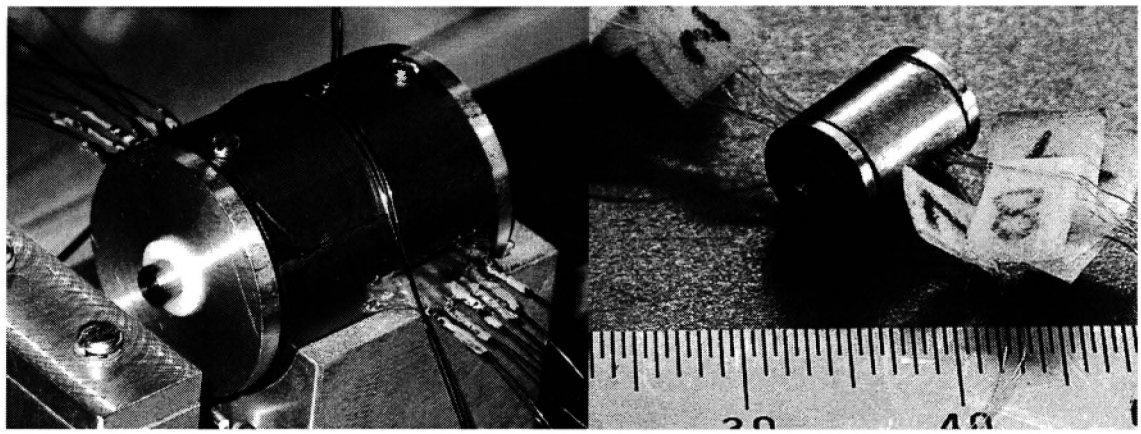

(a) (b)

Fig.6-15 (a) Completed large sized prototype
(b) Completed small sized prototype

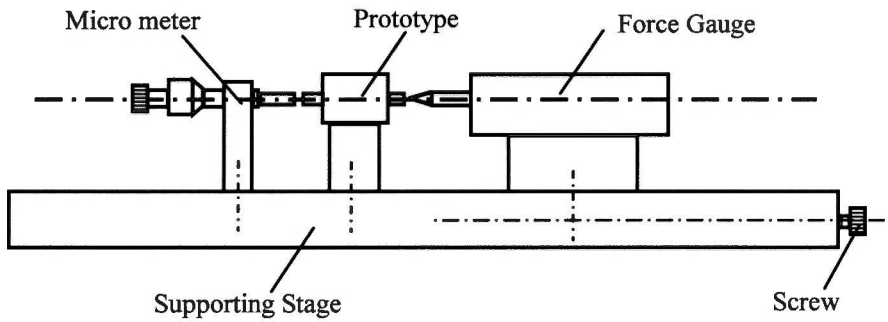

Fig.6-16 Schematic diagram of the test bench

exerted by the force gauge. As a result, the performance measurements of the actuator, such as the phase inductances and actuation forces, can be conducted at any desired translator positions. In addition, the test bench can also be used for the assembly of the actuator as explained previously. Fig.6-17 shows a photo of the actual test bench.

6.3 Prototype-Based Characteristic Analysis - A Reassessment

Because of the issues in the prototype construction, such as the lamination effect of the magnetic core, the tolerances required for the components machining and laboratory installation, the characteristics of the prototypes may not be the same as those obtained from the model with the ideal dimensions, especially for the small sized prototype.

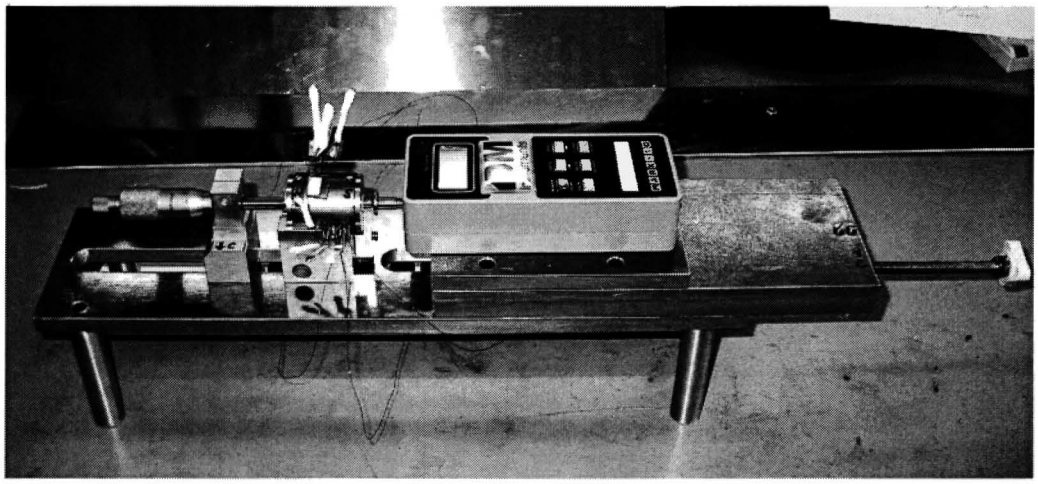

Fig.6-17 Photo of the actual test bench

Therefore, it is necessary to re-examine the performances of the prototypes by considering these practical factors. Based on the results of the re-examination, the FE model for the actuator can be modified to reproduce the machine reality more accurately.

6.3.1 Considerations in magnetic modelling of the prototype

6.3.1.1 The pole pieces

According to the number of sheets used in the pole pieces, the lamination factors of the pole pieces, k_s, can be obtained by

$$k_s = \frac{N_s t_s}{\tau_c}, \tag{6.1}$$

where N_s is the number of sheets in the pole pieces, t_s the thickness of the pole piece sheet, and τ_c the nominal thickness of the pole pieces. Accordingly, the effective thickness of the pole piece, which represents the pure magnetic material, is given by $k_s \cdot \tau_c$. The regions other than the effective thickness, namely $(1-k_s)\cdot\tau_c$, can be regarded as the distributed air gaps.

In the FE analysis of the actuator characteristics, the lamination factors of the pole

pieces should be considered. However, it is difficult to find a simple method to model the distributed air gaps in the pole pieces due to the non-linear property of the magnetic material. If the pole pieces are modelled by using a number of single sheets with air gaps between them, the meshing of the FE model would be difficult and a large quantity of elements would be generated, which results in a long computational time. As an approximate method, two concentrated air gap regions will be introduced in the FE model to reproduce the lamination effect of the pole pieces, as shown in Fig.6-18. The thickness of the air gaps at the each side of the pole piece will be $1/2(1-k_s)\cdot\tau_c$. The method can be easily applied to the established FE model of the actuator without increasing the complexity of the model.

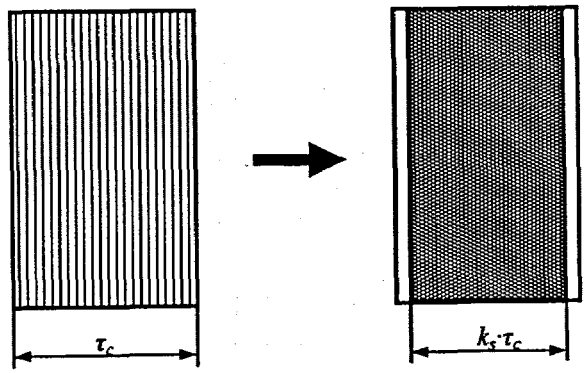

Fig.6-18 Modelling of lamination effect by introducing concentrated air gap

However, the simple introduction of the concentrated air gaps at each side of the pole pieces, which will reduce the cross sectional area of the magnetic flux path under the pole pieces, is inaccurate in practice. A better way for considering the air gaps in the pole pieces while keeping the cross sectional area of the magnetic flux path is to merge the concentrated air gaps into magnets because of linearity of the PM material. This method can be explained by using Fig.6-19. If adding the concentrated air gaps in the pole piece to the both sides of the magnet, the new thickness of the magnet becomes

$$\tau_m' = \tau_m + \frac{1}{2}(1-k_{s1})\tau_c + \frac{1}{2}(1-k_{s2})\tau_c, \qquad (6.2)$$

where k_{s1} and k_{s2} are the lamination factor of two pole pieces adjacent to the magnet. As a result, when considering that the magnetic permeability of the magnet is the same as that of air, the reluctance of a single magnet will be

$$\Re_m = \frac{\tau'_m}{\mu_0 A_m}, \tag{6.3}$$

where A_m is the cross sectional side area of the magnet. Considering that the actual thickness of the magnet can not be changed in the FE model, (6.3) is then rewritten as follows

$$\Re_m = \frac{\tau_m(\tau'_m/\tau_m)}{\mu_0 A_m} = \frac{\tau_m}{(\tau_m/\tau'_m)\mu_0 A_m} = \frac{\tau_m}{\mu'_m A_m} \tag{6.4}$$

where $\mu'_m = (\tau_m/\tau'_m)\mu_0$ is defined as the computational magnetic permeability of the magnet. By introducing μ'_m in (6.4), the lamination effect of the pole pieces can be incorporated in the FE analysis while the dimensions of the pole pieces and magnets are keeping unchanged in the model.

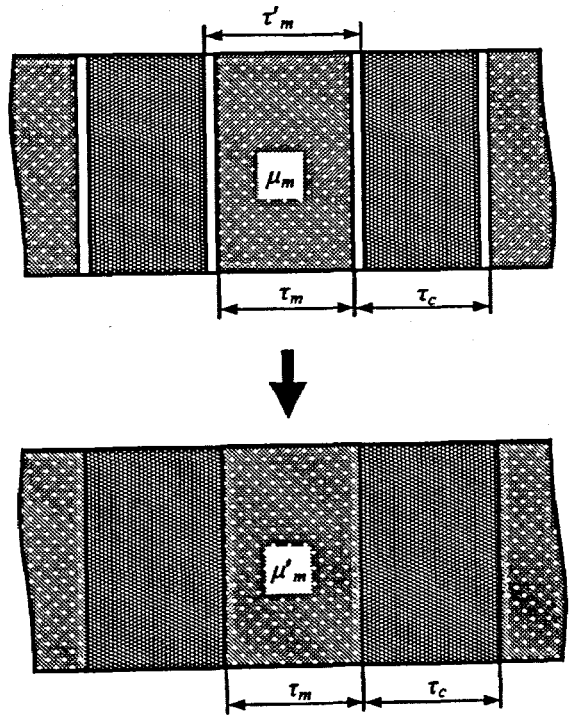

Fig.6-19 Introduction of the computational permeability for the magnet

It should be noted that during the application of the method, the approximation of increasing the effective thickness of the pole piece to τ_c will not cause much errors during the analysis. The reason is that the magnetic permeability of the magnetic core is extremely high and the increase of the thickness can hardly affect the entire reluctance of the model.

6.3.1.2 The stator core

There are two kinds of air gaps in the stator of the prototype. One is caused by the lamination of the material as in the pole pieces and the other is the air gap between the stator core and the stator winding. The latter air gap is necessary for the installation of the phase coils. In the prototype based FE model, the two air gaps are combined together and modelled by one concentrated air gap between the stator core and stator windings, and the thickness of the stator is accordingly reduced.

6.3.2 Predicted characteristics of the prototypes

The characteristics of both prototypes, including the forces and phase inductances, are computed by using the prototype based FE models. Figs.6-20 to 22 show the predicted force and phase inductances of the large sized prototype and Figs.6-23 to 25 plot the results of the small sized prototype.

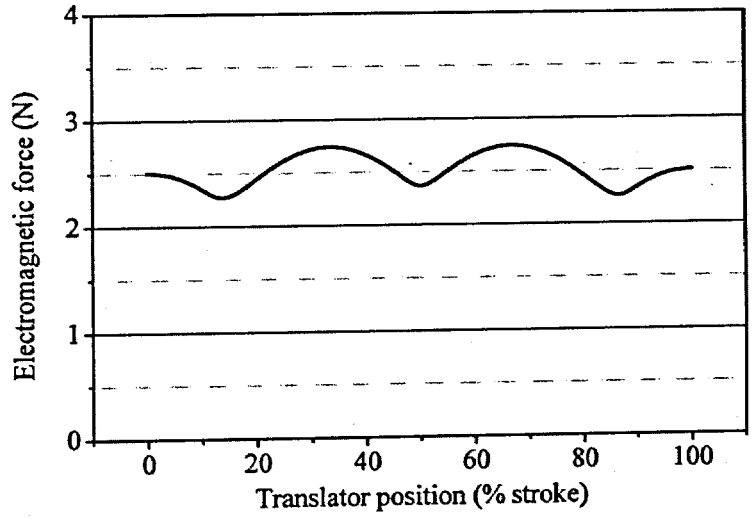

Fig.6-20 Predicted force of the large sized prototype

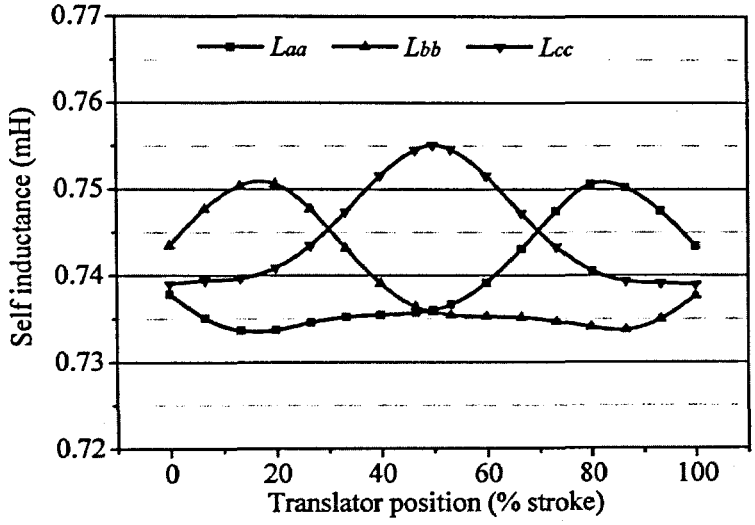

Fig.6-21 Predicted self inductances of the large sized prototype

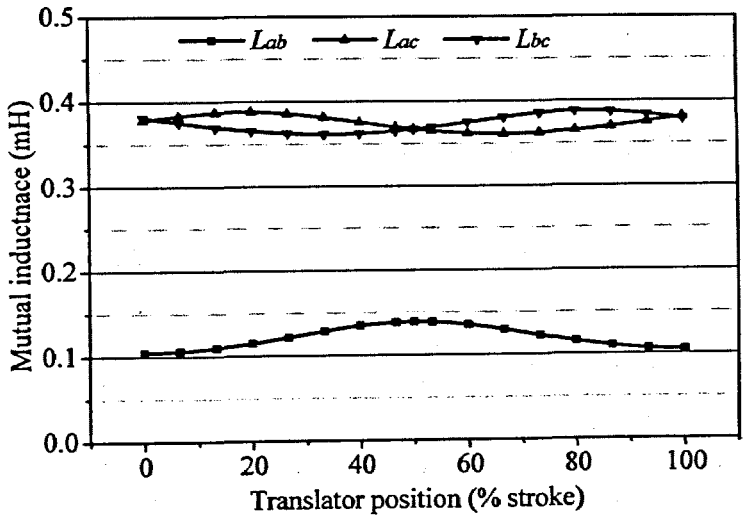

Fig.6-22 Predicted mutual inductances of the large sized prototype

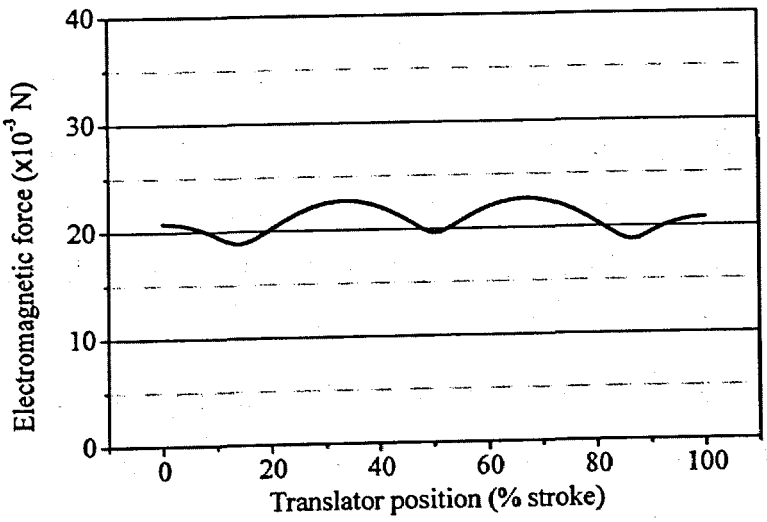

Fig.6-23 Predicted force of the small sized prototype

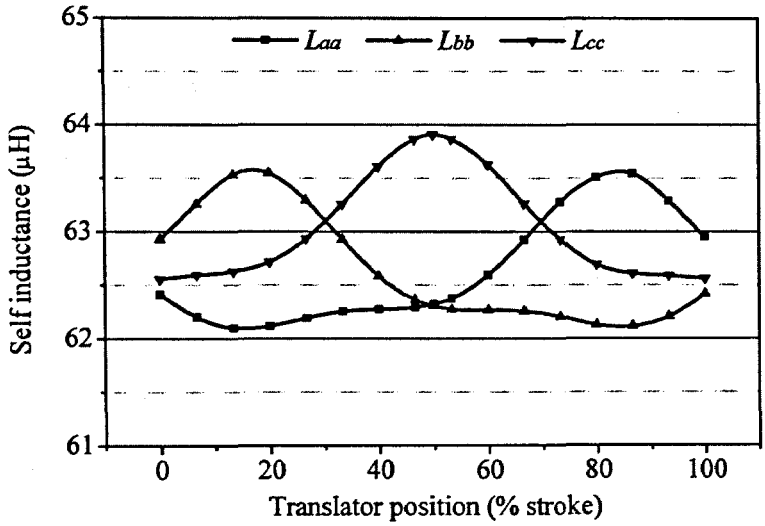

Fig.6-24 Predicted self inductances of the small sized prototype

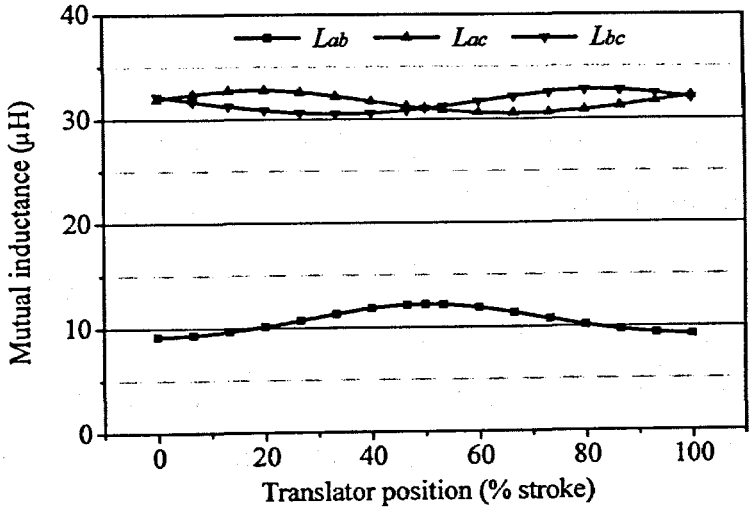

Fig.6-25 Predicted mutual inductances of the small sized prototype

The characteristics of small sized prototype with ideal dimensions have been analysed in chapter 5. Compared to the results obtained from the ideal model, the inductances of the small sized prototype are larger due to the increased number of turns in the prototype phase coils. On the other hand, the variations of the self inductances of the prototype are quite different from those of the ideal model, and they are similar to the inductances in the linear condition. This is because the magnetic core of the prototype is much less saturated due to the decrease of the flux density in the system, which is caused by the introduction of many air gaps during the fabrication.

Moreover, because of the reduction of the flux density, the generated force of the prototype is also decreased significantly, which is over 20% less than the force obtained by the ideal model. Consequently, the performance of the small sized actuator will be somewhat limited due to the smaller force output. Improvement on the fabrication techniques of the actuator to achieve the desired performances should be considered in the future.

6.4 Measurement of the Actuation Force

6.4.1 Measurement setup

The setup for measuring the actuation force of the prototypes of the PM TLA is shown in Fig.6-26. The actuator being tested is placed between the micro meter and force gauge. In order to measure the forces at different translator positions, the position of the translator is preset by the micro meter and a preloaded clamping force is exerted by moving the force gauge to prevent the movement of the translator. The force gauge used for measuring the force is the Mark-10 digital force gauge from IDM Instrument Inc. Two force gauges with different measuring range are selected to meet the accuracy demand of the measurement, which a 25N force gauge is used for the large sized

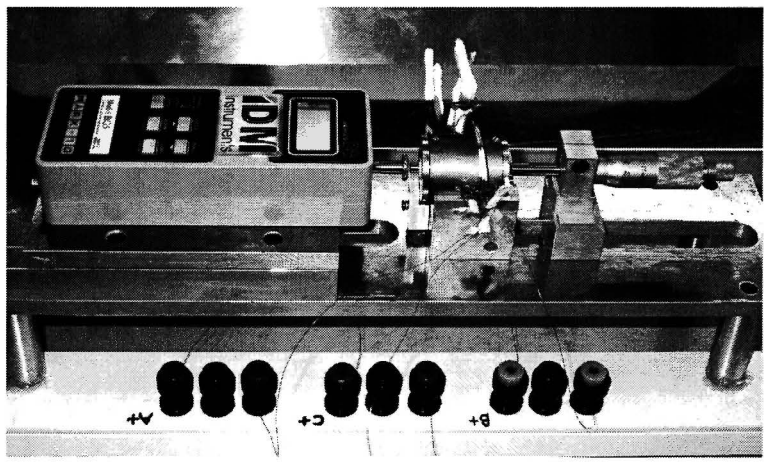

Fig.6-26 Experimental setup for force measurement

prototype and the other with 1N range is for the small sized prototype.

During the measurement, a rated DC phase current is applied to the actuator based on the brushless DC excitation method. Which phases are to be energised is determined by the preset translator positions and the switching sequence obtained by the force analysis conducted in chapter 5. Much care should be taken with the static friction between the linear bearings and the translator shaft while testing. The friction should be reduced as much as possible for acquiring better measuring results.

6.4.2 Measurement results

The measured actuation forces of two different sized prototypes are shown in Figs.6-27 and 28, respectively. The predicted forces are also plotted in the figure for comparison. In general, the measured forces are close to the predicted values. The force of the large prototype agrees quite well with the predicted result. The force of the small sized prototype, however, has relatively large errors compared to the predicted result. This is because the force of the small sized prototype is quite small, and the frictional force as well as the error during the measurement becomes significant. In addition, the comparison between the forces of the two different sized prototypes verifies the truth of the scaling effect discussed in chapter 3.

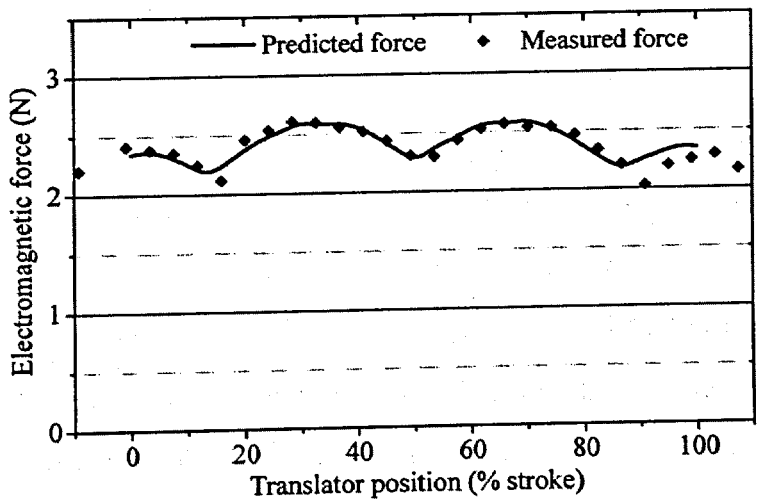

Fig.6-27 Output force of the large sized prototype

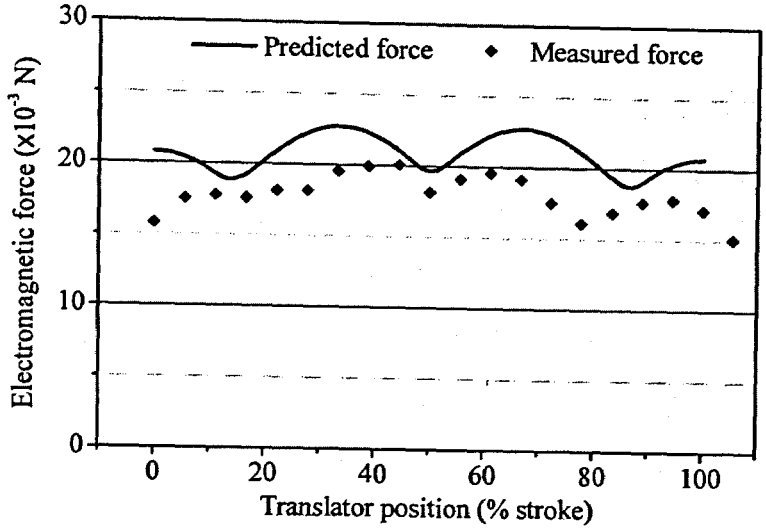

Fig.6-28 Output force of the small sized prototype

6.5 Measurement of the Phase Inductances

6.5.1 Measurement setup

The experimental setup for the measurement of phase inductances of the prototypes is shown in Fig.6-29 and the corresponding electrical circuit diagram of the measurement system is illustrated in Fig.6-30.

When measuring of the phase inductances, a pure sinusoidal voltage is imposed to each phase of the actuator and the corresponding phase current and voltage are recorded. The induced voltages in the other two unexcited phases are also recorded for finding the mutual inductances. Because the phase resistances of the actuators are very small (<35Ω) and most of the signal generator can only work with a load of which the resistance is larger than 50Ω, a precision signal amplifier is then used as the power amplifier for energising the phase windings. The amplitude of the excitation voltage is set as small as possible to minimise the effect of the magnetic field of the excitation current on the magnetic operational condition of the actuator. A small current can avoid the temperature effect on the phase resistances caused by the ohmic loss. In addition, the

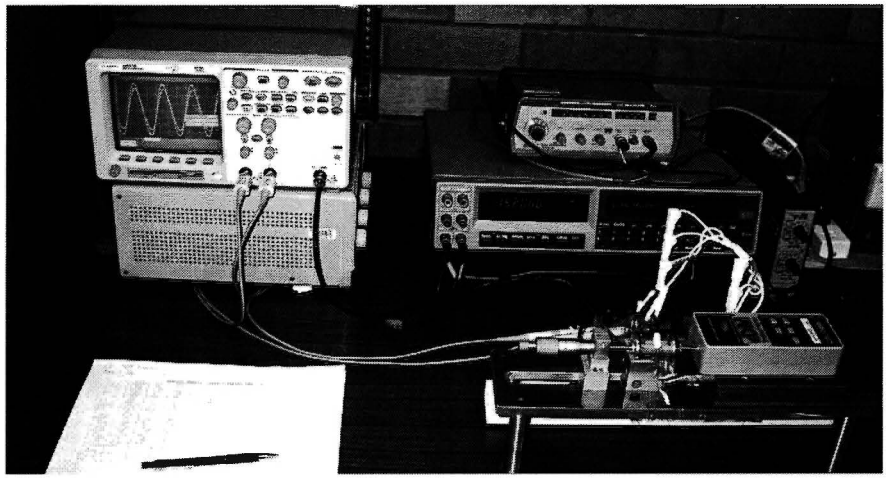

Fig. 6-29 Experimental setup for the inductances measurement

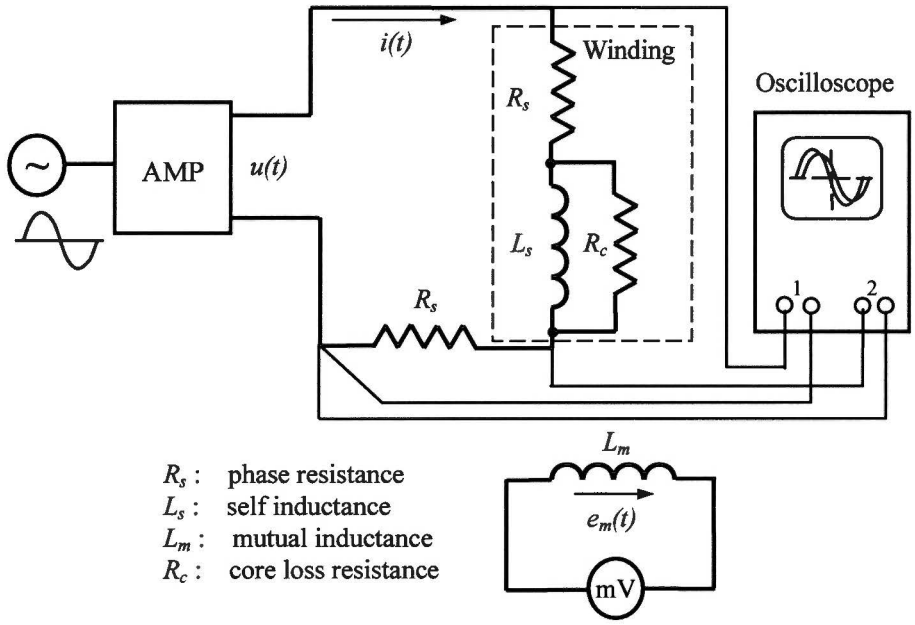

Fig. 6-30 Electrical circuit for the inductances measurement

frequency of the excitation current is determined by the trade-off between the precision of measurement and the effect of the eddy current in the magnetic core. In the experiment, the frequencies for measuring the inductances of the large and small prototypes are set as 500Hz and 1300Hz, respectively.

The phase current is measured by a 1Ω precision resistor. The waveforms of the measured phase current and voltage are recoded by a digital signal oscilloscope (DSO) and the induced voltages in the unexcited phases are measured by a millivolt meter.

Based on the measured results, the inductances can be calculated by the following equations

$$L_a = \frac{\sqrt{Z^2 - \Sigma R^2}}{2\pi f}, \tag{6.5}$$

$$L_m = \frac{E_m}{2\pi f I}, \tag{6.6}$$

where the impedance Z and total resistance ΣR of the measuring circuit can be obtained by the waveforms recorded by the DSO. During the calculation, the core loss resistance R_{core} is not take into account since the core loss in the magnetic core is considerably small.

6.5.2 Measurement results

The measured phase inductances of the large and small sized prototypes are shown in Figs.6-31 to 34, respectively. The predicted values are also plotted in the figures for comparison. It can be seen that the measured inductances are close to the predicted values. In particular, the saliency effects on the profiles of the inductances caused by the structure of the actuator can be clearly seen in the measured self inductances of the large sized prototype as well as in the measured mutual inductances of both prototypes. The variations of the self inductances of the small sized prototype are not very clear because more errors might be introduced during the measurement.

It is also noticed that the measured mutual inductances are all less than the predicted results. These differences are considered being caused by the construction of the stator winding since the phase windings are not ideally coupled each other as in the theoretical FE models.

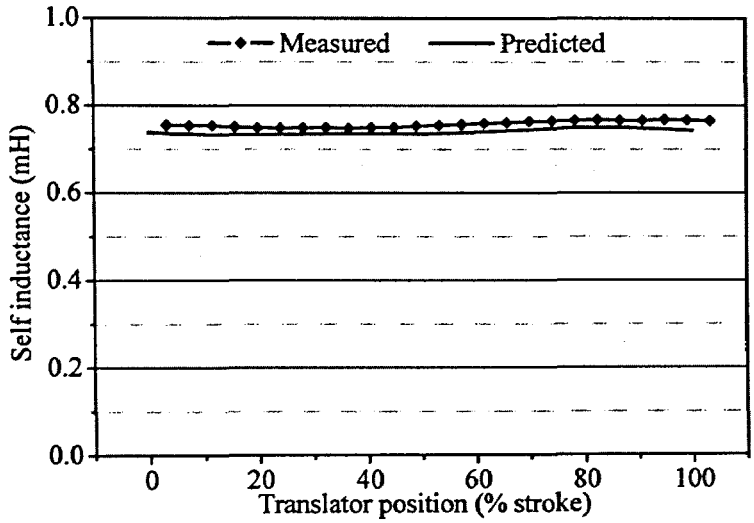

(a) Phase *A*

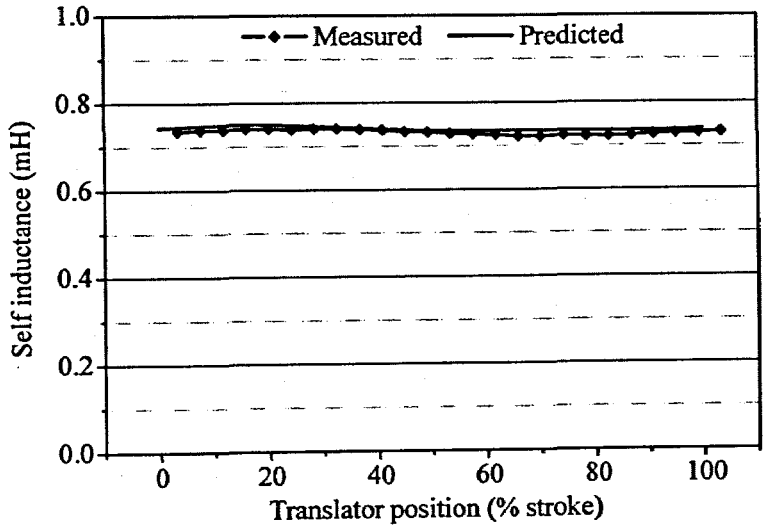

(b) Phase *B*

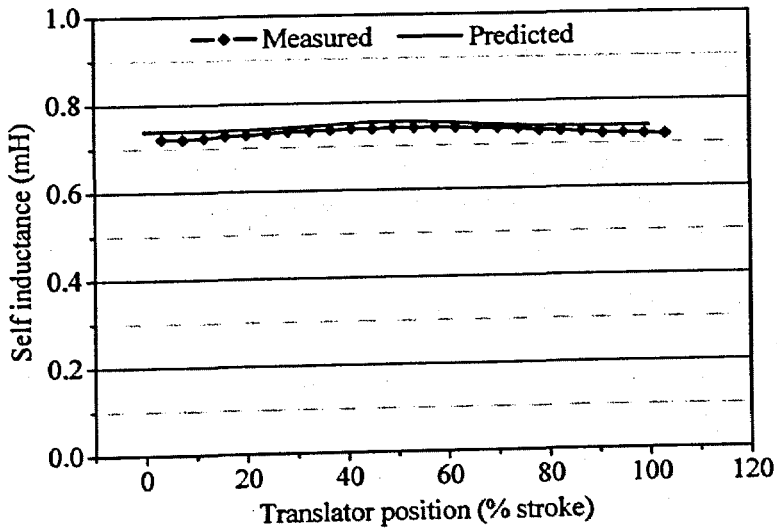

(c) Phase *C*

Fig.6-31 Measured self inductance of the large sized prototype

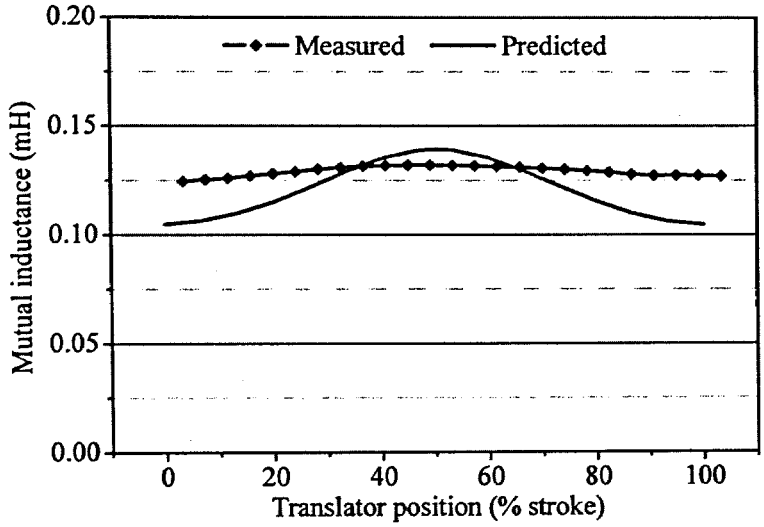

(a) L_{ab}

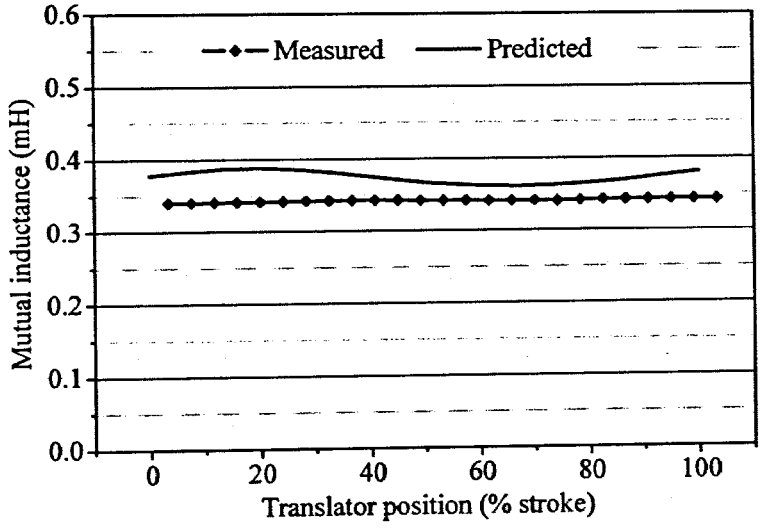

(b) L_{ac}

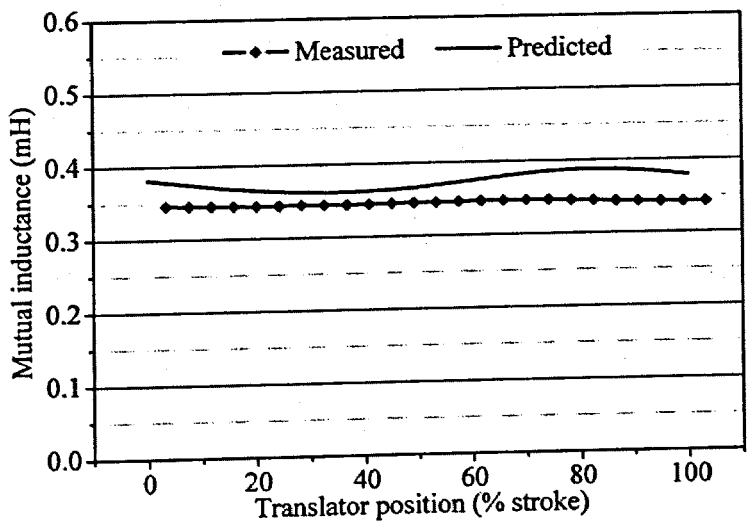

(c) L_{bc}

Fig.6-32 Measured mutual inductances of the large sized prototype

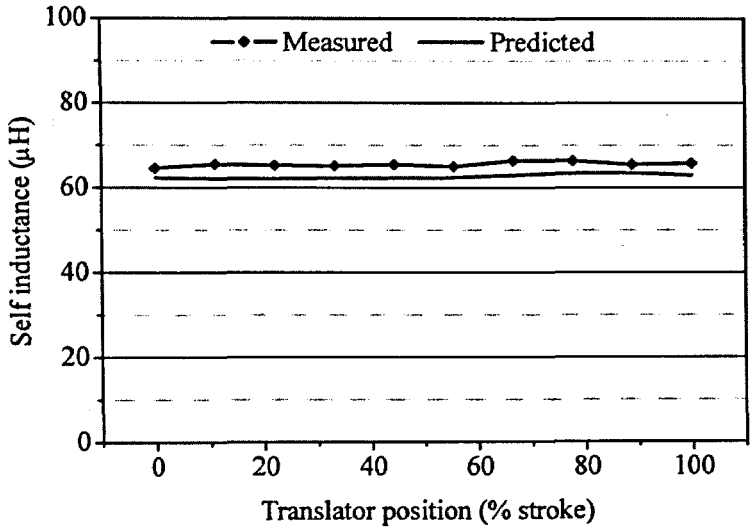

(a) Phase *A*

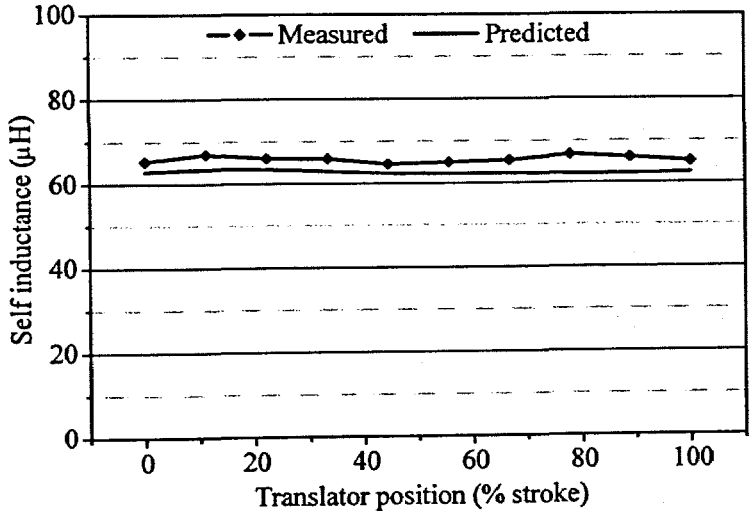

(b) Phase *B*

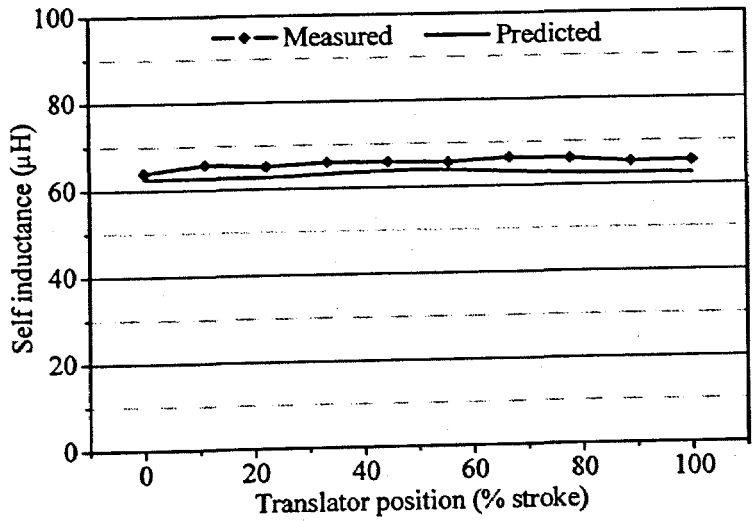

(c) Phase *C*

Fig.6-33 Measured self inductances of the small sized prototype

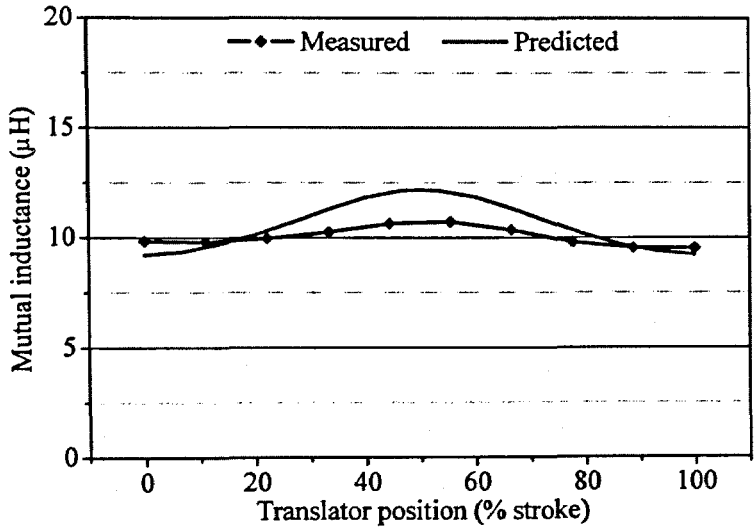

(a) L_{ab}

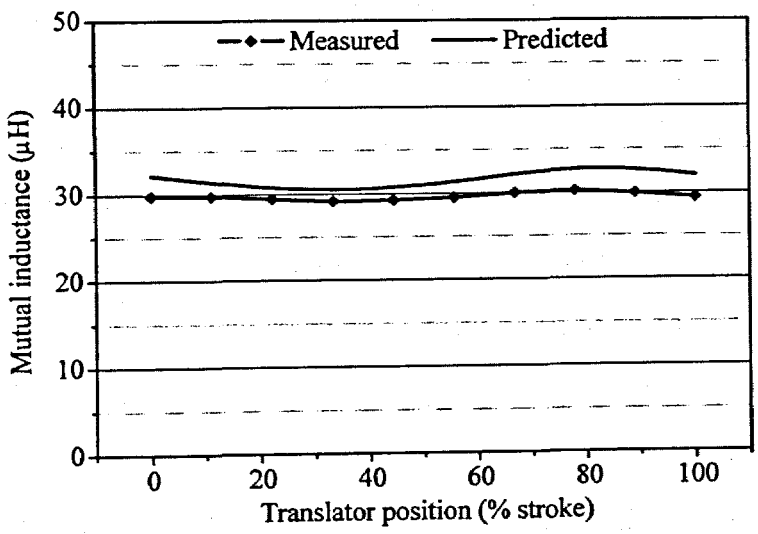

(b) L_{bc}

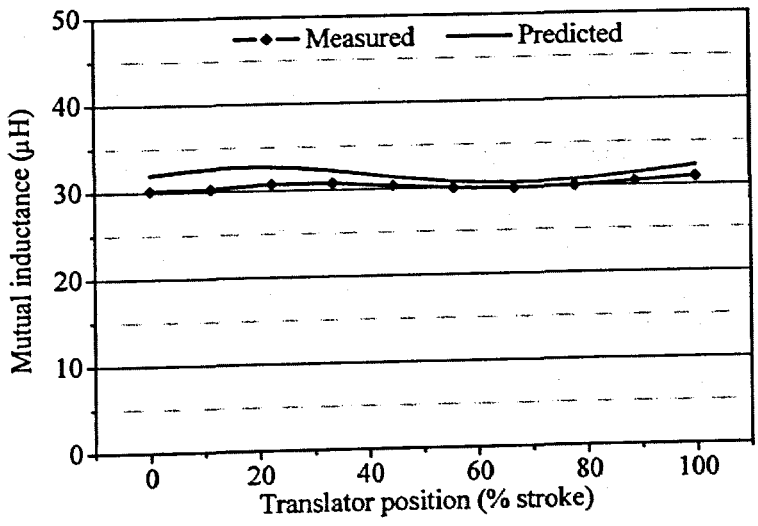

(c) L_{ac}

Fig.6-34 Measured mutual inductances of the small sized prototype

6.6 Conclusion

The detailed fabrication process of the designed moving magnet PM TLA is presented in this chapter. Because of the small sizes of the actuator, precision machining technology is employed for fabrication of actuator components. In addition, some tolerances of the components are introduced during the machining of the components for easier assembly of the prototypes in the laboratory, which are required to be considered during the prediction of the machine characteristics.

Based on the actual dimensions for constructions of the prototypes, the characteristics of the prototypes, including the electromagnetic forces and phase inductances, are re-examined by the FE analysis. Due to the precision and tolerance problems in the construction, the performances of the prototypes, especially the small sized prototype, are degraded as the errors and tolerances in the fabrication are more significant in the small sized actuator. These results provide a useful guidance for future improvements in micro actuator fabrications.

The forces and the phase inductances of both prototypes are measured and the results are compared with the predicted values. The comparisons of the results show that the performances of the prototypes are close to the expected, which indicates the effectiveness of the method used in the numerical analysis of the actuator. Furthermore, the force ratio between the large scaled prototype and small scaled prototype is close to 5^3, which is consistent with the analysis of scaling effect of the electromagnetic actuator under the constant current density condition.

Chapter 7

CONTROL OF THE TUBULAR LINEAR ACTUATOR

7.1 Introduction

Nowadays, electrical control plays a key role in electric machine drives. Thanks to the rapid development of modern electronics and power conversion technologies, high performance electric machine drive systems become increasingly dependant on the high performance electronic control schemes. Control-based machine design makes it possible that the optimal performances of the integration of the machine and control system can be achieved.

This chapter presents the electronic control of the proposed PM TLA. In order to analyse the actuator performances with the electronic converter, an enhanced machine dynamic model is developed and implemented in SIMULINK. According to the locomotive application of the actuator, an appropriate sensorless control scheme is designed and analysed based on the information obtained from the machine design. By using the proposed control scheme, the hardware of the electronic control system is designed and implemented based on the dSPACE prototyping system.

7.2 Operation of Brushless DC Machines and Its Sensorless Control

The proposed PM TLA is in fact a type of three phase brushless PM synchronous machine and it can be operated either as a brushless AC machine or a brushless DC machine (in particular, a brushless AC machine is designed with sinusoidal flux density distribution while a brushless DC machine is designed with trapezoidal flux density distribution to minimise the torque/force ripple). As discussed in chapter 5, the brushless DC drive method would be more preferable because of its simple implementation, compact structure, silent operation, and high efficiency, which are essential for the micro applications.

Although it is so called DC machine, from the point of view of the terminal excitation of machine windings, the brushless DC machine is indeed an alternative current electric machine. Different from the conventional balanced three-phase sinusoidal voltages for a brushless AC machines, a brushless DC machines uses rectangular shaped voltages as its driving source, which are obtained by an electronic converter from a DC power supply, as shown in Fig.7-1.

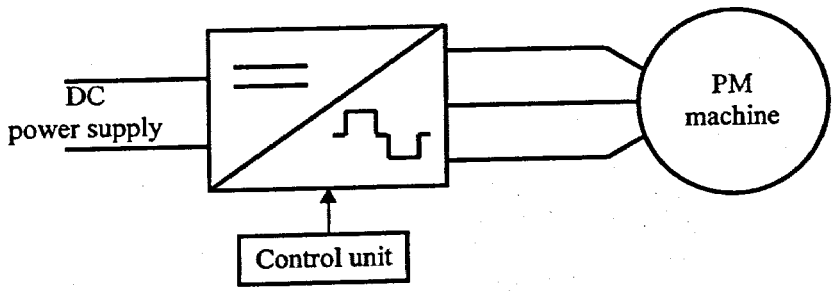

Fig.7-1 Schematic of brushless DC machine

The commonly used electronic converter is the three phase bridge inverter as shown in Fig.7-2. The circuit contains six solid-state switches, such as transistors, and MOSFETs, etc., connected to the high and low sides of the DC power supply. T1, T3 and T5 are the high side switches and T2, T4 and T6 the low side switches of the circuit. Through proper switching behaviours of the switches in the circuit, the DC voltage can be

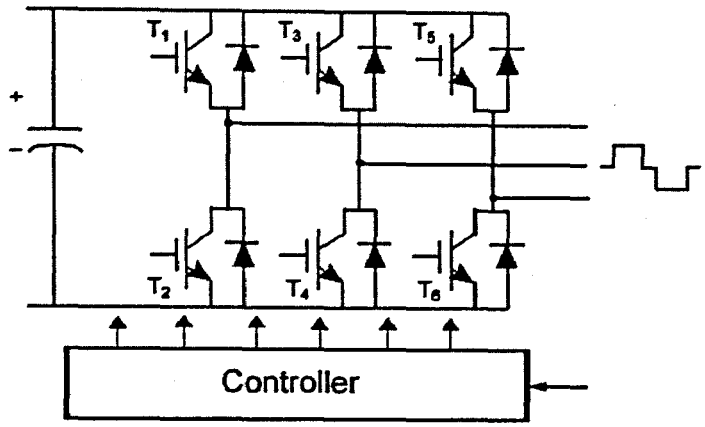

Fig.7-2 Three phase bridge inverter

converted into the required three-phase alternative rectangular waveforms. To operate the brushless DC machine, the stator windings of the machine should be energised in a proper sequence. It is important to know the rotor position to determine which windings shall be energised following the energising sequence. The rotor position is usually sensed by using mechanical position sensors installed on the machine stator. Most rotary brushless DC machines have three Hall sensors embedded into the stator on the non-driving end of the machine [Yedamale 2003], as shown in Fig.7-3. Whenever the rotor magnetic poles pass near the Hall sensors, they give a high or low signal, indicating the N or S pole is passing near the sensors. Based on the combination of these three Hall sensor signals, the exact sequence of commutation can be determined.

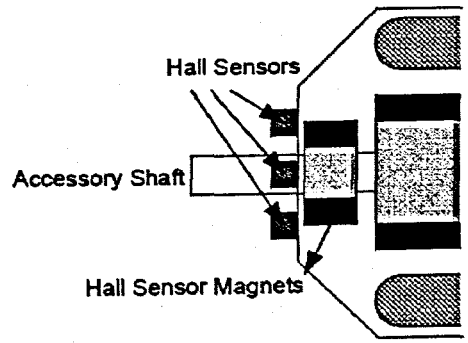

Fig.7-3 Hall position sensors

During each commutation sequence, there can be either three phases or two phases of stator windings that are energised by the electronic converter and the torque is produced by the interaction between the magnetic fields generated by the stator windings and

PMs. In the three-phase conduction mode, one phase is connected to the positive or negative terminal and the other two phases are connected to the opposite side of the DC power at any time. By this method, each switch will conduct 180 electrical degrees during every electrical cycle. In the two-phase conduction mode, there will be only two phases energised in each sequence, say, one phase is connected to positive terminal and the other is connected to the negative terminal. The third phase will remain non-energised. In this mode, the conducting interval of each switch is 120 electrical degrees. Although both conduction modes are applicable for the operation of brushless DC machine, the three-phase conduction mode does not achieve extra output benefits but with more power consumption compared to two-phase conduction mode. This can be explained by using the torque generation principle illustrated in Fig.7-4 when phase *A* is positively energised. Therefore, two-phase conduction mode is employed in most of the brushless DC machine drives.

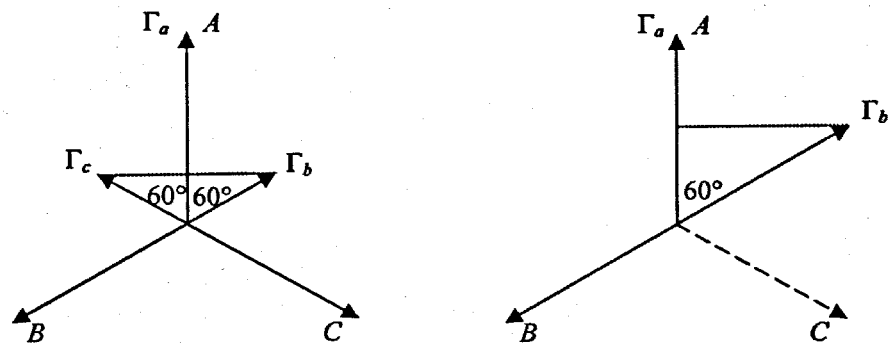

Three phase conduction mode:
A+, B−, C−
$I_b = I_c = 1/2 I_a$
$|\Sigma\Gamma|_{max} = 1.5|\Gamma_a|$

Two phase conduction mode:
A+, B−
$I_a = I_b$
$|\Sigma\Gamma|_{max} = 1.5|\Gamma_a|$

Fig.7-4 Comparison of three phase and two phase conduction mode

Ideally, the peak torque occurs when the fields of stator and rotor are at 90° to each other and falls off as the fields move together. In order to keep the machine running, the magnetic field produced by the stator windings should shift position as the rotor moves to catch up with the stator field. Fig.7-5 shows an example of Hall sensor signals with respect to the back EMF and phase currents, where the back EMF refers to the position

of the magnetic field generated by the PMs on the rotor. Fig.7-6 shows the switching sequence that should be followed with respect to the Hall sensors. The sequence numbers on Fig.7-5 correspond to the numbers given in Fig.7-6. Every 60 electrical degrees of rotation, one of the Hall sensors changes the state. Given this, it takes six steps to complete an electrical cycle. In synchronous mode, with every 60 electrical degrees, the phase current switching should be updated.

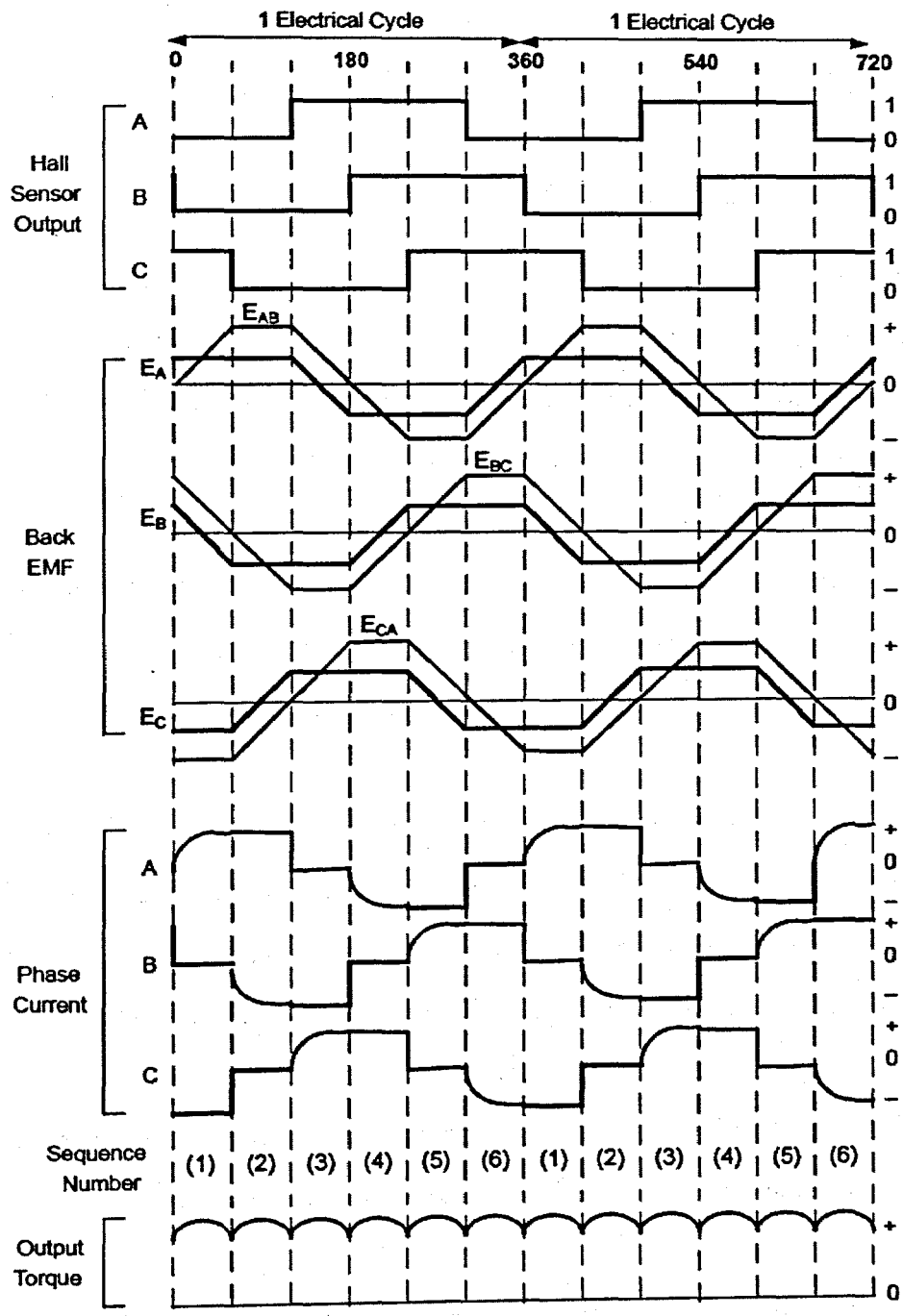

Fig.7-5 Hall sensor signals, back EMFs, phase currents and output torque

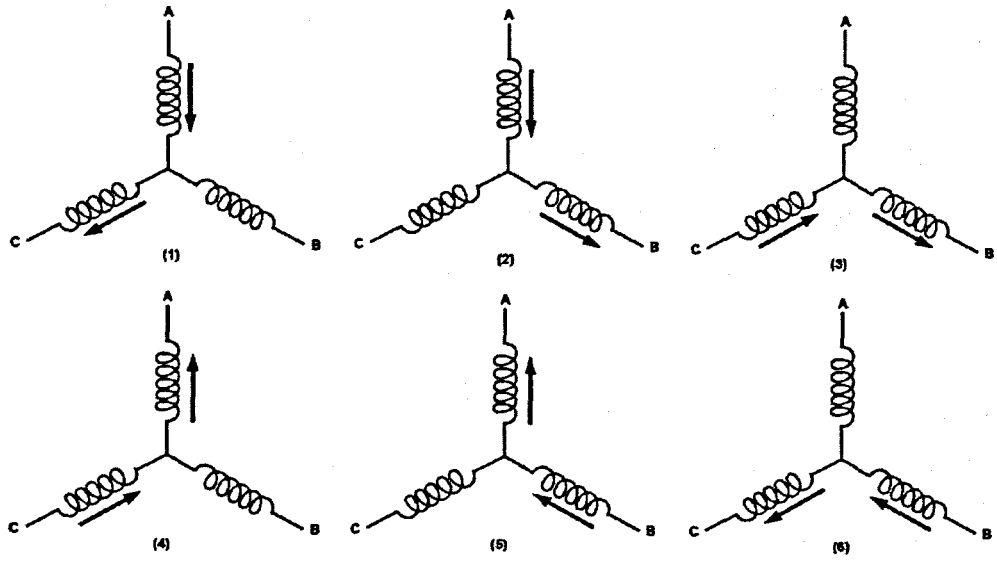

Fig.7-6 Winding energising sequence with respect to the hall sensor

It can be seen that the measurement of rotor position is crucial for the operation of brushless DC machine. However, the employment of mechanical position sensors results in a higher drive cost due to sensors, wiring and implementation in the machine. Moreover, sensors cannot be used in those applications where space is extremely restricted or the rotor is in closed housing and the number of electrical entries must be kept to a minimum such as in a compressor, or in those where the machine is immersed in a liquid. Therefore, for cost and technical reasons, the sensorless drive is an essential capability of a brushless DC machine controller.

Basically, two types of sensorless control technique can be found in the literature [Shao 2003]. The first type is the position sensing using back EMF of the machine, and the second one is the position estimation using machine parameters, terminal voltages, and currents. The second scheme usually needs high performance micro processors such as digital signal processors (DSPs) to implement the complicated algorithm of rotor position estimation, and the cost of the system is relatively high. So the back EMF sensing scheme is the most commonly used method for brushless DC machines.

In the back EMF sensing method, the commutation sequence is based on the detection of the back EMF induced by the movement of a PM rotor in front of stator winding.

Thanks to the two-phase conduction method used in the brushless DC machine drive, the remaining non-energised phase makes it possible for the measurement of back EMF during the inactive state. By examining the relationship between the signals of Hall sensors and back EMF in each phase, with respect to the phase current, as shown in Fig.7-5, the corresponding commutation occurs just after the voltage polarity of the back EMF of unexcited phase crosses from a positive to negative or from negative to positive with a 30 electric degree phase shift. Hence, the detection of such zero-crossing point (ZCP) of the back EMF in the unexcited phase can be used for determination of the coming commutation sequence without a mechanical position sensor. A speed dependent time delay will be necessary after the detection of the ZCPs of the back EMF to obtain the exact commutation moment.

The amplitude of back EMF is proportional to the rotor speed, which implies that the rotor should turn at a minimum speed to generate sufficient back EMF detectable for the sensorless control. When the rotor is stationary, there is no back-EMF. The rotor position is unknown and it might be at any one of the six possible commutation states. Thus, a special procedure is required to start the machine. One of the methods is that the rotor of the brushless DC machine is aligned to a known position by applying a specific small voltage to the stator. Then the machine can be controlled based on the known initial rotor position set by the alignment. Another starting up method is to apply an open-loop low frequency excitation at the beginning so that the rotor speed could gradually increase till it can produce the enough back EMF required for the zero-crossing detection.

7.3 Dynamic Machine Model for Electronic Converters

When an electric machine is fed by an electronic converter with DC link, the terminals of the machine windings will be connected to either positive or negative terminal in any

of the switching patterns. As a result, the voltage of the neutral point of machine windings will fluctuate and no longer be zero at all times. Under this circumstance, each phase cannot be retreated as independent as in the analysis of the machine under balanced three-phase energisation. Therefore, the formulation of the actuator obtained based on single phase behaviour in chapter 5 is no longer valid for the analysis of the machine operating with the electronic converter. A modified machine model should be derived upon the converter conditions.

7.3.1 Universal model for electronic converters

Since the voltage of the neutral point of machine winding u_n is not always zero when the machine is fed by an electronic converter, it should be considered in the machine model. Accordingly, based on the analysis in chapter 5, the electrical dynamic equations of the machines will become

$$R_a i_a + L_{aa}\frac{di_a}{dt} + L_{ab}\frac{di_b}{dt} + L_{ac}\frac{di_c}{dt} = u_{a0} - e_{am} - e_{as} - u_n, \tag{7.1}$$

$$R_b i_b + L_{ba}\frac{di_a}{dt} + L_{bb}\frac{di_b}{dt} + L_{bc}\frac{di_c}{dt} = u_{b0} - e_{bm} - e_{bs} - u_n, \tag{7.2}$$

$$R_c i_c + L_{ca}\frac{di_a}{dt} + L_{cb}\frac{di_b}{dt} + L_{cc}\frac{di_c}{dt} = u_{c0} - e_{cm} - e_{cs} - u_n, \tag{7.3}$$

where u_{a0}, u_{b0}, and u_{c0} are the terminal voltages applied to each phase. By introducing the net voltages on each phase,

$$u_{ae} = u_{a0} - e_{am} - e_{as}, \tag{7.4}$$

$$u_{be} = u_{b0} - e_{bm} - e_{bs}, \tag{7.5}$$

$$u_{ce} = u_{c0} - e_{cm} - e_{cs}. \tag{7.6}$$

Equations (7.1) to (7.3) can be simplified as follows

$$R_a i_a + L_{aa}\frac{di_a}{dt} + L_{ab}\frac{di_b}{dt} + L_{ac}\frac{di_c}{dt} = u_{ae} - u_n, \tag{7.7}$$

$$R_b i_b + L_{ba}\frac{di_a}{dt} + L_{bb}\frac{di_b}{dt} + L_{bc}\frac{di_c}{dt} = u_{be} - u_n, \tag{7.8}$$

$$R_c i_c + L_{ca}\frac{di_a}{dt} + L_{cb}\frac{di_b}{dt} + L_{cc}\frac{di_c}{dt} = u_{ce} - u_n. \tag{7.9}$$

Because the wye connection is employed in most of the machines powered by electronic

converters, the following relationship will be true at any time:

$$\frac{di_a}{dt}+\frac{di_b}{dt}+\frac{di_c}{dt}=0. \tag{7.10}$$

By solving (7.7) to (7.10), the derivatives of phase currents can be obtained as

$$\frac{di_a}{dt}=b1-b2+b3, \tag{7.11}$$

$$\frac{di_b}{dt}=b2-b3, \tag{7.12}$$

$$\frac{di_c}{dt}=-b1, \tag{7.13}$$

where

$$b1=\frac{c1\times v1-c2\times v2}{c1\times c3-c2\times c4}, \tag{7.14}$$

$$b2=\frac{c4}{c1}b1, \tag{7.15}$$

$$b3=\frac{v2}{c1}, \tag{7.16}$$

and

$$c1=L_{aa}-L_{ab}-L_{ca}+L_{cb}, \tag{7.17}$$

$$c2=L_{aa}-L_{ab}-L_{ba}+L_{bb}, \tag{7.18}$$

$$c3=L_{aa}-L_{ac}-L_{ba}+L_{bc}, \tag{7.19}$$

$$c4=L_{aa}-L_{ac}-L_{ca}+L_{cc}, \tag{7.20}$$

$$v1=u_{ae}-u_{be}-R_a i_a+R_b i_b, \tag{7.21}$$

$$v2=u_{ae}-u_{ce}-R_a i_a+R_c i_c. \tag{7.22}$$

The neutral voltage of the machine windings can also be found as

$$u_n=u_{ae}-R_a i_a+L_{ac}b1+L_{aa}(-b1+b2-b3)+L_{ab}(-b2+b3). \tag{7.23}$$

Equations (7.11), (7.12) and (7.13) constitute the dynamic model of the actuator when driven by a three-phase electronic converter and (7.23) is the electrical output equation of the model.

7.3.2 Dynamic model for the brushless DC drive

As discussed, there are only two phases being energised in the brushless DC drive and

the third phase is floating. Accordingly, the dynamic model for the actuator driven by the brushless DC method must be revised to meet the corresponding circuit conditions of the converter.

Considering the switching sequence in the brushless DC drive, there are three combinations of phase connections caused by the switching pattern of the solid-state switches: *A-B*, *B-C* and *C-A*. The formulation of the actuator model will be derived according to these connection modes.

When phases *A* and *B* are connected to the power rail and phase *C* is floating, the electrical equations of the actuator will only involve phases *A* and *B*:

$$R_a i_a + L_{aa}\frac{di_a}{dt} + L_{ab}\frac{di_b}{dt} = u_{ae} - u_n, \tag{7.24}$$

$$R_b i_b + L_{ba}\frac{di_a}{dt} + L_{bb}\frac{di_b}{dt} = u_{be} - u_n, \tag{7.25}$$

$$\frac{di_a}{dt} + \frac{di_b}{dt} = 0. \tag{7.26}$$

Similar to the analysis in three phase excitation, the derivatives of phase currents can be found by solving the above three equations as

$$\frac{di_a}{dt} = -\frac{di_b}{dt} = \frac{(u_{ae} - R_a i_a) - (u_{be} - R_b i_b)}{L_{aa} + L_{bb} - L_{ab} - L_{ba}}, \tag{7.27}$$

and the neutral voltage of the windings can be obtained as

$$u_{nab} = \frac{(L_{bb} - L_{ba})v_{ae} + (L_{aa} - L_{ab})v_{be} - (L_{bb} - L_{ba})R_a i_a - (L_{aa} - L_{ab})R_b i_b}{L_{aa} + L_{bb} - L_{ab} - L_{ba}}. \tag{7.28}$$

Considering that the current in phase *A* and *B* are the same, i.e. $i_a=i_b=i_{ab}$, the equations can be further written as

$$\frac{di_{ab}}{dt} = \frac{u_{ae} - u_{be} - (R_a + R_b)i_{ab}}{L_{aa} + L_{bb} - L_{ab} - L_{ba}}, \tag{7.29}$$

$$u_{nab} = \frac{(L_{bb} - L_{ba})u_{ae} + (L_{aa} - L_{ab})u_{be} - [(L_{bb} - L_{ba})R_a + (L_{aa} - L_{ab})R_b]i_{ab}}{L_{aa} + L_{bb} - L_{ab} - L_{ba}}. \tag{7.30}$$

Because phase *C* is floating, the current in phase *C* will be zero and the terminal voltage

of phase C is equal to the summation of its back EMF and neutral voltage u_n.

Same method applies to the cases when phases B and C and phases C and A are energised, the corresponding derivatives of the phase currents and neutral voltage can be found as follows

$$\frac{di_{bc}}{dt} = \frac{u_{be} - u_{ce} - (R_b + R_c)i_{bc}}{L_{bb} + L_{cc} - L_{bc} - L_{cb}}, \tag{7.31}$$

$$u_{nbc} = \frac{(L_{cc} - L_{cb})u_{be} + (L_{bb} - L_{bc})u_{ce} - [(L_{cc} - L_{cb})R_b + (L_{bb} - L_{bc})R_c]i_{bc}}{L_{bb} + L_{cc} - L_{bc} - L_{cb}}, \tag{7.32}$$

and

$$\frac{di_{ca}}{dt} = \frac{u_{ce} - u_{ae} - (R_c + R_a)i_{ca}}{L_{aa} + L_{cc} - L_{ac} - L_{ca}}, \tag{7.33}$$

$$u_{nca} = \frac{(L_{aa} - L_{ac})u_{ce} + (L_{cc} - L_{ca})u_{ae} - [(L_{aa} - L_{ac})R_c + (L_{cc} - L_{ca})R_a]i_{ca}}{L_{aa} + L_{cc} - L_{ac} - L_{ca}}. \tag{7.34}$$

Equations (7.29), (7.31) and (7.33) constitute the dynamic model of the actuator when operating under brushless DC drive mode, and (7.30), (7.32), and (7.34) are the electrical output equations of the model.

By applying the equations obtained above with the kinetic equations (5.97) and (5.98) shown in chapter5, the dynamic performances of the actuator driven by the electronic converters can be readily analysed.

7.3.3 Implementation of the actuator model in SIMULINK

SIMULINK is a powerful software package that comes with MATLAB for modelling, simulating and analysing dynamic systems [Mathworks 2005]. With the comprehensive simulation components, blocks and tool boxes, SIMULINK is able to deal with various application systems, such as electrical power, mechanical, communication, etc., and different control strategies. Users can also customise and create own blocks using

S-Functions written either in m-scripts, C, C++, Ada, or FORTRAN. For modelling, SIMULINK provides a graphical user interface (GUI) for building models as block diagrams, just as with pencil and paper. This is a far cry from previous simulation solutions that require users to formulate a number of equations in a language or program. SIMULINK has also the interface with real time systems via its embedded Real Time Workshop or other third part prototyping development tools such as dSPACE. This capability simplifies and accelerates most phases of system development, and reduces repetitive and error-prone tasks.

In order to take advantage of the powerful tools provided by SIMULINK, the developed dynamic model of the PM TLA is implemented in the SIMULINK environment via S-Functions so that it can seamlessly interface with the power electronic and control blocks provided in the SIMULINK and the results can be easily post processed by the measurement and analysis tools in the SIMULINK and MATLAB.

S-Function is a computer language description of a SIMULINK block using a special calling syntax that enables customer created models to interact with SIMULINK equation solvers. Because most of the system dynamic models consist of a set of differential equations and corresponding output equations, a basic S-Function comprises a set of call-back functions that perform output calculations and integrations with necessary initialisations. Fig.7-7 illustrates the structure of the S-function within the SIMULINK for the model of the PM TLA.

The initialisation function in S-function is used for configuring the simulation block parameters. The input and output of the model are defined in this function. The inputs of the machine model include the terminal voltages and the speed and position of the translator. The gate control signals for the electronic converter is also input to the simulation block for determination of the phase conduction pattern when the actuator is driven by brushless DC method. The outputs contain the phase currents, back EMFs, and the generated force. The global variables used for the simulation and machine

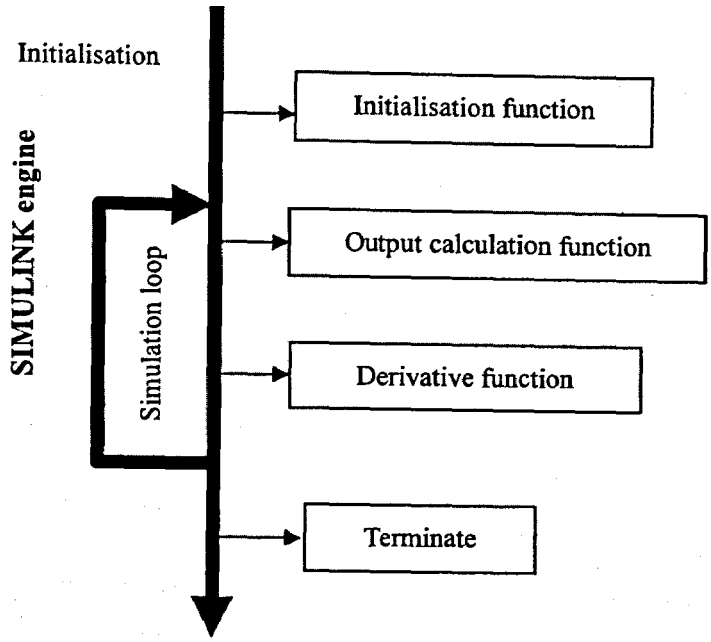

Fig.7-7 S-Function structure within SIMULINK

parameters such as the phase inductances and coil flux densities that are necessary for the model computation are also defined in the initialisation function and can be input from the magnetic field analysis.

The output calculation function computes all the outputs of the model according to the system formulation and put the results onto the output ports of the simulation block. A detailed flow chart of the output computation is shown in Fig.7-8. The derivative function performs the derivative computation. The derivatives of the state variables are calculated according to the state equations of the dynamic model and the state variables can be obtained automatically by using the designated SIMULINK equation solver. The flow chart of the derivative function is illustrated in Fig.7-9. In order to make the model to be used in any driving methods, the universal model and the model for brushless DC drive are all included in the model.

The S-Function of the PM TLA model is implemented by C language and the simulation block generated based on the S-Function is shown in Fig.7-10. Because the block only involves the electrical model of the actuator, it is called the electrical block of the

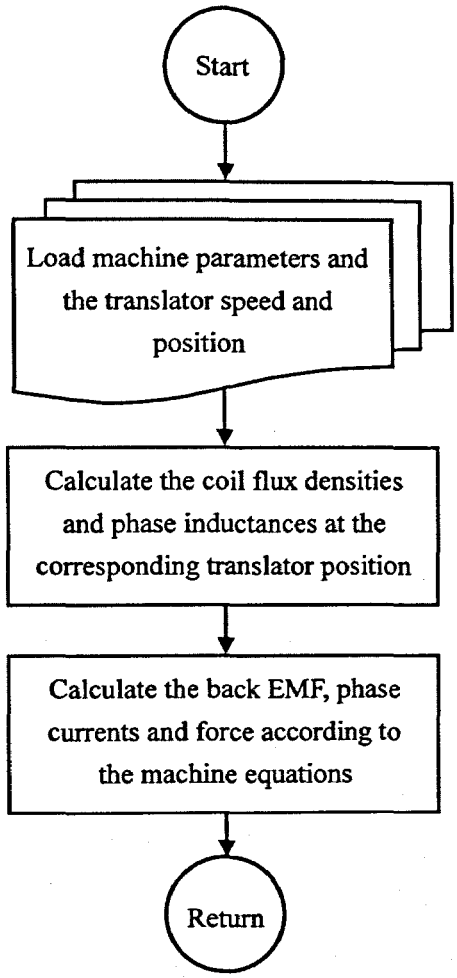

Fig.7-8 Flow chart of output function

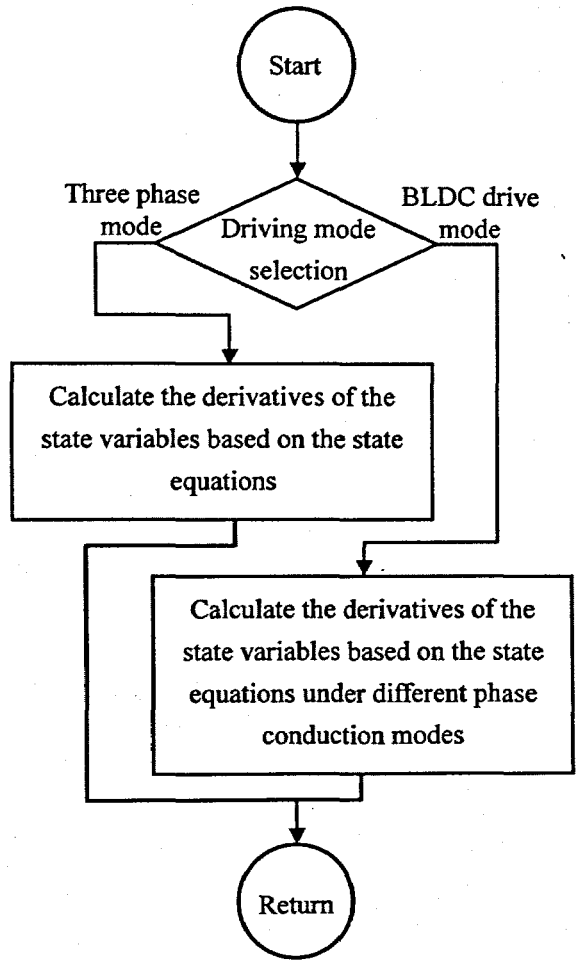

Fig.7-9 Flow chart of derivative function

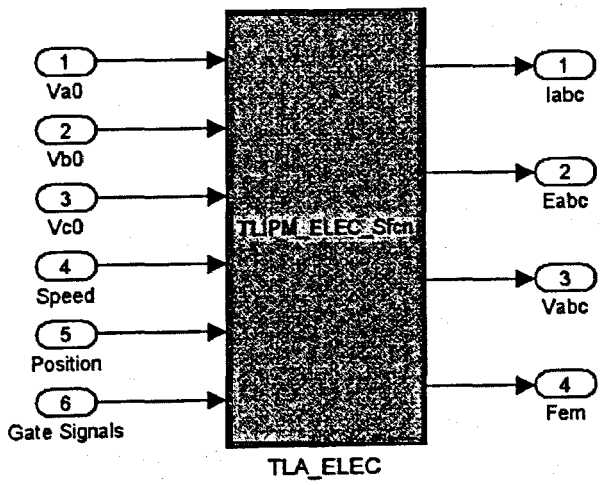

Fig.7-10 Electrical block of the SIMULINK model for the actuator

SIMULINK model of the actuator.

To analyse the dynamic performances of the actuator, kinetic model of the system is also required to be included. According to the kinetic equations of the actuator, the S-Function for the mechanical model and the corresponding simulation block can be similarly developed. Fig.7-11 shows the mechanical block of the actuator model and the complete SIMULINK model for the PM TLA is shown in Fig.7-12.

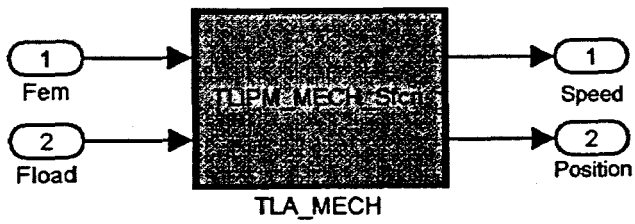

Fig.7-11 Mechanical block of the SIMULINK model for the actuator

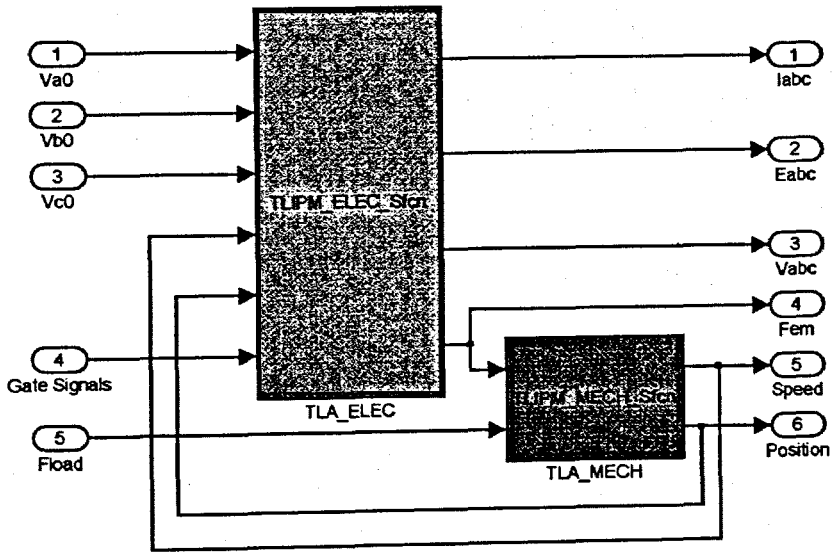

Fig.7-12 Complete SIMULINK model for the actuator

By defining the model shown in Fig.7-12 as a subsystem block, the SIMULINK model of the PM TLA can be used in the simulation just like an embedded block in the SIMULINK environment and can work with any other blocks provided in the software package. To verify the SIMULINK model of the actuator, a 60Hz balanced three-phase sinusoidal voltage is applied and the performances obtained by the simulation in SIMULINK are exactly the same as those obtained by solving the dynamic equations

using m-scripts as illustrated in chapter 5. Moreover, in order to investigate the operation of the PM TLA under switched power source, a three-phase full bridge converter with sinusoidal PWM (SPWM) is applied to the model and Fig.7-13 shows the diagram for the analysis. The orange coloured subsystem block is the SIMULINK model of the actuator. The full bridge converter and SPWM generator are the standard blocks provided by the SimPowerSystem toolbox in the SIMULINK package.

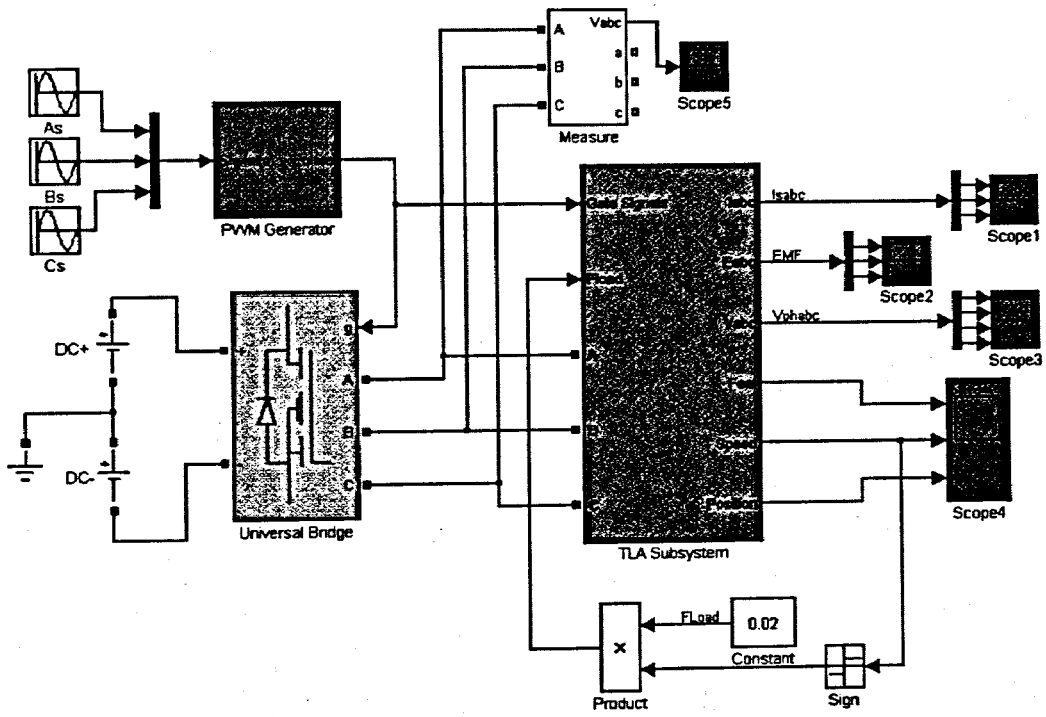

Fig.7-13 Actuator model with electronic converter

Figs.7-14 and 15 plot the simulated results when the actuator is driven by a 60Hz SPWM voltage. The switching frequency of the electronic converter is set as 25 kHz. Because the winding inductances of the actuator are too small, the phase currents are discontinued when the actuator is driven by PWM voltage, and the resultant electromagnetic force is a pulsed waveform as shown in Fig.7-14 and the effective actuation force is insufficient to drive the translator in phase with the stator field. As a result, the translator loses phase with the stator excitation and the actuator cannot run through the entire stroke (Fig.7-15) as in case when it is applied with pure sinusoidal voltages.

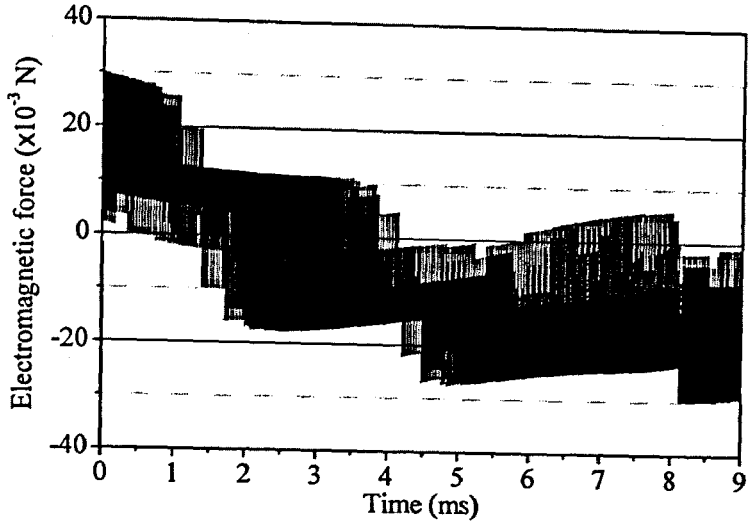

Fig.7-14 Force of the actuator when driven by SPWM voltage

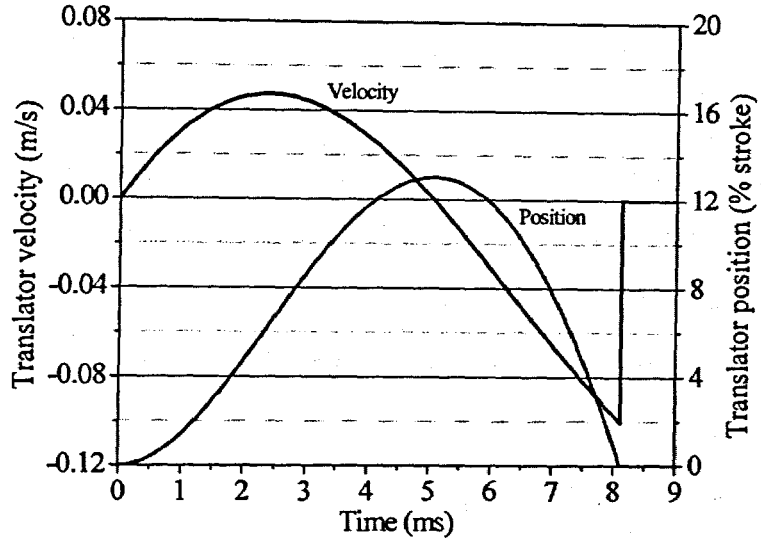

Fig.7-15 Operation of the actuator when driven by SPWM voltage

Therefore, it can be concluded that, due to the low phase inductances, the designed actuator is not suitable for working with PWM techniques, which are widely used in the electric machine control. Fortunately, for micro applications, the power supplies are usually low voltage sources, such as batteries, and electronic drive without using the PWM technique is possible. Without using PWM technique, the switching losses of the switching devices can also be eliminated and the power consumption of the system can hence be reduced. Furthermore, the control system can be simplified if the PWM function is not employed.

7.4 Drive Control of the PM TLA

The designed linear actuator is used for the locomotion of micro mobile robot. It is obvious that there is no spare room for the installation of any type of linear mechanical position sensor within the restricted robot body. A sensorless control scheme must be developed for the control of the designed actuator.

7.4.1 Sensorless control of the actuator

As mentioned in section 7.2, detection of ZCP of inactive phase EMF is the most commonly used method for the sensorless drive of brushless DC machines. The method is suitable for micro applications because of its simple implementation and effectiveness. It is possible to integrate the entire control units onto one single chip device and attached to the actuator so that the actuator and control system could become an integrated device. Therefore, the sensorless control using the back EMF detection method is adopted for the control of the proposed linear actuator

The principle of the sensorless scheme by using the back EMF detection has been discussed in section 7.2. Based on the characteristic analysis of the proposed PM TLA conducted in chapter 5, the back EMF in each phase can be estimated by using the summation of the magnetising flux density in each phase coil (hereinafter called the magnetising flux density in each phase). When neglecting the EMF caused by the machine saliency and the magnetic field generated by the phase current, according to (5.57) to (5.58), the magnetising flux density in each phase can be obtained as

$$B_{am} = B_r\big|_{x_{a01+}} + B_r\big|_{x_{a02+}} - B_r\big|_{x_{a01-}} - B_r\big|_{x_{a02-}}, \tag{7.35}$$

$$B_{bm} = B_r\big|_{x_{b01+}} + B_r\big|_{x_{b02+}} - B_r\big|_{x_{b01-}} - B_r\big|_{x_{b02-}}, \tag{7.36}$$

$$B_{cm} = B_r\big|_{x_{c01+}} + B_r\big|_{x_{c02+}} - B_r\big|_{x_{c01-}} - B_r\big|_{x_{c02-}}. \tag{7.37}$$

By the magnetic field analysis conducted in chapter 5, the magnetising flux density in

each phase under different translator positions can be found. Fig.7-16 plots the variations of the magnetising flux densities versus translator positions and the back EMF in each phase is proportional to the corresponding flux density in the figure.

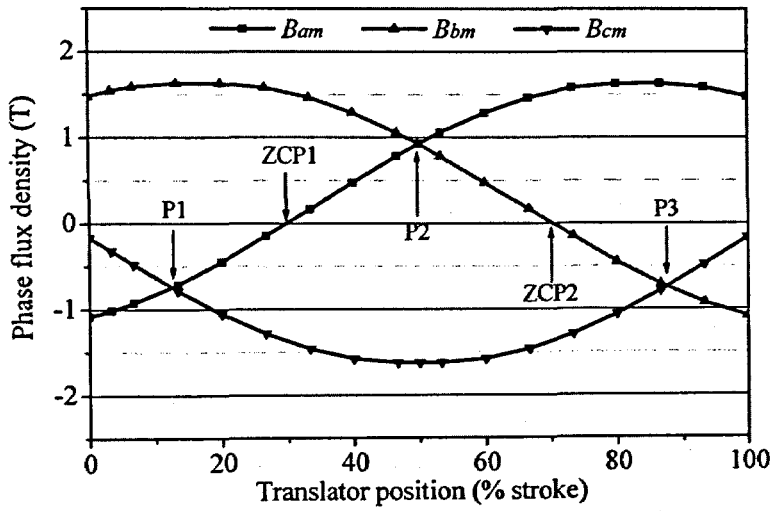

Fig.7-16 The magnetising flux density in each phase

As per the sensorless drive principle, it can be seen that there are three commutation positions during the entire stroke of the translator, i.e. P1, P2 and P3 shown in Fig.7-16. If the translator is starting from zero position, the commutation positions P2 and P3 can be determined by the detection of ZCPs in the back EMFs of phase *A* and phase *B*, which are ZCP1 and ZCP2 shown in Fig.7-16. The method for detection of ZCPs of the back EMF implemented in SIMULINK is illustrated in Fig.7-17.

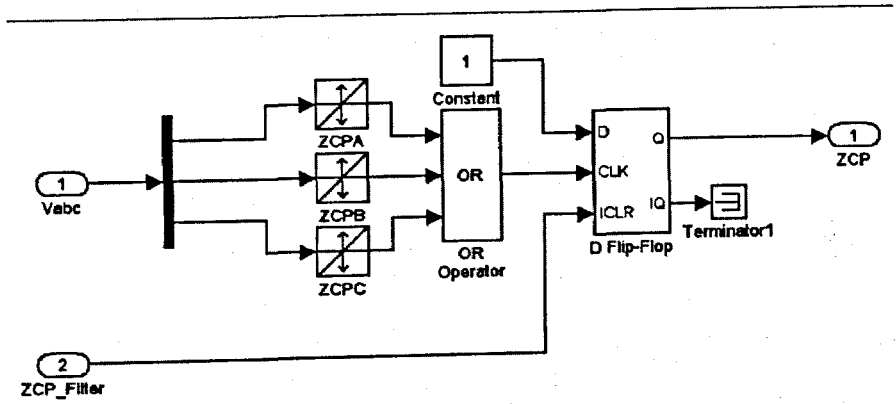

Fig.7-17 Implementation of ZCP detection method

During the operation, each of the measured phase voltages passes through a zero-crossing detection component and a positive pulse will be generated at the output

of the component whenever a zero-crossing occurs. All the pulses generated by the three zero-crossing detection components are then combined together as the trig signal of a D flip-flop. If any of the phase voltages experiences zero-crossing, the D flip-flop will be trigged and its output is set as the indicator of a zero-crossing event to the up-level control algorithm. Because of the noises during the measurement of phase voltages, the zero-crossing detection component usually produces several pulses when a zero-crossing occurs. The use of D flip-flop can eliminate the unwanted signals and the device will be only trigged once for a single zero-crossing event.

Only the ZCPs of the back EMF in the floating phase are useful for the determination of commutation sequence. However, the commutation of phase currents will also produce ZCPs in the voltages of energised phases and they can be detected as well because the phase voltages are always connected to the ZCP detection unit during the operation. These ZCP signals irrelevant to the back EMFs will mislead the control algorithm and result in wrong commutation sequences. To get rid of this problem, a ZCP filter signal generated by the control algorithm is applied. When an effective ZCP signal is detected, the ZCP filter signal will be cleared so that the D flip-flop is disabled. The output of the detection unit is therefore locked to zero and no ZCP indication signal can be generated. The ZCP filter signal will remain cleared until the commutation corresponding to the detected zero-crossing event is completed. Fig.7-18 illustrates the function of the ZCP filter signal.

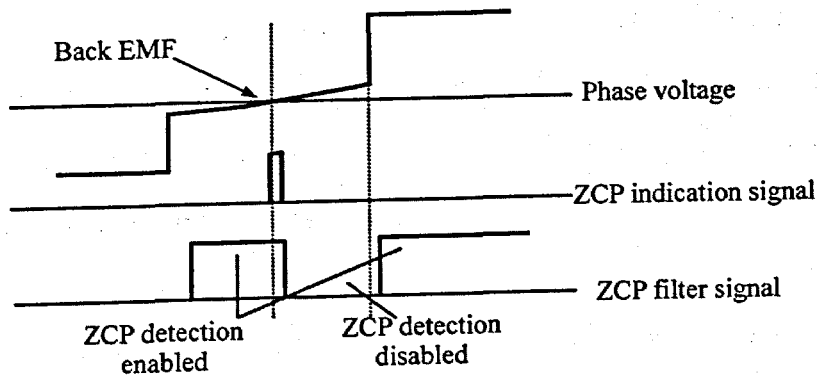

Fig.7-18 Function of the ZCP filter signal

Because the corresponding commutation occurs after the ZCP of the back EMF with a

30 electric degree phase shift, a time shift is required to accomplish the desired commutation on time. The time shift is translator speed related and can be obtained by using the speed of the translator when ZCP occurs via the following equation

$$t_{shift} = (\tau / 6) / v_{sm\_est}, \tag{7.38}$$

where $\tau/6$ gives the distance for 30 electric degrees in the actuator and the v_{sm_est} is the translator speed estimated according to the time duration between ZCPs.

7.4.2 Start up strategy and the detection of first commutation position

The start up of the machine is a problem in the brushless DC drive due to lack of back EMF when machine is stationary. However, according to the application of the designed actuator, the translator of the actuator can be automatically drawn back to the start position, namely, zero position, because a restoration spring is used for the robotic actuation mechanism. Therefore, the translator will always start near the zero position and the corresponding conduction mode is known. This mechanism greatly simplifies the sensorless control of the actuator. Nevertheless, to improve the robustness of the drive system, the translator alignment method can be still applicable whenever the translator accidentally fails to restore its starting position.

Although the linear actuator can be started up easily from its initial position, the first commutation position cannot be determined by ZCP detection because there is no ZCP taken place before the corresponding commutation no matter which side the translator is started from. To overcome this issue, one of the methods that can be used to determine the commutation position other than finding the ZCP in the back EMF is to integrate the back EMF of the unexcited phase [Becerra 1991].

Considering the back EMF of an unexcited phase of the PM TLA, the integration of the back EMF in a period of time from t_0 to t_1, as shown in Fig.7-19, can be given by

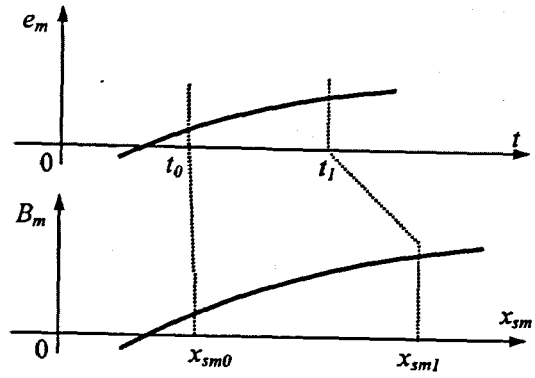

Fig.7-19 Back EMF and magnetising flux density

$$\int_{t_0}^{t_1} e_m dt = \int_{t_0}^{t_1} 2\pi r_c N_t B_m v_{sm} dt \,, \tag{7.39}$$

where B_m is the magnetising flux density in the phase winding described in section 7.4.1 and it is a function of the translator position with respect to the stator x_{sm}. Considering $v_{sm}=dx_{sm}/dt$, the above integration can be further expressed as,

$$\int_{t_0}^{t_1} e_m dt = 2\pi r_c N_t \int_{t_0}^{t_1} B_m(x_{sm}) dx_{sm} = 2\pi r_c N_t \int_{x_{sm0}}^{x_{sm1}} B_m(x_{sm}) dx_{sm} \,, \tag{7.40}$$

where x_{sm0} and x_{sm1} are the translator positions with respect to the stator at time t_0 and t_1, respectively. According to (7.40), it can be concluded that, if the translator is travelling from a certain position x_{sm0} to another known position x_{sm1} in a time period of $\Delta t=t_1-t_0$, the integration of the back EMF in the phase winding $\int_{t_0}^{t_1} e_m dt$ will be a certain value independent to the travelling velocity of the translator because $\int_{x_{sm0}}^{x_{sm1}} B_m(x_{sm}) dx_{sm}$ is constant for the given positions of x_{sm0} and x_{sm1}. Based on this principle, the integration of the back EMF in the unexcited phase during the time when the translator is travelling from the starting position to the first commutation position, e.g. P1, will be a constant and it can be used as the threshold for the control algorithm to carry on the desired commutation operation. However, this method is highly machine-dependant because the designed flux density is quite distinct from different machines. The integration threshold can only be appropriately set based on a good understanding of the magnetic characteristics of the machine.

By adopting this method, when the linear actuator is started by a proper switching state,

an integration of the back EMF in the floating phase will be initiated. Once the integration result reaches the preset threshold, the corresponding commutation will be executed and the subsequent commutation can then be accomplished by ZCP detection.

7.4.3 Flow chart of the sensorless control scheme

Fig.7-20 shows the complete flow chart of the sensorless control for the designed actuator.

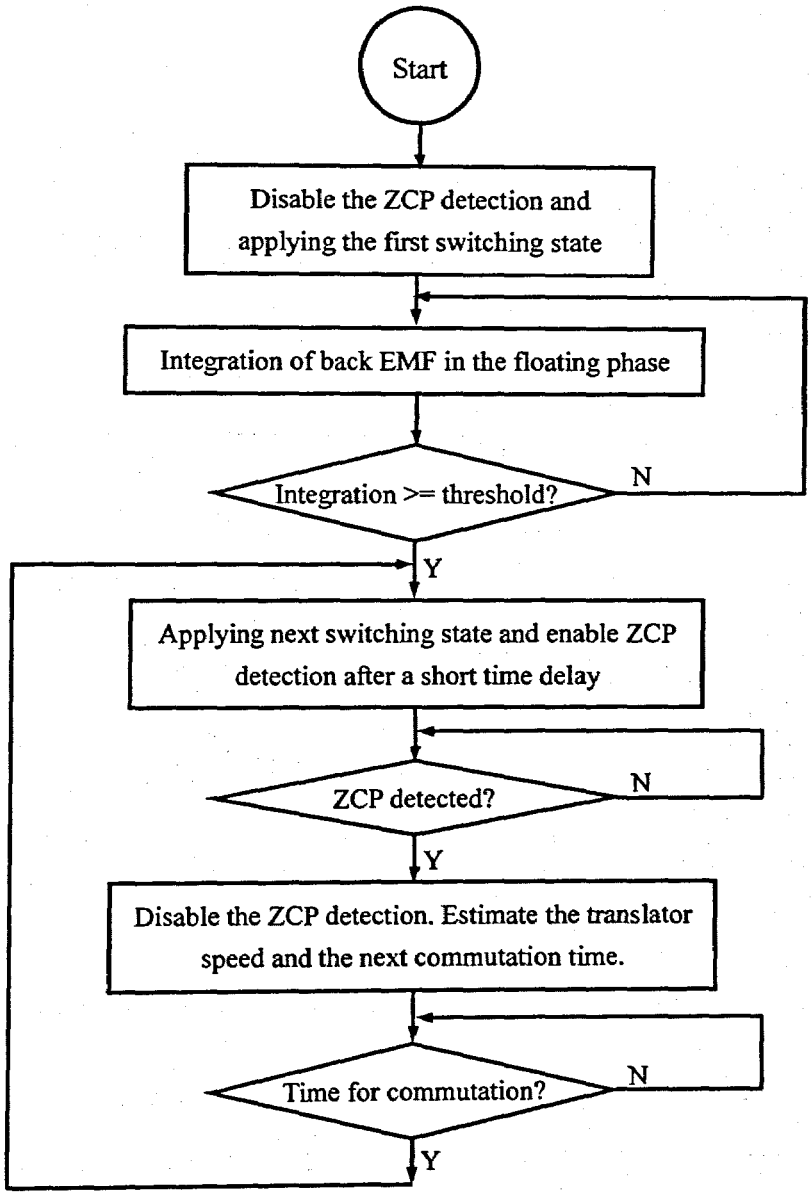

Fig.7-20 Flow chart of the sensorless control for the PM TLA

7.5 Performance Simulation of the Control Scheme

7.5.1 System model in SIMULINK

According to the sensorless control scheme discussed in section 7.4, the control algorithm for the PM TLA is implemented in SIMULINK. Together with the developed SIMULINK model of the actuator, the performance of the actuator with the developed sensorless control scheme can be simulated and analysed. Fig.7-21 shows the completed drive system of the PM TLA with sensorless control scheme. As discussed in section 7.3, no PWM technique will be employed in the electronic converter.

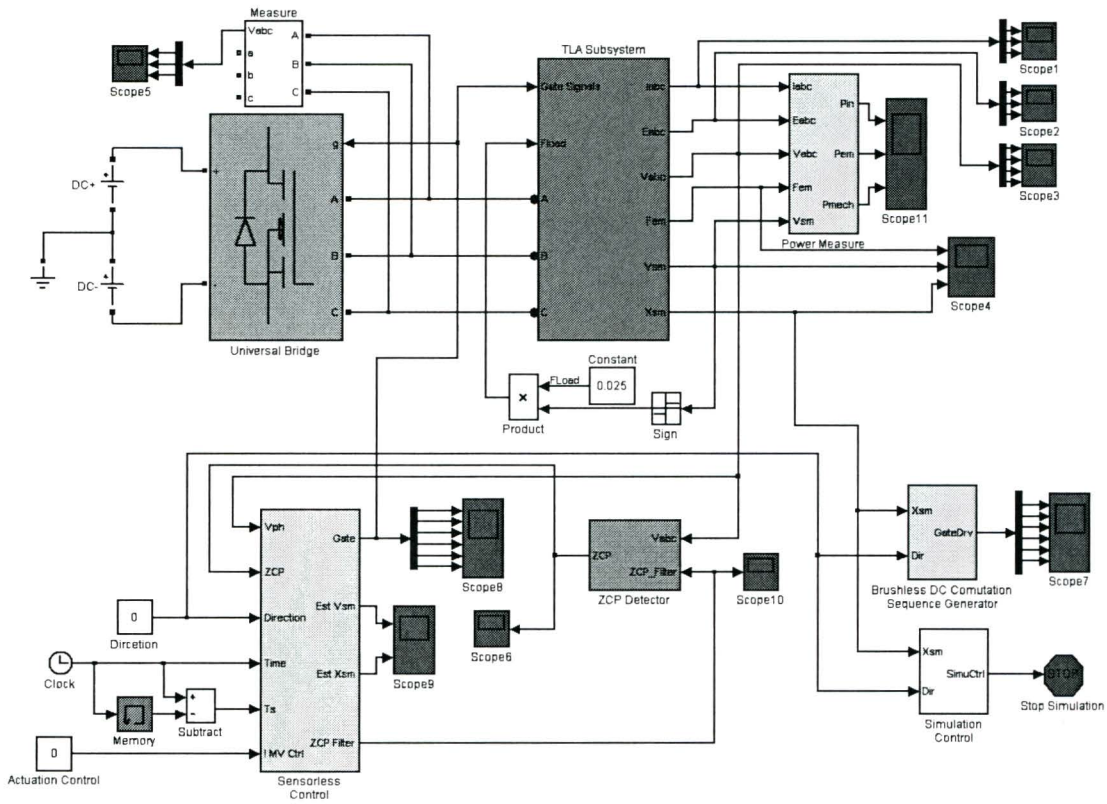

Fig.7-21 SIMULINK model of the sensorless control system of the PM TLA

In the system, the sensorless control is realised by the S-Function of the control algorithm. An actuation control signal is also introduced in the sensorless control algorithm so that the control of the system can be enabled/disabled by the signal. The signal would be very useful when applying the control to the locomotion control of

robotics. The ZCP detection block is the subsystem illustrated in Fig.7-17. Because the external load is always against the movement of the translator, a sign function is used for the generation of load force. In order to have a comparison to the commutation sequence generated by the mechanical position sensor, a commutation sequence generator based on the actual translator position is also included in the simulation system. In addition, a power measurement block is constructed for computing the input and output power of the linear actuator. The simulation control block in the system is used for the controlling the simulation process. When the translator of the actuator completes its full journey within the stator, the block generates a stop command to the SIMULINK and the simulation will be terminated.

7.5.2 Actuation performance without load

The driving performance of the actuator with no load is firstly simulated. The following graphs show the simulated electrical and mechanical results. The control signals generated by the sensorless algorithm are also plotted.

The excitation voltages and the phase currents displayed in Figs.7-22 and 23 show that the commutation of the electronic converter operates effectively with the movement of translator. The commutation positions obtained by EMF integration and ZCP detection are accurate. The comparison between the control signals generated by the sensorless algorithm and those derived from the actual translator position (Fig.7-24) show that the implemented sorserless control for the actuator is satisfactory. As a result, the transition of the electromagnetic force of the actuator is appropriate and smooth, as shown in Fig.7-25.

Figs.7-26 and 27 plot the simulated translator velocity and position with respect to the stator. The velocity and position estimated by the sensorless control algorithm are also plotted in the figures. It is shown that the estimated translator velocity and position throughout the entire stroke are very close to the actual values. This is very important in

the locomotion control of the robotic system since the gait control of the robot will be completely based on translator positions.

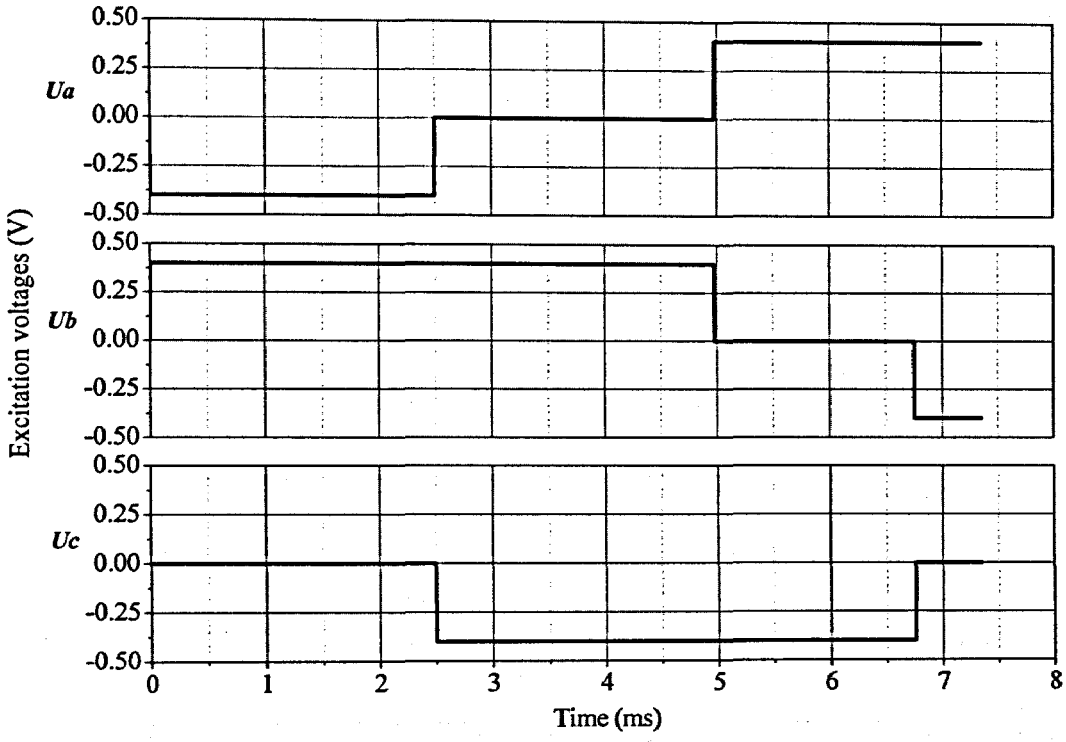

Fig. 7-22 Excitation voltages applied to the PM TLA

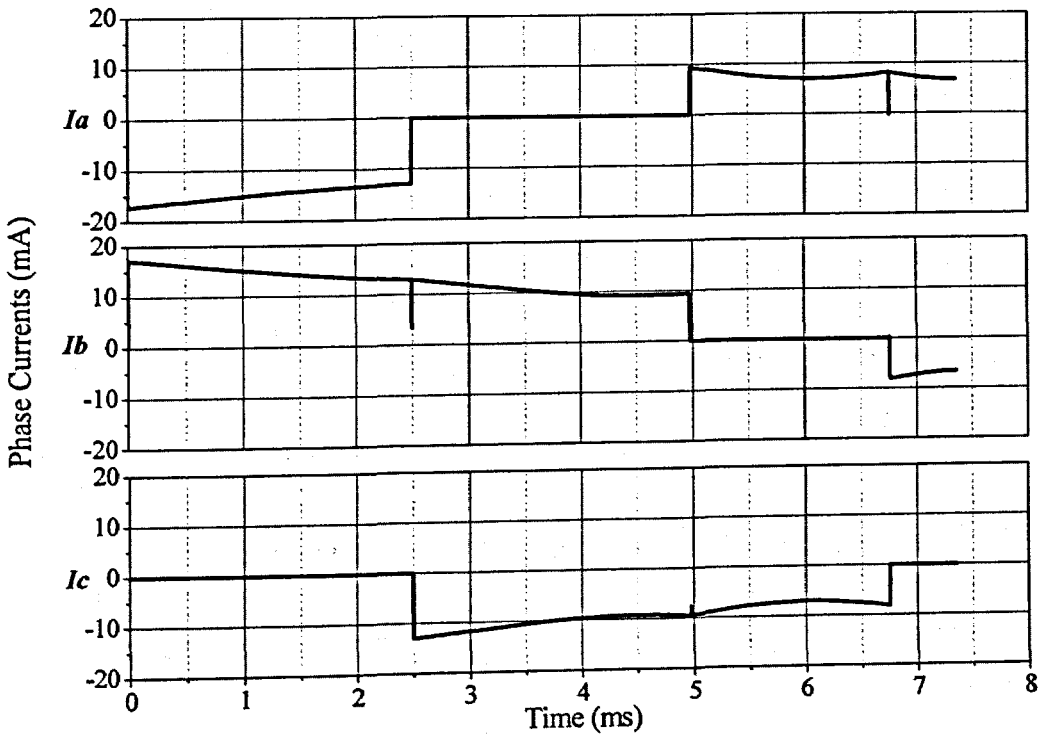

Fig. 7-23 Phase currents in each phase of the PM TLA with no load

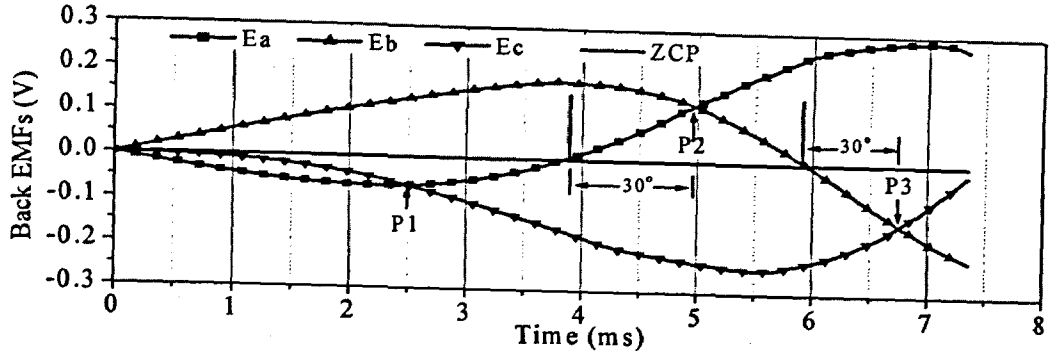

(a) Back EMFs and ZCP signal for the sensorless control

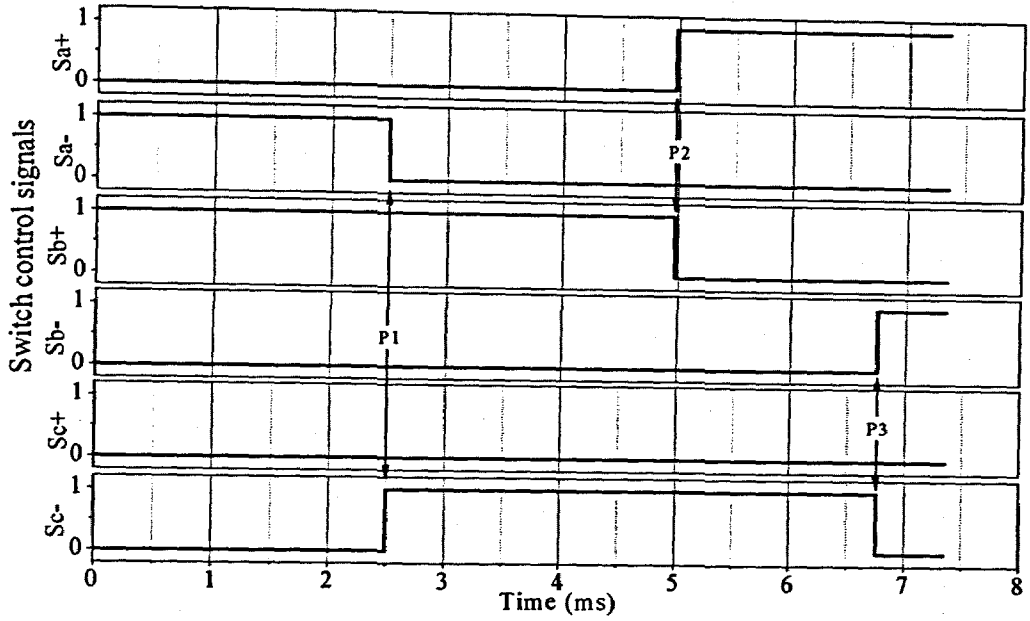

(b) Switch control signal generated by the sensorless algorithm

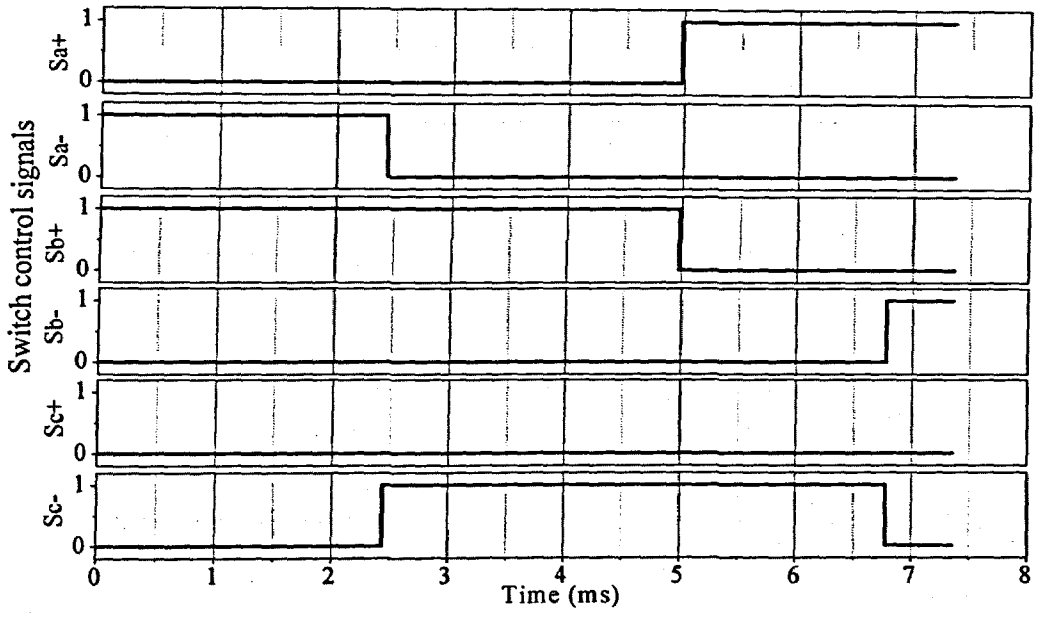

(c) Switch control signal according to actual translator position

Fig.7-24 Control signals for sensorless drive of the PM TLA

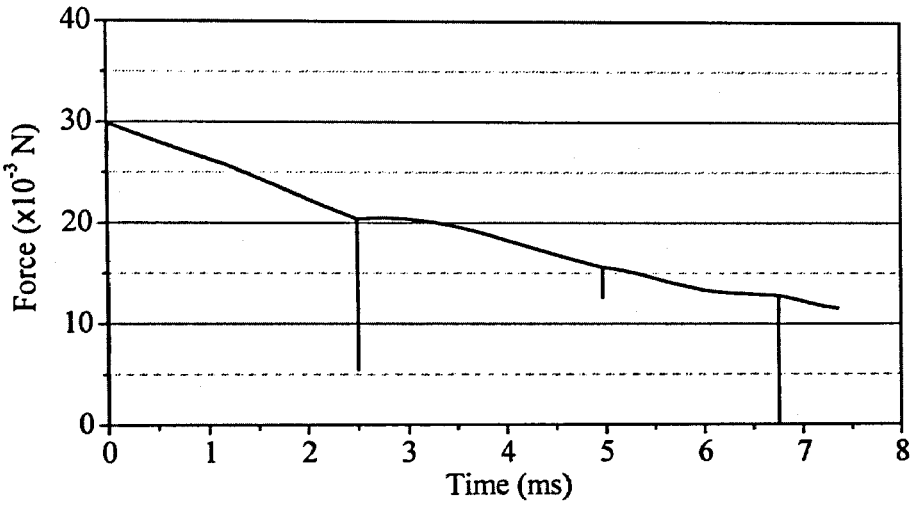

Fig.7-25 Actuation force of the PM TLA with no load

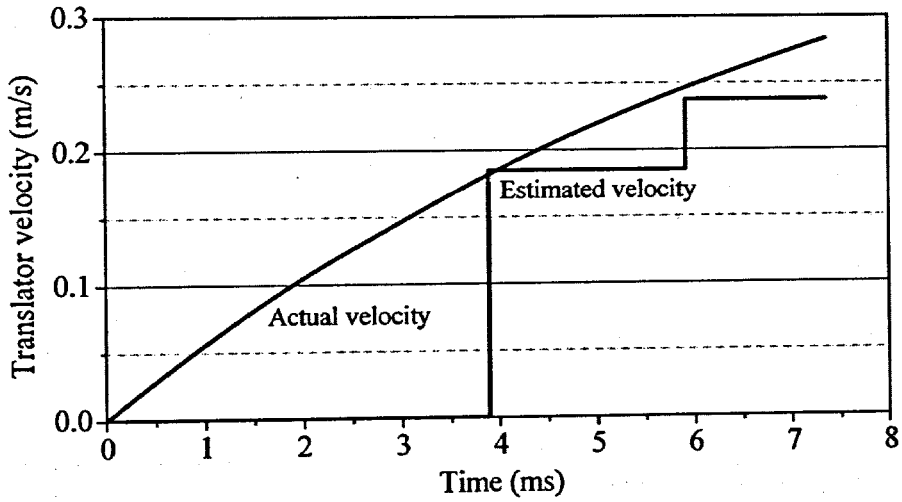

Fig.7-26 Actual and estimated translator velocities

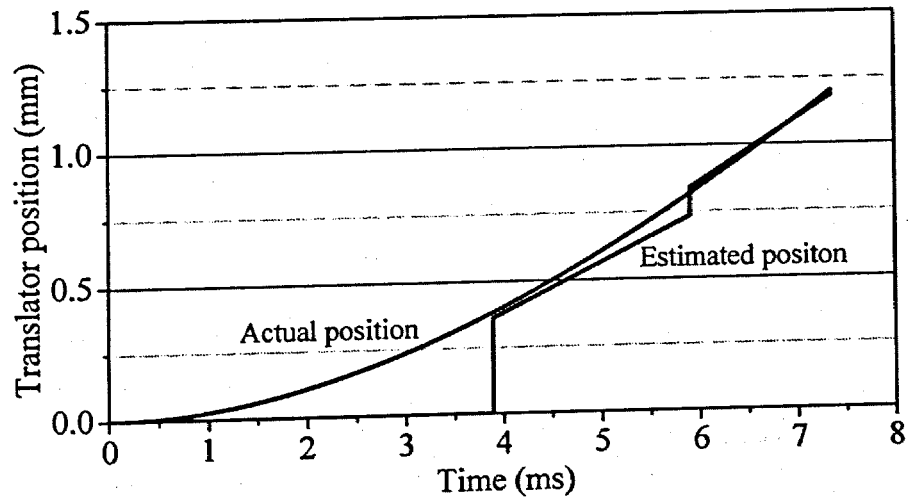

Fig.7-27 Actual and estimated translator positions

7.5.3 Actuation performance with load

Figs.7-28 to 31 show the actuator performances with an external load of 25mN, which is the load capability of the designed actuator shown in the characteristic analysis in chapter 5. Under this load condition, the current required for driving the actuator is about 15mA, which is the rated current designed for the linear actuator. The actuation force of the actuator is plotted in Fig.7-29. It can be seen that the actuator is working at its optimal force output condition throughout the operation, which is just the control algorithm aims to achieve.

Figs.7-30 and 31 show the translator velocity and its position with respect to the stator together with the estimated values. The maximum velocity the translator can acquire is about 75mm/s. However, because the external load is close to the maximum force that the actuator can produce and the output force of the actuator will be less during the commutation of the phase currents, the velocity of the translator displays somewhat fluctuating due to such force ripples during the operation.

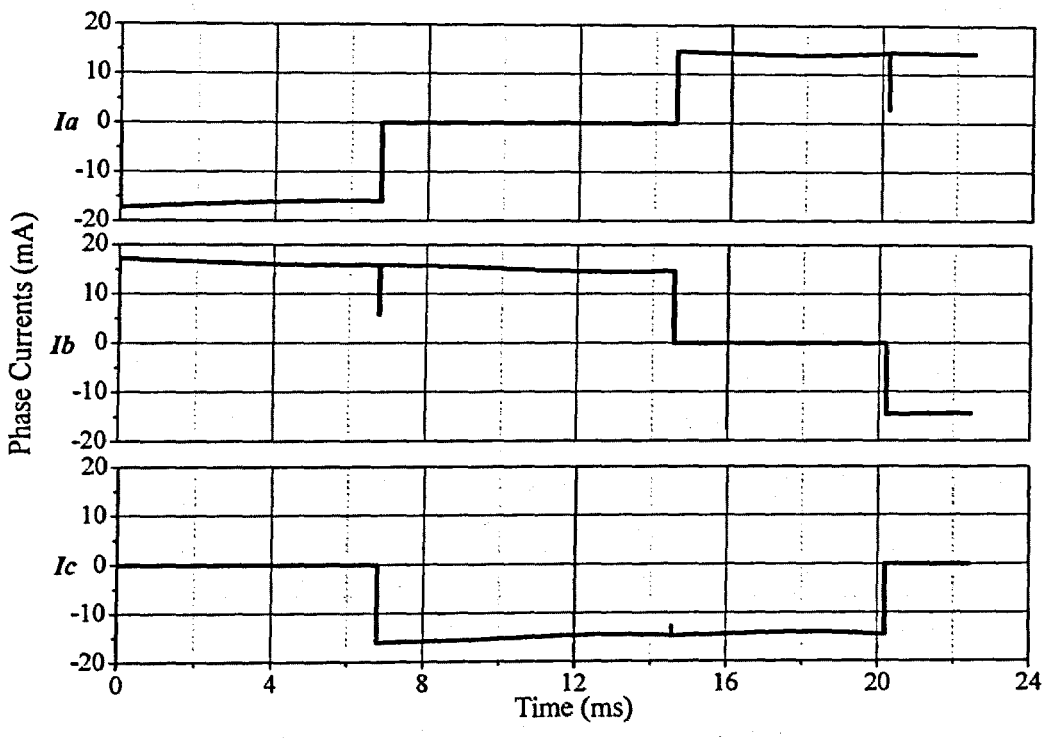

Fig.7-28 Phase currents in each phase of the PM TLA with maximum load

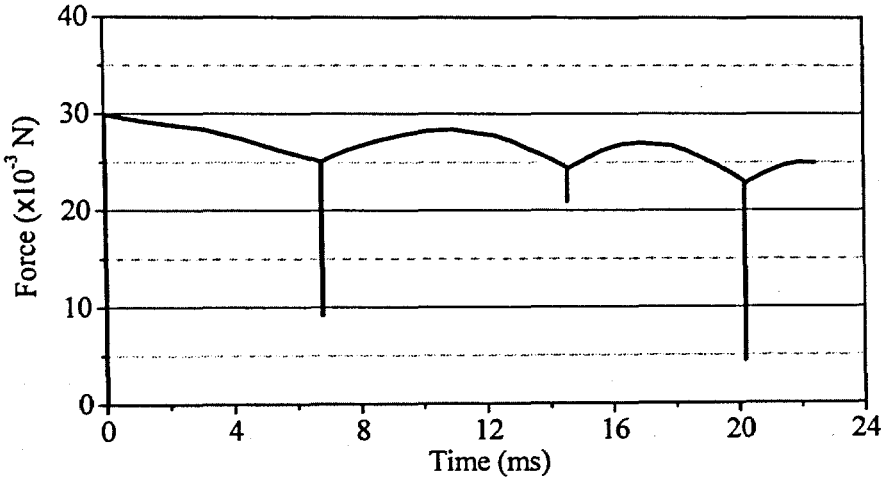

Fig.7-29 Actuation force of the PM TLA with maximum load

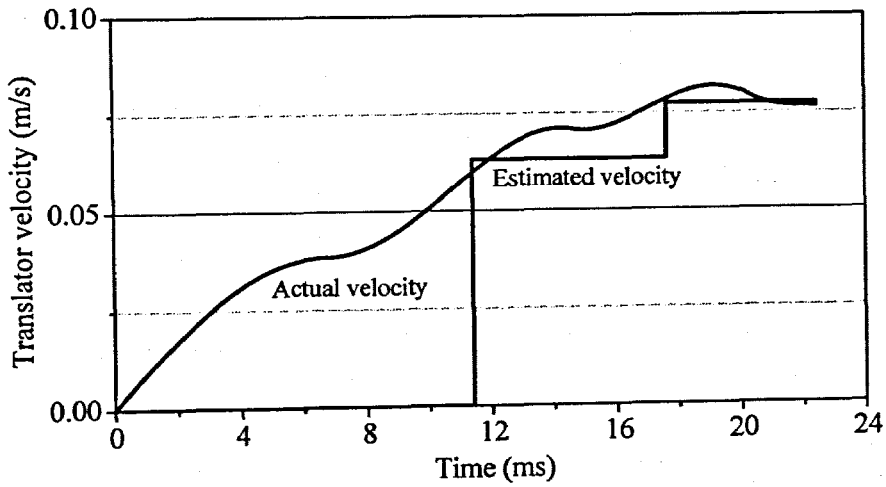

Fig.7-30 Actual and estimated translator velocities

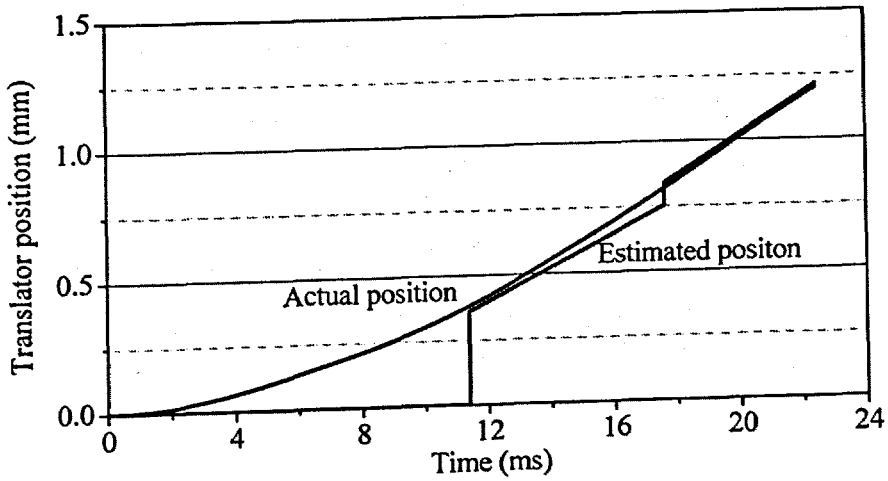

Fig.7-31 Actual and estimated translator positions

The power consumption and output power of the actuator is also calculated and displayed in Figs.7-32 and 33. When the actuator reaches steady state, the input electric power of the actuator is around 12mW and the output mechanical power is about 2.0mW. Hence, the overall efficiency of the system at full load will be about 16%. The rest of the energy is mostly consumed on the resistances of the windings of the actuator. The rest of the energy is mostly consumed on the resistances of the windings of the actuator. Hence, the efficiency of the actuator could be improved by reducing the winding resistances. However, a compromise should be taken in to account between the resistance and the working voltage. Less winding resistances will lead to a very low working voltage that would make it difficult in back EMF detection for the sensorless control scheme.

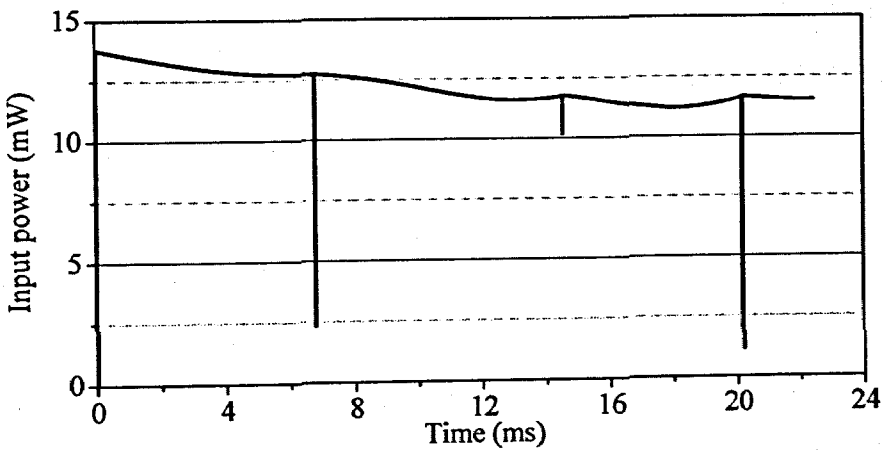

Fig.7-32 Input electrical power during the operation

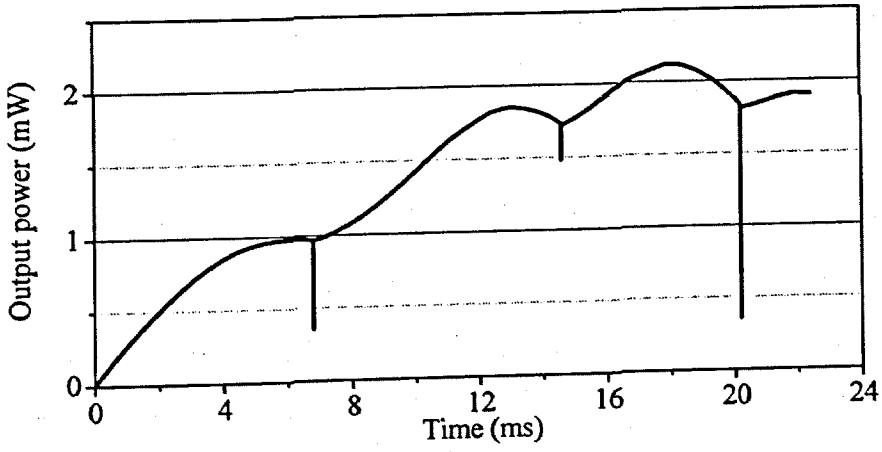

Fig.7-33 Output mechanical power of the PM TLA

7.6 Implementation of the Actuator Control System

This section presents the implementation of the control system for the designed linear actuator including the hardware design. The control system of the actuator is designed based on the dSPACE DS1104 prototyping system. With the tool, the control algorithm developed in the SIMULINK environment can be directly put into practice by using its controller board and the corresponding software. The application of the prototyping system can effectively reduce the time during the prototype development.

7.6.1 Introduction to dSPACE DS1104 prototyping system

The DS1104 prototyping system is one of the controller development products produced by dSPACE GmbH in Germany. The prototyping system comprises a PCI-slot controller board, the corresponding Real-Time Interface (RTI) for SIMULINK and the experimental software ControlDesk. Fig.7-34 [dSPACE 2007] illustrates the basic structure of the DS1104 prototyping system.

The DS1104 controller board is a dual-microprocessor board containing a master microprocessor PowerPC MPC8240 and a digital signal processor TMS320F240. The combination of the both processors with extra powerful I/O interface makes it an ideal hardware solution for the development of controllers in various fields, such as drives and robotics, etc.

RTI is the linkage between the SIMULINK software and dSPACE real time hardware. By using RTI, the implemented SIMULINK model can readily access and manage the components in the real time hardware and the physical objectives of the system can be controlled or manipulated by the SIMULINK environment. ControlDesk is a comprehensive, virtual instrument-oriented experiment environment that can intuitively manage, control, and automate experiments. Through its GUI, it is convenient to change

parameters, loading look-up tables and recording data during an experiment. The bypass system is a customised application-specified hardware used between the DS1104 controller board and real control objectives. This unit usually contains the necessary signal pre-processing components and power converter if needed.

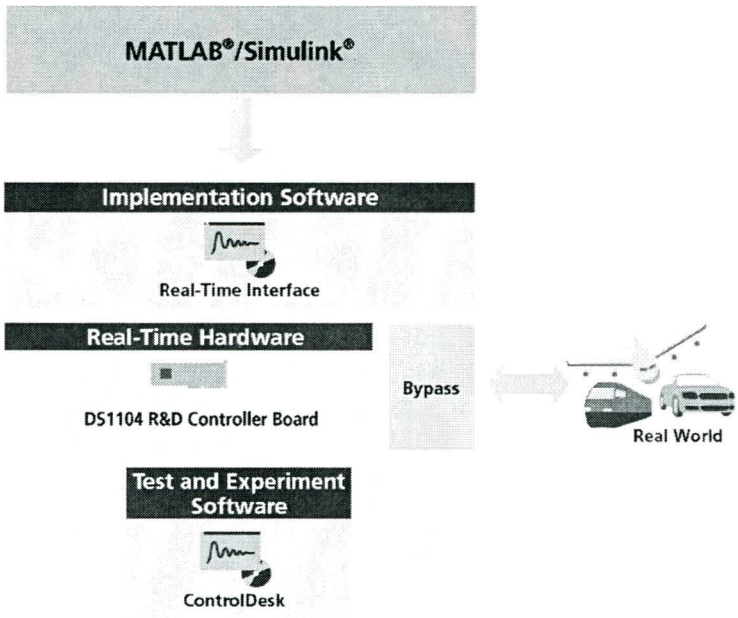

Fig.7-34 Basic structure of the dSPACE prototyping system

7.6.2 Hardware of the control system

7.6.2.1 Hardware configuration

Fig.7-35 shows the block diagram of the hardware for the actuator control system. The driving board shown in the figure is the bypass system required between the DS1104 controller board and the PM TLA as the power driving and signal collecting system. The driving board contains three major function blocks: the gate driver, 3-phase full bridge converter and 3-channel signal amplifier. The gate driver is used to receive control signals from the DS1104 controller board and to generate the six gate control signals required for the power devices in the 3-phase full bridge converter. It also provides the necessary protections for the power transistors to avoid the damages to the devices. Because the back EMF of the designed actuator is quite small, the levels of the voltage

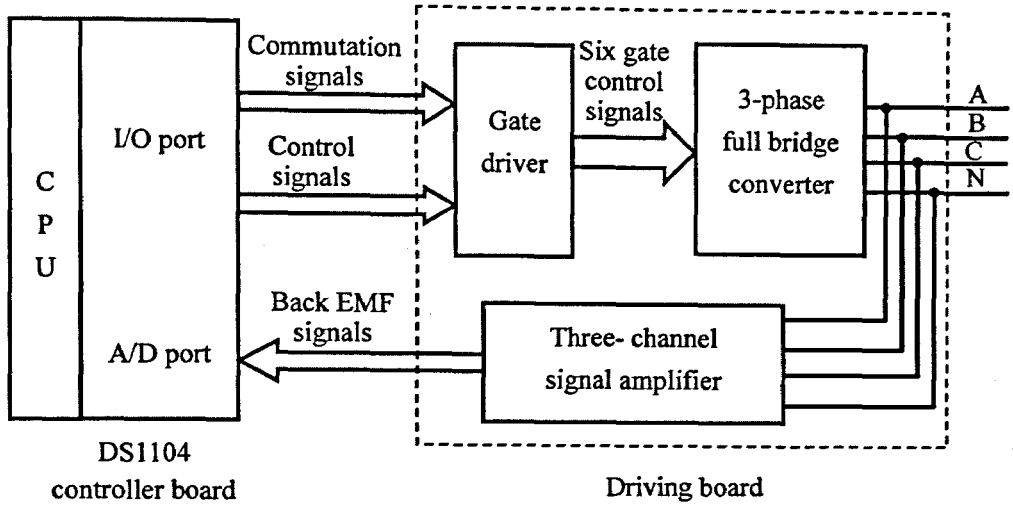

Fig.7-35 Block diagram of the actuator control system

signals from the actuator are required to be increased so that they can meet the voltage requirement of the A/D converter in the DS1104 controller board. Hence, a 3-channel signal amplifier is designed for the purpose. The processed voltage signals are then input to the A/D ports of the controller board. A complete hardware schematic diagram of the driving board can be found in Appendix C.

7.6.2.2 Implementation of the gate driver

The gate driver is the most important component in the driving board. It translates the control signals generated by the controller board to the signals required by the electronic power converter. There is a wide range of commercially available products can be selected for the application. For our design, A3932 from Allegro Microsystems Inc. is applied. A3932 is a three-phase MOSFET controller for the use with bipolar brushless DC machines [Allegro 2002]. The A3932 implements the commutation logic for Hall sensors configured with 120 degree spacing. Its bootstrapped high-side drive blocks provide the floating positive supplies for the gate drives and minimise the component count normally required. The high-side circuitry also employs a unique FET monitoring circuit that ensures the safe switching operation of the MOSFET devices. The peak load current is limited by an input reference voltage and external sensing resistor, which can

be selected by the designers. Power MOSFET protection features include bootstrap capacitor charging current monitor, under voltage monitor, motor-lead short-to-ground, and thermal shutdown.

The gate drive circuit by using A3932 is illustrated in Fig.7-36. C15, C16 and C19 are the bootstrap capacitors for the gate drivers. With the electrical charges stored in these capacitors, the voltages for driving the high-side MOSFETs can be provided and hence no extra high-side power supply is needed. R33, R17 and C13 form the current sensing circuit, providing the load current information for the current limitation when a current reference is set by the potentiometer R31. However, this function will not be used in the actuator control because no PWM technique is employed for the current control. This current control circuit is only for the protection purpose that limits the load current during exceptional conditions.

HA, HB, and HC are the commutation control signals and DIR is used for determining the operation direction. Because A3932 is designed with the commutation logic for Hall position sensors in the brushless DC drive, the control signals for HA, HB and HC from

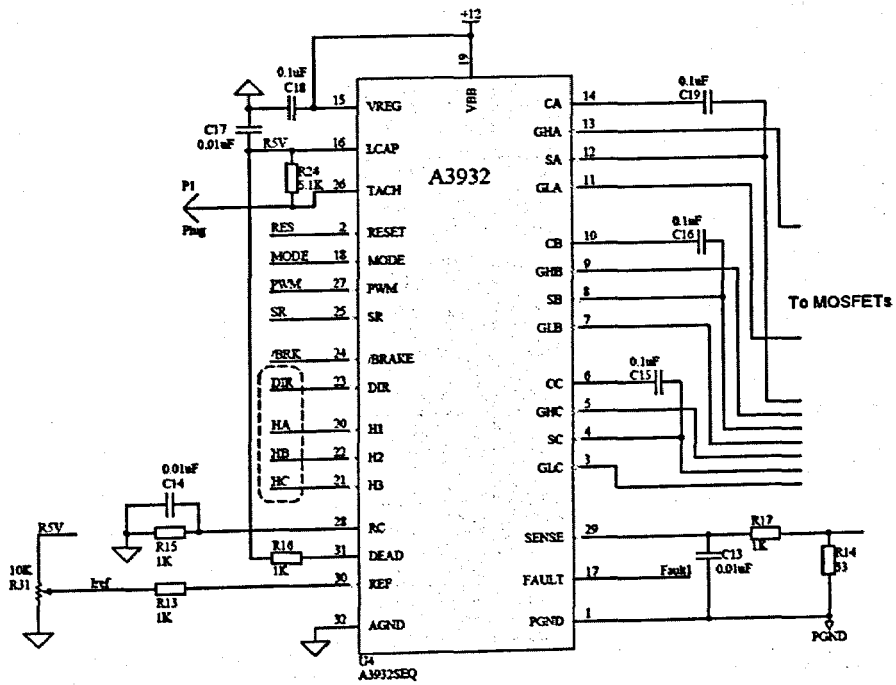

Fig.7-36 Implementation of gate drive circuit

the controller board should be generated as if they are generated by the Hall sensors. Table 7-1 shows the commutation truth table of the device. According to the machine terminals state shown in the table, the proper input logics of HA, HB, and HC used for the PM TLA can be established. Because the input logics with all zeros or all ones are not possible for the Hall sensors during normal operation, these signals are regarded as invalid and a fault will be generated by the device. If a fault occurs, all the MOSFET drivers will be turned off until the fault logic is cleared by a valid RESET signal. However, for the designed sensorless control algorithm, the invalid commutation logic can be useful for switching off the electronic power converters when the actuator reaches its maximum stroke. RESET is the enable signal for the device. A logical low input allows the gate drivers to follow the commutation logic input by HA, HB and HC. If a logic high input is set on RESET terminal, the device is disabled and the all the faults will be cleared if any.

Table 7-1 Commutation truth table of A3932

Input logics				MOSFET driver output						Machine terminals		
HA	HB	HC	DIR	GHA	GHB	GHC	GLA	GLB	GLC	SA	SB	SC
1	0	1	0	0	0	1	1	0	0	L	Z	H
1	0	0	0	0	0	1	0	1	0	Z	L	H
1	1	0	0	1	0	0	0	1	0	H	L	Z
0	1	0	0	1	0	0	0	0	1	H	Z	L
0	1	1	0	0	1	0	0	0	1	Z	H	L
0	0	1	0	0	1	0	1	0	0	L	H	Z
1	0	1	1	1	0	0	0	0	1	H	Z	L
1	0	0	1	0	1	0	0	0	1	Z	H	L
1	1	0	1	0	1	0	1	0	0	L	H	Z
0	1	0	1	0	0	1	1	0	0	L	Z	H
0	1	1	1	0	0	1	0	1	0	Z	L	H
0	0	1	1	1	0	0	0	1	0	H	L	Z
0	0	0	X	0	0	0	0	0	0	Z	Z	Z
1	1	1										

L = Low (less positive) level H = High (more positive) level

Z = High impedance (floating)

X = Do not care

1 = Active or true logic condition 0 = Inactive or false logic condition

MODE, PWM, SR, and BRAKE terminals are the signals used for the current and speed control in the operation of common brushless DC machines and will not be used for the drive control of the proposed actuator.

7.6.2.3 Three-phase full bridge converter

As the designed PM TLA is a low voltage device, low voltage MOSFETs would be the suitable choice for the electronic power converter because of their high switching frequency, very low on-state resistances and switching losses. The schematic diagram of the power converter for the actuator is shown in Fig.7-37. The MOSFETs used for the converter are three NTHD4508N ChipFETs manufactured by ON Semiconductor Inc. NTHD4508N is a dual N-channel MOSFET device in one package. The maximum endurable drain-to-source voltage is 20V and the continuous drain current can be up to 3A at 25°C junction temperature. One of attractive features of the device is that the operational gate drive voltage can be as low as 2.5V so that it can be used in the low voltage electronic devices.

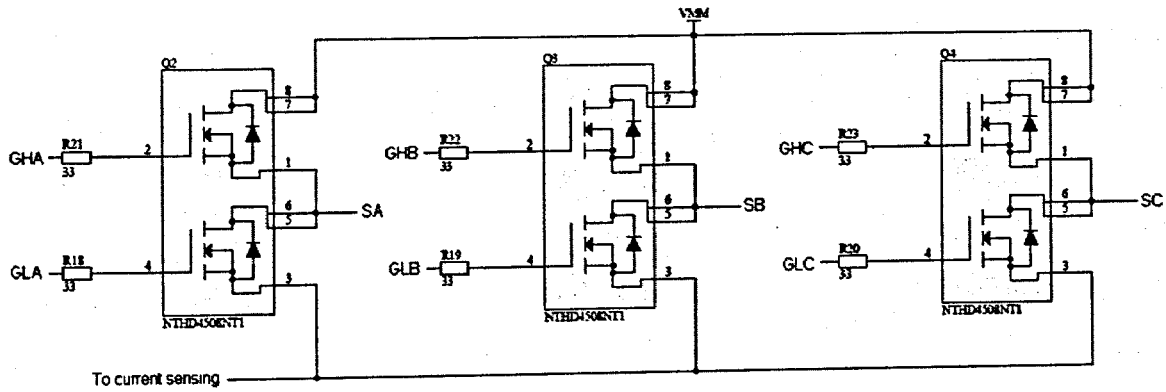

Fig.7-37 Implementation of electronic power converter

7.6.2.4 Design of 3-channel signal amplifier

Since the sensorless control of the PM TLA relies on the measurement of the back EMF of the machine, the pre-processing function plays a key role in the control system. As

mentioned before, a signal amplifier is required for the measurement of the back EMF of the actuator as the voltage level of the machine is too low to be processed by the DS1104 controller board. To obtain the suitable phase voltages from the actuator, the three phase windings of the actuator are connected into the wye connection and each phase voltage is measured separately by using an operational amplifier with differential inputs as shown in Fig.7-38.

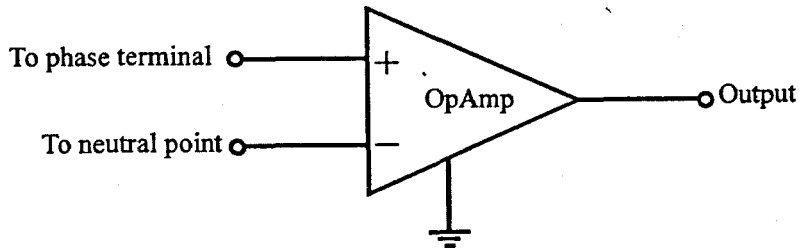

Fig.7-38 Detection of the phase voltage

In order to avoid the unsatisfied measurement due to the limited performance of the signal amplifier used during the prototyping stage, high performance signal amplifiers is considered in the design. The AD524 from Analog Devices Inc. is a precision monolithic instrumentation amplifier specifically designed for data acquisition applications requiring high accuracy under worst-case operating conditions [Analog 1999]. It features an outstanding combination of high linearity, high common mode rejection, low offset voltage drift and low noise. The AD524 also has a wide gain bandwidth product and high output slew rate to make it suitable for high speed data acquisition systems. Furthermore, the AD524 can be functionally configured with pin programmable gains of 1, 10, 100, and 1000, and only a single external resistor is required for acquiring any gain. Fig.7-39 shows the schematic of one channel signal amplifier implemented with AD524. The zener diodes placed in front the input terminals of the device are used to protect the device from possible external high voltages.

According to the circuit connection for the gain selection of AD524, the gain of the designed amplifier can be calculated by following equation:

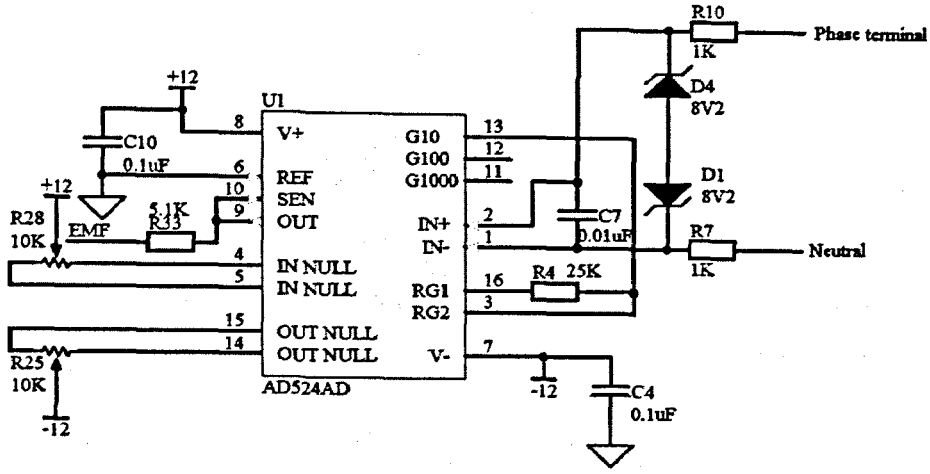

Fig.7-39 One channel of the signal amplifier for detection of the phase voltage

$$\text{Gain} = 1 + \frac{40000}{R4 // 4444.44} \tag{7.41}$$

Through the performance simulation, it is known that the back EMF of the PM TLA is less than 1V. In order to make full use of the voltage range of the A/D converter in the DS1104 controller board (±10V), a suitable gain of the amplifier would be around 10. Hence, a 25kΩ resistor is connected to RG1 terminal of the AD524 and the resultant gain is 11.6. It should be noted that, by this gain, the output of the amplifier may be saturated when the corresponding phase is being excited. However, this will not cause any problem because only the signals of unexcited phases are useful.

7.6.3 dSpace RTI implementation

By using the RTI provided by the dSPCAE prototyping software package, a SIMULINK model can be constructed to perform the control of the developed driving board via the DS1104 controller board. The implementation of the SIMULINK model with RTI for the sensorless control of the linear actuator is demonstrated in Fig.7-40.

In the SIMULINK model with RTI, the simulation model blocks of the PM TLA and electronic power converters used in the SIMULINK model for the system simulation are replaced by a series of interface blocks provided by the RTI. Via these interface blocks, the control signals generated by the control algorithm are pass to the external

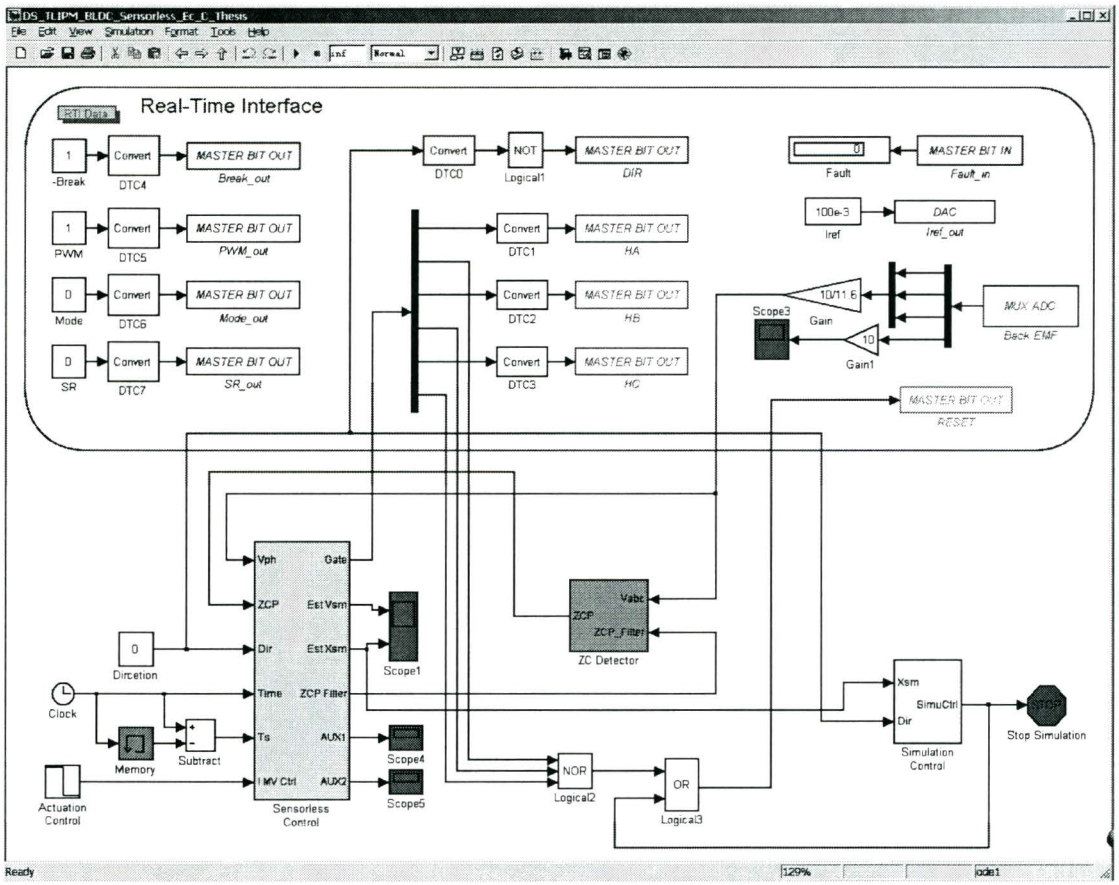

Fig.7-40 Implementation of the SIMULINK model with RTI for the sensorless control

hardware system. Meanwhile, the digitalised back EMF signals collected by the external hardware are input to the control algorithm for generating the appropriate commutation sequences.

In addition to the commutation control signals, a process control signal is generated based on the actuation control signal, commutation sequence and estimated translator position, and is exported to the RESET terminal of the gate driver, as shown in Fig.7-40. Whenever the control of the actuator is disabled by the actuation control signal or the translator reaches its maximum stroke, the process control signal will be set and sent to the external hardware to disable the gate driver and stop the actuator excitation. If the actuator is ready for operation and a valid gate signal is generated by the control algorithm, the signal will be cleared and the external gate driver is enabled to receive the commutation commands from the control system.

7.7 Experimental Results

7.7.1 Experimental setup

By using the SIMULINK model with RTI and the developed hardware, the control of the designed PM TLA can be put into practice. The block diagram for the control experiment of the actuator is illustrated in Fig.7-41.

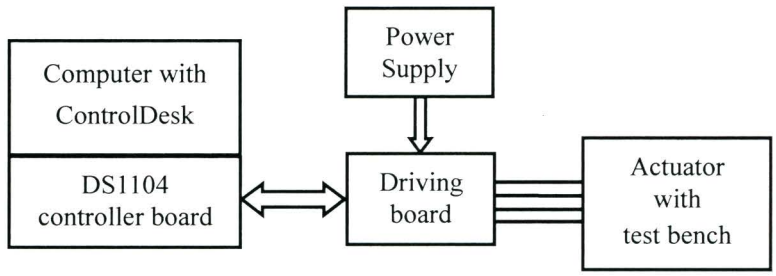

Fig.7-41 Block diagram of the experimental system

The control panel designed within the ControlDesk for the experiment is shown in Fig.7-42. Through this control panel, the experiment on the actuator control system can be fully manipulated and the concerned information can be measured and recorded. The

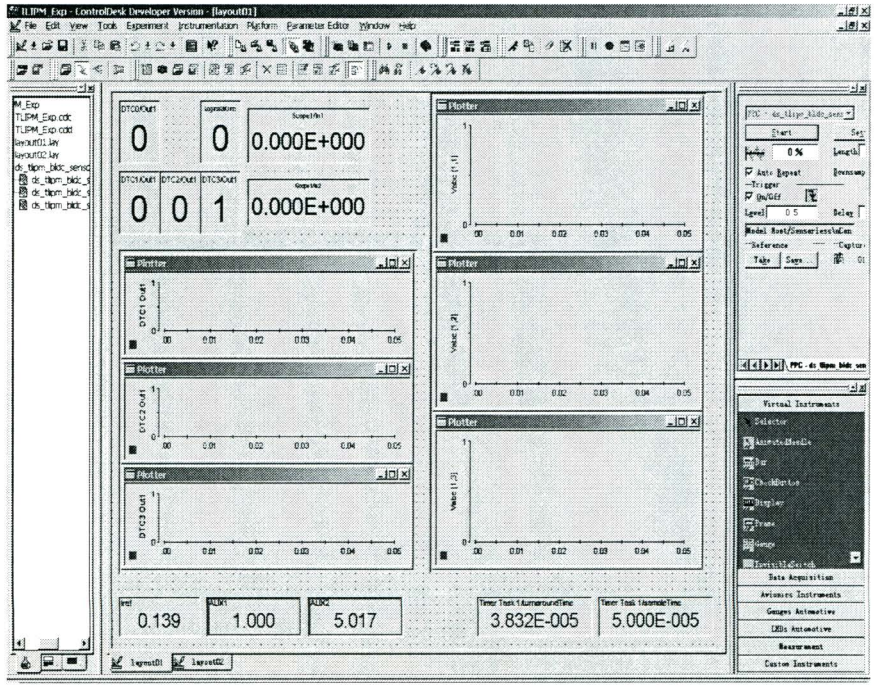

Fig.7-42 Control panel within ControlDesk for the experiment

measured data can also export to disk files for further analysis.

7.7.2 Measurement of the back EMF

The back EMFs of the phase windings are the key information for the sensorless control of the designed actuator. In particular, the value of back EMF will be used for the determination of the first commutation position after the actuator is started. Therefore, in order to verify the back EMF of the prototype and to obtain the proper threshold value for the first commutation point, the back EMF of the actuator is firstly tested by manually moving the translator of the actuator.

The measured back EMF of the small sized prototype is shown in Fig.7-43. The variation of the back EMFs are just the same as the theoretical results illustrated in Fig.7-15 except some ripples caused by the unstable of the translator velocity. The three commutation positions P1, P2 and P3 are indicated in the figure. If the actuator is running in positive direction, P2 and P3 can be determined by the ZCP detection in the back EMF in phases *A* and *B*, respectively. The first commutation point P1, on the other hand, is determined by the integration of the back EMF in phase *C* as discussed in section 7.4.2. If the actuator is running backward, P3 will become the first commutation point and can also be determined by the integration of the back EMF in phase *C*. The

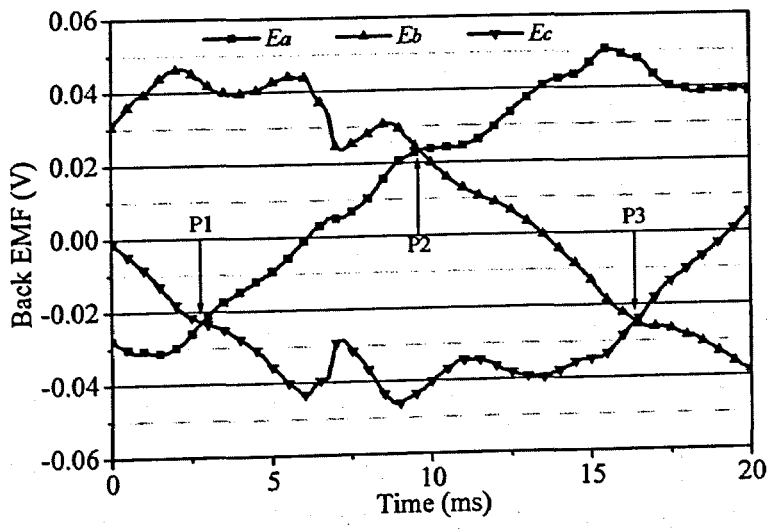

Fig.7-43 Measured back EMFs of the small sized prototype

threshold used for initiating the first commutation can be achieved by finding the integration value of the back EMF of phase *C* between zero and P1, as shown in Fig.7-43. According to the measured results, the threshold for the small prototype is found as 3.6×10^{-2} mV·sec.

7.7.3 Motion test of the actuator

By applying the above integration threshold, the motion control of the small sized prototype is realised by utilising the SIMULINK model of the sensorless control algorithm and the dSPACE based control system. Figs.7-44 and 45 show the control signals generated by the control algorithm and the measured phase voltages when actuator is running in positive direction. There is no external load applied to the actuator and only the frictional force between the translator and stator acts as the load. It is shown that the commutation of the electronic converter is accurately carried out as in the performance simulation and the thrust control of the actuator is effectively implemented.

Figs.7-46 and 47 plot the estimated translator velocity and position with respect to the stator and they are closed to those obtained from the performance simulation as well. However, because of the frictional force between the translator and the stator, a phase current larger than the designed value is applied to the actuator to overcome the friction. The average velocity of the translator during the movement is hence a bit lower than the result from the simulation and the resultant operation time of the actuator is slightly longer.

A motion picture was taken during the movement of the actuator to give an intuitional observation of the actuator operation. Fig.7-48 shows the frames taken from the motion picture which can demonstrate the movement of the translator during the operation. Because the motion picture only has a 30 frame/second sampling rate, the entire motion process was recorded within the second frame in Fig.7-48.

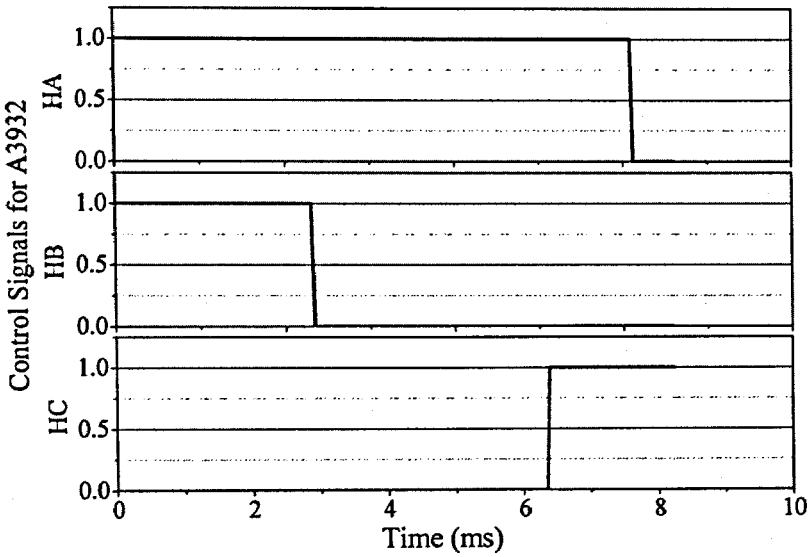

Fig.7-44 Control signals generated by sensorless algorithm

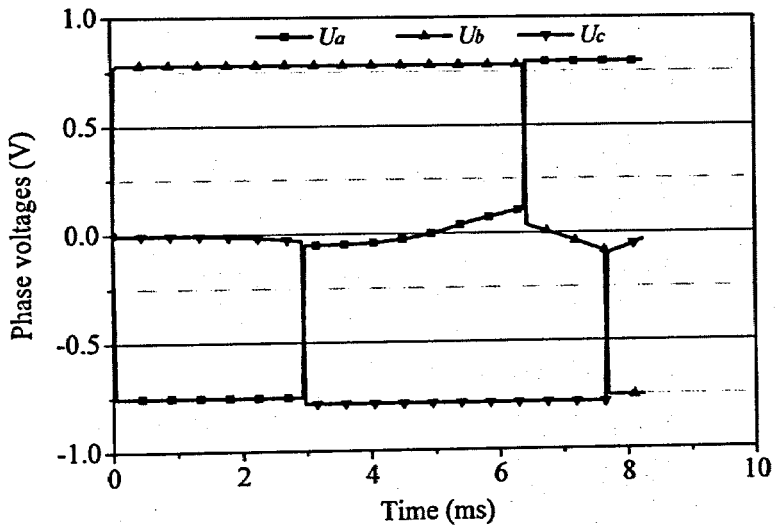

Fig.7-45 Measured phase voltages of the small sized prototype

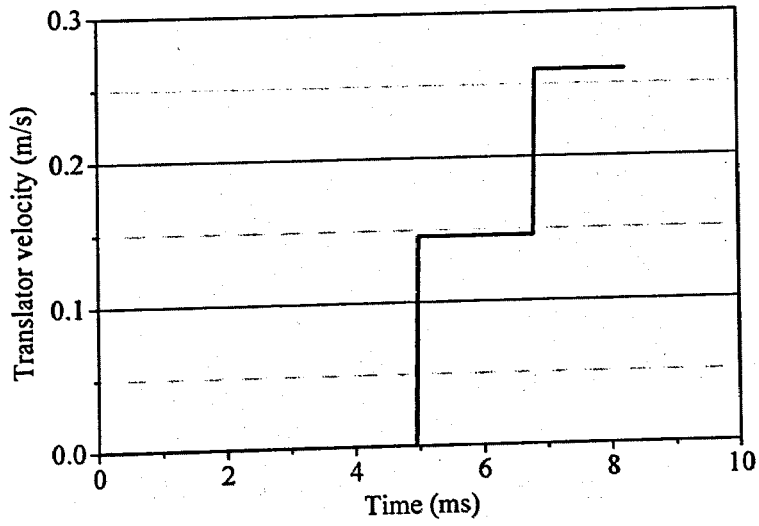

Fig.7-46 Estimated translator velocity during the operation

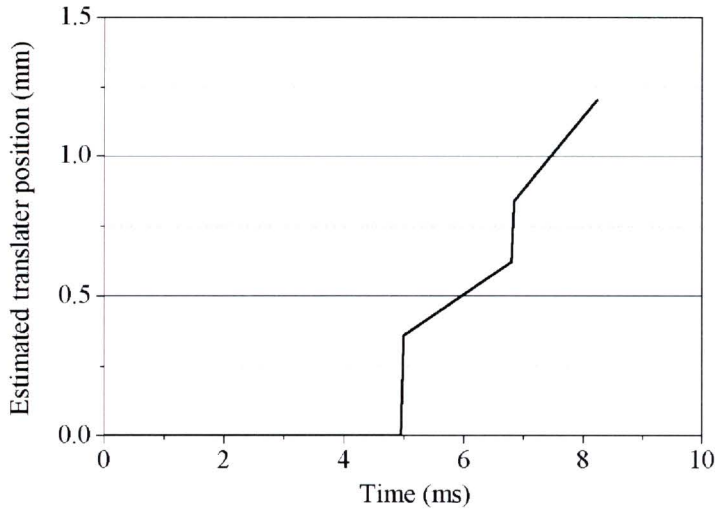

Fig.7-47 Estimated translator position during the operation

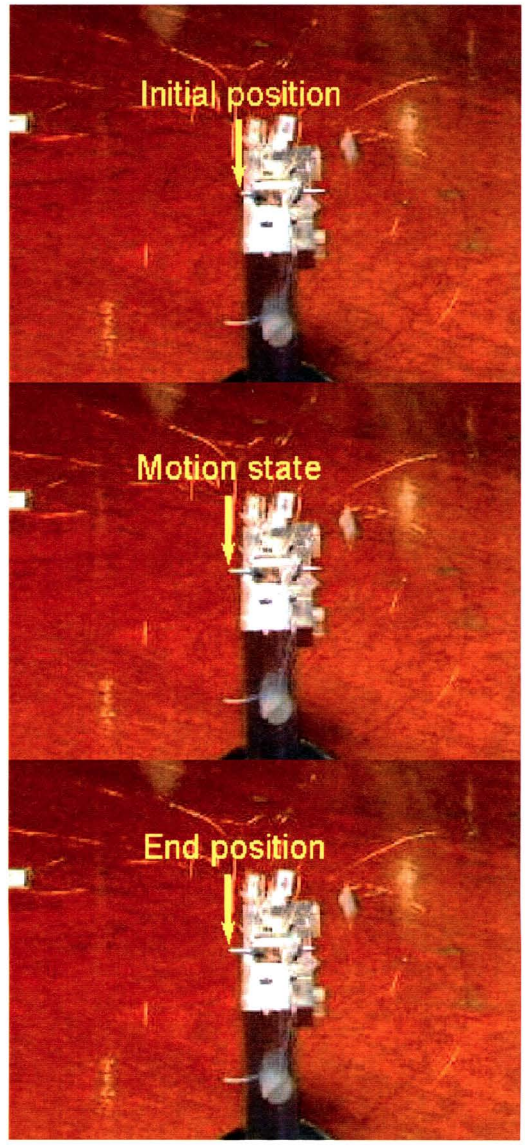

Fig.7-48 Motion of the small sized PM TLA prototype

The motion test in the backward direction is also performed. The results are similar to the forward operation. Figs.7-49 and 50 show the phase voltages and estimated translator position during the backward operation.

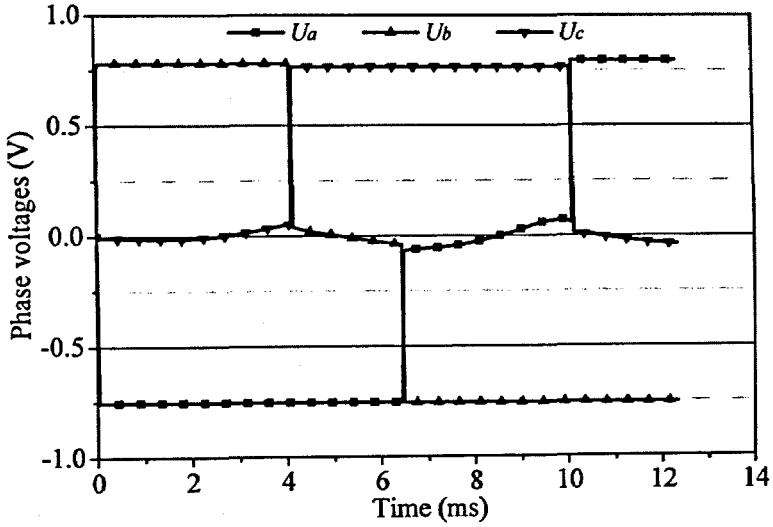

Fig.7-49 Measured phase voltages of the small sized prototype during backward operation

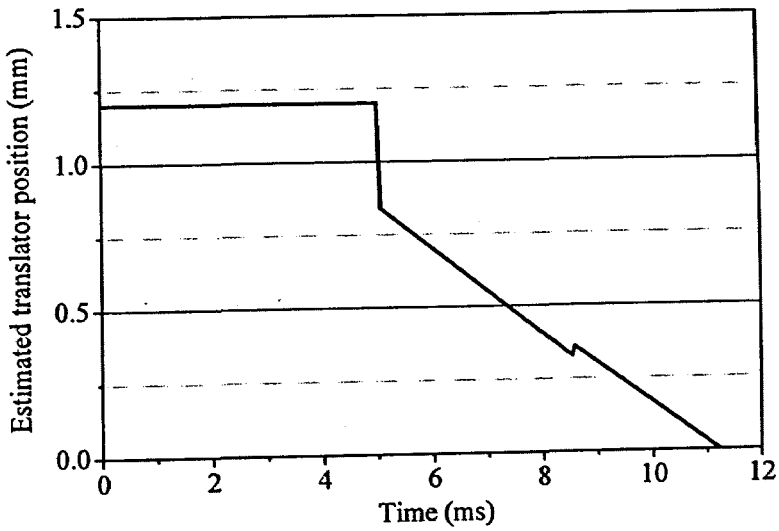

Fig.7-50 Estimated translator position during backward operation

7.8 Conclusion

To achieve a good performance of the proposed linear actuator, the corresponding control system is essential. For designing the control system for the actuator, the

brushless DC drive and its sensorless control method is reviewed and an appropriate sensorless control scheme is developed based on the knowledge of the actuator characteristics obtained during the machine design. The extensive system modelling incorporating the actuator and control system provides an effective method to investigate the validity and performance of the entire actuation system.

The analyses through the system simulation show that the performance of the developed control scheme for the actuator is satisfactory. With the driving control method, the actuator can work well under various load conditions and can operate at its optimum state throughout the travelling stroke.

The developed control scheme is implemented based on the dSPACE prototyping system. A driving hardware containing the power converter and back EMF sensing circuit is designed and realised as the bypass system between the dSPACE controller and the linear actuator. The experiment of the actuator control system is carried out on the small sized prototype. The results show the successful designs of the PM TLA and its sensorless control system.

Chapter 8

LOCOMOTION CONTROL OF THE MICROROBOT

8.1 Introduction

The design and analysis of the proposed PM TLA and its control system have been demonstrated. In this chapter, the application of the actuator to the locomotion of the micro mobile robot will be discussed. The schematic configuration of the microrobot has been shown in chapter 4 and its locomotive performance by using moving-coil linear actuator and IDM method is also examined. The analysis results show that the locomotion of the microrobot is practicable but with some structural and operational restrictions. By taking advantage of the better performance of the newly designed PM TLA, the original robotic design can be significantly improved.

To improve the locomotion performance, a leg-based locomotion mechanism will be employed to the microrobot with PM TLA. Detailed analysis of the locomotive performance is to be performed by establishing the corresponding dynamic model of the system. Based on the effective SIMULINK model of the actuator developed in the last chapter, the dynamic model of the mobile microrobot is created by incorporating the kinetic characteristic of the robotic system. In order to realise the locomotion of the robot, an intermittent control strategy is employed with the drive control of the actuator. Experiments on the application of the actuator and the developed control method will be carried out to verify the effectiveness of the locomotive system.

8.2 Improvement on the Locomotion Mechanism

In chapter 4, the performance analysis of the mobile microrobot driven by the IDM method shows that the locomotion of the robot will be greatly affected by the masses of the components of microrobot as well as the frictional force between the microrobot and the travelling surface because the IDM is a driving method based on the frictional and inertial force during the locomotion. Therefore, the masses of the main body and movable unit of the robot must be deliberately designed to achieve the desired the performance. Even though, the operational conditions of the microrobot can be still restricted due to its excessive dependence on the frictional force to the travelling surface.

Besides the IDM method, another effective way that can generate frictional force for the locomotion of microrobots is to imitate the function of the scales of a worm or snake, which can have anisotropic frictional forces when contacting the travelling surface. Examples of this type of frictional locomotion mechanism are shown in Figs.2-17 and 43 in chapter 2. In those designs, a unidirectional movement can be achieved by using the artificial bristles or blades mounted under the designed autonomous robots. Like the IDM method, this mechanism does not require extra power, and hence it would be more attractive in designs with limited power supply.

The schematic structure of the mobile microrobot utilising the tilted blades as its locomotion mechanism is shown in Fig.8-1(a). Compared to the original design shown in Fig.3-17 in chapter 3, two blades are added to the robot body. The front leg is attached to the main body while the other is attached to the movable unit. The blades are made by single leaf springs and are mounted diagonally with a pre-adjusted angle so that they can provide unidirectional movement. Moreover, if circular-shaped blades are employed circumferentially around the robot body, they can function as the fins when travelling in liquid, as shown in Fig.8-1(b).

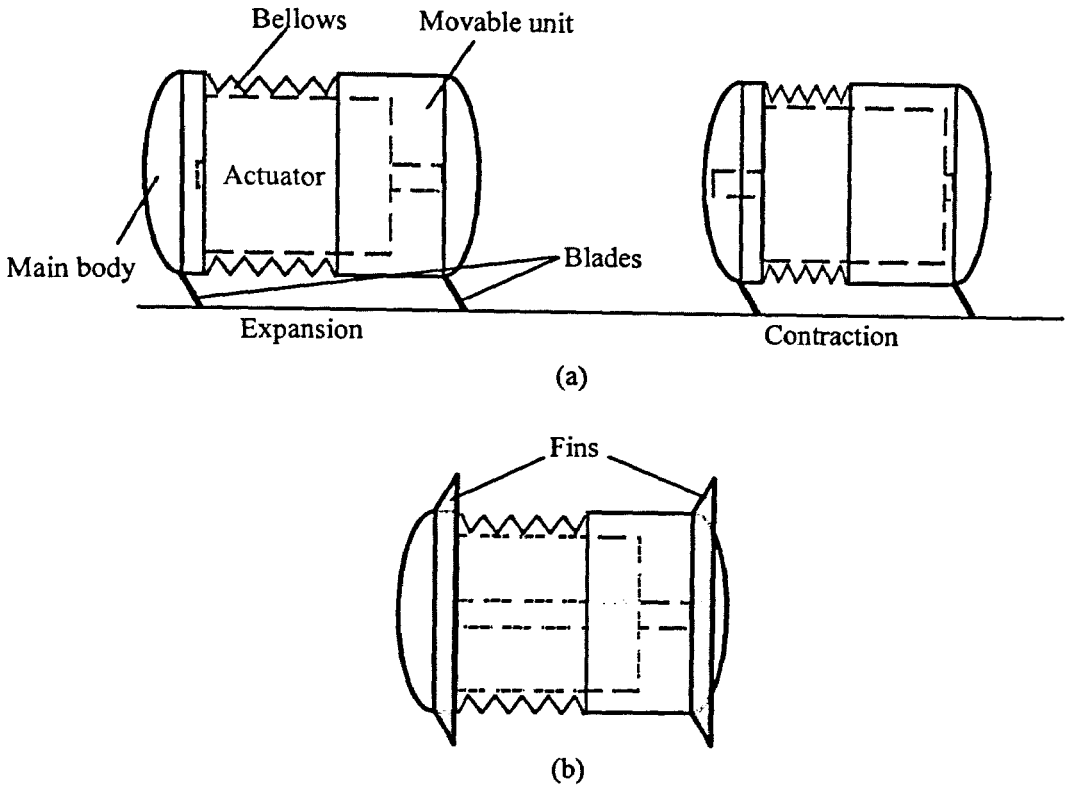

Fig.8-1 Schematic of the micro mobile robot with tilted blades

The internal structure is similar to the design using moving-coil actuator. The stator of the PM TLA constitutes the main body of the robot. The movable unit is attached to the translator so that it can move back and forth. The bellows acts as the restoration spring as well as the seal joint between the main body and the movable unit.

The principle of the locomotion mechanism using the tilted blades can be explained by the following analysis of frictional force between the blade tip and travelling surface. When the mechanism does not move, there are only normal force between the legs and travelling surface, which is depending on the mass of the system. When the microrobot starts to move, the forces on the tips of the blades in the forward locomotion direction can be analysed based on Fig.8-2(a) and the frictional force is give by [Gmiterko 2002]

$$F_{f1} = \frac{\mu_f F_{N1}}{1 + \mu_f \tan\alpha}. \tag{8.1}$$

Analogically, the frictional force during moving backward (Fig.8-2(b)) can be derived as

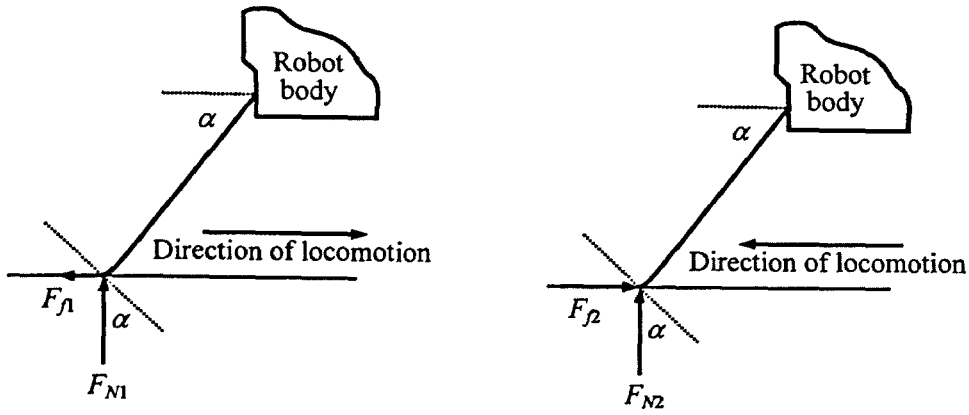

Fig.8-2 (a) Frictional force on blade tip in forward motion
(b) Frictional force on blade tip in backward motion

$$F_{f2} = \frac{\mu_f F_{N2}}{1 - \mu_f \tan\alpha}, \tag{8.2}$$

where F_{f1} and F_{f2} are the frictional forces between the blade and travelling surface in forward and backward locomotion direction, respectively; F_{N1} and F_{N2} the normal forces on the blade in forward and backward locomotion direction, respectively; μ_f is the frictional coefficient, and α the installation angle of the blade.

Assuming that the normal force on the blades will not change with the locomotion direction, i.e. $F_{N1}=F_{N2}=F_N$, one can combine (8.1) and (8.2) into a common equation as

$$F_{f1,2} = \frac{\mu_f F_N}{1 \pm \mu_f \tan\alpha}. \tag{8.3}$$

From (8.3), it can be seen that the frictional force in the forward direction is always less than that in the backward direction, and can result in a motion being better forward than backward. Ideally, if the angle of the blade α is selected to make tanα converges to $1/\mu_f$, the frictional force in the backward direction will approach infinity and the mechanism can be automatically locked in backward direction independent of the normal force on the blade (self-locking mechanism). Therefore, to achieve the maximum difference between the frictional forces of the forward and backward directions, optimum design of the legs, especially the angle of the blade, is required. However, if the microrobot is travelling over an uneven and soft surface, the self-locking behaviour can be easily

accomplished as long as the legs are designed with a slanted angle towards the locomotive direction, since the slanted legs will be always blocked from moving backward by the surface. Based on this principle, the frictional force on the tilted blade can be modelled as

$$F_f = \begin{cases} \mu_f' F_N \cdot sign(v), & v \geq 0^+ \\ -\sum F_{others}, & v = 0^- \end{cases}, \tag{8.4}$$

where $\mu'_f = \mu_f / (1+\mu_f \tan\alpha)$ is the equivalent coefficient of friction between the tilted blade and travelling surface. By using this self-locking mechanism, when the microrobot changes its length by alternative extending and contracting, a forward locomotion can be achieved.

8.3 Dynamic Modelling of the Robotic System

In order to examine the locomotion performance of the mobile robot actuated by the proposed linear actuator and the control strategy, a dynamic model of the robotic system is necessary. By considering the configuration of the microrobot, the dynamic model of the robot can be derived by incorporating the kinetic characteristics of the robot with the previously developed dynamic model of the PM TLA.

8.3.1 Kinetic equations of the microrobot

The kinetic system of the microrobot can be illustrated by using the PM TLA model with blades attached to it, which is shown in Fig.8-3. The stator of the model stands for the main body of the robot and the translator represents the movable unit. Each of the units has a diagonal blade attached to it. A spring between the two units symbolises the elastic effect of the bellows. The initial positions of the stator and translator are just as the way shown in the figure. Accordingly, the length of the spring in free state is l_{sp} and the initial position of the translator with respect to the stator is l_{sm}.

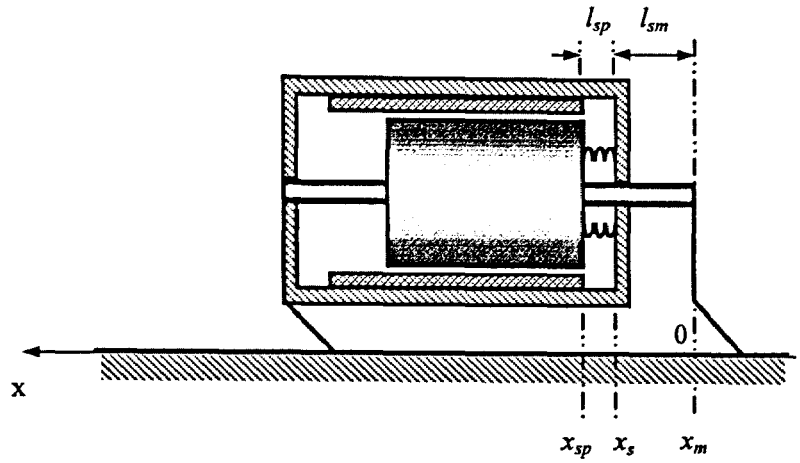

Fig.8-3 Kinetic model of the microrobot

By using the kinetic model, the forces on each of the unit can be analysed and the results are shown in Fig.8-4. The forces in the system include the electromagnetic force generated by the linear actuator F_{em}, elastic force of the spring F_{sp}, the frictional force between the stator and translator due to the linear bearings F_{fb}, and the friction between the blades and travelling surface, F_{fgs} and F_{fgm}.

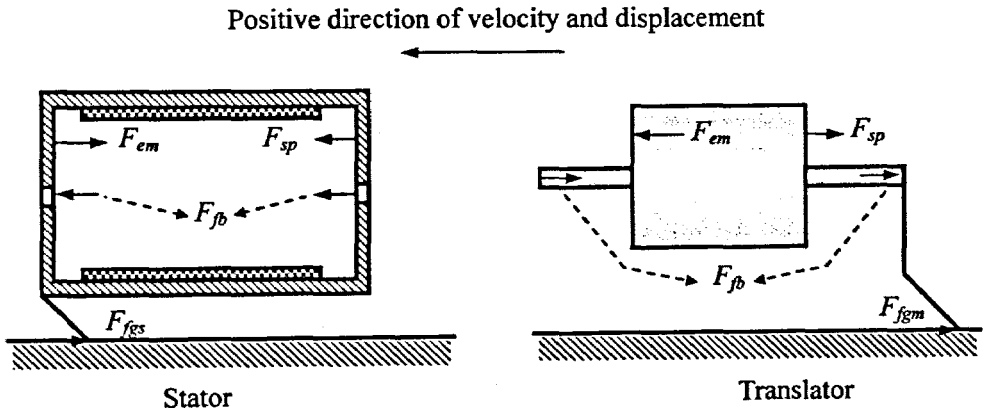

Fig.8-4 Forces in the microrobot

By Newton's law, the kinetic performance of the system is given by the following equations:

$$F_{em} - F_{sp} - F_{fb} - F_{fgm} = m_a \frac{dv_m}{dt}, \tag{8.5}$$

$$-F_{em} + F_{sp} + F_{fb} - F_{fgs} = m_s \frac{dv_s}{dt}, \tag{8.6}$$

where m_s, m_a, v_s, and v_m are the masses and velocities of the stator and the translator, respectively. The actuation force F_{em} can be obtained by the dynamic model of the linear

actuator with proper control method.

The elastic force of the spring is given by the Hooke's law,

$$F_{sp} = K_{sp} \cdot \Delta x_{sp}, \tag{8.7}$$

where K_{sp} and Δx_{sp} are the elastic coefficient and strain of the spring, respectively. The strain of the spring can be further found by

$$\Delta x_{sp} = l_{sm} + x_m - x_s \ , \tag{8.8}$$

where x_s and x_m are the positions of the stator and translator as shown in Fig.8-3. Similar to the system design of the moving-coil actuator, the elastic coefficient of the spring is designed so that the elastic force of the spring is equal to the average electromagnetic force of the actuator when the translator reaches its maximum stroke.

The frictional force between the stator and translator can be found by the Coulomb's law of friction,

$$F_{fb} = \mu_{fb} F_{Nb} \cdot sign(v_m - v_s), \tag{8.9}$$

where F_{Nb} is the total pressing force on the linear bearings and the μ_{fb} the coefficient of friction between the translator shaft and linear bearing.

Based on the friction analysis of the tilted blades in section 8.2, the frictional forces on the blades of the robot when travelling on a proper surface can be modelled as follows:

$$F_{fgm} = \begin{cases} \mu_{fg}(m_s + m_a)g/2 \cdot sign(v_m), & v_m \geq 0^+ \\ F_{em} - F_{sp} - F_{fb}, & v_m = 0^- \end{cases}, \tag{8.10}$$

$$F_{fgs} = \begin{cases} \mu_{fg}(m_s + m_a)g/2 \cdot sign(v_s), & v_s \geq 0^+ \\ -F_{em} + F_{sp} + F_{fb}, & v_s = 0^- \end{cases}, \tag{8.11}$$

where μ_{fg} is the frictional coefficient between the blade tips and the travelling surface.

Equations (8.5) to (8.11) constitute the analytical kinetic model for the mechanical system of the microrobot. By combining this kinetic model with the dynamic model of the PM TLA, a complete dynamic model of the robotic system can be obtained.

8.3.2 Collision between stator and translator

Due to the structure of the linear actuator, collision between the stator and translator is possible when there is a relative movement between them. Although the collision can be avoided by a deliberate design of the attainable spring force and the control strategy of the actuator, it is still inevitable under various operation conditions. On the other hand, because of the unidirectional property of the locomotion mechanism, the collision between the stator and translator could be useful during the locomotion of the microrobot.

According to the impact mechanics, there exist three types of collisions between two rigid objects: perfectly elastic collision, perfectly inelastic collision and imperfectly elastic collision. The resultant velocities of impacted objectives can be found by the following equations [Stronge 2000]:

$$v_1 = \frac{(m_1 - k_p \cdot m_2)v_{10} + (1+k_p)m_2 v_{20}}{m_1 + m_2}, \tag{8.12}$$

$$v_2 = \frac{(m_2 - k_p \cdot m_1)v_{20} + (1+k_p)m_1 v_{10}}{m_1 + m_2}, \tag{8.13}$$

where m_1 and m_2 are the masses of the impacted objectives, v_{10} and v_{20} the initial velocities before impact, and v_1 and v_2 the resultant velocities after impact. $k_p=(v_2-v_1)/(v_{10}-v_{20})$ is defined as the coefficient of restitution while $k_p = 1$ for a perfectly elastic collision, $k_p = 0$ for a perfectly inelastic collision, and $0 < k_p < 1$ for an imperfectly elastic collision. Because the stator and translator of the PM TLA and compressed spring can be regarded as rigid objectives in the kinetic analysis, it is more likely to be a perfectly elastic collision if an impact happens between them. Thus, $k_p = 1$ is employed during the kinetic analysis of the actuation system in the case of collision.

In order to incorporate the collision between the stator and translator, a judgement of the occurrence of collision in the system model should be created according to the relative position and velocity between the stator and translator. Generally, it can be concluded

that, if there is no clearance between the stator and translator while the relative velocity between them at the instant would make them even closer, a collision will happen. A criterion for a collision event can then be set as follows:

$$\text{Collision} = \text{true, if } \begin{cases} l_{sp} + \Delta x_{sp} = l_{sp\_\min} & \& \; v_s > v_m \\ l_{sp} + \Delta x_{sp} = DA & \& \; v_s < v_m \end{cases},$$

where $l_{sp\_\min}$ is the minimum compressible length of the spring and DA the maximum travel length of the translator within the stator. The value of $l_{sp\_\min}$ could be zero if only the bellows is used in the system. If there is a collision, the resultant velocities of the stator and translator are required to be modified based on (8.12) and (8.13), respectively.

8.3.3 SIMULINK model of the microrobot

Similar to the analysis of the linear actuator, the dynamic model of the microrobot is also developed in the SIMULINK environment. By replacing the mechanical model of the PM TLA with the derived mechanical model of the microrobot, the SIMULINK model can be obtained. The completed model is shown in Fig.8-5. The electrical component of the model stands for the PM TLA, which is the same as the electrical block in the SIMULINK model of the actuator developed in chapter 5. The mechanical component of the system is the S-Function that describes the mechanical behaviour of the microrobot using the equations obtained from the above kinetic analysis.

The outputs of the mechanical component of the model are the positions and velocities of the stator (main body) and the translator (movable unit). The relative position and velocity between the stator and translator are also computed as they are the important information for the simulation of actuator model. The elastic coefficient of the spring (bellows) and the equivalent friction coefficient between the blades and travelling surface are load conditions input to the model so that the corresponding forces can be worked out by the model.

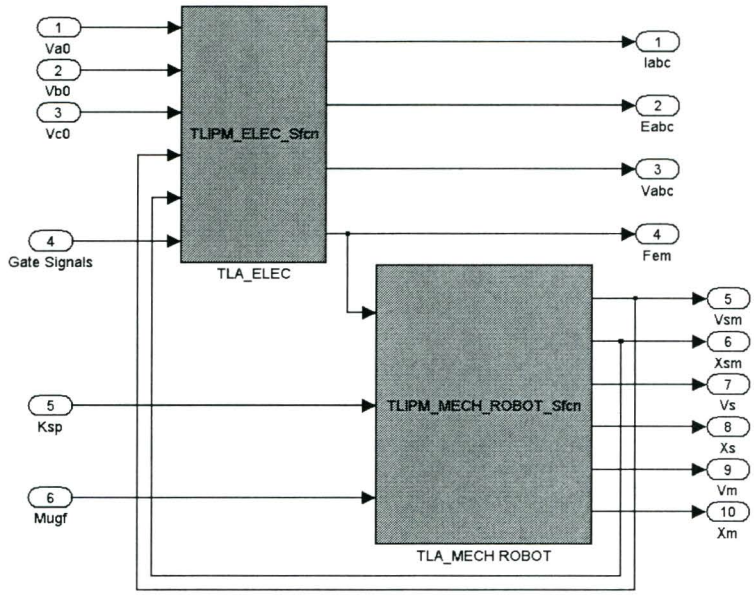

Fig.8-5 SIMULINK model of the microrobot

8.4 Locomotion Control of the Microrobot

8.4.1 Locomotion control method

As previously discussed, the forward locomotion of the micro mobile robot can be realised by alternatively expanding and contracting its body along the locomotion direction, and the expansion and contraction the robot body can be readily accomplished by the reciprocative movement of the linear actuator.

The developed sensorless control scheme for the linear actuator can effectively drive the actuator in either direction with a single stroke. The restoration of the translator position to the initial position is carried out by the elastic force of bellows. In order to implement the consecutively reciprocation of the actuator, an intermittent drive strategy is designed and integrated with the sensorless control of the actuator. The block diagram of the robotic control system is shown in Fig.8-6.

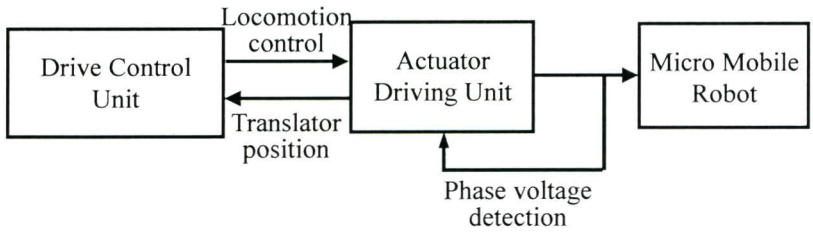

Fig.8-6 Block diagram of the microrobot

As shown in the figure, the intermittent drive control is based on the estimated position of the translator of the actuator with respect to the stator. When the translator reaches its maximum travelling stroke, the drive control unit will disable the operation of the actuator driving unit. During the switching-off period of the actuator driving unit, the translator will coast forward and then go back to its initial starting position by the restoration force produced by the bellows. When the actuator is ready for the next locomotion cycle, the actuator control unit will be re-enabled by the drive control unit and a new locomotive motion is initiated. By repeating this drive sequence, a consecutive locomotion can be accomplished.

The intermittent control strategy implemented in the SIMULINK is shown in Fig.8-7. A pulse generator is used to determine the intermittent drive frequency of the robotic system. When the translator position arrives at the maximum stroke length, the D flip-flop will be set and the sensorless driving block is disabled. The control of the actuator will remain inactive until the D flip-flop is cleared by the next falling edge generated by the pulse generator and the locomotion of the robot is then restarted.

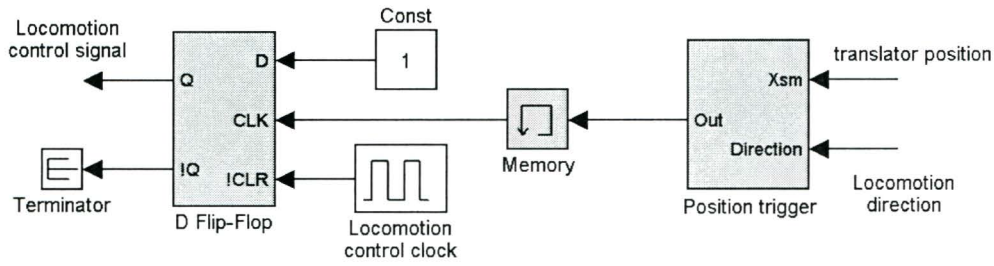

Fig.8-7 Implementation of the intermittent drive control in SIMULINK

8.4.2 Simulation of the locomotive performance

Based on the developed SIMULINK model of the microrobot and its locomotion control system, the locomotive performances are simulated and analysed. Fig.8-8 shows the entire SIMULINK model used for the analysis. The intermittent locomotion control uses estimated translator position for the generation of its control signal as there is no physical sensor in the actuator driving system. The elastic coefficient of the bellows used in the simulation is 21.6N/m, which is obtained based on the average force of the designed linear actuator. The equivalent friction coefficient between the blades and travelling surface is assumed as 1, which results in a load force close to the actuator's attainable load capability.

The phase currents and the actuation force generated by the linear actuator during the locomotion of the microrobot are plotted in Figs.8-9 and 10. It can be seen that the

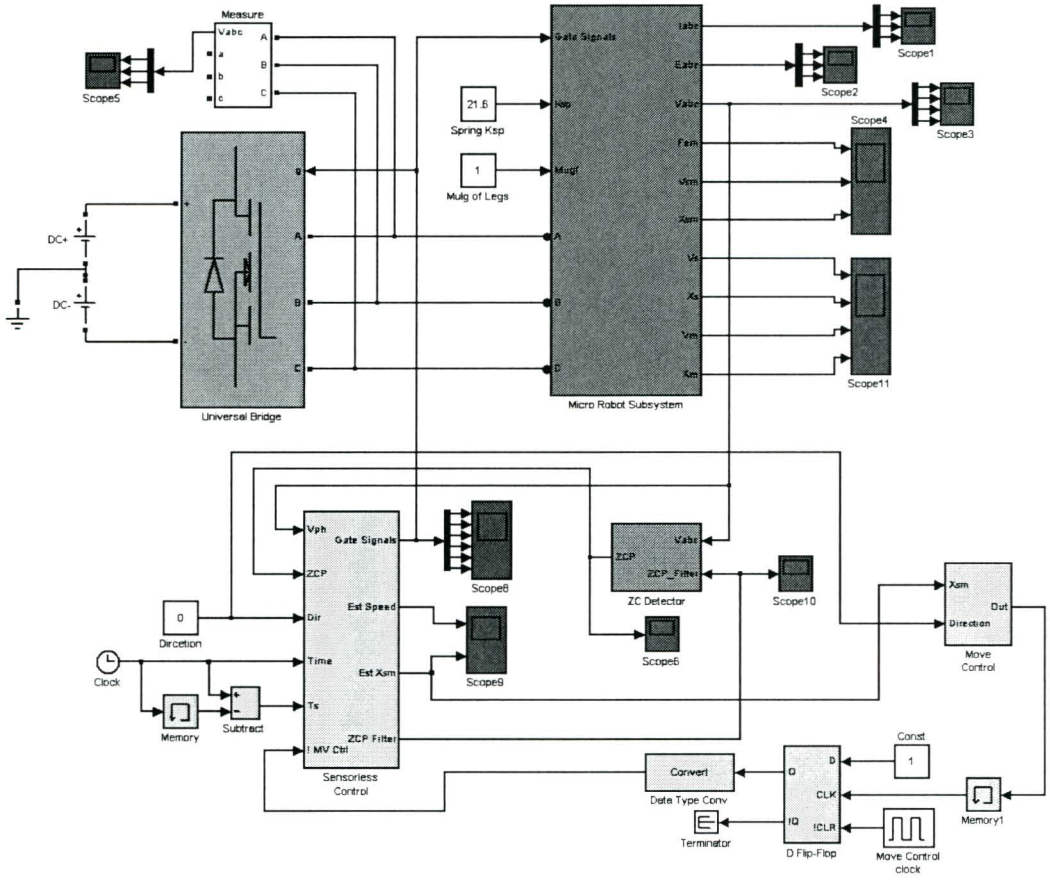

Fig.8-8 SIMULINK model of the microrobot and its locomotion control system

control of the linear actuator can work properly with the intermittent drive control for the robot and the force can be correctly generated during the locomotion.

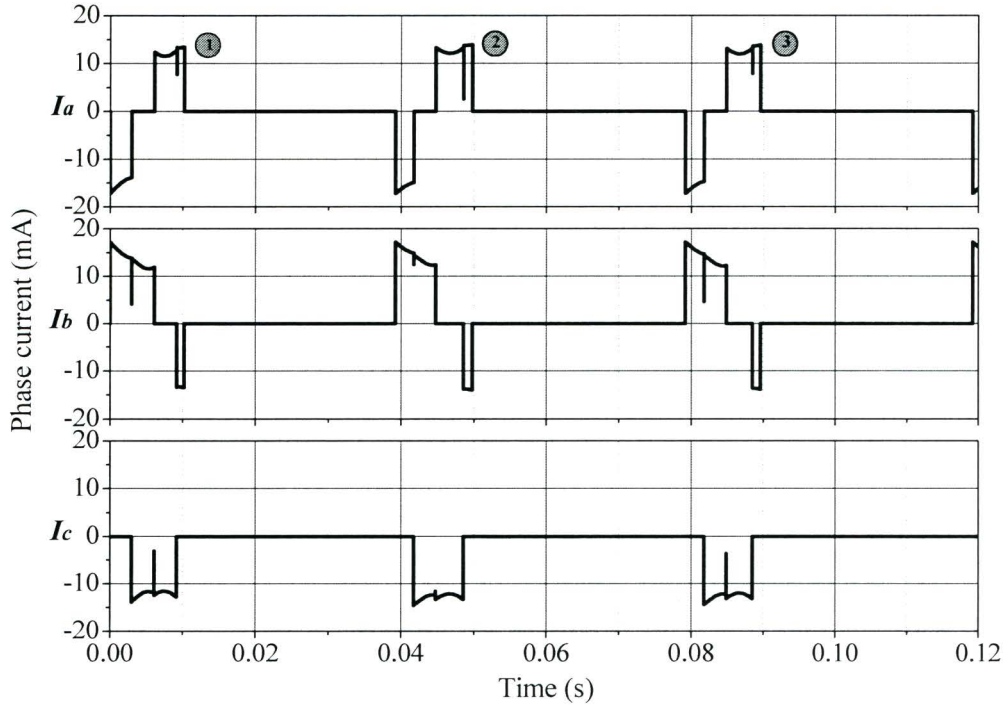

Fig.8-9 Phase currents of the actuator during the locomotion

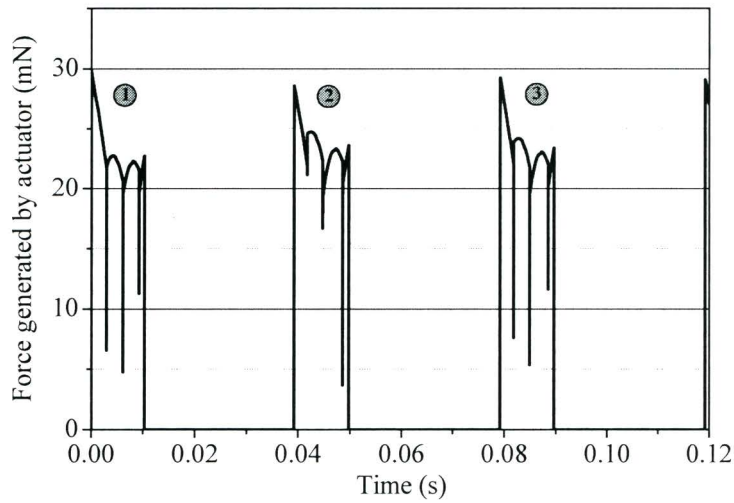

Fig.8-10 Actuation force generated by the actuator

The positions of the stator (main body) and translator (movable unit) and their velocities during the locomotion are illustrated in Figs.8-11 and 12. In the simulation, the values of l_{sm} and l_{sp} used for the analysis are 2.2mm and 0.8mm, respectively, which are obtained from the prototype. From the results, it is shown that the forward locomotion is

achieved and there is no backward movement due to the self-locked mechanism. The locomotion speed is about 1.5mm per cycle and the average travelling speed of the robot can be estimated as 38mm/s when the intermittent control frequency is 25Hz. In addition, it can be found that there exist collisions between the stator and translator when the stator is moving forward by the elastic force of bellows while the translator is standstill. The translator acquires forward motion after the collision and hence more displacement can be achieved.

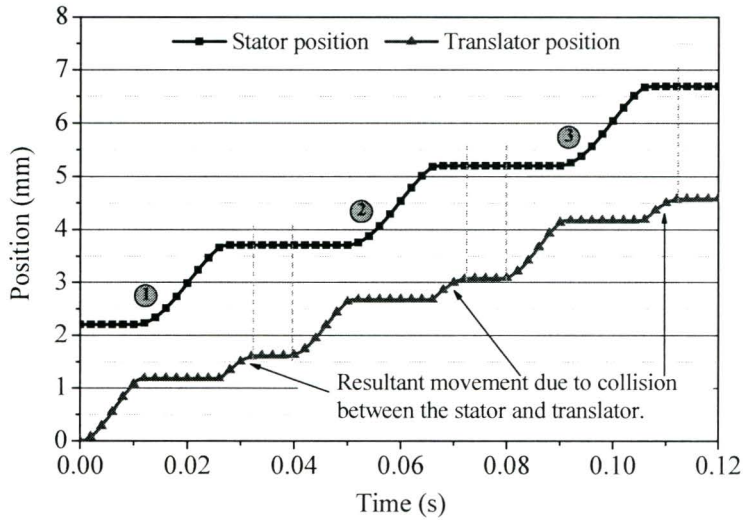

Fig.8-11 Movement of the stator and translator during locomotion

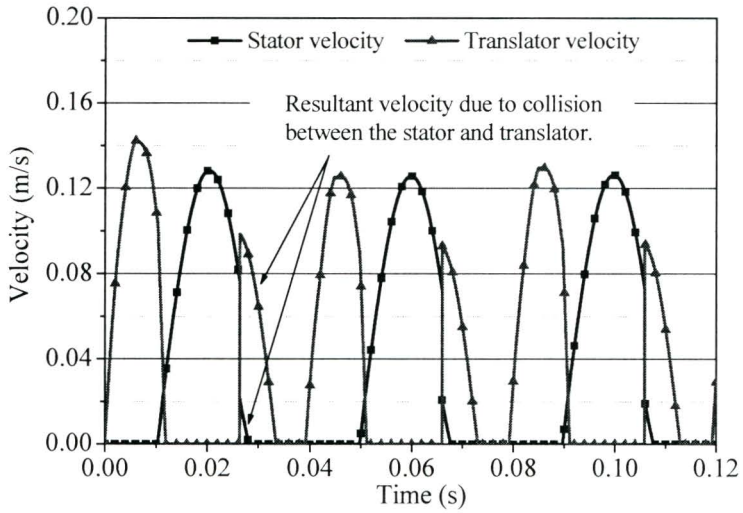

Fig.8-12 Velocities of the stator and translator during locomotion

The translator position with respect to the stator is plotted in Fig.8-13. The estimated translator position during the operation of the actuator is consistent with the actual value,

and therefore the actuator control can be properly switched off at the right time. On the other hand, it can be noticed that the translator position could not exactly go back to its original starting position in the succedent locomotion cycles. The reason is that the spring (bellows) could not return to its free-state length because of the frictional forces between the stator and translator and the two blades, and a certain strain of the spring is required to counteract the frictions between them.

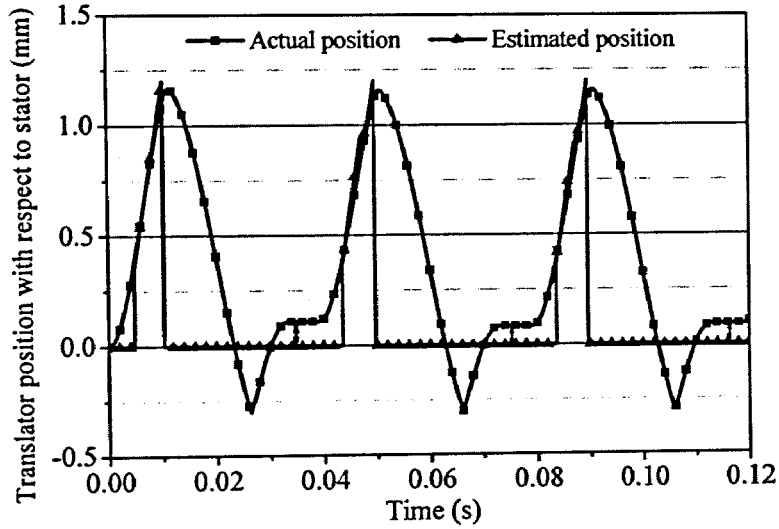

Fig.8-13 Translator position with respect to the stator during locomotion

This difference in the start position of the translator will affect the determination of the first commutation time in the sensorless control algorithm for the linear actuator and it would be aggravated in case of larger frictional load. The influence to the control performance can be seen when comparing the force of the actuator during the first locomotion cycle to those during the subsequent cycles in Fig.8-10. However, appropriate design of the elastic coefficient can alleviate the problem. As shown in the simulation, the frictional force caused by the blades is already set close to the load capability of the system and the restoration force generated by the spring can keep the position of translator within an acceptable difference (<10% stroke) so that the sensorless control algorithm can still perform the proper commutation control during the operation.

8.5 Experiment on the locomotion control

The experimental verification of the locomotion control is carried out based on the dSPACE system and the developed driving circuit for the designed linear actuator described in chapter 7. The SIMULINK RTI model used for the locomotion control is shown in Fig.8-14.

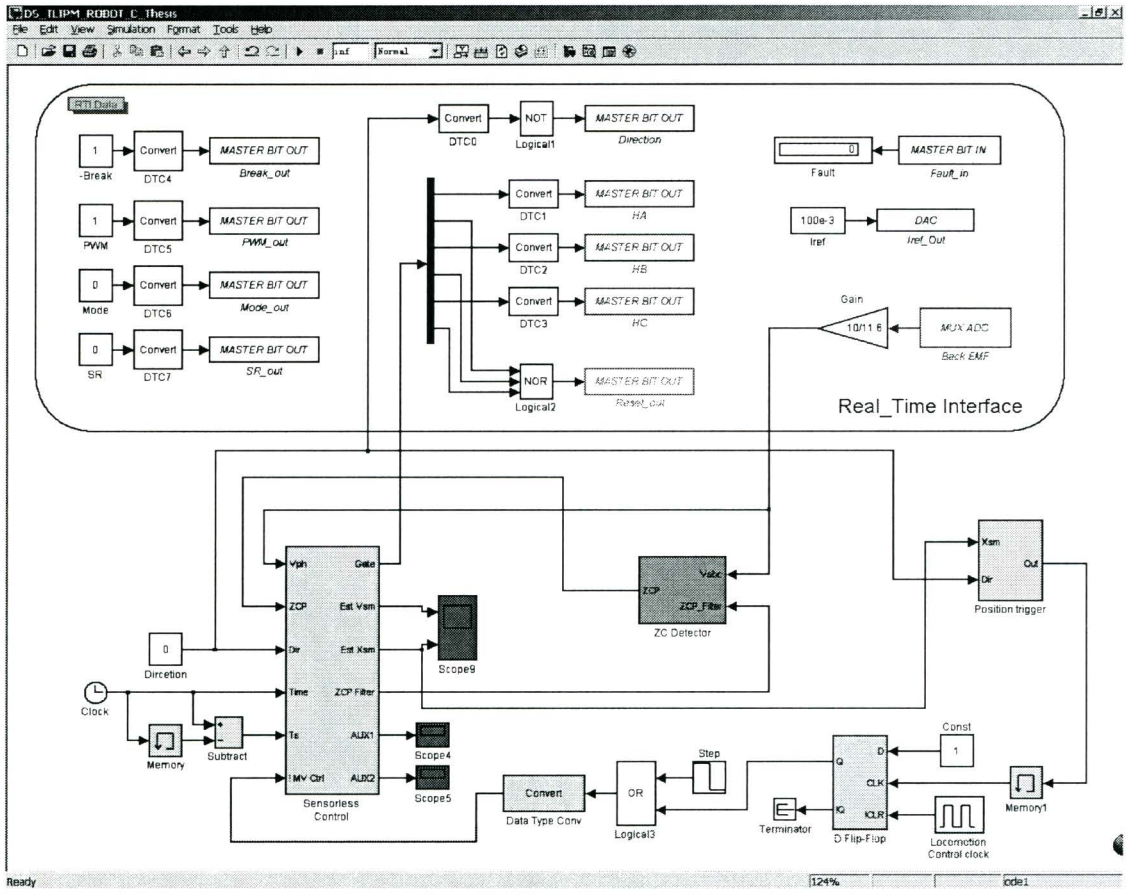

Fig.8-14 SIMULINK RTI model used for the locomotion control

The actuator with the locomotion mechanism for test purpose is shown in Fig.8-15. It is the small sized prototype with two tilted blades attached to the stator and translator, respectively. The blades are made up of thin copper sheet with a pre-adjusted angle around 50 degrees. The actuator is connected to the driving board via thin copper wires. The entire experimental system is illustrated in Fig.8-16. The operational frequency of the intermittent control applied to the system is three cycles in every two seconds duration.

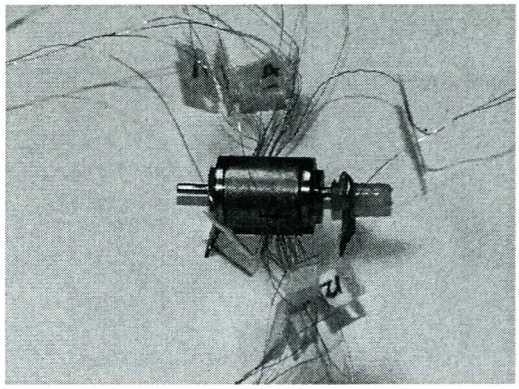

Fig.8-15 Actuator with locomotion mechanism for testing

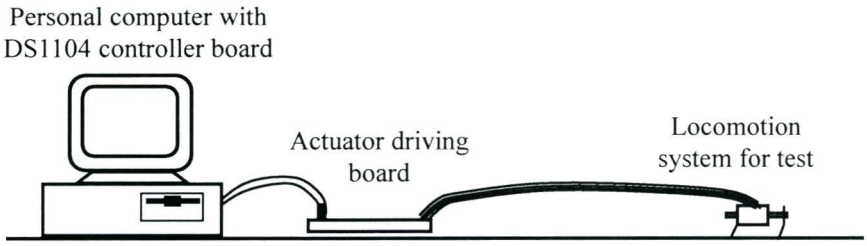

Fig.8-16 Test system for the locomotion mechanism

The locomotion tests are conducted on both the smooth and uneven surface to examine the performance of the system. When the locomotion system is operated on a smooth plane, such as a surface of a flat table, the system cannot move properly and stays at the same place despite the actuator is running a reciprocative way (Fig.8-17). The sliding of the blades on the travelling surface could not make the system to move forward on the plane. Hence, it is shown that the mechanism with tilted blades cannot work on the flat and smooth surface as the frictional force discussed in section 8.2 does not take effect in such a condition. This phenomenon can be imaged when thinking of a snake not being able to move effectively on a glass surface.

The locomotion performance when the system is running on an uneven plane is demonstrated in Fig.8-18. It can be seen that the locomotion can be realised as the sliding of the blades can be effectively reduced due to the increase of the friction on the surface. The average locomotion speed achieved on the applied uneven surface is about 0.47mm per cycle. This value, however, is smaller than the simulated result shown in the performance analysis. Because the angle of the blade and its shape are not as ideal

as discussed in section 8.2, the locomotion performance will be affected by the normal force on the blades. Since the mass of the testing actuator system is rather small, the frictional force on the blades could not completely prevent the sliding of the blades on the travelling surface. An improved locomotion performance could be realised by adjusting the shapes and angles of the blades, as well as the blade material. In addition, unbalanced frictional forces on the blades lead to a right turning behaviour of the locomotion system, which can be observed in the experiment.

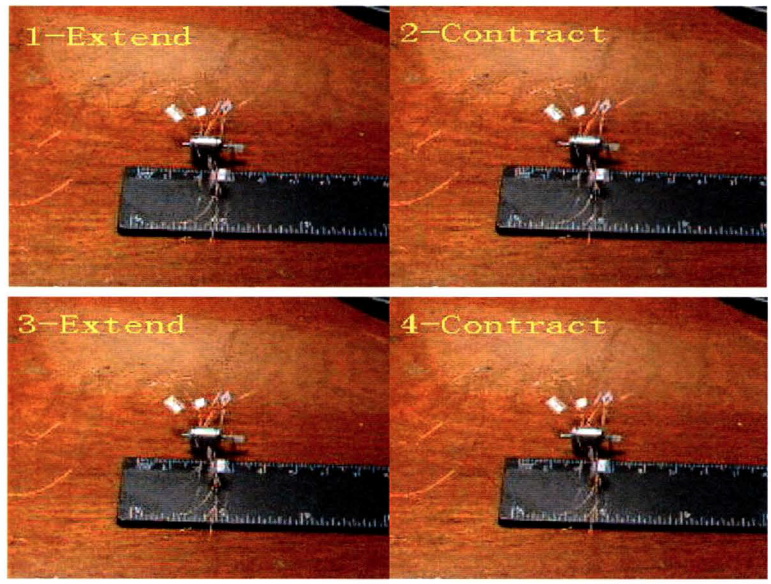

Fig.8-17 Locomotion test on a smooth surface

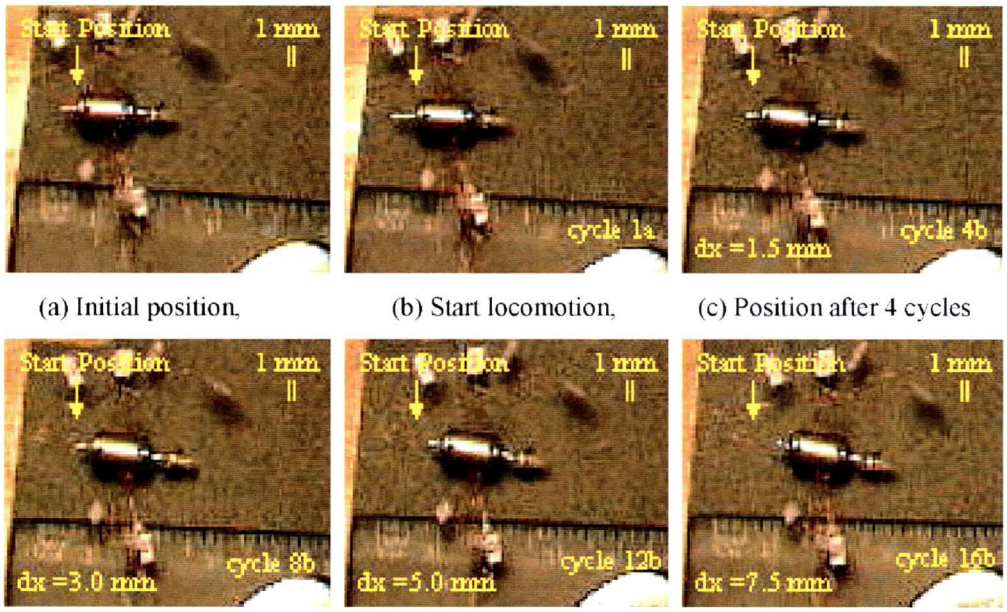

(a) Initial position, (b) Start locomotion, (c) Position after 4 cycles

(d) Position after 8 cycles, (e) Position after 12 cycles, (f) Position after 16 cycles

Fig.8-18 Locomotion test on a uneven surface

8.6 Conclusion

The design, analysis, and performance test of the locomotion mechanism and its control system are presented and discussed in this chapter. In order to achieve a better locomotion performance and robust adaptability to the working environment, the original design of the microrobot is improved by utilising the tilted blades mechanism. The anisotropy of the locomotion mechanism can provide a self-locking behaviour when travelling over an uneven or soft surface. The mechanical characteristics of the microrobot incorporating the proposed locomotion mechanism are analysed and modelled in the SIMULINK environment. By applying the developed SIMULINK model of the PM TLA, the comprehensive model of the designed microrobot is developed and implemented in SIMULINK.

An intermittent drive strategy is proposed for the continuous locomotion of the microrobot based on the developed drive scheme for the actuator. SIMULINK based performance simulation show that the whole locomotion system can work properly under desired load conditions and an average locomotion speed of 1.5mm per cycle. The experimental verification of the locomotion control is carried out by using the designed control circuit under the dSPACE prototyping system. The test results show the effectiveness of the designed locomotion system although the locomotion speed is less than the expected value because of the difference between the designed ideal and the fabricated real blades.

Chapter 9

CONCLUSION AND FUTURE WORK

9.1 Conclusion

Linear electromagnetic actuators for the locomotion of in-pipe/endoscopic mobile microrobot are developed and analysed in this dissertation. The main work was focused on the following aspects:

(1) Selection of suitable actuation principle for the proposed micro robotic application;

(2) Mechanical and electromagnetic design of the linear actuator and corresponding locomotive mechanism for the desired application;

(3) Characteristic analysis of the designed actuator including electromagnetic and kinetic performances;

(4) Development of the actuation control scheme for the actuator and its application to the locomotion of the micro robotic application.

The work carried by the author can be summarised as following:

(1) Based on an extensive survey on the development and state-of-the-art of technologies in microrobots and relevant actuation mechanism, it was concluded that electromagnetic and piezoelectric actuators are the two preferred candidates for mobile micro robotic applications as they are of good force capability, high efficiency and they do not need an extreme energy supply.

(2) A detailed comparative study on the piezoelectric and electromagnetic actuators principles was conducted. Important issues concerned in micro applications such as the scaling effect and power density limits of two types of actuators, are analysed. The analytical case study on the dynamic performances shows that both types of actuator can have the similar scaling effects and energy densities. In particular, the electromagnetic actuator is a current source device while the piezoelectric actuator is a voltage source device. In consideration of the actuation requirements in the application of this thesis, a PM type linear electromagnetic actuator was employed because of its moderate force output with quite large fractional stroke, low voltage operation capability with wireless powered potential, and silicon technology compatibility in microelectronics.

(3) As the first attempt of the development of the suitable actuator, a PM moving-coil linear actuator was proposed based on the investigation of various types of linear electromagnetic machines. The characteristics and parameters of the actuator was analysed and calculated by the 3D FE magnetic field analysis. Based on the field analysis, the dynamic models for the actuator and microrobot were derived and applied for the analysis of the locomotive performance by using the IDM method. Although the designed moving-coil linear actuator was proved to be less practical for the proposed application, the applied design and analysis methods build up the basic tools for the actuator design in the thesis.

(4) Based on the experiences achieved through the first design, a new moving-magnet tubular linear actuator (PM TLA) was designed. Due to the multi-pole and multi-phase structure of the moving-magnet actuator, more complicated optimal design and performance analysis were carried out. A comprehensive dynamic model of the actuator was developed and employed in dynamic analysis by coupled field-circuit simulation. The characteristics analyses show an improved performance of the actuator.

(5) An enhanced numerical method for calculating the differential inductances of an electromagnetic device was developed and applied to the prediction of the phase inductances of the designed linear actuator. The results were verified by the measured inductances of the actuator prototypes.

(6) Two prototypes of PM TLA with different scale sizes were fabricated for the verification of the design. The performances of the prototypes were re-evaluated by considering the issues in fabrication and the measurement of the performance verified the actuator design and the scaling analysis. In addition, the fabrication of the prototypes explored the techniques used for the manufacture of micro actuators and provided valuable experiences in the future development.

(7) An appropriate sensorless control scheme is developed based on the understanding of the actuator characteristics. Through the extensive system modelling incorporating the actuator and control system, the performance of the developed control scheme for the actuator was simulated and the results are satisfactory. A driving system was designed and realised base on the dSPACE prototyping system. The experiment of the actuator control system was carried out and the results showed the successful designs of the PM TLA and its sensorless control system.

(8) The designed control scheme for the actuator was applied to the locomotion of the proposed microrobot. A leg-based locomotion mechanism was proposed to improve the performance of IDM method in dealing with uneven and soft surfaces. SIMULINK based system simulation showed that the locomotion system can work properly under desired load conditions. The experimental verification of the locomotion control is carried out and the results showed the effectiveness of the designed locomotion system.

1.2 Future Work

The possible future work that can be considered after this project could be:

(1) Redesign the mechanical structure of the PM TLA to acquire higher precision assembly during the fabrication so that the unwanted strains and frictions between components of the actuator could be reduced as less as possible. The eccentricity of the translator is also to be reduced to a low level by improving the precision of the components and assembly. A possible solution for construction the stator is conceived as that the stator winding of the actuator will be fabricated as a whole component to obtain a good shape and smooth surface. The stator will be divided into two identical pieces with half annular shape for containing the winding. This configuration could effectively improve the performance of stator assembling.

(2) Optimal design of the blades of the microrobot to improve the locomotion performance of the system. The material, structure and dimensions of the blades are to be considered in detail.

(3) Design of the control and driving system in a small sized board or in a single chip solution so that the electronic component could be integrated with the actuator and could be powered by button batteries or microwave power.

(4) After improvement of fabrication technique, an even smaller actuator, e.g. an outer diameter about 3mm or less, can be tried.

References

Ahn, C. H., Kim, Y. J., and Allen, M. G., 1993, "A planar variable reluctance magnetic micromotor with fully integrated stator and coils", Journal of Microelectromechanical Systems, vol. 2 pp. 165-173

Allegro Microsystems Inc., 2002, *A3932 Data Sheet*

Analog Devices Inc., 1999, *AD524 Datasheet*, Rev. E

Anderson, R. A., 1986, "Mechanical stress in a dielectric solid from a uniform electric field", Physics Review B, vol. 33, pp. 1302-1307

Andrew, B. M., 2002, "Laser cutting", Medical Device Technology, Jan/Feb, 2002

Anthierens, C., Ciftci, A., and Betemps, M., 1999, "Design of an electro pneumatic micro robot for in-pipe inspection", Proceedings of the IEEE International Symposium on Industrial Electronics, vol. 2, pp. 968-972

Anthierens, C., Libersa, C., Touaibia, M., Betemps, M., Arsicault, M., and Chaillet, N., 2000, "Micro robots dedicated to small diameter canalization exploration", Proceedings of IEEE/RSJ International Conference on Intelligent Robots and Systems, vol. 1, pp. 480-485

Aoshima, S. and Yabuta, T., 1989, "Design and analysis of midget mobile robot using piezo vibration for mobility in a thin tube", Proceedings of the International Conference

on Advanced Mechatronics, pp. 659-664

Aoyama, H., 1993, "Precision machining and measurement organized by miniature robots", Proceedings of the American Society for Precision Engineering Annual Meeting, pp. 126

Asari, V. K., Kumar S., and Kassim, I. M., 2000, "A fully autonomous microrobotic endoscopy system", Journal of Intelligent and Robotic Systems, vol. 28, pp. 325-341

Bang, Y. B. and Lee, K. M., 2003, "Linear motor for ejector mechanism", Proceedings of the IEEE International Conference on Electric Machines and Drives, vol. 3, pp. 1702-1708

Bao, X. and Bar-Cohen, Y., 2000, "Complete modeling of rotary ultrasonic motors actuated by traveling flexural waves", Proceedings of SPIE's 7th Annual International Symposium on Smart Structures and Materials, Paper No. 3992-103

Basak, A., 1996, *Permanent-magnet DC linear motors*, Oxford University Press

Basset, P., Buchaillot, L., Kaiser, A., and Collard, D., 2001, "Design of an autonomous micro robot", Proceedings of the IEEE International Conference on Emerging Technologies and Factory Automation, vol. 2, pp. 795-798

Becerra, R. C., Jahns, T. M., and Ehsani, M., 1991, "Four-quadrant sensorless brushless ECM drive", Proceedings of the IEEE Applied Power Electronics Conference and Exposition, pp. 202-209

Bianchi, N., Bolognani, S., and Tonel, F., 2001, "Design consideration for a tubular linear PM servo motor," EPE Journal, vol. 11, pp. 41-47

Bianchi, N., Bolognani, S., Corte, D. D., and Tonel, F., 2003, "Tubular linear permanent magnet motors: an overall comparison", IEEE Transactions on Industry Applications, vol. 39, pp. 466-475

Birch, M. C., Quinn, R. D., Hahm, G., and Phillips, S. M., 2000, "Design of a cricket microrobot", Proceedings of IEEE International Conference on Robotics and Automation, vol. 2, pp. 1109-1114

Boldea, I. and Nasar, S. A., 1997, "Linear electric actuators and generators", Conference Record of the IEEE International Conference on Electric Machines and Drives, pp. MA1/1.1-MA1/1.5

Carrozza, M. C., Lencioni, L, Magnani, B., and Dario, P., 1996, "A microrobot for colonoscopy", Proceedings of the IEEE International Symposium on Micro Machine and Human Science, pp. 223-228

Chapman, P. L., and Krein, P. T., 2001, "Micromotor technology: electric drive designer's perspective", Conference Record of the IEEE Industry Applications Annual Meeting, vol. 3, pp. 1978-1983

Codourey, A., Zesch, W., Büchi R., and Siegwart, R., 1995, "A robot for automated handling in micro-world", Proceedings of the IEEE/RSJ International Conference on Intelligent Robots and Systems, vol. 3, pp. 185-190

Dario, P., Valleggi, R., Carrozza, M. C., Montesi, M. C., and Cocco, M., 1992, "Microactuators for microrobots: a critical survey", Journal of Micromechanical and Microengineering, vol. 2, pp. 141-157

Dario, P., Carrozza, M. C., Menciassi, A., Eisinberg, A., Benvenuto, A., and Beccai, L., 2000, *Advances in Micromechatronics*

D'Attanasio, S., Lazzarini, R., Stefanini, C., Carrozza, M.C., and Dario, P., 1997 "A one cubic centimeter mobile microrobot with a steering control", Proceedings of the 1997 IEEE/RSJ International Conference on Intelligent Robots and Systems, vol. 3, pp. 1318-1324

Demerdash, N. A. and Nehl, T. W., 1999, "Electric machinery parameters and torques by current and energy perturbations from field computations - Part I: theory and formulation", IEEE Transactions of Energy Conversion, vol. 14, pp. 1507-1513

Dimarogonas, A., 1993, "The Origins of machines and mechanisms", in *Modern Kinematics, Developments in the Last Forty Years,* Edited by Erdman, A., John Wiley and Sons.

Dong, S. X., Lim, S. P., Lee, K. H., Zhang, J. D., Lim, L. C., and Uchino, K., 2003, "Piezoelectric ultrasonic micromotor with 1.5 mm diameter", IEEE Transactions on Ultrasonics, Ferroelectrics and Frequency Control, vol. 50, pp. 361-367

Drapier, M., Steenbrugghe, V., and Successeurs, B., 1961, "Perfectionnements aux cathéters médicaux", France Patent 1,278,965

dSPACE GmbH, 2007, "dSPACE prototyping system" in *dSPACE Catlogue 2007*, pp. 28-75

Eastham, J. F., 1990, "Novel synchronous machines: linear and disc", IEE Proceedings, vol. 137, part E, pp. 49-58

EDO Ceramic Inc., 1998, *EDO Electro-Ceramic Products*

Fahlbusch, S., Fatikow, S., Seyfried, J., and Buerkle, A., 1999, "Flexible microrobotic system MINIMAN: design, actuation principle and control", Proceedings of the

IEEE/ASME International Conference on Advanced Intelligent Mechatronics, pp. 156-161

Fan, L.-S., Tai, Y.-C., and Muller, R. S., 1989, "IC-processed electrostatic micromotors", Sensors Actuators, vol. 20, pp. 41-48

Fearing, R. S., 1998, "Powering 3 dimensional microrobots: power density limitations", Tutorial on Micro Mechatronics and Micro Robotics, University of California, Berkeley, CA, USA

Feynman, R. P., 1992, "There's plenty of room at the bottom [data storage]", Journal of Microelectromechanical Systems, vol. 1, pp. 60-66

Fleischer, M., Stein, D., and Meixner, H., 1989, "Ultrasonic piezomotor with longitudinally oscillating amplitude-transforming resonator", IEEE Transactions on Ultrasonics, Ferroelectrics, and Frequency Control, vol. 36, pp. 607-613

Flynn, A. M., Tavrow, L. S., Bart, S. F., Brooks, R. A., Ehrlich, D. J., Udayakumar, K. R., and Cross, L. E., 1992, "Piezoelectric micromotors for microrobots", Journal of Microelectro-mechanical Systems, vol. 1, pp. 44-51

Frazer, R. E., 1979, "Apparatus for endoscopic examination", U.S. Patent 4,176,662

Fuchiwaki, O. and Aoyama, H., 2003, "Precise manipulation control on three versatile microrobots for flexible micro handling", Proceedings of the American Society for Precision Engineering Annual Meeting, pp. 287-290

Fujita, H., 1997, "A decade of MEMS and its future", Proceedings of the IEEE Annual International Workshop on Micro Electro Mechanical Systems, pp. 1-7

Fukuda, T., Hosokai, H., Ohyama, H., Hashimoto, H., and Arai, F., 1991, "Giant magnetostrictive alloy (GMA) applications to micro mobile robot as a micro actuator without power supply cables", Proceedings of the Annual IEEE International Workshop on Micro Electro Mechanical Systems, pp. 210 - 215

Fukuda, T., *et al.*, 1993a, "A study on micro mobile robot", Transactions of the Japan Society of Mechanical Engineers, vol. C59, pp. 1787-1794

Fukuda, T. and Arai, F., 1993b, "Microrobot and applications", Proceedings of the IEEE International Workshop on Design and Operations of Intelligent Factories, pp. 1-8

Gao, R. X., Fang, J., Rao, B., and Warrington, R. O., 1997, "Miniaturized surface-driven electrostatic actuators: design and performance evaluation", IEEE/ASME Transactions on Mechatronics, vol. 2, pp. 1-7

Ghouti, N. E., 2000, "Hybrid modeling of a traveling wave piezoelectric motor", PhD Thesis, Department of Control Engineering, Aalborg University, Denmark

Gilles, P. -A., Delamare, J., Cugat, O., and Schanen, J. -L., 2000, "Design of a permanent magnet planar synchronous micromotor", Conference Record of the IEEE Industry Applications Conference, vol. 1, pp. 223-227

Given Image Inc., 2004, http://www.givenimaging.com/ (last visited in Feb. 2007)

Gmiterko, A., Dovica, M., Kelemen, M., Fedak, V., and Mlynkova, Z., 2002, "In-pipe bristled micromachine", the 7th International Workshop on Advanced Motion Control, pp. 599 - 603

Gong, F., Swain, C. P., and Mills, T. N., 2000, "Wireless endoscopy", Gastrointestinal Endoscopy, vol. 51, pp. 725-729

Grant, D. and Hayward, V., 1997, "Variable structure control of shape memory alloy actuators", IEEE Control Systems Magazine, vol. 17, pp. 80-88

Guckel, H., 1998, "Progress in magnetic microactuators", Microsystem Technologies, Springer-Verlag, No.5, pp. 59-61

Guo, S., Sasaki, Y., and Fukuda, T., 2003, "A new kind of microrobot in pipe using driving fin", Proceedings of the IEEE/ASME International Conference on Advanced Intelligent Mechatronics, vol. 2, pp. 697-702

Guo, Y. G., 2003, "Development of low cost high performance permanent magnet motors using new soft magnetic composite materials", PhD Dissertation, University of technology, Sydney, Australia

Guru, B. S. and Hiziroglu, H. R., 1998, *Electromagnetic field theory fundamentals*, PWS Publishing Company

Haga, Y., Tanahashi, Y., and Esashi, M., 1998, "Small diameter active catheter using shape memory alloy", Proceedings of the IEEE Annual International Workshop on Micro Electro Mechanical Systems, pp. 419-424

Hammons, T. J., 2000, "1999 PowerTech review", IEEE Power Engineering Review, pp. 16-20

Hasegawa, Y., Itoh, K., Izawa, H., and Itoh, T., 1995, "Development of micro mobile machine with wheels", Proceedings of the International Symposium on Micro Machine and Human Science, pp. 219-224

Hayashi, I. and Iwatuki, N., 1998, "Micro moving robotics", Proceedings of the 1998 International Symposium on Micromechatronics and Human Science, pp. 41-50

Henkenius, M., 1991, "Electric Motor", in *Popular Mechanics*

Higuchi, T., Yamagata, Y., Furutani, K., and Kudoh, K., 1990, "Precise positioning mechanism utilizing rapid deformations of piezoelectric elements", Proceedings of the IEEE Annual International Workshop on Micro Electro Mechanical Systems, pp. 222-226

Hirose, S., Ikuta, K., and Umetani, Y., 1984, "A new design method of servo-actuators based on the shape memory effect", in *Theory and Practice of Robots and Manipulators*, MIT Press, Cambridge, MA

Hollar, S., Bergbreiter, S., and Pister K. S., 2003, "Bidirectional inchworm motors and two-DOF robot leg operation", Proceedings of the IEEE International Conference on Solid State Sensors, Actuators and Microsystems, vol. 1, pp. 262-267

Hollerbach, J., Hunter, I. and Ballantyne, J., 1992, "A comparative analysis of actuator technologies for robotics", in *The Robotics Review* 2, MIT Press, Cambridge, MA, pp. 299-342

Honma, D., Yoshiyuki, M., and Igushi, N., 1985, "Micro robots and micro mechanisms using shape memory alloy", Journal of Robotic Systems, vol. 2, pp. 3-25

Hyun, J. M., Hvung, J. L., Young, M. L., Juang, J. P., Byungkyu K., and Soo, H. K., 2001, "Magnetic impact actuator for robotic endoscope", Proceedings of International Symposium on Robotics, pp. 1834-1838

Idogaki, T., Kanayama, H., and Ohya, N., 1995, "Characteristics of piezoelectric locomotive mechanism for an in-pipe micro inspection machine", Proceedings of International Symposium on Micro Machine and Human Science, pp. 193-198

Iizuka, T. and Fujita, H., 1996, "A threaded wobble motor with 6-pole stator", Proceedings of the IEEE International Symposium on Micro Machine and Human Science, pp. 189-193

Ikuta, K., 1988a, "The application of micro/miniature mechatronics to medical robotics", Proceedings of the IEEE International Workshop on Intelligent Robots, pp. 9 -14

Ikuta, K., Tsukamoto, M., and Hirose, S., 1988b, "Shape memory alloy servo actuator system with electric resistance feedback and application for active endoscope", Proceedings of the IEEE International Conference on Robotics and Automation, pp. 427-430

Ikuta, K., Kawahara, A., and Yamazumi, S., 1991, "Miniature cybernetic actuators using piezoelectric device", Proceedings of the IEEE Annual International Workshop on Micro Electro Mechanical Systems, pp. 131-136

Ikuta, K., Aritomi, S., and Kabashima, T., 1992, "Tiny silent linear cybernetic actuator driven by piezoelectric device with electromagnetic clamp", Proceedings of the IEEE Annual International Workshop on Micro Electro Mechanical Systems, pp. 232-237

Ikuta, K., Nokata, M., and Aritomi, S., 1994, "Biomedical micro robots driven by miniature cybernetic actuator", Proceedings of the IEEE Annual International Workshop on Micro Electro Mechanical Systems, pp. 263 -268

Ikuta, K., Ichikawa, H., Suzuki, K., and Yamamoto, T., 2003, "Micro hydrodynamic actuated multiple segments catheter for safety minimally invasive therapy", Proceedings of IEEE International Conference on Robotics and Automation, vol. 2, pp. 2640 -2645

Ioi, K., 1999, "A mobile micro-robot using centrifugal forces", Proceedings of the IEEE/ASME International Conference on Advanced Intelligent Mechatronics, pp.

736-741

Ishihara, H., Fukuda, T., Kosuge, K., and Arai, F., 1994, "Approach to autonomous micro robot - micro line trace robot with reflex algorithm", Proceedings of the IEEE Symposium on Emerging Technologies and Factory automation, pp. 78-83

Ishiyama, K., Arai, K.I., Sendoh, M., and Yamazaki, A., 2000, "Spiral-type micro-machine for medical applications", Proceedings of the IEEE International Symposium on Micromechatronics and Human Science, pp. 65-69

Jenkins, D. F. L., Clegg, W. W., Cattan, E., and Remiens, D., 2001, "PZT thin film bi-layer devices for phase controlled actuation in MEMS", Journal of Electroceramics, vol. 7, pp. 5-11

Jordan, T. L. and Ounaies, Z., 2002, "Characterization of piezoelectric ceramic materials", in *Encyclopedia of Smart Materials*, John Wiley & Sons, Inc.

Jufer, M., *et al.*, 1995, "Electromagnetic high speed micromotor", Proceedings of the 26th Symposium on Incremental Motion Systems & Devices

Kanerva, S., 2005, "Simulation of electrical machines, circuits, and control systems using finite element method and system simulator", PhD Dissertation, Helsinki University of Technology, Finland

Kassim, I., Phee, L., Ng, W., Gong. F., Dario, P., and Mosse, C. A., 2006, "Locomotion techniques for robotic colonoscopy", IEEE Engineering in Medicine and Biology Magazine, vol. 25, pp.49-56

Kim, B., Lee, M. G., Lee, Y. P., Kim, Y. I., and Lee, G. H., 2006, "An earthworm-like micro robot using shape memory alloy actuator", Sensors and Actuators A, vol. 125 pp.

429-437

Lagorce, L. K. and Allen, M. G., 1996, "Micromachined polymer magnets", Proceedings of the IEEE Annual International Workshop on Micro Electro Mechanical Systems, pp. 89-90

Laithwaite, E. R., 1971, *Linear electric motors*, Mills & Boon Ltd.

Lang, W., 1999, "Reflection on the future of microsystems", Sensors and Actuators A, vol. 72, pp.1-15

Lehr, H., *et al.*, 1996, "Microactuators as driving units for microrobotic systems", SPIE proceedings, vol. 2906, pp. 202-210

Lesquesne, B., 1992, "Permanent magnet linear motors for short strokes", Conference Record of the IEEE Industry Applications Society Annual Meeting, vol. 1, pp. 162-170

Lewis, E. V., 1988, *Principles of naval architecture*, Society of Naval Architects and Marine Engineers, Jersey City, NJ., USA

Lim, Y. M., Lee J., Park, J., Kim, B., Park, J.-O., Kim, S. H., and Hong, Y.-S., 2001, "A self-propelling endoscopic system", Proceedings of the IEEE/RSJ International Conference on Intelligent Robots and Systems, vol. 2, pp. 1117-1122

Lind, M., Kallio, P., and Koivo, H. N., 1998, "Linear motion miniature actuators", Proceedings of 2nd Tampere International Conference on Machine Automation

Lu, H., Zhu, J., and Guo, Y., 2005, "Development of a slotless tubular linear interior permanent magnet micro motor for robotic applications," IEEE Transactions on Magnetics, vol. 41, no. 10, pp. 3988-3990

Magnussen, B., Fatikow, S., and Rembold, U., 1995, "Actuation in microsystems: problem field overview and practical example of the piezoelectric robot for handling of microobjects", Proceedings of the INRIA/IEEE Symposium on Emerging Technologies and Factory Automation, vol. 3, pp. 21-27

Martel, S., Sherwood, M., Helm, C., Garcia de Quevedo, W., Fofonoff, T., Dyer, R., Bevilacqua, J., Kaufman, J., Roushdy, O., and Hunter, I., 2001, "Three-legged wireless miniature robots for mass-scale operations at the sub-atomic scale", Proceedings of IEEE International Conference on Robotics and Automation, vol. 4, pp. 3423 -3428

Mathworks Inc., 2005, *MATLAB R14 Service Pack 3 Help Documentation*

Mavroidis, C., Pfeiffer, C., and Mosley, M., 1999, "Conventional actuators, shape memory alloys, and electrorheological fluids", Invited Chapter in *Automation, Miniature Robotics and Sensors for Non-Destructive Testing and Evaluation*, Edited by Bar-Cohen

Measurement Specialties, Inc., 2006, *Piezo Film Sensors Technical Manual*, Rev. D

Mehregany, M., Nagarkar, P., Senturia, S. D., and Lang, J. H., 1990, "Operation of microfabricated harmonic and ordinary side-drive motors", Proceedings of the IEEE Annual International Workshop on Micro Electro Mechanical Systems, pp. 1-8

Mehregany, M., Tai, Yu-Chong, 1991, "Surface micromachined mechanisms and micromotors", Journal of Micromechanics and Microengineering, vol. 1, pp. 73-85

Metglas Inc., 2004, *Metglas® Magnetic Alloy 2605SA1 Data Sheet*

Mitumoto, N., Tsuruta, K., Shibata, T., and Kawahara N., 2001, "Wireless link system for communication and energy transmission of microrobot", Proceedings of the IEEE

International Symposium on Micromechatronics and Human Science, pp. 57-62

Nasar; S. A. and Boldea, I., 1976, *Linear motion electric machines*, John Wiley & Sons Inc.

Ng, W. S., Phee, S. J., Seow, C., and Davies, B. L., 2000, "Development of a robotic colonoscope", Digestive Endoscopy, vol. 12, pp. 131-135

Nicoud, J.-D. and Matthey, O., 1997, "Developing intelligent micro-mechanisms", Proceedings of the International Symposium on Micromechatronics and Human Science, pp. 119-124

Nishikawa, H., Sasaya, T., Shibata, T., Kaneko, T., Mitumoto, N., Kawakita, S., and Kawahara, N., 1999, "In-pipe wireless micro locomotive system", Proceedings of International Symposium on Micromechatronics and Human Science, pp. 141-147

Pelrine, R. and Bush-Vishniac, I., 1987, "Magnetically levitated micro machines", Proceedings of the IEEE Micro Robots and Teleoperators Workshop, pp. 34-37

Quirini, M., Menciassi, A., Stefanini, C., Gorini, S., Pernorio, G., and Dario, P., 2005, "Development of a legged capsule for the gastrointestinal tract: an experimental set-up", Proceedings of the IEEE International Conference on Robotics and Biomimetics, pp.161-167

RF Norika online, 2004, http://www.rfnorika.com/ (last visited in Feb. 2007)

Robert, P., 2004, "Mems actuation: a range of principles and technologies", 6th annual review of CEA-LETI

Rosheim, M., 1994, *Robot Evolution: The Development of Anthrobotics*, John Wiley &

Sons.

Rover, B., 2006, "A short history of robots", available online at http://prime.jsc.nasa.gov/ROV/history.html (last visited in Feb. 2007)

Saunders, R. M., 1954, "Digital computers as an aid in electrical machine design", Transactions of American Institute of Electrical Engineering, vol. 73, pp. 189-192

Shao, J. W., 2003, "Direct back EMF detection method for sensorless brushless DC (BLDC) motor drives", Master Thesis, Virginia Polytechnic Institute and the State University, USA

Shibata, T., Sasaya, T., and Kawahara, N., 1998, "Microwave energy supply system for in-pipe micromachine", Proceedings of the IEEE International Symposium on Micromechatronics and Human Science, pp. 237-242

Shields, J., 1966, *Basic Piezoelectricity*, Howard W. Sams and Co. Inc., Indianapolis, Indiana

Shimoyama, I., 1995, "Scaling in microrobots", Proceedings of the IEEE/RSJ International Conference on Intelligent Robots and Systems, vol. 2, pp. 208-211

Slatkin, A. B., Burdick, J., and Grundfest, W., 1995, "The Development of a robotic endoscope", Proceedings of the IEEE/RSJ International Conference on Intelligent Robots and Systems, vol. 2, pp. 162-171

Slocum, A., 1992, *Precision machine design*, Prentice Hall, Englewood Cliffs (N.J)

Stefanini, C., Corrozza, M.C., and Dario, P., 1996, "A mobile microrobot driven by a new type of electromagnetic micromotor", Proceedings of the IEEE International

Symposium on Micro Machine and Human Science, pp. 195-201

Stewart, H., 1987, *Pneumatics and Hydraulics*, revised by Tom Phibin, Macmillan Publishing Company, New York, 4th Edition

Stronge, W. J., 2000, *Impact Mechanics*, Cambridge University Press

Sun, L., Sun, P., and Qin, X., 1998, "Study on micro-robot in small pipe", UKACC International Conference on Control, vol. 2, pp. 1212-1217

Suzuki, M., Yamada, N., Tsuchida, N., and Imai, K., 1994, "A study on position detection and control system of self-movable micro robot", Journal of the Japanese Society of Precision Engineering, vol. 60, pp. 1365-1369

Suzumori, K., Iikura, S., and Tanaka, H., 1991, "Development of flexible microactuator and its applications to robotic mechanisms", Proceedings of the IEEE International Conference on Robotics and Automation, vol.2, pp. 1622-1627

Suzumori, K., Miyagawa, T., Kimura, M., and Hasegawa, Y., 1999, "Micro inspection robot for 1-in pipes", IEEE/ASME Transaction on Mechatronics, vol. 4, pp. 286-291

Takeda, M., 2001, "Applications of MEMS to industrial inspection", Proceedings of the IEEE Annual International Workshop on Micro Electro Mechanical Systems, pp. 182-191

Toki Corporation, 1987, *Biometal Guidebook*, Tokyo, Japan

Torii, A., Koyanagi, T., and Ueda, A., 1999, "Structure of microrobots using electromagnetic actuators", Proceedings of the International Symposium on Micromechatronics and Human Science, pp. 235-240

Trimmer, W. and Jebens, R., 1989, "Actuators for micro robots", Proceedings of the IEEE International Conference on Robotics & Automation, vol. 3, pp. 1547-1552

Utsugi, M., 1979, "Tubular medical instrument having a flexible sheath driven by a plurality of cuffs", U.S. Patent 4,148,307

Wallace, R. S., 1993, "Miniature direct drive rotary actuators", Robotics and Autonomous Systems, vol. 11, pp. 129-33

Wallace, R. S., 1994, "Building and interfacing miniature direct drive actuators", Tutorial Notes, International Conference on Robotics and Automation

Wang, J., Jewell, G. W., and Howe, D., 2001, "Design optimisation and comparison of tubular permanent magnet machine topologies", IEE Proceedings of Electrical Power Applications, vol. 148, pp. 456-464

Wang, J., Howe, D., and Jewell, G. W., 2004, "Analysis and design optimization of an improved axially magnetized tubular permanent-magnet machine", IEEE Transactions on Energy Conversion, vol.19, pp. 289-295

Wood, D., Burdess, J. S., and Harris, A. J., 1998, "Actuators and their mechanisms in microengineering", Engineering Science and Education Journal, vol. 7, pp. 19-27

Yamaguchi, T., Kagawa, Y., Hayashi, I., Iwatsuki, N., Morikawa, K., and Nakamura, K., 1999, "Screw principle microrobot passing steps in a small pipe", Proceedings of the IEEE International Symposium on Micromechatronics and Human Science, pp. 149-152

Yedamale, P., 2003, "Brushless DC (BLDC) motor fundamentals", Microchip Technology Inc., AN885

Zhang, B. and Zhu, Z., 1997, "Developing a linear piezomotor with nanometer resolution and high stiffness", IEEE/ASME Transactions on Mechatronics, vol. 2, pp. 22-29

Zhang, Q., Wang, F., Wu, X., Li, W., and Jing, L., 2004, "A novel inchworm type linear magnetostrictive motor", Proceedings of the 4th International Power Electronics and Motion Control Conference, vol. 2, pp. 557-559

APPENDIX A

ELECTRICAL TETHER ESTIMATION

For an isolated hot surface (T_2) in proximity to a cooler surface (T_1), both surfaces of area A_s and separated by vacuum, the rate of heat transfer is given by,

$$P = A_s e_r \sigma (T_2^4 - T_1^4), \tag{A.1}$$

where e_r is the surface emissivity and σ = 5.67 x 10^{-8} W/m^2-K^4 the Stefan-Boltzmann constant.

Considering an uninsulated single conductor of length l_c, square cross-sectional area A_c, surface area A_s ($A_s = 2\sqrt{\pi} A_c^{1/2} l_c$), resistivity ρ_e, carrying a steady current I (A), and developing power P (W), which heats the wire from ambient temperature T_0 up to the maximum desired operating temperature T_{max}, following relationships can be obtained from the standard electrical formulas and (A.1):

$$R = \frac{\rho_e L}{A_c} \tag{A.2}$$

$$I = \left(\frac{P}{R}\right)^{1/2} = \left(\frac{2\sqrt{\pi} e_r \sigma A_c^{\frac{3}{2}} \left(T_{max}^4 - T_0^4\right)}{\rho_e}\right)^{1/2} \tag{A.3}$$

Thus for a copper wire of 0.1mm in diameter, with ρ_e = 1.724 x 10^{-8} Ω-m, e_r = 0.03 for polished copper, T_{max} = 373K (boiling point of water) and T_0 = 310K (body temperature), the current I can be found as 50mA and current density J will be 6.3×10^6A/m^2. Wires with electrical and thermal insulation can safely carry higher currents. Moreover, if the device is operating in a non continuous conduction mode, the endurable current of the copper wire can be even higher.

Reference:

Robert A. Freitas Jr., 1999, *Nanomedicine*, Volume I: Basic Capabilities, Landes Bioscience, Georgetown, TX, USA

APPENDIX B

CENTRAL DIVIDED DIFFERENCE

The second order partial derivative can be approximated using central divided difference technique. Considering a function with one variable, $f(x)$, its second order partial derivative $\partial^2 f(x)/(\partial x)^2$ can be solved approximately as

$$\left.\frac{\partial f(x)}{\partial x}\right|_{x+\frac{1}{2}\Delta x} = \frac{f(x+\Delta x)-f(x)}{\Delta x}, \tag{B.1}$$

$$\left.\frac{\partial f(x)}{\partial x}\right|_{x-\frac{1}{2}\Delta x} = \frac{f(x)-f(x-\Delta x)}{\Delta x}, \tag{B.2}$$

$$\begin{aligned}\left.\frac{\partial f^2(x)}{\partial x^2}\right|_x &= \frac{[f(x+\Delta x)-f(x)]/\Delta x-[f(x)-f(x-\Delta x)]/\Delta x}{\Delta x} \\ &= \frac{f(x+\Delta x)-2f(x)+f(x-\Delta x)}{\Delta x^2}\end{aligned} \tag{B.3}$$

A function with two variables, $f(x_1, x_2)$, its second partial derivative $\partial^2 f/\partial x_1 \partial x_2$ can be solved similarly as

$$\frac{\partial f(x_1,x_2)}{\partial x_1} = \frac{\partial f(x_1+\Delta x_1,x_2)-\partial f(x_1-\Delta x_1,x_2)}{2\Delta x_1}, \tag{B.4}$$

$$\begin{aligned}\frac{\partial^2 f(x_1,x_2)}{\partial x_1 \partial x_2} &= \left[\frac{f(x_1+\Delta x_1,x_2+\Delta x_2)-f(x_1-\Delta x_1,x_2+\Delta x_2)}{2\Delta x_1}\right. \\ &\quad \left.-\frac{f(x_1+\Delta x_1,x_2-\Delta x_2)-f(x_1-\Delta x_1,x_2-\Delta x_2)}{2\Delta x_1}\right]/2\Delta x_2 \\ &= [f(x_1+\Delta x_1,x_2+\Delta x_2)-f(x_1-\Delta x_1,x_2+\Delta x_2) \\ &\quad -f(x_1+\Delta x_1,x_2-\Delta x_2)+f(x_1-\Delta x_1,x_2-\Delta x_2)]/4\Delta x_1\Delta x_2\end{aligned} \tag{B.5}$$

APPENDIX C

SCHEMATIC OF THE DRIVING CIRCUIT

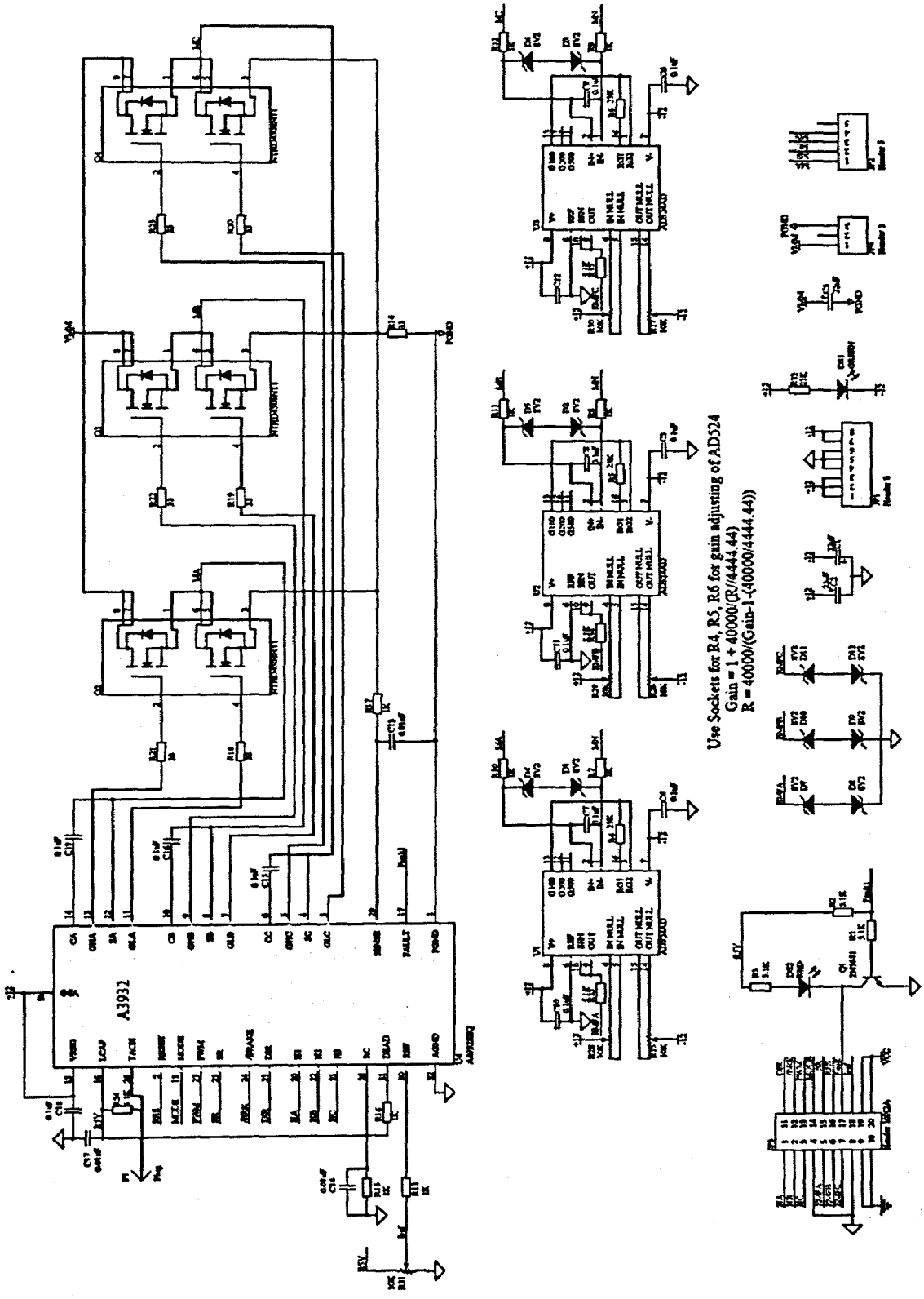

APPENDIX D

LIST OF PUBLICATIONS

Papers as the first author

[1] Haiwei Lu, Jianguo Zhu, Youguang Guo, and Zhiwei Lin, "A miniature short stroke tubular linear actuator and its control", the International Conference on Electrical Machines and Systems, 8-11 Oct., 2007, Seoul, Korea. (Accepted)

[2] Haiwei Lu, Jianguo Zhu, Zhiwei Lin, and Youguang Guo, "An inchworm mobile robot using electromagnetic linear actuator", submitted to Mecharonics, Elsevier.

[3] Haiwei Lu, Jianguo Zhu, Zhiwei Lin, and Youguang Guo, "A miniature short stroke linear actuator: design and analysis", submitted to IEEE transactions on Magnetics.

[4] Haiwei Lu, Jianguo Zhu, and Youguang Guo, "Calculation of differential inductances of a tubular linear PM motor", Journal of Japanese Society of Applied Electromagnetics and Mechanics (JSAEM), vol.15 Supplement, Sept. 2007.

[5] Haiwei Lu, Jianguo Zhu, and Youguang Guo, "Nonlinear inductances of a permanent magnet linear motor", Proceedings of the Australasian Universities Power Engineering Conference, Melbourne, Australia, 10-13 Dec. 2006, paper: TS10.2.

[6] Haiwei Lu, Jianguo Zhu, and Youguang Guo, "A permanent magnet linear motor for micro robots", Proceedings of the 6th IEEE International Conference on Power Electronics and Drive Systems, vol. 1, 28 Nov. - 01 Dec. 2005, Kuala Lumpur, Malaysia, pp. 590-595.

[7] Haiwei Lu, Jianguo Zhu, Youguang Guo, "Development of a slotless tubular linear interior permanent magnet micromotor for robotic applications", IEEE Transactions on Magnetics, vol. 41, No. 10, Oct. 2005, pp. 3988-3990.

[8] Haiwei Lu and Jianguo Zhu, "A study on characteristics of electromagnetic and piezoelectric micro actuators", Proceedings of the IEEE International Conference on Mechatronics, 10-12 July 2005, Taipei, Taiwan, pp. 591-595.

[9] Haiwei Lu, Jianguo Zhu, and Youguang Guo, "A tubular linear motor for micro robotic applications", Proceedings of the IEEE International Conference on Mechatronics, 10-12 July 2005, Taipei, Taiwan, pp. 596-601.

[10] Haiwei Lu, Jianguo Zhu, and Youguang Guo, "Development of a slotless tubular linear interior permanent magnet micro motor for robotic applications", Digests of the IEEE International Magnetics Conference, 4-8 April 2005, Nagoya, Japan, pp. 209-210.

[11] Haiwei Lu and Jianguo Zhu, "A comparison of piezoelectric and electromagnetic microactuators", JSAEM Studies in Applied Electromagnetic and Mechanics, vol. 15, 2005, pp. 101-107.

[12] Haiwei Lu, Jianguo Zhu, "A comparative study of microactuators driven by electric and magnetic principles", Proceedings of the Australasian Universities Power Engineering Conference, Brisbane, Australia, 26-29 September 2004, paper: 79.

[13] Haiwei Lu and Jianguo Zhu, "Microsensors for microrobotic systems - an overview", Proceedings of the Chinese Academy of Science Symposium on Information Acquisition, 24-26 Nov. 2003, HeFei, China, pp. 111-119.

Papers as a co-author

[14] Y. G. Guo, J. X. Chen, J. G. Zhu, H. Y. Lu, H. W. Lu, and J. X. Jin, "Development of a PM linear motor for driving HTS maglev vehicle", the International Conference on Electrical Machines and Systems, 8-11 Oct. 2007, Seoul, Korea. (Accepted)

[15] Z. W. Lin, J. G. Zhu, Y. G. Guo, J. J. Zhong, and H. W. Lu, "B and H sensors for 3D magnetic property testing", International Journal of Applied Electromagnetics and Mechanics, vol. 25, 2007, pp. 517-520.

[16] Y. G. Guo, J. X. Chen, J. G. Zhu, H. W. Lu, H. Y. Lu, and J. X. Jin, "An improved phase variable model for dynamic performance analysis of a PM claw pole SMC motor with brushless DC control", Proceedings of the Australasian Universities Power Engineering Conference, Melbourne, Australia, 10-13 Dec. 2006, paper: TS1.02.

[17] Y. G. Guo, J. G. Zhu, Z. W. Lin, J. J. Zhong, H. W. Lu, and S. H. Wang, "Calibration of sensing coils of a three-dimensional magnetic property tester", IEEE Transactions on Magnetics, vol. 42, No. 10, Oct. 2006, pp. 3243-3245.

[18] Ying Yan, Jianguo Zhu, Youguang Guo, and Haiwei Lu, "Modeling and simulation of direct torque controlled PMSM drive system incorporating structural and saturation saliencies", Proceedings of the 41st IEEE Industry Applications Society Annual Meeting, Florida, USA, 8-12 Oct. 2006, pp. 76-83.

[19] Z. W. Lin, H. W. Lu, J. G. Zhu, J. J. Zhong, X. L. Wang, and S. Y. Ding, "Vector Characterization of Soft Magnetic Materials", Journal of Applied Physics, vol. 97, 2005, paper: 10R306.

[20] Youguang Guo, Jianguo Zhu, and Haiwei Lu, "Design and analysis of a permanent magnet claw pole/transverse flux motor with soft magnetic composite core", Proceedings of the 6th IEEE International Conference on Power Electronics and Drive Systems, vol. 2, 28 Nov. - 01 Dec. 2005, Kuala Lumpur, Malaysia, pp. 1413-1418.

[21] Ying Yan, Jianguo Zhu, Haiwei Lu, Youguang Guo, and Shuhong Wang, "Study of a PMSM model incorporating structural and saturation saliencies", Proceedings of the 6th IEEE International Conference on Power Electronics and Drive Systems, vol. 1, 28 Nov. - 01 Dec. 2005, Kuala Lumpur, Malaysia, pp. 575-580.

[22] Ying Yan, Jianguo Zhu, Haiwei Lu, Youguang Guo, and Shuhong Wang, "A PMSM model incorporating structural and saturation saliencies", Proceedings of the 8th International Conference on Electrical Machines and Systems, vol. 1, 27-29 Sept. 2005, Nanjing, China, pp. 194-199.

[23] Youguang Guo, Jianguo Zhu, and Haiwei Lu, "Design of SMC motors using

hybrid optimization techniques and 3D FEA with increasing accuracy", Proceedings of the 8th International Conference on Electrical Machines and Systems, vol. 3, 27-29 Sept. 2005, Nanjing, China, pp. 2296-2301.

[24] Y. G. Guo, J. G. Zhu, H. W. Lu, Ram Chandru, S. H. Wang, and J. X. Jin, "Determination of winding inductance in a claw pole permanent magnet motor with soft magnetic composite core", Proceedings of Australasian Universities Power Engineering Conference, Hobart, Australia, 25-28 Sept. 2005, pp. 491-496.